PHYSICO-CHEMICAL CHARACTERISTICS AND APPLICATION POTENTIAL OF ADVANCED NICKEL TITANATE AND NICKEL COBALTITE NANOFIBERS

Thesis

Submitted in partial fulfilment of the requirements for the degree of

DOCTOR OF PHILOSOPHY

by

SACHIN KUMAR B.

DEPARTMENT OF METALLURGICAL AND MATERIALS
ENGINEERING
NATIONAL INSTITUTE OF TECHNOLOGY KARNATAKA,
SURATHKAL, MANGALURU – 575025
January, 2019

DECLARATION

by the Ph.D. Research Scholar

I hereby *declare* that the Research Thesis entitled "**Physico-Chemical Characteristics and Application Potential of Advanced Nickel Titanate and Nickel Cobaltite Nanofibers**", which is being submitted to the **National Institute of Technology Karnataka, Surathkal** in partial fulfilment of the requirements for the award of the Degree of **Doctor of Philosophy** in **Metallurgical and Materials Engineering** is a *bonafide report of the research work carried out by me*. The material contained in this Research Thesis has not been submitted to any University or Institution for the award of any degree.

SACHIN KUMAR B.

Register number: 135046MT13F01

Department of Metallurgical and Materials Engineering

Place: NITK-Surathkal

Date: 25-01-2019

CERTIFICATE

This is to *certify* that the Research Thesis entitled "**Physico-Chemical Characteristics and Application Potential of Advanced Nickel Titanate and Nickel Cobaltite Nanofibers**", submitted by **Sachin Kumar B.** (Register Number: **135046MT13F01**) as the record of the research work carried out by him, is *accepted as the Research Thesis submission* in partial fulfilment of the requirements for the award of degree of **Doctor of Philosophy**.

Dr. Sreeram K. Kalpathy

Research guide, IIT Madras

Prof. S. Anandhan

Research guide and Chairman-DRPC

<u>Dedicated to my family, cosmos, and for the philanthropy…</u>

ACKNOWLEDGEMENT

Madras, for his motivation and stimulus that steered this journey with right balance. His emphasis attacking practical problems with theoretical approach and pursuit for simplicity have forever shaped my view towards research. The exchange of knowledge, persuading for the right answer, sustained effort for convincing, and affable behavior made me comfortable in reaching the destiny of this journey. I would also like to thank his family members for their continual love, care, and support they extended me throughout this journey. Special thanks to his brother, Mr. Sreenidhi K., for providing access to phase diagrams at early stages of this work. And patently, for those irresistible yummy cookies, that I use to grab more!

The choice was made, the journey was destined, but without the personification of these two aces, this scientific exploration of *seeing materials in different light* was impossible. They were my de facto eyes in this journey of engineering science and made me explore the beauty of materials chemistry and materials physics. I have witnessed their capacity of knowledge, skills, passion, courage, strategy, integrity, and responsibilities, especially for their students and have always set a benchmark for me in life. They always aspired and made me feel so comfortable with a message that, "*We are here… We are waiting… for you, anytime!*". Without them I would have easily succumb to folly, it's been an honor to be part of their life because I live on discovering the beautiful aspects of the scientific world. My heartfelt sincere thanks to them for their edifying suggestion, insightful discussions, and support. And also, for teaching me to demand for truth throughout this journey, which made me tenacious to this work and yielded the reward.

With sense of pride and dignity, my largest appreciation to my Research Progress Assessment Committee members, Prof. K. Narayan Prabhu, Department of Metallurgical and Materials Engineering, NITK, and Prof. M. N. Satyanarayan, Department of Physics, NITK, for their awe-inspiring support, thoughtful comments, and constructive suggestions on the work.

I owe a very important debt to the great souls that unite to accomplish this work: Dr. S. B. Arya, Department of Metallurgical and Materials Engineering, Prof. M. N. Satyanarayan, Department of Physics, NITK, Prof. A.C. Hedge and Dr. Kartick Tarafder, Department of Chemistry, NITK, Dr. A. M. Shanmugharaj, Department of

I would like to show my greatest appreciation to the technicians and non-teaching staffs in Department of Metallurgical and Materials Engineering, without their timely boundless help, this work or journey was dreadful. With immense pleasure I

record my gratitude to Mrs. Sharmila Dinesh for her constant support in all clerical works, Mrs. Vinaya D. Shettigar, Mr. Sundra Shettigar, Mr. Dinesha Shettigar, Mr. Ismail, and Mr. Sachin for their kind assistance in laboratories and office. I specially thank Mr. Yashvanth K. S. and Mr. Satish P. for their kind aid in building Sudarshan (rotating disc collector) and providing support for technical experiments.

My special appreciation goes to my colleagues who had been a giant shoulder to enjoy journey with meticulous assistance and technical and non-technical discussions. Fruitful results would not have hastened without the engorgement, fun-time, and cooperation of Dr. T. Senthil, Dr. Gibin George, Dr. Akshatha G. Patil, Mr. Shantharama, Mr. Rahul Sathyanath, Ms. Shamitha C., Mr. Mohammed Khalifa, Mr. Nitin Reddy, Ms. Deeksha B., Mr. Sawan Shetty, and Mr. Govind Ekbote.

I am indeed delighted to extend my honest thanks to my all friends for their love and affection, who kept my spirits high during my research work, Navodayans from school, Votrasi and Kaw Kaw Gang from Bachelors, SYMs from Masters, Mr. Shashi U. S., Dr. Melby Chacko, Dr. Shamanth V., Dr. Sharath P. C., Mr. Pranesh Rao K. M., Mr. Makesh M., Dr. Sudheer R., Mr. Basavaraj Nainegali, Mr. Sangamesh Rajole, Mr. Shivaram M. J., Mr. Gurudath B., Mr. Pavankumar R. Sondar, Mr. Chethan Kumar B. are only a few among them. I'm always thankful to Ms. Deeksha Kunder from Mangalore University for her love and affection. I take this opportunity to thank all my teachers, mentors, and to every great soul who has passed on their knowledge to me, sculpted and motivated the curiosity in me to ask questions in scientific world, which was root and foundation to bestow this work.

The dissertation must surely bear the imprint of the prayers, sacrifices made, love, and affection showered on me by my family members. To express my sincere gratitude to my parents in the form of words, is rather restrictive both in expression of quantum. Yet at this juncture, it is my esteemed duty to reserve my high regards to my dad, Mr. K. Balakrishna Murthy, and my mom, Mrs. D. R. Chandrika Balu, and also my proud ancestors, who rooted love for materials engineering and spinning in me. Also, to the most adorable, ever best friend, well-wisher, my brother, Mr. Pavan Kumar B., along with my family members (Mrs. Neetha L., Chintu, and baby Vasishta Devanga) whose sacrifice, love and affection, kindness, confidence, selfless help, and

ABSTRACT

Nickel titanate (NTO) and nickel cobaltite (NCO) nanofibers were synthesized by sol-gel electrospinning process using poly(styrene-*co*-acrylonitrile) [SAN] as a polymeric binder. The as-synthesized precursor nanofibers were pyrolyzed at different pyrolysis conditions based on the results of thermal analysis, such that there was no impurity or phase separation in the obtained inorganic nanofibers. Both pyrolysis soaking temperature (T) and time (t), being the influential factors in crystallite and particle growth kinetics by diffusion, play a vital role in morphological and structural evolution of nanostructures. At an isochronal $t = 2$ h, NTO nanofibers were synthesized at three different T (*viz.*, 773, 973, and 1173 K) to correlate the difference in their physico-chemical properties as a function of T and to optimize the same for proposed applications. Besides, NCO nanofibers were synthesized at three different t (*i.e.*, 2, 4, and 6 h) for isothermal T = 773 K. The morphological, structural, electrochemical, electrical, and magnetic properties of the obtained inorganic nanofibers were characterized using various techniques. It was observed that as the pyrolysis conditions (T and t) were varied the properties of resultant inorganic nanofibers also changed. This in turn influenced their performance and ability in the applications studied. The applicability of NTO nanofibers was explored as bifunctional electrocatalysts for water splitting. The NCO nanofibers developed were used in non-enzymatic sensing of glucose and H_2O_2. In addition, their water splitting ability was also studied. The properties of these nanostructures are relevant to their synthesis routes and particle/fiber shape, as the surface atoms play key role in electrocatalytic reactions, magnetic anisotropies, and electrical conduction mechanism. Furthermore, the results showed that the residues from SAN (binder) degradation and the degradation kinetics itself can impact the properties of as-prepared inorganic nanofibers, which helps in tailoring the structure, composition, and morphology of NTO and NCO nanofibers. Also, a comparative study on NCO nanofibers obtained using precursor nanofibers collected on rotating disc and rotating drum collectors suggest that the former is best suited for metal oxides synthesis to obtain optimal electrospun nanofibers.

Keywords: Poly(styrene-*co*-acrylonitrile), rotating disc collector, spinel, electrocatalyst, magnetic property

CONTENTS

LIST OF SCHEMES

LIST OF FIGURES

LIST OF TABLES

NOMENCLATURE

(F)	Splitting of free-ion in octahedral symmetry
$-Z''$	Imaginary component of impedance
%	Percent or percentage
°	Degree
∂	Partial derivative
ΔG	Change in Gibbs free energy
ΔH	FWHM of the curve $\dfrac{dM}{dH}$
$\varnothing$	Diameter of electrospinning collector
Å	Angstrom
$\Gamma(\varphi)$	Ambient environment function of relative humidity
Λ	Active sites on surface of electrocatalyst
Ω	Angular velocity
Ω	Ohm
α	Absorption coefficient
β, FWHM	Full-width at half maxima
χ^{-1}	Inverse magnetic susceptibility
δ	Partial charge
ε	Microstrain/ Lattice strain
ϕ	Wind-on angle
φ	Relative humidity
η	Overpotential
θ	Theta, Angle
θ_c	Curie temperature
θ_T	Magnetization measuring temperature
θ_w	Weiss temperature
κ	Dimensionless shape factor
μ	Micron

μ_0	Permeability constant
µA	Microampere
μ_B	Bohr magnetons
µM	Micromolar
µm	Micrometer
v	Velocity of a fiber
υ	Frequency of the photon
ρ	Density
ρ_D	Dislocation density
ρ_R	Electrical resistivity
τ	Factor of dislocation density
ω	Magnitude of Ω
ξ	Exponential factor
$2L_O$	First over tone mode
A	Rate constant
A_{1g}, A_g	Irreducible representation of symmetry elements
a_{APD}	Average nanoparticle diameter
AFM	Anti-FM
Ag	Argentum (Silver)
Al	Aluminum
Ar	Argon
at%	Atomic percent
Au	Aurum (Gold)
A_0	Arrhenius pre-exponential factor
B	Boron
b	Tafel slope
Ba	Barium
BET	Brunauer-Emmett-Teller
BJH	Barrett-Joyner-Halenda
BMP	Bound magnetic polaron

Br	Bromine
C	Carbon
C	Curie constant
C_{3i}^{2}	*Schoenflies* notation of point groups of symmetry
CA	Chronoamperometry
CATH	Cobalt (II) acetate tetrahydrate
CB	Conduction band
cc	Cubic centimeter
C_{dl}	Pseudo capacitance of double-layer
CE	Counter electrode
Ce	Cerium
C_{FU}	Coefficient of fiber uniformity
CIE	International Commission on Illumination
C_{m}	Molar C
cm	Centimeter
Co	Cobalt
CO_2	Carbon dioxide
CP	Chronopotentiometry
Cr	Chromium
CT	Charge-transfer
Cu	Cuprum (Copper)
CV	Cyclic voltammetry or voltammograms
D	Dimensional
D	Crystallite size
d	Derivative
d	d-orbital with angular momentum quantum number $= 2$ or in case of d-spacing it is the distance between the planes of atoms that give rise to X-ray diffraction peaks
D_0	Initial crystallite size
D1	Depth obtained after first 25 s of Ar^+ ion etching

D2	Depth obtained after second 25 s of Ar^+ ion etching
d_{AFD} , AFD	Average fiber diameter
dec	Decade (log scale)
DFT	Density functional theory
DMF	N, N-dimethylformamide
DoA	Degree of alignment
DoR	Degree of randomness
DOS	Density of state
D_p	Particle or grain size
DSC	Differential scanning calorimetry or calorimetric
DTG	Differential TGA
E	Applied electric field
E_a	Activation energy
E_{bg}	Band gap energy
E_g , e_g	Irreducible representation of symmetry elements
EDS or EDX	Energy-dispersive X-ray spectroscopy or spectroscope
EIS	Electrochemical impedance spectroscopy
E_{RHE}	Potential at RHE
E_{SCE}	Potential at SCE
etc.	Et cetera
eV	Electron-volt
E_{we}	Potential at working electrode
E-x	Exponential, 10^{-x}
F	Fluorine
f	*f*-orbital with angular momentum quantum number = 3
F_{2g}	Irreducible representation of symmetry elements
FC	Field cooling
F-center	Farbe center is a type of crystallographic defect
Fe	Ferrum (Iron)

FESEM	Field Emission Scanning Electron Microscopy or Microscope
Fig.	Figure
FM	Ferromagnetic or Ferromagnetism
FTIR	Fourier-transform infrared
g	gram
G	Gauss
Gd	Gadolinium
Ge	Germanium
GE	Glassy carbon or Graphite electrode
GL	Graphene-like
Glucose	*Dextrose*-glucose or *D*-glucose
H	Hydrogen
H	Applied magnetic field
h	*Planck's* constant
H_2	Hydrogen gas
H_2O	Water
H_2O_2	Hydrogen peroxide
H_{ads}	Adsorbed hydrogen
H_c	Coercivity or coercive field
HCl	Hydrochloric acid
HER	Hydrogen evolution reaction
HNO_3	Nitric acid
HRTEM	High-resolution transmission electron microscopy or microscope
I	Current
i.e.	That is
ICDD	International Centre for Diffraction Data
In	Indium
INTO	Ilmenite phase NTO
Ir	Iridium

ISO	International Organization for Standardization
j	Current density
K	Kelvin
K	Anisotropy constant
kG	Kilogauss
kJ	Kilo-Joule
KOH	Potassium hydroxide
k-points	Sampling points in the first Brillouin zone of the material
kV	Kilovolt
ℓ	Sheet thickness
La	Lanthanum
Li	Lithium
ln	Natural logarithm
LOD	Limit of detection
log	Logarithm to base 10
LOQ	Limit of quantification
LSV	Linear sweep voltammetry or voltammograms
M	Molar
M	Magnetization
m	Meter
m	Slope
mA	Milliampere
mbar	Millibar
meV	Millielectron-volt
Mg	Magnesium
mg	Milligram
mL	Milliliter
mM	Millimolar
M_{mol}	Molar mass
Mn	Manganese

Mo	Molybdenum
mol	Mole
M_r	Remanence
M_s	Saturation magnetization
MTMO	Mixed transition metal oxide
mTorr	Millitorr
$\overline{M_v}$	Viscosity $\overline{M_w}$
$\overline{M_w}$	Average molecular weight
mV	Millivolt
mW	Milliwatt
$M_y^x O$ or M^x	x is the oxidation or ionic state of element, M, and y is the stoichiometry of compound $M_y O$
MΩ	Mega-Ohm
N	Nitrogen
n	intrinsic semiconductor with an electron donor as doping element
n	Crystallite growth exponent
N-rGO	nitrogen doped-rGO
n→ π*	Excitation of an electron from one of the unshared pairs to the π* orbital
N_2	Nitrogen gas
N_A	Avogadro number
NaOH	Sodium hydroxide
NATH	Nickel (II) acetate tetrahydrate
Nb	Niobium
n_B	Magnetic moment of unit cell
NCO	Nickel cobaltite
NCO-2	GL/NCO nanofibers developed at $t = 2$
NCO-4	GL/NCO nanofibers developed at $t = 4$
NCO-6	GL/NCO nanofibers developed at $t = 6$

Ni	Nickel
NIR	Near infrared
NIST	National Institute of Standards and Technology
nm	Nanometer
nm	Nanometer
N_P	Number of primary particles
NTO	Nickel titanate
O	Oxygen
O_2	Oxygen gas
OER	Oxygen evolution reaction
O_v	Octahedral void
P	Phosphorus
P	Pressure
p	intrinsic semiconductor with an electron acceptor as doping element
p	p-orbital with angular momentum quantum number = 1
PAN	Poly(acrylonitrile)
Pb	Plumbum (Lead)
Pd	Palladium
PEO	Poly(ethylene oxide)
PL	Photoluminescence
Pr	Praseodymium
Pt	Platinum
PVA	Poly(vinyl alcohol)
PVAc	Poly(vinyl acetate)
PVB	Poly(vinyl butyral)
PVDF	Poly(vinylidene fluoride)
PVP	Poly(vinyl pyrrolidone)
q	Columbic charge
Q_{CPE}	Constant phase element
R	Universal gas constant

R	Position or radius vector
RE	Reference electrode
R^2	Correlation coefficient
$R\bar{3}$	Hermann-Mauguin notation of point groups of symmetry
R_{ct}	CT resistance
RDI	Rotating disc
RDI$_c$	Pyrolyzed nanofibers obtained from pyrolysis of RDI$_p$
RDI$_p$	Precursor fibers collected over RDI collector
RDR	Rotating drum
RDR$_c$	Pyrolyzed nanofibers obtained from pyrolysis of RDR$_p$
RDR$_p$	Precursor fibers collected over RDR collector
R_{elect}	Electrolyte resistance
rGO	Reduced graphene oxide
RHE	Reversible hydrogen electrode
R$_S$	Sheet resistance
Ru	Ruthenium
S	Sulphur
S	Surface of the sample
S	Remanence squareness
s	s-orbital with angular momentum quantum number $= 0$
s	Second
SAED	Selected area electron diffraction
SAN	Poly(styrene-*co*-acrylonitrile)
sat	Shake-up satellite peak
S_b	Standard deviation of blank signal
SCE	Saturated calomel electrode
SD	Standard deviation
SFD	Switch field distribution
Si	Silicon
Sn	Stannum (Tin)

SNTO	Spinel phase NTO
Sr	Strontium
SSA	Specific surface area
S_q	Spin quantum number
T	Pyrolysis soaking temperature
T	Stress tensor
t or t	Pyrolysis soaking time
t_{2g}	Irreducible representation of symmetry elements
Ta	Tantalum
T_B	Blocking temperature
Te	Tellurium
t_f	Time of flight
TGA	Thermogravimetry or Thermogravimetric
Ti	Titanium
Ti(O^{i}Pr)$_4$	Titanium (IV) isopropoxide
TiON	Titanium oxynitride
T_N	Neel temperature
TS	Technical specification
T_v	Tetrahedral void
u	Relative velocity of the fiber jet per unit mass
UV	Ultraviolet
V	Vanadium or Volt
VB	Valence band
Vis	Visible
$viz.$	Namely
vs.	Versus
VSM	Vibrating sample magnetometer
W	Wolfram (Tungsten)
w	Weight
w/v	Weight by volume
WE	Working electrode

wt%	Weight percent
XPS	X-ray photoelectron spectroscopy
XRD	X-ray diffraction
Y	Yttrium
Z'	Real component of impedance
ZFC	Zero-FC
Zn	Zinc
Zr	Zirconium

CHAPTER 1

CHAPTER 1

INTRODUCTION AND LITERATURE REVIEW
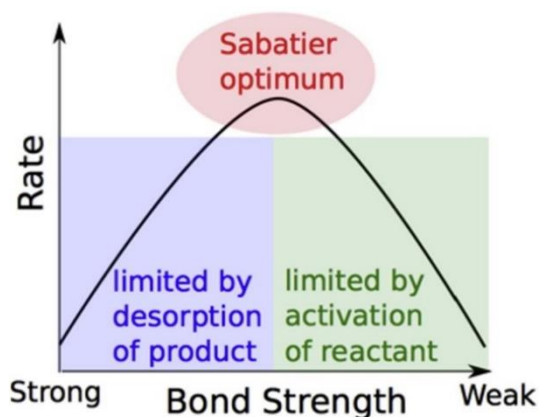
Scheme 1.1 Sabatier's catalytic reactivity principle; rate reaches a maximum at optimum interaction strength of reagent and catalyst (Medford et al. 2015).

This chapter enlightens scanty overview to nanostructured inorganic nanofibers, their synthesis techniques, and their potential applications as electrocatalyst and magnetic materials. An overview of sol-gel assisted electrospinning process in fabricating the inorganic nanofibers are discussed here. The advancement of utilizing poly(styrene-co-acrylonitrile) as a polymeric binder in precursor sol is debated here. Eventually, the motivation for the present research study along with its scope and objective are penned down.

1.1 INTRODUCTION

A material with any external dimension in nanoscale (length ~1 to 100 nm) or having internal structure or surface structure in the nanoscale is termed a "nanomaterial" as per (ISO/TS 80004-1 2015) . The generic term nanomaterial is inclusive of nano-objects and nanostructured materials. A discrete piece of material with one, two or three external dimensions in the nanoscale is termed as "nano-object", whereas a material having internal or surface composition of inter-related constituent parts in which one or more of those parts in a nanoscale is known as "nanostructured materials" as shown in Figure 1.1 (ISO/TS 80004-4 2011; ISO/TS 80004-2 2015). The physical and chemical

properties of nanomaterials are distinct from those of a single atom (or molecule or compound) and bulk matter with the same chemical composition. These differences between nanomaterials and the molecular and condensed-phase materials pertain to the spatial structures and shapes, phase changes, energetics, electronic structure, chemical reactivity, and catalytic properties of large, finite systems, and their assemblies. Some of the important issues in nanoscience relate to size effects, shape phenomena, quantum confinement, and response to external electric, magnetic, and optical excitations of individual and coupled finite systems.
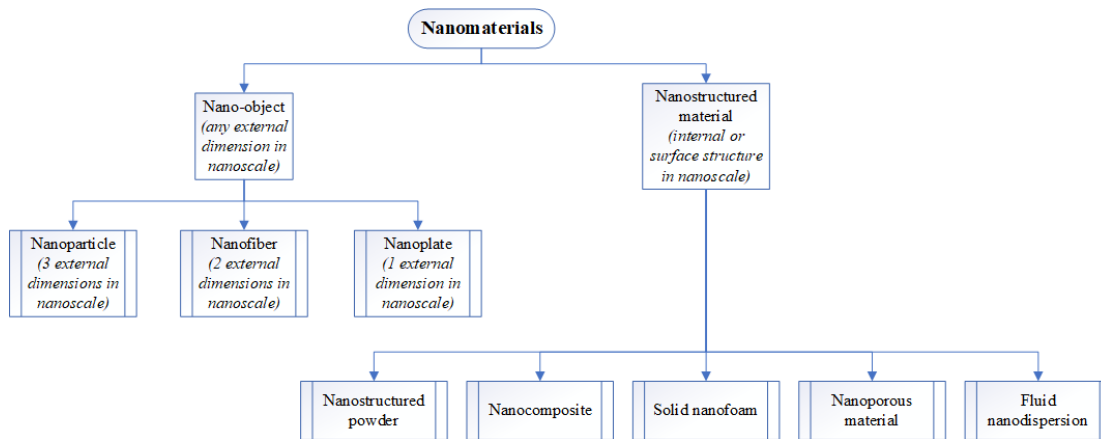
Fig. 1.1 Categories of nanomaterials defined as per ISO technical specification.

An example of this dimensionality of certain properties is the FM coercive force. It has been found that the dependence of H_c on D_p changes dramatically from a $1/D_p$ for larger grains ($D_p > 100$ µm) to a D_p^6 for grain sizes less than about 100 nm as shown in Figure 1.2. This occurs when the D_p becomes smaller than the FM domain wall thickness such that the domain wall now samples several, or many, grains and fluctuations in magnetic anisotropy on the grain size length scale that are then irrelevant to domain wall pinning and therefore to H_c. Thus, the reduction of particle/grain size to the regime of the domain wall width increases H_c towards a maximum controlled by the anisotropies present (Herzer 1997).

Among many nanomaterial architectures, the 1D or quasi-1D nanofibrous morphology has attracted interest due to its high aspect ratio, which enhances the mechanical, physico-chemical properties, and long-range ordering in the material.

These features affects the magnetic property and transport phenomena (electronic and ionic) of the material that is responsible for electrical, thermal, and interfacial properties (Xia et al. 2003). Such unique aspects make these materials suitable for application in various fields such as transistors, sensors, photo- and electrochemical catalytic reactions (Fig. 1.3).

The synergism of sol-gel technique (bottom-up approach) and electrospinning (top-down approach) delivers the tailor-made properties of the desired nanofibers without any defects, by easily controlling the process parameters, unlike the conventional synthesis techniques. The combination allows the design of morphology of the final inorganic nanofibers in such a way that the final product belongs to both nano-object and nanostructured material categories, known as "hierarchical structures". The process involves three major steps: (i) the preparation of a stable sol using sol-gel chemistry with the help of suitable polymeric binder and salts, (ii) the fabrication of precursor fibers by electrospinning, to obtain defect-free uniform nanofibers, and finally (iii) the pyrolysis of the precursor fibers to remove organic matter selectively, for obtaining inorganic nanofibers. Figure 1.4 shows the different morphological features of hierarchical TiO_2 derived nanofibers obtained using sol-gel assisted electrospinning followed by pyrolysis.
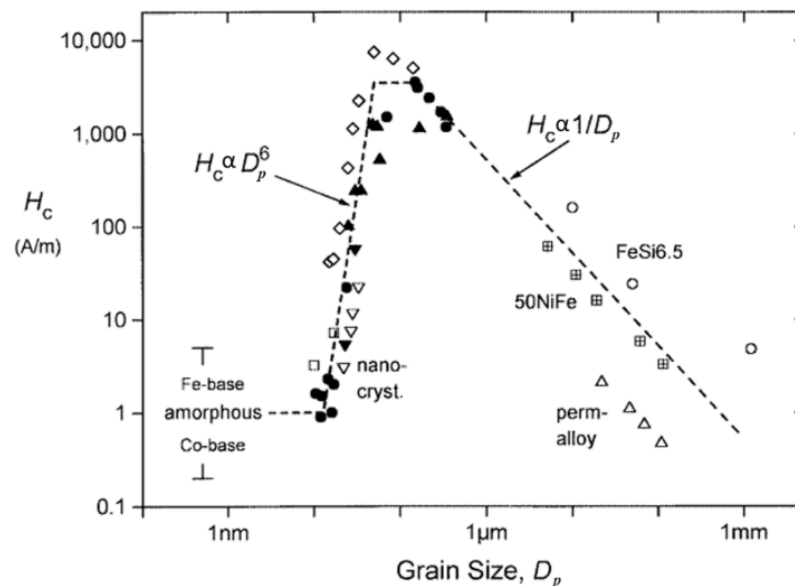
Fig. 1.2 Coercivity as a function of grain size of transition metal alloys (Herzer 1997).

3
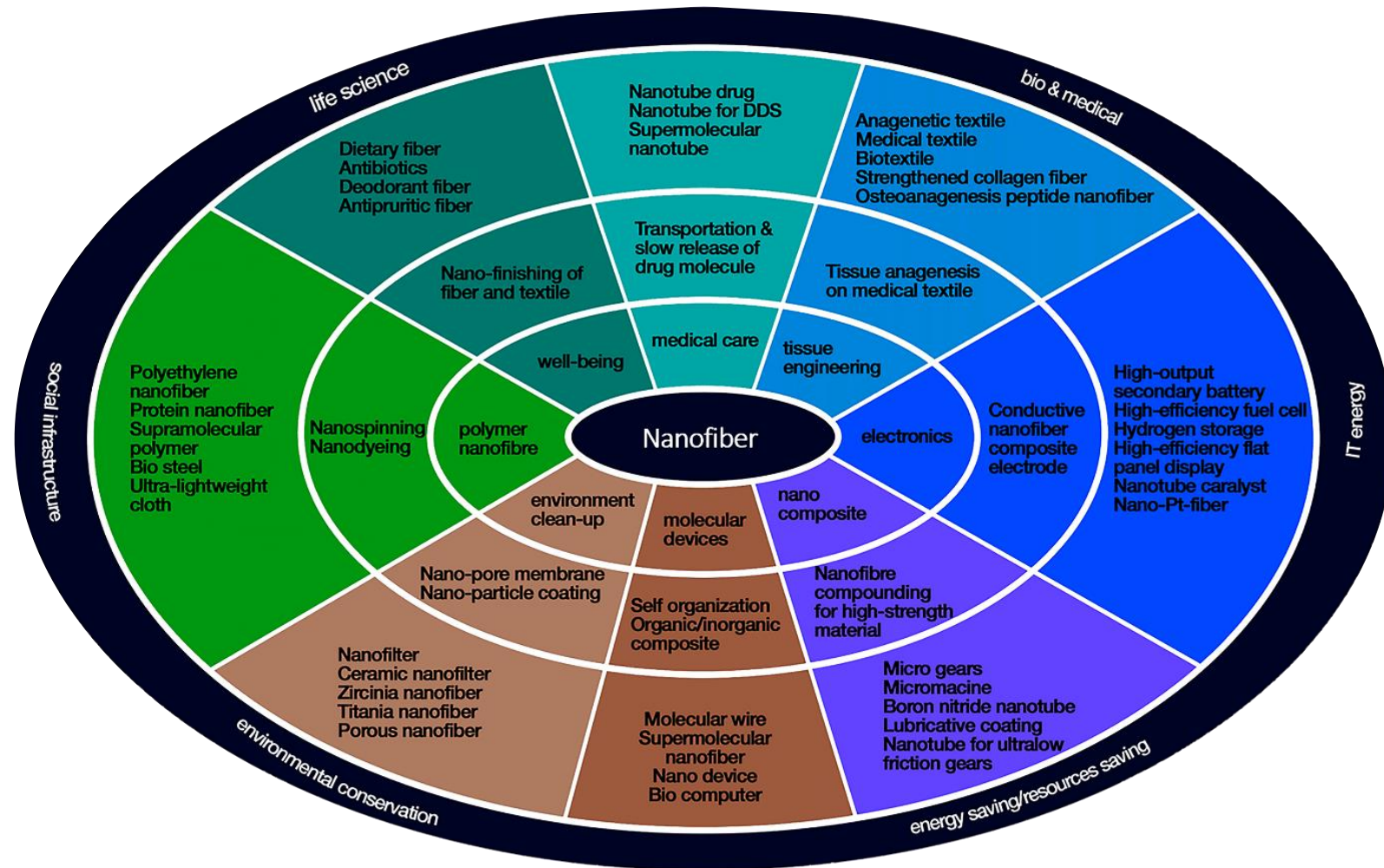
Fig. 1.3 Donut plot depicting the applications of nanofiber materials (Lyngaas 2015).
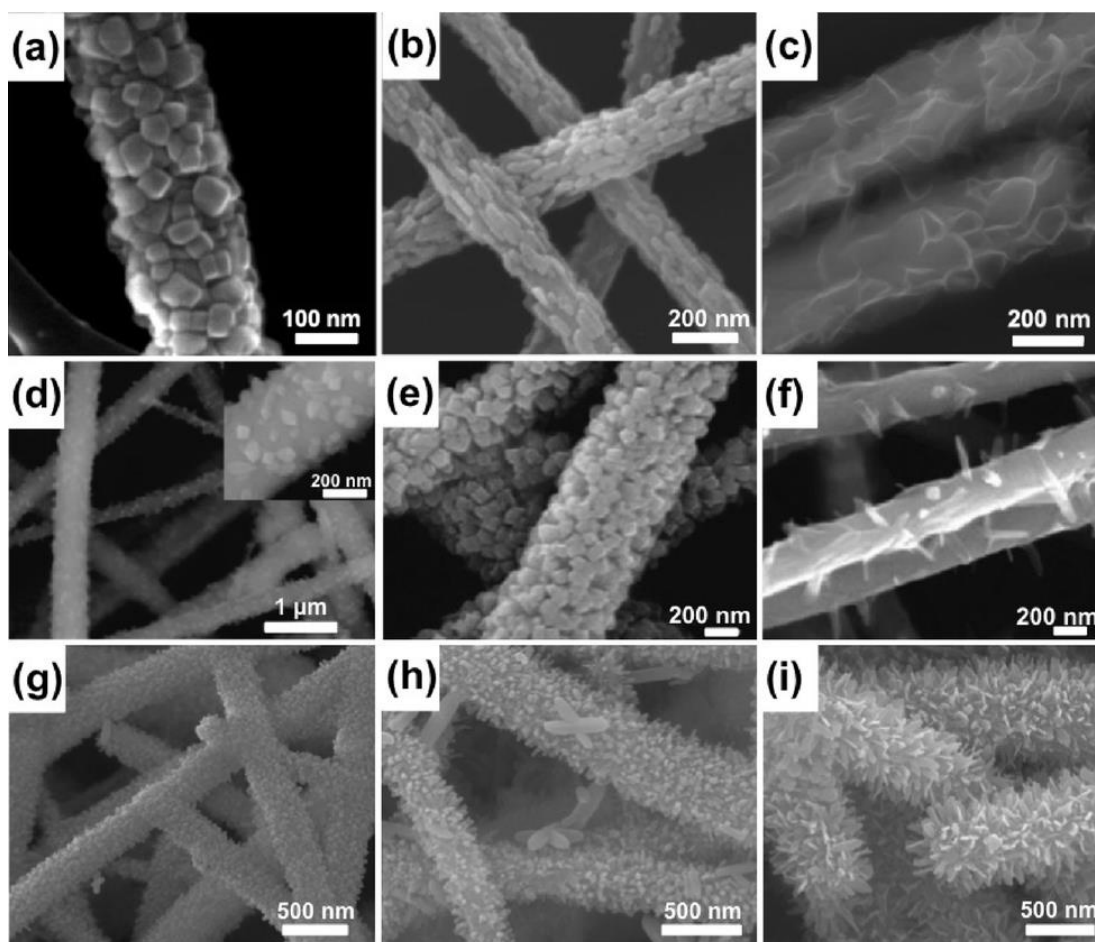
Fig. 1.4 Micrographs of electrospun 1D hierarchical structures: (a) TiO_2 with $SrTiO_3$ nanocubes heterostructures, (b) wheat grain-textured TiO_2/CuO, (c) TiO_2 with MoS_2 nanosheets, (d-f) SnO_2/TiO_2 heterostructures with SnO_2 nanoparticles, nanocrystals, and nanorods architectures, and (g-i) β-FeOOH/TiO_2 heterostructures with nanoparticles, needles and flakes (Gao et al. 2015).

1.1.1 Electrospinning technique

The electro-hydrodynamical phenomena called "electrospinning" launched polymer nanofibers into the broader realms of nanotechnology and materials science during the decades starting in 1990 and 2000. It was only since 2002, the electrospinning was explored as a high efficiency method for synthesis of 1D inorganic materials. Electrospinning has rapidly changed fiber making from a capital intensive, large scale process to a low cost, broadly applicable method that manufactures fibers on a laboratory bench, to serve diverse needs ranging from materials science and technology to life sciences and clinical medicine. In present scenario, the electrospinning technique

has been proven to be the only industrial scalable nanofiber production technology. A comparison of other nanofiber synthesis methods with electrospinning technique is shown in Table 1.1.

Table 1.1: Comparison of different fiber forming techniques (Senthil et al. 2016).

Fabrication technique	Advantages	Disadvantages
Drawing	Single nanofiber at a time. Simple instrumentation.	Time consuming. Non-scalable. Fiber dimensions cannot be controlled. Operator dependent.
Template synthesis	Uniform fibers can be obtained. Fiber dimensions can be varied. Different shapes can be achieved.	Not suitable for mass production. Replacement of templates are necessary.
Temperature-induced phase separation	Simple procedure. Minimal equipment complexity.	Time consuming. Not suitable for all polymeric materials. Non-scalable. Difficult to control fibers dimension.
Molecular self-assembly	Smaller nanofibers can be fabricated.	Time consuming for continuous nanofibers. Well-suitable for short fibers.
Lithography	Suitable for low aspect ratio fibers.	Complex processing. Skilled operator requirements.

	Simple equipment and easy alignment process. Low cost compared to the bottom-up method with industrial scalability. Uniform and high aspect ratio with 3D porous structure fibers. Do not require expensive purification.	Dependent on experimental parameters. Skilled operator is needed. High power consumption.
Electrospinning		

1.1.1.1 Set-up and mechanism of electrospinning

A typical electrospinning apparatus consists of three major components (Fig. 1.5): a high voltage power supply, a spinneret (a metallic capillary tip), and a collector (a grounded conductor). Generally, a syringe with syringe pump (flow rate controller) is used as a single spinneret for laboratory scaled equipment with a DC voltage supply ranging from 1 to 100 kV. The collector and steer come with different geometry to meet the non-woven fiber alignment, besides the commonly used static collector plate. In the electrospinning process, the polymer solution or melt with or without inorganic precursor having optimal Berry number (Ko 2006; Ko and Wan 2014) is feed into the spinneret. At high DC voltage applied, this viscous sol is electrified at positive electrode. When the voltage is optimal, the electrostatic repulsion force overcomes the surface tension of the sol and a fiber is erupted at the singularity of the conical structure called "Taylor cone" (Fig 1.5). This ejected fiber moves towards the grounded collector with high whipping instabilities under the action of solvent evaporation and charge repulsion in the fiber. During this travel, the fiber dries out from solvent and narrows further to obtain ultrafine fiber or nanofiber and collects on the collector. The alignment and additional diameter reduction of the fiber can be controlled by suitable type and geometry of the steer electrode and collector. The inorganic nanofibers are obtained by post treatments of collected precursor nanofiber such as pyrolysis.
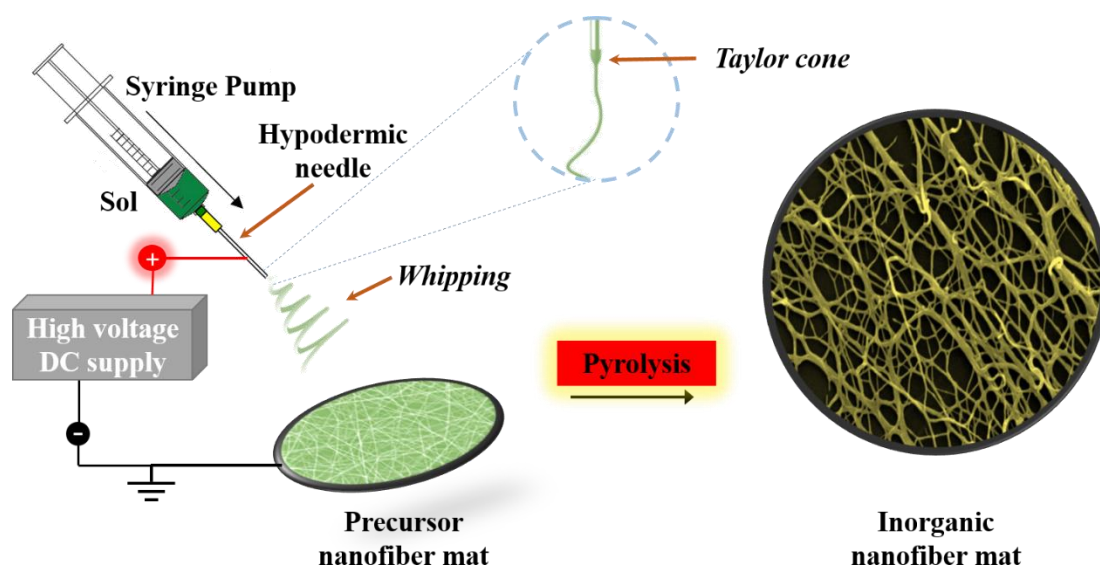
Fig. 1.5 Representation of sol-gel assisted electrospinning process followed by pyrolysis.

1.1.1.2 Controlling factors

The electrospinning process is controlled by many parameters, which mainly comprises of three parts: solution parameters, process parameters, and ambient parameters (Table 1.2). The optimization of these parameters is essential in controlling the fiber morphology such as diameter and porosity of the fiber. Each individual parameter and their interaction plays a vital role in formation of defect-free nanofibers (Senthil et al. 2016). Hence, obtaining an optimal condition regarding these parameters is a must.

Table 1.2: Parameters affecting electrospinning process.

Material parameters	Type of polymer (ionic/non-ionic, polar/non-polar, block/random copolymer, *etc.*)
	Molecular weight of the polymer
	Type of solvent/mixed solvents (Boiling point)
	Berry number
	Surface tension of polymer solution
	Electric conductivity of polymer solution
	Dielectric constant of polymer solution
	Additives
	Solubility and/or sol-gel chemistry of precursors in solvent

Process parameters	Electrostatic potential and Electric field strength
	Flow and Feed rate
	Type and diameter of spinneret or orifice
	Type, material and geometry of spinning equipment, steering and collector electrodes
	Distance between electrodes
	Velocity of rotating collector
Environmental parameters	Humidity
	Temperature
	Local atmosphere flow
	Atmospheric composition
	Pressure

1.1.2 Sol-gel technique

Sol-gel process is a 'bottom-up' approach in which the nanomaterials are chemically assembled from elementary chemical components, just like a wall is constructed from bricks and mortar. By definition, "sol" is a suspension of colloidal particles or molecules in a liquid and "gel" is a 3D network formed when the sol is mixed with a liquid which can help to form the network (Brinker and Scherer 2013). Generally, there are two methods of preparing inorganic nanofibers using sol-gel assisted electrospinning. First, inorganic precursors are mixed with polymers for electrospinning, followed by pyrolysis at high temperatures. Second, the reaction velocity and viscosity of the inorganic precursor solution can be adjusted for direct electrospinning, which is also known as *Pechini's* method. It is, however, difficult to control the rheological properties of the inorganic precursor, which leads to the shape and the diameters of the inorganic nanofibers being difficult to control too. To solve these problems, it is convenient to use first method, one has to introduce a polymer into the solution as a matrix to adjust the rheological properties, as well as an additive, such as a catalyst, to control the hydrolysis rate of the precursor. Hence, a typical spinnable precursor solution should contain an alkoxide or metal salt precursor, a polymer acting as a binder, an additive, and a relatively volatile solvent such as ethanol, water, isopropanol, chloroform, and DMF.

The strategy followed to fabricate inorganic nanofibers has four important steps: (i) mixing of molecules, where the precursor chemicals for the intended inorganic material, a gel forming medium (or a polymer), a solvent and an additive are mixed together, (ii) chemical treatment which will accelerate the polymerization of mixture to form a gel, (iii) shaping of the polymeric gel from the previous step to the final morphology, and finally (iv) high temperature treatment to remove the volatiles and organic phases from the shaped gel to achieve the inorganic material of required shape (Fig. 1.6). In sol-gel assisted electrospinning of synthesis of inorganic nanofibers, the role of electrospinning is to shape the polymeric gel to nanosized fibers. The significant advantage of sol-gel processing of inorganic powders is that homogeneous compositions can be prepared at temperatures lower than of required for conventional powder processes. Added to this, a high purity product with extreme complexity in stoichiometry (such as doping, ternary and quaternary systems) can be easily synthesized. Generally, metal salts of organic acids, in particular acetates but also formates, citrates, tartrates, *etc.*, are used for the metal oxide fiber synthesis.
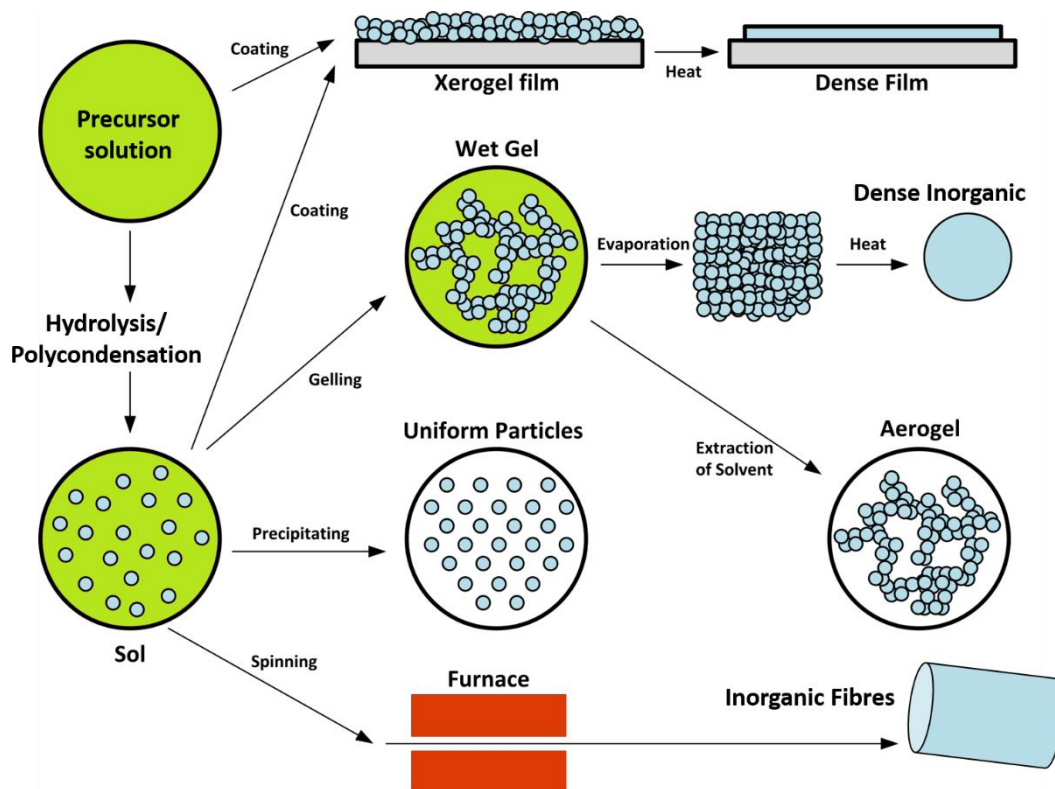
Fig. 1.6 Morphological tailoring of final product using different routes of sol-gel process (Brinker and Scherer 2013).

1.2   REVIEW OF LITERATURE

Inorganic nanomaterials are of special interest due of stability, structural and functional properties, semiconducting nature, abundant resource (some are natural available), low cost and ease of synthesis. Inorganic nanomaterials have proven their ideology especially in their nanofiber form from the lab scale material design to real time biological applications such as bio-imaging, sensing, drug delivery carries, smart materials, *etc.*, (Ramaseshan et al. 2007; Hu 2012; Dibenedetto and Aresta 2013). The combination of two or more synthesis techniques such as sol-gel assisted electrospinning followed by pyrolysis allows to design inorganic materials for desired properties throws high degree of versatility and applicability of the material for an efficient performance with low cost. The final properties and performance of the nanofibers, which is a function of nanofiber morphology is controlled by three major factors: (i) the composition and type of the precursors used, (ii) pressure and atmosphere of pyrolysis chamber, oxidizing or reducing or inert, and (iii) the nucleation and growth kinetics of inorganic nanofiber during pyrolysis, the pyrolysis temperature-time driven diffusion process. The morphology of precursor fibers changes dramatically at different temperature of pyrolysis depending on the polymeric binder and inorganic precursor used (Fig. 1.7).

Table 1.3 shows the various types of inorganic nanofibers synthesized through sol-gel assisted electrospinning process. Inorganic materials with 1D nano-architectures received increasing interest since it provided a good material system to investigate the dependence of electrical, optical, thermal and mechanical properties on dimensionality and size reduction (Wu et al. 2012a). Especially with high aspect ratio and porosity they were desired as building blocks in many applications such as catalysis, electronics, optoelectronics, sensors, energy storage devices and so on. The practical applications in multidisciplinary field, scalable for industrial production and convenient device integration made inorganic nanofibers extremely important for technological advances and progressive studies of these materials. Different classes of inorganic nanofibers such as oxides, carbides, nitrides, and sulfides were synthesized in decades using suitable precursors and studied for various potential applications in the field of textile, catalysis, sensors, batteries, fuel cells (Dai et al. 2011; Wu et al.

2012a; George 2015; Xue et al. 2017). Besides superior stability, mechanical properties and electron density in non-oxide materials; oxides easily interact with cations due to high electronegativity of oxygen, which provides magnificent physico-chemical functional properties and ease of synthesis.
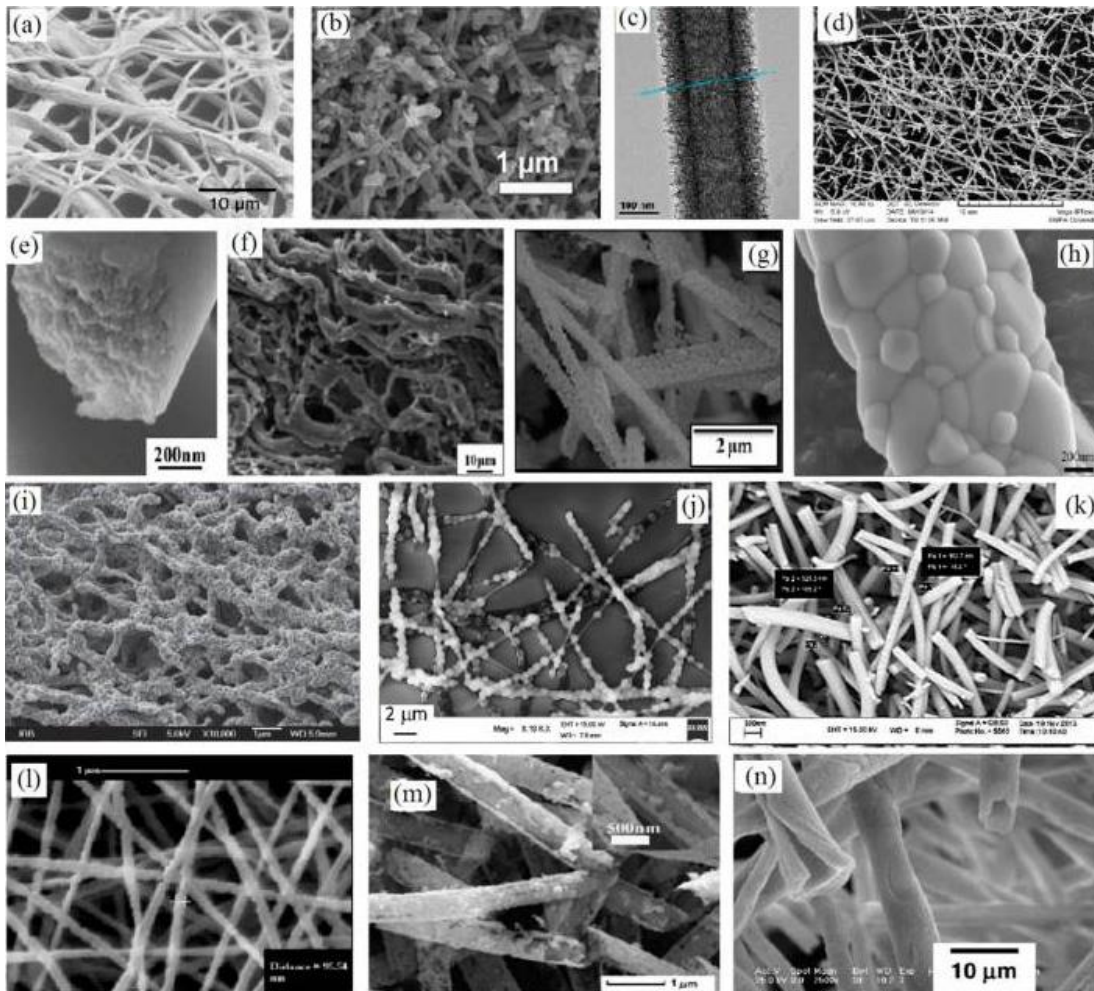
Fig. 1.7 Micrographs of inorganic nanofibers: (a) hydroxyapatite (PVP/ethanol, T = 973 K), (b) $Pr_{0.4}Sr_{0.6}Co_{0.2}Fe_{0.7}Nb_{0.1}O_{3-\delta}$ (PVP/DMF, T = 1073 K), (c) MnO_2 (PAN/DMF, T = 1273 K), (d) $CaCu_3Ti_4O_{12}$ (PVP/ethanol/acetic acid, T = 1173 K), (e) Al_2O_3 (PVP/H_2O, T = 1073 K), (f) $BaFe_{12}O_{19}$ (PVP/DMF, T = 1073 K), (g) $CdTiO_3$ (PVAc/DMF, T = 873 K), (h) $La_2Zr_2O_7$ (PEO/methanol, T = 1673 K), (i) NiO (PVP/ethanol, T = 673 K), (j) SiO_2 (PVP/ethanol, T = 673 K), (k) TiO_2 (PVP/ethanol/acetic acid, T = 773 K), (l) mullite (PVB/ H_2O/ethanol, T = 1473 K), (m) ZrC (PAN/DMF, T = 1673 K, Argon flow), and (n) yttria-stabilized zirconia (PVP/ethanol, T = 1673 K) (Esfahani et al. 2017).

1.2.1 Simple metal oxides

Several metal oxide nanofibers such as CeO_2, Co_3O_4, Cr_2O_3, CuO, Fe_2O_3, In_2O_3, MgO, NiO, TiO_2, ZrO_2, ZnO have been synthesized using sol-gel assisted electrospinning process from alkaline earth metals, to metalloids including many transition and rare earth elements in the field of sensing (Abideen et al. 2017), energy (Thavasi et al. 2008), environmental (Mondal 2017), and biological (Mondal and Sharma 2016) applications. Besides, the nanofibers of transition metal oxides are being recognized as an intelligent class of 1D nanostructured materials for their outstanding properties, including good mechanical strength, thermal stability, excellent flexibility, superior electrical conductivity, selectivity, and large *d-* or *f-*orbital unpaired electrons and wide range of oxidation states, which are responsible for physico-chemical properties of the material (Xia et al. 2016a). Co_3O_4 nanofibers were first synthesized by electrospinning followed by pyrolysis from the precursor solution of CATH salt and PVA in distilled water (Guan et al. 2003a). In similar way, NiO nanofibers were first electrospun using NATH salt (Guan et al. 2003b). However, the first TiO_2 nanofibers (hollow) were prepared by dropping the dilute $Ti(O^iPr)_4$/isopropanol solution on to electrospun poly(L-lactide)/dichloromethane fiber mat and then pyrolyzing (Caruso et al. 2001), as Ti precursor solidifies to TiO_2 the moment it comes in contact with moisture by hydrolysis.

1.2.2 Heterogenous metal oxides

Simple metal oxides lack selectivity and exhibit limited functional properties. Similar to composite materials, composite nanofibers have soon been synthesized and studied for their extended desired properties as multifunctional materials. The hetero companions may be metal, organic or inorganic materials such as Ag, Au, Ni, carbon structures (nanotube, graphene), polymers (PVDF, PVP) (Xia et al. 2003; Sawicka and Gouma 2006; Xue et al. 2017). For example, both p- and n- type semiconducting composite oxide nanofibers were fabricated to have heterojunctions which would easily have selectivity during sensing, NiO/ZnO nanofibers (Li et al. 2015), or have electron transport in photochemical reactions, $BiFeO_3$/TiO_2 (Yang et al. 2014b). The essence of this kind of nanofibers is that a simple oxide can play many roles with different co-partners such as CuO/SnO_2 (Ebrahimi et al. 2012), CuO/TiO_2 (Yousef et al. 2012)and CuO/NiO (Kim et al. 2013) are suitable as H_2S detector, pathogenic inactivation agent,

and magnetic material, respectively. Some of the heterogenous nanofibers are shown in Table 1.3. It has been observed that even in case of heterogenous oxides nanofibers, transition metal oxides have outperformed other simple oxides in the wide area of sensors (Abideen et al. 2017), energy and filters applications, and smart materials (Sahay et al. 2012; Wang et al. 2017b).

1.2.3 Complex metal oxides

The sol-gel process provides the liberty to stoichiometrically tailor the desired mixed metal oxide nanofiber by controlling the stochiometric ratios of the metal precursors. The composite materials provide the control only over the extrinsic properties of the material. However, by appropriate doping or mixing of two or more metal precursors, one can easily design the intrinsic properties of the complex metal oxide nanofiber such as magnetic moment per unit cell, semiconducting nature (p- or n-type), interstitial sites, hybridized band structures. This strategy provides an enhanced physico-chemical functional property of the nanofiber compared to that of its simple or composite form. Some of such examples are alkaline earth/transition metal oxide nanofibers: $Ca_3Co_4O_9$, $MgCo_3O_5$, $CaTiO_3$, $BaTiO_3$, *etc.*, (Li et al. 2009; Wu et al. 2016) for water-splitting application.

1.2.4 Mixed transition metal oxides

MTMOs, typically ternary metal oxides with two different transition metal cations, with stoichiometric or even non-stoichiometric compositions, have received huge interest in recent years due to their promising roles in many sensing, energy, and environmental related applications (Tajik et al. 2017). The coupling of two metal species could render the MTMOs with multiple hybridized band structures, variety of spin orbitals, rich redox reactions, and improved electronic conductivity, which are beneficial to magnetic and photo-electrochemical applications, while being efficient, reliable, and low cost (Gawande et al. 2012; Yuan et al. 2014; Osgood et al. 2016). MTMO nanofibers with large SSA and porosity favors the efficient redox reactions due to following features: (i) better accommodation of the strain during insertion/removal of cations, thus enhancing the cycle performance, (ii) improved reactivity triggering new reactions that are impossible for bulk materials, (iii) large electrode/electrolyte contact surface, resulting in sufficient active sites, (iv) short path length for electronic transport at active

sites with external ions, permitting operation with low electrical conductivity or at high power, (v) convenient diffusion paths for external ions transport to the active sites, which is due to the porosity; and (vi) ease of electron/ionic transport within the nanofiber, because of the connectivity. In decades, many MTMO nanofibers have been synthesized and studied for their potential application in several areas such as magnetic storage devices, piezo/ferroelectrics, catalysts, solar cells, fuel cells, batteries, supercapacitors, *etc.*, (Li et al. 2006a; Ramaseshan et al. 2007; Thavasi et al. 2008; Dai et al. 2011).

Nickel based MTMOs provide high performance, long cyclic life, multifunctionality, low cost compared to other MTMOs or their simple oxides due to their variability of electronic states. Thus, they acquire a variety of beneficial structural forms such as spinel (NiA_2O_4) which aids redox electrochemical reactions (Ruan et al. 2016):

$$NiA_2O_4 + OH^- + H_2O \xleftrightarrow{\text{Alkaline medium}} NiOOH + 2AOOH + e^- \tag{1.1}$$

The most common is the spinel form along with Al, Cr, Fe, Mn, *i.e.*, $NiAl_2O_4$ (Ragupathi et al. 2014), $NiCr_2O_4$ (Xu et al. 2016), $NiFe_2O_4$, and $NiMn_2O_4$ (Osgood et al. 2016). However, Co and Ni being the closest iron triad have an interesting exclusivity to form normal, partial, and inverse spinel structure as NCO ($NiCo_2O_4$). This unique structural feature with varied cationic distribution, which alters the physico-chemical properties of NCO, makes them material of choice in various applications (Loche et al. 2017). NCO has widely been used as supercapacitor. Another exclusive structure of Ni-based MTMOs is with Ti, *i.e.*, ilmenite type NTO ($NiTiO_3$, INTO) which is recognized for its photo-electrochemical reactions owing to high density of surface states (Moghiminia et al. 2014). Even though, spinel form of NTO (Ni_2TiO_4, SNTO) was discovered in early 1960's, there had been no much study on this material till date due to its high temperature formation (above 1673 K) and metastability (Datta and Roy 1965; Qiu et al. 2011). Hence, NCO and NTO were selected as material of interest in the present study.

Table 1.3: Inorganic nanofibers synthesized using sol-gel assisted electrospinning technique followed by pyrolysis.

Inorganic nanofiber	Precursor, polymer, solvent, additive	Remarks	Potential applications	References
AlN	Aluminum nitrate nonahydrate + urea PVP, H_2O, ethanol	Sol-gel, *carbothermal reduction* and *nitridation* during pyrolysis	Optoelectronics	(Sun et al. 2009)
Al_2O_3	Aluminum di-sec-butoxide Ethanol, H_2O + HCl	Aged sol; α-alumina formed	Filter membranes	(Larsen et al. 2003)
Al_2O_3 (Transparent)	Aluminum 2,4-pentanedionate PVP, ethanol, acetone	α-alumina formed	Pyrotechnics, rocket propellant	(Azad 2006)
B_4C	Boric acid PVA, H_2O	Sol-gel, pyrolysis at 1573 K	High temperature thermoelectric	(Uslu and Tunç 2012)
CeO_2	Cerium nitrate PVA, H_2O	Co-precipitation	Biomedical, catalyst	(Yang et al. 2005)
Co_3O_4	CATH PVA, H_2O	Sol-gel	Biomarkers	(Guan et al. 2003a)
Cr_2O_3	Chromium chloride PVA, H_2O	In situ gelation, ammonia treatment	Pigments	(Hao et al. 2006)

CuO	Copper acetate PVAc, H_2O	Sol-gel	Catalysis, semiconductors	(Wu et al. 2006)
Fe_3O_4	Iron (II) chloride + iron (III) chloride Graft copolymer, PEO or PVA	Initial co-precipitation reaction polymer not removed	Reinforcement for glass, fibers in electronic devices	(Wang et al. 2004)
GeO_2	Germanium isopropoxide + Isopropanol, H_2O, propionic acid PVAc, acetone	Precursor sol preparation first, then polymer solution addition, α–quartz like structure	Semiconductors	(Viswanathamurthi et al. 2004)
In_2O_3	Indium nitrate PVP, ethanol	Sol-gel	Gas sensors	(Zhang et al. 2007)
MoS_2	Ammonium tetrathiomolybdate PVA, Dimethyl sulfoxide	Sol-gel, H_2 and argon gas atmosphere during pyrolysis	Hydrogen storage	(Liu et al. 2012)
SiO_2	Tetraethyl orthosilicate, Ethanol + HCl	Sol-gel	Drug carriers	(Zhang et al. 2005)
SnO_2	Dimethyl dineodecanoate tin PEO, Chloroform	Sol-gel, rutile form	Sensors	(Wang et al. 2006a)

Ta$_2$O$_5$	Tantalum isopropoxide, ethanol PVAc, DMF, acetic acid	Sol-gel	Rectifiers, biomedical implants, dielectric	(Dharmaraj et al. 2006)
TiO$_2$	Titanium butoxide Pluronic P-123 copolymer	Sol-gel; mesoporous fibers below 973 K anatase; above 973 K, anatase and/or rutile	Photocatalysis, solar cell	(Madhugiri et al. 2004)
ZnO	Zinc acetate PVAc, H$_2$O	Sol-gel	Light emitting diodes, photodetectors, varistors	(Wu and Pan)
ZrO$_2$	Zirconium oxychloride PVA, H$_2$O	Sol-gel	Electroceramics	(Shao et al. 2004a)
WO$_3$	Tungsten powder, 30% H$_2$O$_2$ PVP, ethanol	Tungstenic acid preparation first, then polymer, solvent addition	Field emission instruments	(Lu et al. 2006)
	Tungsten isopropoxide PVAc, DMF	Sol-gel chemistry, ammonia sensing	Sensor	(Wang et al. 2006a)

Al_2O_3/B_2O_3	Aluminum acetate, boric acid PVA, H_2O	Aging for 5 h before spinning	Reinforcement for glass, fibers in electronic devices	(Dai et al. 2002)
$Co_3O_4/CuO/MnO_2$	Manganese (II) acetate tetra hydrate, copper (II) acetate mono hydrate, and CATH PVA, H_2O	Polymer solution preparation first, then precursors addition	Solid state sensors	(Kanjwal et al. 2008)
Erbia modified TiO_2	$Ti(O^iPr)_4$ PVP, ethanol	After TiO_2 sol-gel preparation erbium (III) oxide particles added	Fuel cells	(Tomer et al. 2005)
Gd_2O_3 doped CeO_2	Ammonium cerium nitrate, Gadolinium nitrate PVP, ethanol	Sol-gel	Fuel cells	(Azad et al. 2005)
Hydroxyapatite on TiO_2	$Ti(O^iPr)_4$, simulated body fluid PVAc	TiO_2 nanofiber treated with simulated body fluid	Surgical implants	(K.C. et al. 2008)
Mn_2O_3/Mn_3O_4	Manganese acetate PVA, H_2O	Sol-gel; pyrolysis-controlled phase formation	Catalysts	(Shao et al. 2004b)

Mn$_2$O$_3$/TiO$_2$	Ti(O^{i}Pr)$_4$, manganese acetate tetrahydrate PVP, ethanol	Sol-gel	Bacterial growth, dye degradation, water desalination	(Panthi et al. 2013)
NiO/ZnO	NATH, zinc acetate PVA, H$_2$O	Sol-gel; two phase inorganic fibers	Smart materials and semiconductors	(Shao et al. 2004c)
V$_2$O$_5$/TiO$_2$	Ti(O^{i}Pr)$_4$, vanadium oxytriisopropoxide + hexadecyltrimethylammonium bromide PVP, isopropanol	V$_2$O$_2$ nanorods on TiO$_2$ nanofiber	Fuel cells	(Ostermann et al. 2006)
Y$_2$O$_3$ stabilized ZrO$_2$	Zirconyl chloride, yttrium nitrate PVP, ethanol	Sol-gel	Automobile thermal barrier coatings, catalysis	(Azad et al. 2005)
BaTiO$_3$	Barium acetate, Ti(O^{i}Pr)$_4$ + acetic acid PVP, ethanol	Sol-gel	Piezoelectric, microwave material	(Yuh et al. 2005)

Co doped SrTiO$_3$	Tetrabutyl titanate, strontium nitrate, and cobalt nitrate hexahydrate PVP, ethanol	Polymer solution preparation first, then precursors addition	Ferromagnetism	(Zhang et al. 2012b)
Hydroxyapatite Ca$_{10}$(PO$_4$)$_6$(OH,F)$_2$	Ca(NO$_3$)$_2$, P(C$_2$H$_5$O)$_3$ Ethanol, H$_2$O	24 h aging for 10 days, then addition of NH$_4$F	Biomedical implant artificial bone	(Kim et al. 2006b)
La$_2$Zr$_2$O$_7$	Zirconium oxychloride, lanthanum nitrate PVP, ethanol	Sol-gel	Fuel cells, catalysts	(Li et al. 2006b)
LiCoO$_2$	Lithium acetylacetonate, CATH + acetic acid PVP, ethanol	Precursor sol preparation first, then polymer solution addition	Batteries, alternative energy sources	(Fu et al. 2005)
LiMn$_2$O$_4$	Lithium chloride, manganese acetate PVA, H$_2$O	Sol-gel	Magnetic and energy storage devices	(Yu et al. 2005)
MgTiO$_3$	Magnesium ethoxide, Ti(O^{i}Pr)$_4$ + 2-ethoxyethanol PVAc, DMF	Precursor sol preparation first, then polymer solution addition	Catalyst, dielectric	(Dharmaraj et al. 2004b)

$NaCo_2O_4$	Sodium acetate trihydrate, cobalt (III) acetate tetrahydrate PAN, DMF	Polymer solution preparation first, then precursors addition	Thermoelectric sensors	(Maensiri and Nuansing 2006)
$NiFe_2O_4$	Iron (III) ethylhexano isopropoxide, nickel ethylhexano isopropoxide + acetic acid PVP, isopropanol	Sol-gel; spinning in glove box; hydrolysis after spinning	Magnetic and energy storage devices	(Li et al. 2003)
$NiTiO_3$	NATH, $Ti(O^iPr)_4$ + ethanol, HNO_3 PVAc, DMF	Precursor sol preparation first, then polymer solution addition	Tribological coatings, pigments	(Dharmaraj et al. 2004a)
$Pb(Zr_{0.52}Ti_{0.48})O_3$	Zirconium propoxide, $Ti(O^iPr)_4$, and lead (II) ethyl hexanoate Xylene	Precursors as such spun, hydrolysis from the atmosphere	Piezo-transducers	(Wang and Santiago-Avilés 2003)

1.2.4.1 Nickel titanate

NTO is an important ternary transition metal oxide, which exhibits polymorphic crystal structures, including a spinel variant (Fig. 1.8). The non-existence of pure SNTO has been investigated from centuries. A non-stoichiometric SNTO was discovered experimentally for compositions between 63 and 97 mol% of NiO (Fig. 1.9a) at temperatures above 1653 K (Laqua et al. 1977). Later, the non-stoichiometric SNTO was found to be a result of excess solubility of NiO due to its high preference to octahedral void (O_v). The $NiO-TiO_2$ phase diagram (Fig. 1.9b) was further developed both theoretically and experimentally, which showed SNTO having NiO content between 92 wt% at SNTO-NiO boundary at 1690 K to 67 wt% at the SNTO-INTO boundary at 1903 K (Muan 1992; Qiu et al. 2011). The spinel solid solution can be represented as $Ni_{2+2y}Ti_{1-y}O_4$, with the y ranging between 0.03 and 0.75, hence stoichiometric SNTO composition (x = 0) lies slightly outside the domain of spinel solid solution. The present study is attributed to the synthesis and characterization of INTO nanofibers accompanied with SNTO phase with y = 0.31, whose empirical formula is given by $Ni_{2.62}Ti_{0.69}O_4$.

(a) INTO   **(b) SNTO**

Both Ni and Ti ions at O_v Ti ions only at T_v

⬤ Ti ions   ⬤ Ni ions   ⬤ O ions
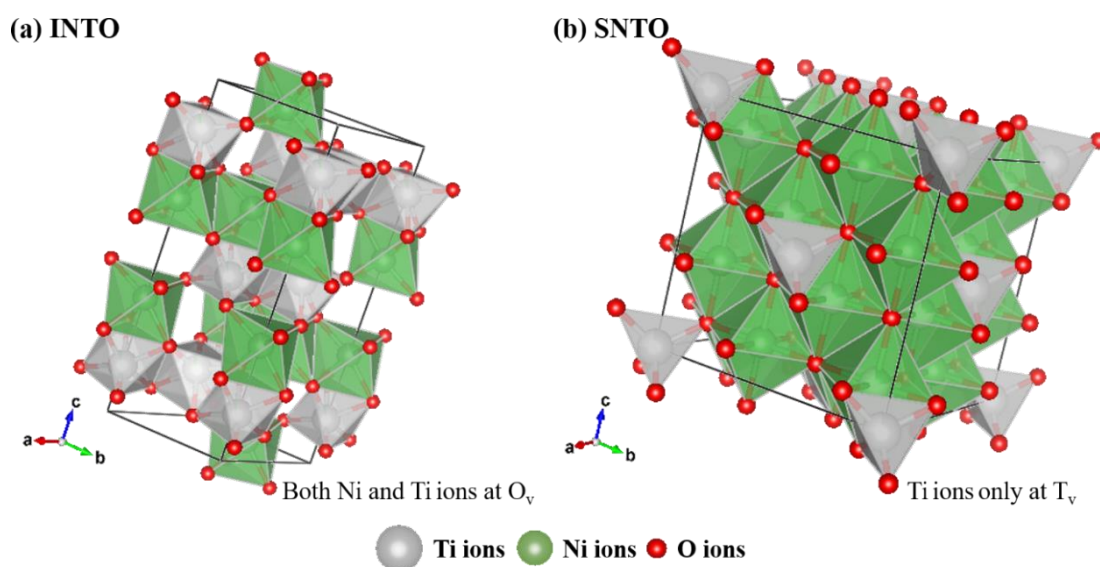
Fig. 1.8 Unit cell of NTO: (a) ilmenite type and (b) non-stoichiometric spinel type.

NTO is known for its exceptional photon induced properties and well-established applications in yellow pigments, solar energy reflectors (Wang et al. 2013a), photovoltaics (Sobhani-Nasab et al. 2015), optics (Vijayalakshmi and

Rajendran 2012), photocatalysts (Hyun Kim et al. 2006; Qu et al. 2012; Bellam et al. 2015) as well as temperature dependent electrical and magnetic devices (Yuvaraj et al. 2013). Different synthesis techniques have been used in recent years to develop cost- and performance-efficient NTO nanomaterials. Some of these synthesis techniques include solvothermal (Nguyen-Phan et al. 2014), molten salt (Yuvaraj et al. 2013), co-precipitation and impregnation (Gabal et al. 2013), stearic acid gel method (Sadjadi et al. 2008), polymeric precursor route (Lopes et al. 2009), modified *Pechini* method (Lin et al. 2006), surfactant assisted method (Zhou and Kang 2006) and sol-gel method (Gambhire et al. 2008; Mohammadi and Fray 2010). However, the conventional methods typically require high operating temperatures (> 1073 K), and lead to formation of impurity phases (Zhou et al. 1997). Therefore, the synthesis of NTO nanofibers in the present work was accomplished *via* sol-gel assisted electrospinning technique followed by pyrolysis at relatively low-temperature (between 673 K and 1273 K), suitable for producing continuous and uniform fibers of high purity.
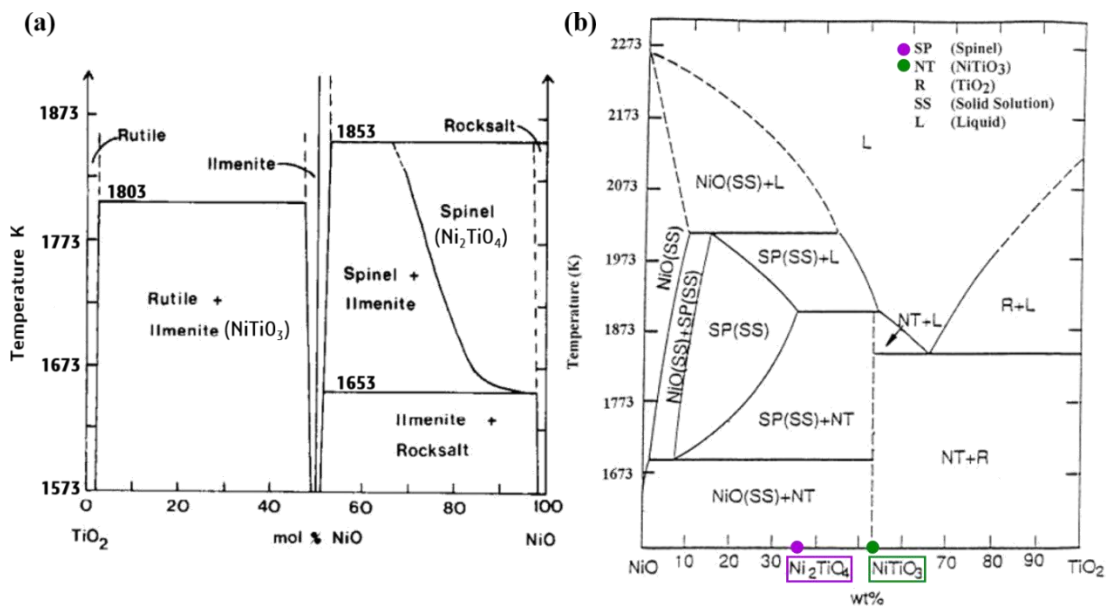
Fig. 1.9 High temperature phase diagram of NiO-TiO$_2$: (a) (Laqua et al. 1977) and (b) (Muan 1992)

The use of electrospinning for synthesizing NTO nanofibers is rather scarce in the literature. Among two noteworthy contributions are the ones by (Dharmaraj et al. 2004a), and (Yang et al. 2014a). In the former, INTO nanofibers with 150-200 nm diameter were obtained after the pyrolysis of polymer precursor fibers at T ranging

from 873-1273 K. Although the nanofibers retained their nature after pyrolysis, the rutile TiO_2 phase was still present. This was improved upon in the latter, where nanofibers of INTO with highly crystalline structure were fabricated without any impurity phases. Continuous INTO nanofibers were obtained after pyrolysis at 873 K, having AFD of 175 nm. Optical spectroscopy showed that these nanofibers exhibit an excellent UV-Vis light response. In contrast, nanoparticles of INTO synthesized under identical conditions by a sol–gel route had impurities including TiO_2 and NiO. Further, it was reported that the electrospun INTO nanofibers possessed higher SSA than the INTO nanoparticles, which could be beneficial for various surface-dependent applications such as photocatalysis and sensors (Yang et al. 2014a). The present work uses a similar strategy as in references (Dharmaraj et al. 2004a) and (Yang et al. 2014a), but with a different chemistry for the precursor sol and the polymeric binder, which in turn drastically alters the structural and functional properties of the resulting nanofibers.

1.2.4.2 Nickel cobaltite

NCO is a ternary transition metal oxide, which possesses both normal (Fig. 1.10) and inverse spinel structures, due to exceptional variations in the valence and distribution of cations (Marco et al. 2000, 2001; Iliev et al. 2013; Loche et al. 2017). In a normal spinel (AB_2O_4), the A cations occupy one eighth of the tetrahedral void (T_v) and the B cations occupy half of the O_v; while in an inverse spinel, all the A cations occupy O_v with the B cations equally distributed between the O_v and T_v. The first NiO-CoO phase diagram (Fig 1.11a) was described experimentally by (Kinoshita et al. 1973), which showed the phase separation of NiO-CoO solid solution at different temperatures and compositions. This was further corrected for the magnetic effect on miscibility of the solid solution as shown in Fig. 1.11a (Bergman and Agren 1986). Both Ni and Co, being close iron triads having common rock salt structures, are fully interchangeable as per *Pauling's rules*. However, the phase diagram discovered shows miscibility gap suggesting the two-phase region at low temperatures. From the phase diagram (Fig. 1.11b), cobalt oxide has a high solubility in nickel oxide at reaction temperatures from 653 to 823 K (Han et al. 2016b). This explains the good selection of low T (773 K) for synthesis of NCO nanofibers in the present study. And the atomic ratio of Co:Ni equal to 2 (66.7 at%) in present study suggests the formation of metastable spinel NCO during

synthesis. At a given pressure, as T is increased, different structural, magnetic, and electronic phases such as amorphous phase (T < 523 K), spinel ferrimagnet with decreasing θ_c that displays metallic (523-673 K) and insulating (673-923 K) behaviors, and highly insulating rock salt phase (T > 923 K), are encountered (Bitla et al. 2015). Furthermore, T decides not only the rate of cation-disorder/inversion but also their redistribution with mixed valences.
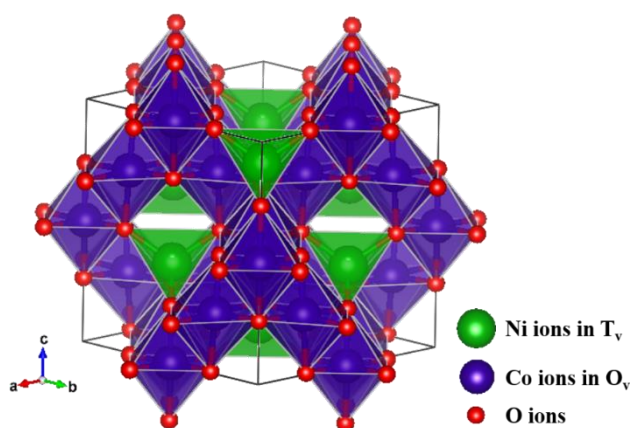
Fig. 1.10 Unit cell of normal spinel NCO.

NCO possesses enhanced electrochemical, electrocatalytic, electrical, and ferromagnetic properties, especially when hybridized with the carbon-based materials such as carbon nanotubes or graphene (Hu et al. 2012; Chen and Qiao 2013; Liu et al. 2014a; Iqbal et al. 2016; Tong et al. 2016). Some of the well-known applications are in supercapacitors (Chen et al. 2013b; Liu et al. 2013b; Dubal et al. 2015; Naveen and Selladurai 2015), batteries (Alcántara et al. 2002; Li et al. 2013a), catalysts (Cui et al. 2008), sensors (Li et al. 2011; Prathap et al. 2015), p-type semiconductors (Windisch et al. 2001a), photodetectors (Liu et al. 2013b), weak ferromagnets (Babu et al. 2015), oxygen reduction reaction (Zhang et al. 2014), solar cells (Zhang et al. 2017a), and water-splitting (Chen and Qiao 2013; Gao et al. 2016). Several innovative and cost-effective techniques have been reported for the synthesis of high-performance NCO nanomaterials. The notable ones are hydrothermal (Umeshbabu et al. 2014), ball milling (Ding et al. 2012), co-precipitation (Cui et al. 2008), sputtering (McCloy et al. 2015), photolithography (Hu et al. 2012), nanocasting (Cabo et al. 2009), surfactant-assisted (Babu et al. 2015), thermal decomposition (Kuboon and Hu 2011), substrate-

assisted (Iliev et al. 2013), electrospinning assisted pyrolysis (Guan et al. 2004), and hybrids of these techniques (Un Lee et al. 2013; Liu et al. 2014a; Mondal et al. 2017). Most of these conventional techniques which operate at low T ($<$ 623 K) have the drawback of retaining organic moieties in the final material. The by-products of the precursor remain as impurities in NCO nanostructures due to low T (less than or equal to 623 K), which act as impurities that deteriorate the performance of the material (Verma et al. 2008; Garg et al. 2013).
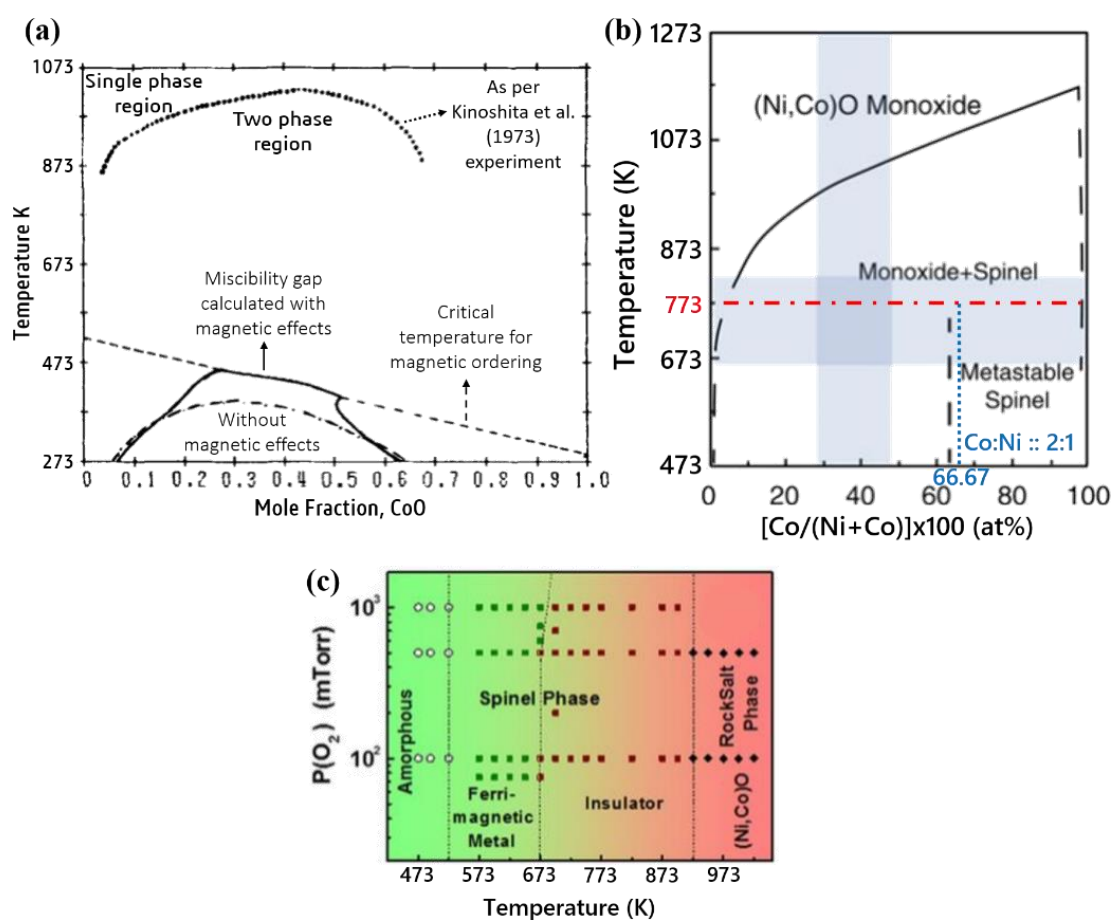
Fig. 1.11 (a) Calculated and experimental (dotted) miscibility gap in NiO-CoO system (Bergman and Agren 1986), (b) temperature-composition phase diagram of NiO-CoO-O_2 in air at one atmosphere pressure (Han et al. 2016b), and (c) pressure-temperature phase diagram of NCO with idealized sharp phase boundaries, frequency of actual experimental points is reduced for the sake of clarity (Bitla et al. 2015).

On the other hand, at T exceeding 623 K, the process yields phase separation (Verma et al. 2014), large crystallites (Babu et al. 2015) or particles (Umeshbabu et al.

2015; Nakate and Kale 2016; Yang et al. 2017), which again deteriorates the physicochemical properties such as magnetic performance of the material. Hence, it is vital to choose optimal precursor and pyrolysis parameters to obtain NCO nanofiber with tailor-made morphological and structural properties. Sol-gel assisted electrospinning followed by pyrolysis scores over other techniques by offering the necessary flexibility for selection of process parameters, and thereby, to obtain preferred structures, compositions, and morphologies of nanofibers and nanoparticles. The present study reports a novel synthesis technique for NCO, based on sol-gel assisted electrospinning and pyrolysis, which causes certain structural variations that are fundamentally responsible for its tailor-made physical properties. NCO in nanostructured forms is especially valuable, as it allows fine-tuning of its properties for a desired application (Dubal et al. 2015).
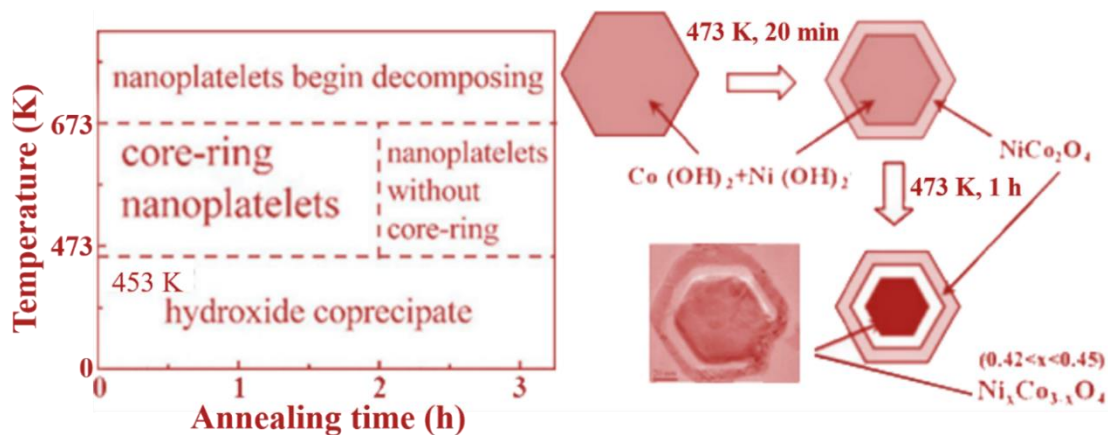
Fig. 1.12 T-*t* dependence in formation of core-ring NCO nanoplatelets (Cui et al. 2008).

In the electrospinning process, the thinning and morphology of the fibers is dictated by a competition between electrostatic, viscous, and gravitational forces. Recently, it has been suggested that the magnetic interactions between the Ni and Co ions in the hybrid precursor salts is responsible for the formation of precursor nanobelts, which eventually yielded NCO of nanobelt morphology during pyrolysis (Harilal et al. 2017). Aside from these factors, which govern morphological changes in the precursor fibers at the pre-pyrolysis stage, certain morphological features may also emerge during pyrolysis. It was observed that the morphological changes were predominantly influenced by *t* than T. The core-ring NCO existence depended on both T and *t* as shown in Fig. 1.12 (Cui et al. 2008). The present study reports some observations along these

lines and discusses some plausible mechanisms for such morphological and physico-chemical features.

1.2.5 Electrocatalyst

The development of electrocatalyst materials for various applications could reduce the cost, which is required to facilitate the economy of catalysis economy. It is crucial to enable this vision of improving the electrocatalysts with an appropriate efficiency and selectivity for the photo- or electrochemical reactions involved. Electrocatalytic reactions occur at the surface of the material, thus, significant consideration needs to be given in designing not only the composition, but, also the morphology and crystallinity of the electrocatalysts. Figure 1.13 illustrates the different type of strategies used to enhance the performance of an electrocatalyst.
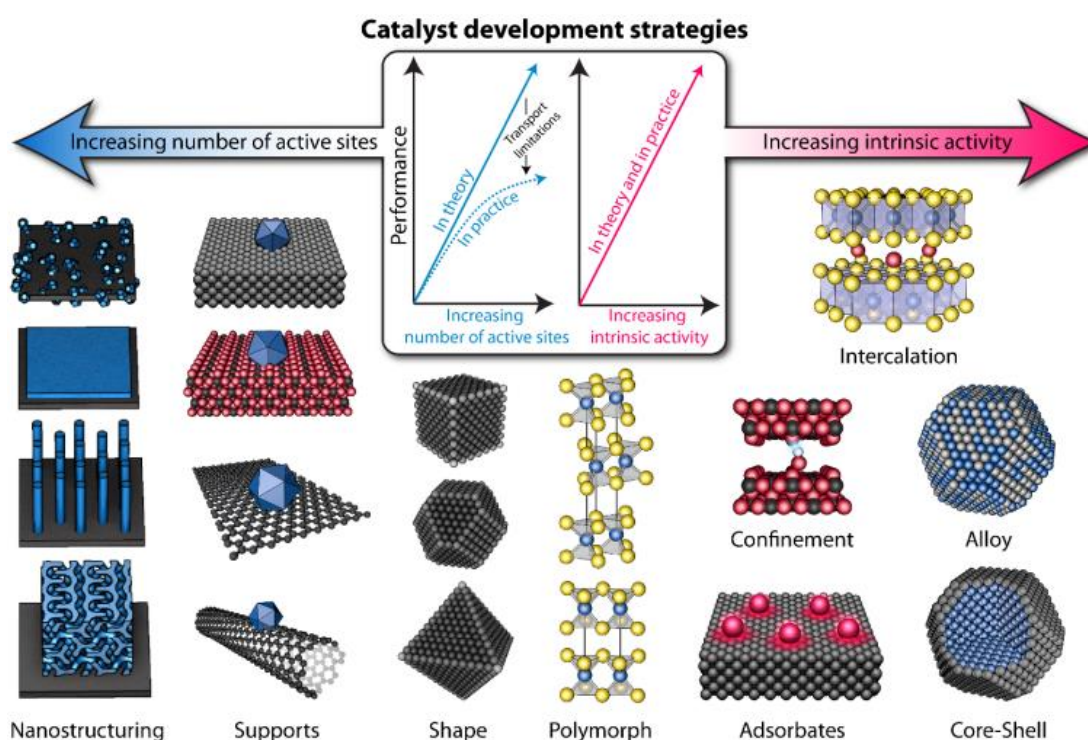
Fig. 1.13 Catalyst development strategies (Seh et al. 2017).

There are generally two strategies to improve the activity (or reaction rate) of an electrocatalyst system: (i) increasing the number of active sites on a given electrode (for example, through increased loading or improved catalyst structuring to expose more active sites per gram), or (ii) increasing the intrinsic activity of each active site (Seh et al. 2017). These strategies are not mutually exclusive and can ideally be

addressed simultaneously, leading to the greatest improvements in electrocatalytic activity. At the same time, there are physical limits to the later as how much catalyst material can be loaded onto an electrode without affecting other important processes such as charge and mass transport. Hence, increase in intrinsic activity by alloying or hybridizing material is significant with optimal nanostructure. The present study concentrates on improving the electrocatalytic performance by all categories in one platform of synthesis, *i.e.*, sol-gel assisted electrospinning followed by pyrolysis.
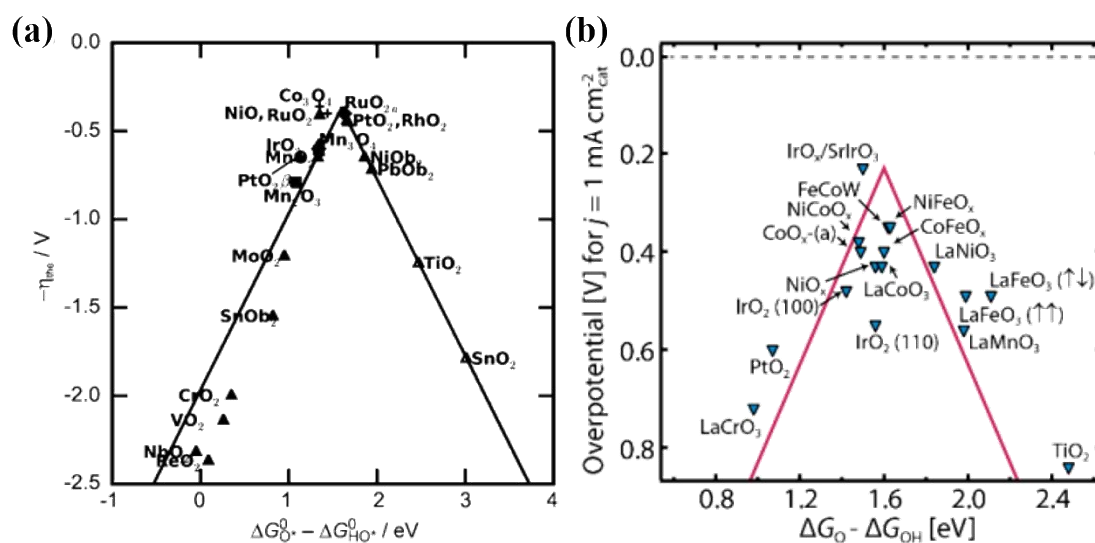
Fig. 1.14 OER volcano plot for various metal oxides (a) (Jiao et al. 2015) and (b) (Seh et al. 2017).

The illustration for increased electrocatalytic performance by alloying or MTMOs can be derived from Sabatier-type volcano plots for OER, where the pristine (001) surfaces of MO_y having too weak or strong M-O adsorption are the worst electrocatalysts with activities down from the peak (Fig. 1.14a). NiO and CoO_x are to the left and TiO_2 to the right to the bottom of peak. Hence, the electrocatalytic performance of the simple oxides can be improved just by combining the effects of these oxides as MTMOs, where they move up to the peak by reducing the overpotential for OER as seen in Fig. 1.14b. Furthermore, another method that depicts good catalytic activity, stability, and electrochemically active surface area of electrocatalyst for OER in acid/alkaline solutions is by the comprehensive plot (Fig. 1.15). The ideal catalyst will have a low overpotential, stability over a longer duration, and high specific activity (or low surface area). The best electrocatalysts for OER will be positioned toward the

bottom left corner of the comprehensive plots (Fig. 1.15) and should appear light green in color (McCrory et al. 2013) . The ongoing discussions suggests that NTO nanofibers can be promising electrocatalysts, and NCO electrocatalyst can be improved by compositional and morphological changes with/without hybridization.
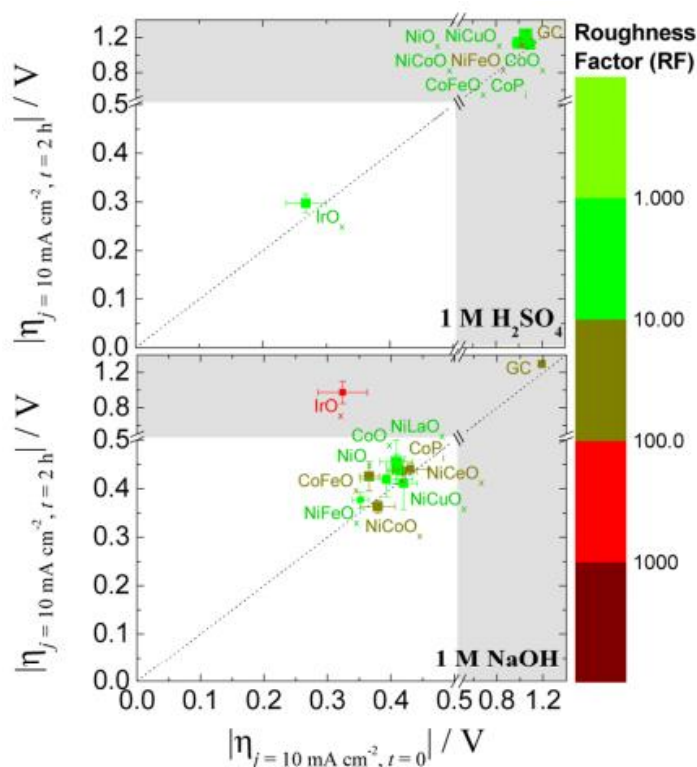
Fig. 1.15 Comprehensive plots for OER electrocatalysts in acidic (top) and alkaline (bottom) solutions. The diagonal dashed line is the expected response for a stable catalyst (McCrory et al. 2013) .

MTMO nanofibers are promising candidate materials for electrocatalysis given the earth crustal abundance of these transition metals as well as the size benefits associated with nanofibers. The high aspect ratio and high specific surface area of nanofibers enables efficient charge transport, which makes them attractive for electrocatalytic applications such as biosensors (Mondal and Sharma 2016) and energy harvesting devices (Shi et al. 2015; Liao et al. 2016). For example, simple transition metal oxide nanofibers such as Co_3O_4, CuO, NiO, TiO_2 have shown immense potential for non-enzymatic glucose sensing (Si et al. 2013; George and Anandhan 2016), which boosts the health industry through improved management of diabetes (Heller and Feldman 2008; Chen et al. 2013a; Tian et al. 2014). Another emerging area of their

application is in electrocatalytic water splitting for hydrogen production (Frites et al. 2014; Wu et al. 2016; Long et al. 2018; Song et al. 2018), due to the increasing need for renewable energy technologies. A variety of techniques have also evolved over the last decade, which facilitate the easy synthesis and fabrication of MTMO (Yuan et al. 2014; Guo et al. 2015). Figure 1.16a and b shows the significance of using NTO and NCO in various photo- and/or electrochemical reaction applications. In addition to these, a lot of effort and study has been carried out to understand the effects and performance of the morphology of these materials in the form of 1D nanostructures (Fig. 1.16c and d). All these factors motivate studies for developing MTMO nanofibers with enhanced catalytic and sensing properties as well as to improve the understanding of the underlying mechanisms.
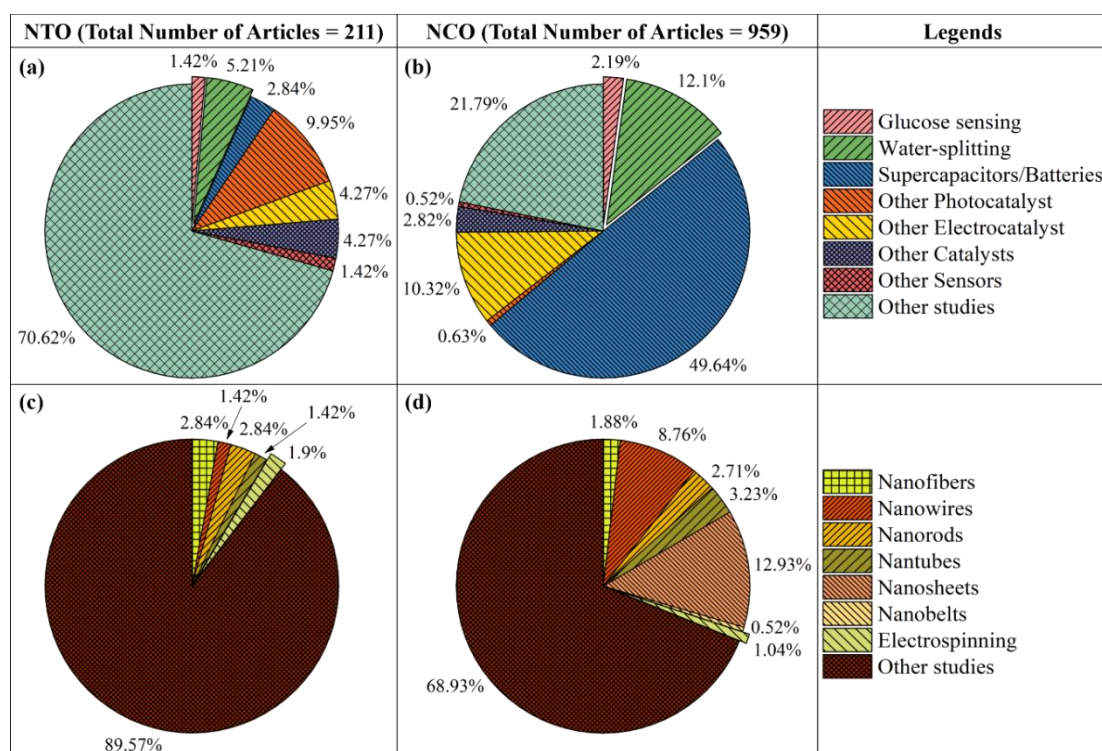
Fig. 1.16 Number of articles in NTO and NCO for (a and b) specified field of applications and (c and d) various 1D nanostructure morphologies.

Among transition metal oxides, NCO has seized the field of supercapacitors (Dubal et al. 2015), biosensors (Huang et al. 2017a) and electrocatalysis (Gao et al. 2016); due to its remarkable oxidation states and better electrical conductivity than simpler oxides such as NiO or CoO_x (Wang et al. 2017a). Extensive studies on glucose

detection and water oxidation have been reported in literature using NCO in the form of various nanostructures (Chen et al. 2015; Cui et al. 2017; Huang et al. 2017a), hybrid composites (Cai et al. 2016; Naik et al. 2017; Wang et al. 2018) and carbon-based composite materials (Chen and Qiao 2013; Wang et al. 2013b). Previously, electrospun NiO and Co_3O_4 nanofibers have been explored for use in biosensors for glucose monitoring (Zhang et al. 2012c; George and Anandhan 2016) and as cells for electrocatalysis (George et al. 2015). It was soon realized that NCO exhibits superior performance due to its high electronic conductivity and presence of plenty active sites. NCO has spinel structure, where O_v cations are easily accessed by electrolyte at the interface (Su et al. 2014; Huang et al. 2017a). Apart from these, graphene based materials have been explored in depth for various electroanalytical methods (Shao et al. 2010). Hence, NCO has been extensively investigated in the presence of graphene derived materials, and their combination showed excellent electrocatalytic performance towards glucose sensing and oxygen reduction reaction than base NCO due to the synergistic effect of heterostructures (Chen and Qiao 2013; Wang et al. 2013b; Ko et al. 2017; Mondal et al. 2017). Another important aspect of glucose sensing is that the oxidation of glucose is always associated with the production of H_2O_2, especially in enzymatic sensors (Ko et al. 2017). Hence the first-generation glucose sensors were based on H_2O_2 detection. Given this, it is important that studies involving electrocatalytic and glucose sensing properties of NCO be also conducted in presence of added H_2O_2. Furthermore, the enzymatic glucose detection is always associated with H_2O_2 liberation and sensing (Huang et al. 2017b). In addition, electrocatalytic H_2O_2 detection has been a major focus in biological, pharmaceutical, food, and textile manufacturing applications (Chen et al. 2012). Therefore, H_2O_2 detection is an essential aspect of biosensing applications along with glucose sensing; in this process, it is also important to avoid interference from other organic and inorganic moieties present with glucose. Some of these species are ascorbic acid, lactic acid, uric acid, dopamine, tryptophan, glycocoll, L-valine, L-proline, L-lysine, sucrose, fructose, maltose, carrageenan, NaCl, and cations (K^+, Na^+, Ca^{2+}, Mg^{2+}, Zn^{2+}) (Naik et al. 2015, 2017; Cui et al. 2017; Huang et al. 2017a, 2017b; Qin et al. 2017; Rao et al. 2017; Saraf et al. 2017; Wang et al. 2017a; Yin et al. 2017). Therefore, NCO nanofibers synthesized in the present study were explored for their glucose sensing potential.

The global demand for clean and renewable energy technologies has increased extensively during the last few decades. In this context, hydrogen is being looked upon as the energy alternative for the next century. Water electrolysis is one of the greener and cleaner ways for the large scale production of H_2 gas, scoring over other industrial methods such as hydrolysis *via* metal hydrides or steam reforming of hydrocarbons (Anantharaj et al. 2018). However, water electrolysis is more efficient in acidic conditions for HER and alkaline condition for OER (Zeng and Zhang 2010; Lee et al. 2012). The downside is that these involve the use of precious noble metals as electrocatalysts, such as Pt-based material for HER and Ru- or Ir-based material for OER (Lee et al. 2012; Morales-Guio et al. 2014). The efficient, economical, and eco-friendly electrocatalyst is a vital prerequisite for water-splitting technology. Several efforts have been directed in recent times towards replacing these materials with transition metal-based materials (Han et al. 2016a). Among these, Ni-based materials have especially emerged as promising candidates for both electrocatalyst and photocatalyst applications (Xu and Xu 2015; Gong et al. 2016).

In the fields of electrocatalysis and photocatalysis, Ni-based materials have also gained increasing attention for their bifunctional electrocatalytic activity. In other words, they can simultaneously catalyze HER and OER in the same media, which helps in obtaining improved water-splitting efficiency and cost-effective large scale H_2 production (Ledendecker et al. 2015; Sivanantham et al. 2016). Besides, multiple adsorption/desorption processes that occur during electrolysis can be synchronized using heterostructures of Ni-based materials, thereby forming more active catalytic sites. Many Ni-based heterostructures have been explored in literature for their applicability as electrocatalysts (Gong et al. 2016) as well as photocatalysts (Xu and Xu 2015), such as Ni-W alloy (Elias et al. 2015), Co-Ni-graphene composite (Subramanya et al. 2015), $Ni(OH)_2/Ni$ (Danilovic et al. 2012), $NiTiO_3/Ni$ (Dong et al. 2017), NiO/TiO_2 (Zhao et al. 2016). However, these materials as electrocatalysts have some drawbacks such as high overpotential or are based on metallic Ni. Metallic Ni being expensive and easily vulnerable to environment hazards, an alternative idea is to use highly defective oxides, which inherit semi-metallic properties. Hence, NTO

nanofibers synthesized in the present study are characterized for their ability in water-splitting.

1.2.6 Magnetic properties

The magnetic properties of titanates has become a prominent research topic (Mufti et al. 2011; Harada et al. 2016) due to their direct technological relevance. In this context, the magnetoelectric properties of INTO have been studied recently after preparation by precipitation (Harada et al. 2016), evaporation induced self-assembly (Modak et al. 2018), and molten salt synthesis (Yuvaraj et al. 2013) methods. However, the materials thus synthesized possessed impurities such as simple oxides (*viz.*, NiO and TiO_2) or had larger particle size adversely affecting their magnetic behavior. The $LiNbO_3$-type or perovskite polymorph of NTO (epitaxial) is understood to have excellent multiferroic nature based on theoretical (Fennie 2008; Pontes Ribeiro et al. 2016) and experimental studies, *i.e.*, the epitaxial NTO prepared by pulsed laser deposition on different substrates (Varga et al. 2013, 2015b, 2015a). These works reveal some morphological correlations with magnetic properties such as the influence of the substrate-exerted strain on crystal of epitaxial NTO (Varga et al. 2015b, 2015a), film thickness, off-stoichiometry and the growth temperature of epitaxial NTO (Varga et al. 2015b). Besides, the grain/crystallite size reduction of INTO (~ 70 nm) achieved in submicron NTO particles (150-300 nm) prepared by annealing at 1123 K for 10 h is found to be important (Yuvaraj et al. 2013). In spite of several efforts to study the magnetic behavior of Ni-doped TiO_2 (Sangaletti et al. 2006; Typek et al. 2016), NTO (Heller et al. 1963; Watanabe et al. 1980; Yuvaraj et al. 2013) and NTO-based nanocomposites (Harada et al. 2016; Modak et al. 2018), a comprehensive description of the NTO morphological changes and magnetic properties of NTO polymorph composites is missing in literature. In this study, an attempt has been made to explore the correlation between the magnetic behavior of NTO nanofibers in presence of SNTO and the morphological changes (that occur at different T).

Various techniques have been used for synthesis of NCO nanostructures in earlier works, for tailoring the morphology and magnetic properties of NCO. The notable ones are synthesis by rapid combustion (Verma et al. 2008, 2014), hydrothermal reaction (Liu et al. 2013c; Umeshbabu et al. 2015; Yang et al. 2017), pulsed laser

deposition (Iliev et al. 2013), microwave irradiation (Babu et al. 2015; Nakate and Kale 2016). Most of these techniques, which operate at low T (< 623 K) have the drawback of retaining organic moieties in the final material. The by-products of the precursor remain as impurities in NCO nanostructures due to low synthesis T (less than or equal to 623 K); the by-products may act as impurities that could probably deteriorate the performance of the inorganic material (Verma et al. 2008; Garg et al. 2013). On the other hand, at T > 623 K, the process yields phase separation (Verma et al. 2014), larger crystallites (Babu et al. 2015) or particles (Umeshbabu et al. 2015; Nakate and Kale 2016; Yang et al. 2017), which again deteriorates the magnetic performance of the material. Hence, it is vital to choose optimal precursor and pyrolysis parameters to obtain NCO nanofiber with tailor-made morphological and structural properties. Sol-gel assisted electrospinning followed by pyrolysis scores over the other techniques by offering the necessary flexibility for the selection of process parameters, and thereby, to obtain preferred structures, compositions, and morphologies of nanofibers and nanoparticles.

1.2.7   Effect of polymeric binders

Various polymers have been explored as polymeric binders in electrospinning among which a majority has polar functional groups, and soluble in both water and organic solvents (Table 1.3). Water-soluble polymeric binders lead to defective fibers in presence of hygroscopic precursor salts. Further, the thermal stability of poly(styrene-*co*-acrylonitrile) [SAN] is better than many conventional polymers such as PVA, PVAc, PEO, PVP, and PAN. Therefore, SAN can better support the nucleation and growth of inorganic nanofibers during pyrolysis. In addition, the interaction between the polymer and precursor salts is significant factor which affects the structural, compositional, and morphological changes in the electrospun nanofibers (George and Anandhan 2015b, 2015a).

The use of electrospinning for fabricating NTO nanofibers is rather scarce in the literature. Among two noteworthy contributions are the ones by (Dharmaraj et al. 2004a), and (Yang et al. 2014a). In the former, rhombohedral NTO nanofibers with 150-200 nm diameter were obtained after the pyrolysis of precursor nanofibers at T ranging from 873-1273 K. Although the nanofibers retained their nature after pyrolysis,

the rutile TiO_2 phase was still present. This was improved upon in the latter, where nanofibers of NTO with highly crystalline structure were fabricated without any impurity phases. Continuous NTO nanofibers were obtained after T = 873 K, having average diameter of 175 nm. Optical spectroscopy showed that these nanofibers exhibit an excellent UV light response. In contrast, nanoparticles of NTO synthesized under identical conditions by a sol-gel route had impurities including TiO_2 and NiO. Further, it was reported that the electrospun NTO nanofibers possessed higher SSA than the NTO nanoparticles, which could be beneficial for various surface-dependent applications such as photocatalysis and sensors (Yang et al. 2014a). In similar lines, the commonly used polymeric binders for NCO nanofibers are PVA, PVP, and PAN, which possess lower thermal stability than SAN and yielded large AFD nanofibers with impurity phases (Guan et al. 2004; Li et al. 2013b; Zhang et al. 2017a). However, the NCO nanofibers thus obtained showed enhanced performance when used in solar cells and supercapacitors due to its nanostructure and mesoporous architecture.

1.2.7.1 *Effect of acrylonitrile and styrene functional groups*
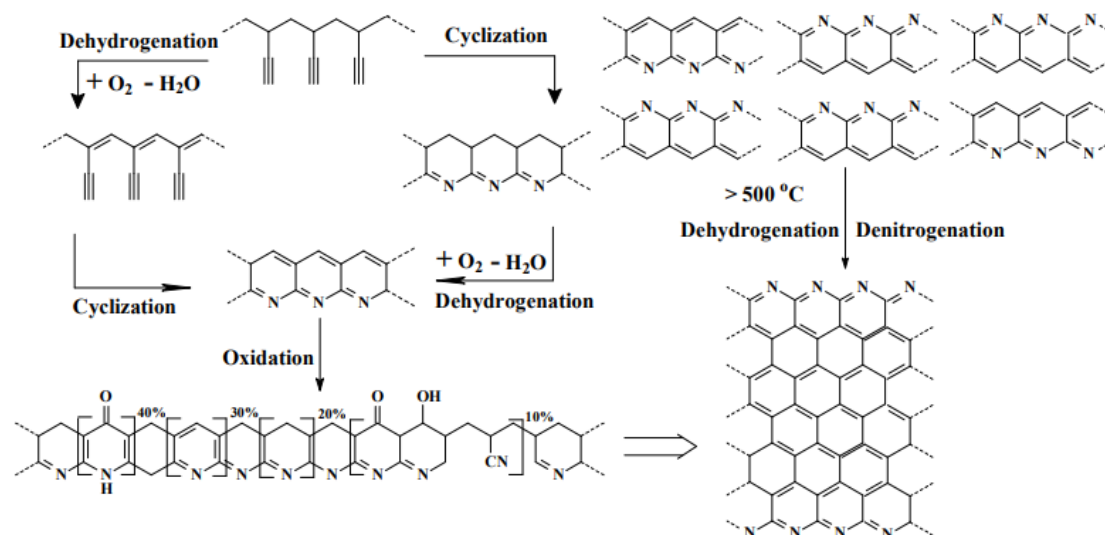
Fig. 1.17 Reaction sequence of transformation of PAN to GL structure: (left) thermal stabilization and (right) pyrolysis, which eventually lead to partially graphitic structure (Yan et al. 2015a).

It's a well-established fact that transition metal-based compounds such as those of iron triads (Fe, Co, and Ni) are excellent catalyst for the formation of carbon nanostructures from aromatic or unsaturated bond organic compounds. Hence, the formation of

carbon-based nanostructures cannot be ruled out when structural moieties such as aromatic ring (from styrene) and nitrile (from acrylonitrile) are present in the polymer, especially at low T (Volkov et al. 2007; Wen et al. 2015; Yan et al. 2015a). Figure 1.17 shows the reaction sequence of transformation of block polymer having nitrile functional group (*i.e.* PAN) to graphene-like (GL) structure by dehydrogenation and denitrogenation. However, the SAN used here is a random copolymer and hence, the formation of well-defined GL structures is difficult.

1.2.8   Effect of type of collector

The commonly used RDR collector, aligns and reduces the diameter of fibers along the direction of drum rotation (Katta et al. 2004; Kumar et al. 2016), by mechanical drawing process. Some applications demand a well-defined alignment of fibers, which is fulfilled by electrostatic, magnetic or mechanical means (Teo and Ramakrishna 2006; Yang et al. 2007). Whereas, this may turn disastrous in case of synthesis of MTMO nanofibers such as NCO as they agglomerate during the pyrolysis due to high ionic conductivity in presence of carbon-based impurities. Besides, the increase in applied voltage or spinneret to collector distance and the presence of additives has been reported to increase or reduce the AFD (Arumugam et al. 2009; Kumar et al. 2016, 2017). However, such cases lead to fiber bundling and alignment (Zhang et al. 2012a), and thus the desired fiber morphology remains unattained. In the present study, a specific RDI collector was built indigenously and used, which additionally allows the centrifugal and Coriolis forces to influence the AFD/morphology and eliminate or reduce defects.

It is a well-known fact that fictitious forces such as centrifugal and Coriolis forces are always associated with any relative motion in which there is a rotating non-internal frame of reference. Various attempts have made in modelling and understanding the mechanism of these fictitious forces during centrifugal spinning or force-spinning of nanofibers to obtain aligned fiber mats (Padron et al. 2013; Xu et al. 2014; Zhang and Lu 2014; Valipouri et al. 2015). These fictitious forces, which act at the jet initiation (rotating spinneret and static collector) play a vital role in forming deflected spiral paths, stretching the fibers and control thus morphology of the nanofibers. However, the AFD obtained from centrifugal spinning are typically larger

than those from electrospinning due to insufficient stretching in the absence of electric field (Liu et al. 2015). A similar approach was adapted to revisit the electrospinning forces on nanofibers.

1.3   PROBLEM IDENTIFICATION

Till now there is no report in literature on understanding the possible changes in structural and other properties of NTO and NCO nanofibers obtained using SAN as polymeric binders or changing pyrolysis parameters. Degradation behavior of a polymeric binder can affect the properties of sol-gel assisted electrospun inorganic nanofibers, especially at the nanoscale. The atomic/ionic and molecular level of interactions can lead to a slight change in nanoscale composition of materials, which in turn bring drastic change in several physico-chemical properties of the inorganic nanofibers. SAN as a polymeric binder has been studied, only in the recent past for limited simple oxides, such as ZnO (Senthil and Anandhan 2014), NiO (George and Anandhan 2015b), Co_3O_4 (George and Anandhan 2015a), and $ZnMn_2O_4$ (Shamitha et al. 2017). It has been observed previously that the use of SAN as the polymeric binder gives rise to interesting structural and morphological changes in the above described inorganic nanofibers. Further, the pyrolysis parameters had a significant influence on SAN degradation, which impacted the physico-chemical properties of the inorganic nanofibers. Therefore, in the present study NTO and NCO nanofiber mats were synthesized using SAN as the sacrificial polymeric binder and their possible applications were explored. Based on the thermal analysis, the pyrolysis parameters where chosen and optimized for the synthesis of inorganic nanofibers.

The ease of dissolvability in polar aprotic solvents, such as DMF, makes it a good choice for sol-gel assisted electrospinning process. Further, DMF is also hydrophilic which can readily dissolve a wide range of metal precursor salts (hygroscopic ones). SAN was first electrospun with different organic solvents and optimized with DMF at a solution concentration of 20 wt% to obtain defect-free nanofibers (Senthil and Anandhan 2015). Further, the interaction between polar functional groups and precursor salt ions, ensure a good dispersion of the later in sol. SAN in recent studies, was found to have good thermal and dimensional stabilities, thus can sustain for a long duration during pyrolysis, which helps in nucleation and growth

of inorganic particles, and can sustain homogeneity in AFD of inorganic nanofibers respectively (George 2015). Simultaneously, the bulky styrene functional groups of SAN can reinforce the precursor fibers, which will help transform the morphology of the precursor fibers to the inorganic nanofibers during pyrolysis. Therefore, SAN is proven to be an appropriate polymeric binder compared with the other water-soluble polymers or conventional polymers (Senthil and Anandhan 2014; George and Anandhan 2015a; Shamitha et al. 2017) .

1.4 SCOPE AND OBJECTIVES OF THE PRESENT STUDY

The main objective of this work was to synthesize NCO and NTO nanofibers using SAN as a polymeric binder and characterize the nanofibers alongside exploring their application potential in various fields. The influence of some of the significant process parameters, which required optimization and revisiting, were also studied to yield defect-free inorganic nanofibers.

1.4.1 Scope

The physico-chemical properties of inorganic nanofibers depend on the synthesis techniques and its parameters. SAN was used as polymeric binder in DMF to synthesize NTO and NCO nanofibers by sol-gel assisted electrospinning process followed by pyrolysis. SAN has excellent binding strength due to the presence of polar functional groups, which ensure the miscibility of the precursor salts in the sol. Also, it can result in the homogenous and flawless morphology of MTMO nanofibers. The process parameters were varied for the synthesis of MTMO nanofibers depending on the thermal analysis as they influence the structural, and morphological changes in the material. An apt collector was used for different MTMOs to obtain defect-free nanofibers. Further, the application potential of these MTMO nanofibers were explored in electrocatalysis.

1.4.2 Objectives

- Synthesis of NTO and NCO nanofibers using SAN as polymeric binder in sol-gel assisted electrospinning followed by pyrolysis with optimal collector conditions for obtaining precursor nanofibers.

- To understand the possible changes that would occur in the process of synthesizing NTO and NCO nanofibers using SAN as polymeric binder obtained at different pyrolysis conditions.

- To study the changes in morphological, structural, and physico-chemical properties of precursor, NTO, and NCO nanofibers obtained at different pyrolysis conditions.

- To study the electrocatalytic and magnetic behavior of NTO and NCO nanofibers obtained at different pyrolysis conditions.

CHAPTER 2

CHAPTER 2

MATERIALS AND METHODS
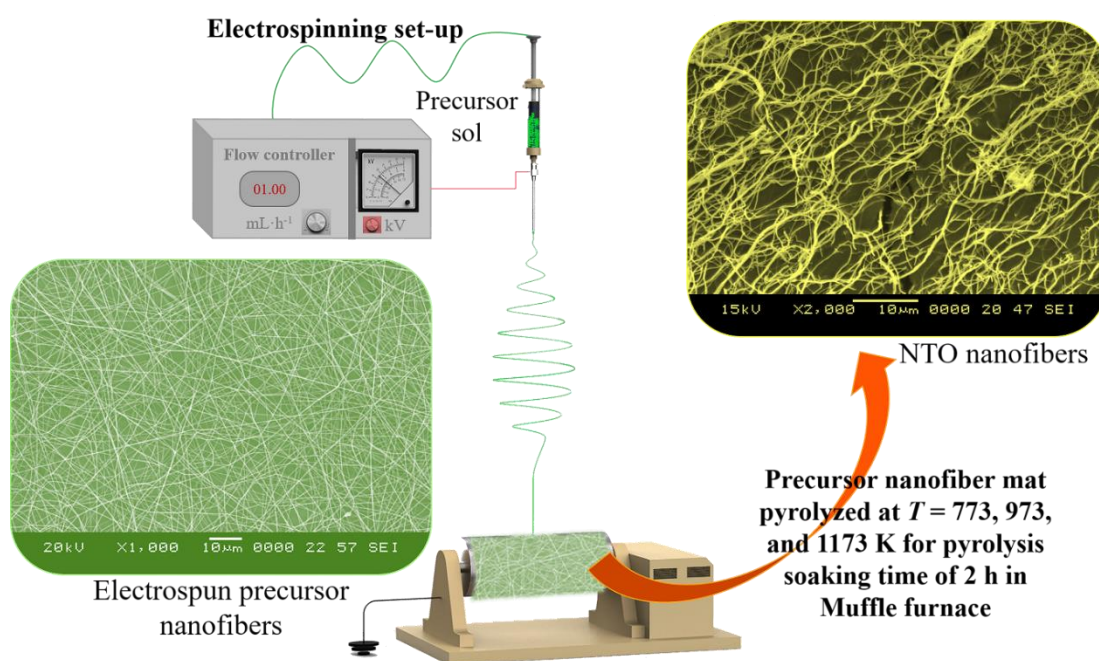
Scheme 2.1 Schematic depicting the synthesis and morphological characterization of NTO nanofibers.

This chapter deliberates the materials used for the synthesis of NTO and NCO nanofibers and the assessment of those nanofibers in various applications. The preparation of electrospinnable sol, electrospun precursor fiber mats and their sea change to inorganic nanofibers are discoursed, followed by a brief portrayal on the several characterization techniques adopted in this study. The methods and the setups casted to study the applications of the developed inorganic nanofibers are also scrutinized.

In general, there are two methods of preparing inorganic nanofibers using sol-gel assisted electrospinning. First, inorganic precursors are mixed with polymers to from a sol for electrospinning, followed by pyrolysis. Second, the reaction velocity and viscosity of the inorganic precursor solution without any polymeric binder can be adjusted for direct electrospinning, which is *Pechini's* method. It is, however, difficult

to control the rheological properties of the inorganic precursor alone, which leads to the shape and the diameters of the inorganic nanofibers being difficult to control too. To solve such problems, it is convenient to use the first method, one has to introduce a polymer into the solution as a matrix to adjust the rheological properties. Besides, an additive can also be used as a catalyst, to control the hydrolysis rate of the precursor. Hence, a typical spinnable precursor sol should contain an alkoxide or metal salt precursor, a polymer acting as a binder, an additive, and a relatively volatile solvent such as water, ethanol, isopropanol, chloroform, DMF, *etc.* Some of the most popular spinnable precursor systems and their applications are shown in Table 1.3. Some additives, such as catalysts and salts, are usually added into the sol to stabilize the precursor and facilitate the electrospinning process. Although only a small amount is required, these additives play an important role in stabilizing the solution as well as the jet. A catalyst, such as acetic acid (Li and Xia 2003), hydrochloric acid (Choi et al. 2003), and propionic acid (Viswanathamurthi et al. 2004); can be used to adjust both the hydrolysis and gelation rates, preventing the solution from blocking the spinneret, thus ensuring a continuous spinning. A salt, such as sodium chloride or tetramethylammonium chloride, can increase the charge density on the liquid jet and thus eliminate the formation of beads, which is a common problem in electrospinning (Li and Xia 2004).

2.1 MATERIALS

SAN (Santron IMS 1000, 30% acrylonitrile content) of $\overline{M_v} = 2.46 \times 10^6$ was procured from Bhansali Engineering Polymers, Sirohi, Rajasthan, India. The inorganic precursors, NATH (assay > 98%) and CATH (both of assay > 98%) were obtained from Sisco Research Laboratories Private Limited, Taloja, Maharashtra, India. The liquid precursor Ti(O^{i}Pr)$_4$ (assay > 97%) was acquired from Sigma-Aldrich, Bangalore, Karnataka, India. DMF (assay > 99%) was purchased from Sisco Research Laboratories Private Limited, Taloja, Maharashtra, India, while the glacial acetic acid (assay > 99.5%) was procured from Nice Chemicals Private Limited, Edappally, Kerala, India. Millipore water (resistivity 18.2 MΩ·cm at 298 K) was used for all experiments.

Glucose ($C_6H_{12}O_6$, assay > 99%) and sodium hydroxide (NaOH, pellets, assay > 99%) were procured from NICE Chemicals Private Limited, Mumbai, Maharashtra,

India. Hydrogen peroxide (H_2O_2, 30% w/v, assay > 99%) was bought from Spectrum Reagents and Chemicals Private Limited, Mumbai, Maharashtra, India. PVDF (Solef® 1015, Solvay, Italy) of $\overline{M}_w = 575 \times 10^6$ was purchased from Prakash Chemicals Private Limited, Vadodara, Gujarat, India. Potassium hydroxide (KOH, pellets, assay > 99%) was also purchased from Nice Chemicals Private Limited, Mumbai, Maharashtra, India. Graphite rods for preparing WE were procured from Speciality Graphites, Puttur, Karnataka, India. No further purification of these chemicals was done, and they were used in as-procured condition for preparing the sol for the electrospinning process.

2.2   METHODOLOGY

The spinnable sol of SAN/inorganic precursor/DMF was prepared, and electrospun for desired time to obtain precursor nanofibers mats. As obtained xerogel mats of precursor nanofibers were pyrolyzed at suitable T and t to acquire inorganic nanofibers. The fabricated inorganic nanofibers were characterized and used as electrocatalyst for applications mentioned. The detail procedure is described in the following section; with a schematic of the process chain shown in Figure 2.1.
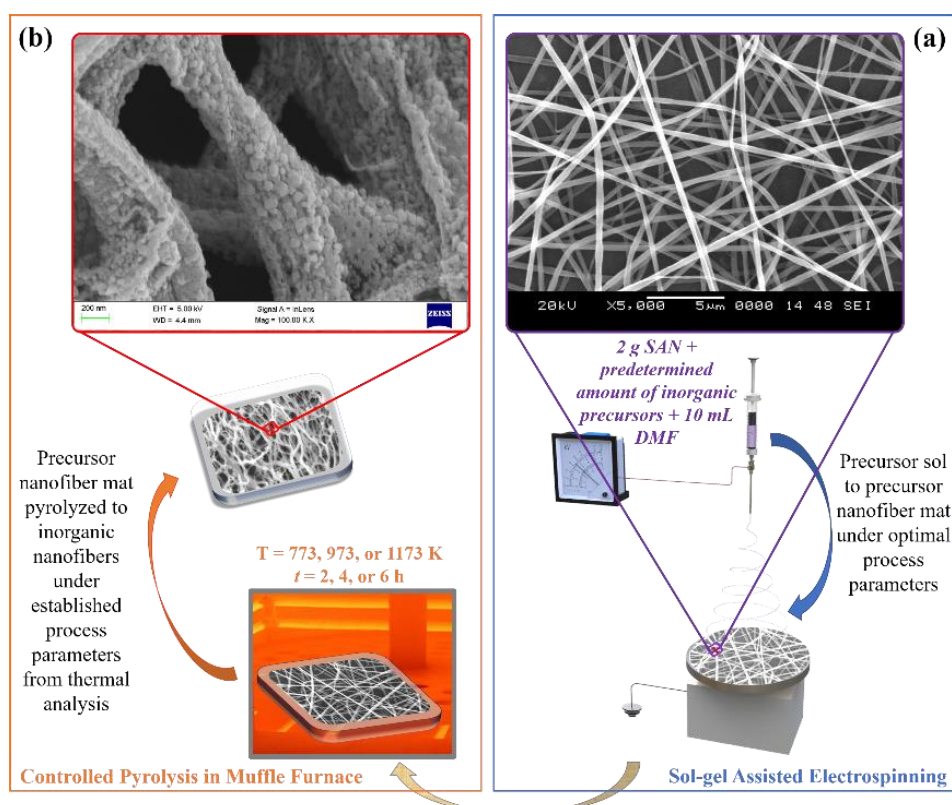
Fig. 2.1 Process chain showing inorganic nanofiber synthesis.

2.2.1 Preparation of electrospinning sol

In preparation of NTO precursor sol, first, 1.102 g of NATH was dissolved in 10 mL of DMF in a stoppered glass vial for one hour by continuous stirring. Later, 0.898 g of Ti(O^{i}Pr)$_4$ solution was added with equal amount of acetic acid for formation of Ti^{4+} complex with acetate groups attached to Ti^{4+} ion by *olation* and *oxolation* as shown in Figure 2.2 (Parra et al. 2008). To this inorganic precursor solution, 2 g of SAN was added such that the inorganic precursor to SAN weight ratio is 1:1. The solution was stirred vigorously for 4 h to ensure complete dissolution of SAN and homogeneity of the precursor sol. Figure 2.3a depicts the schematic of the Ni^{2+} ions and Ti^{4+} complex, interacting with the polar group of SAN, *i.e.*, styrene ring and nitrile functional groups.
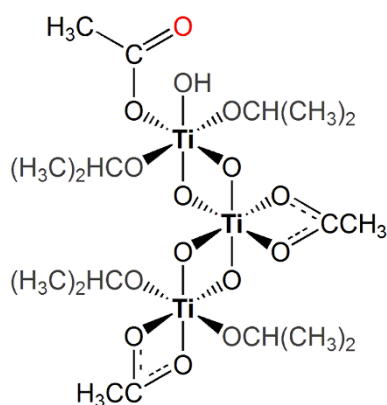
Fig. 2.2 Structure of Ti^{4+} complex formed *via olation* and *oxolation* reactions.
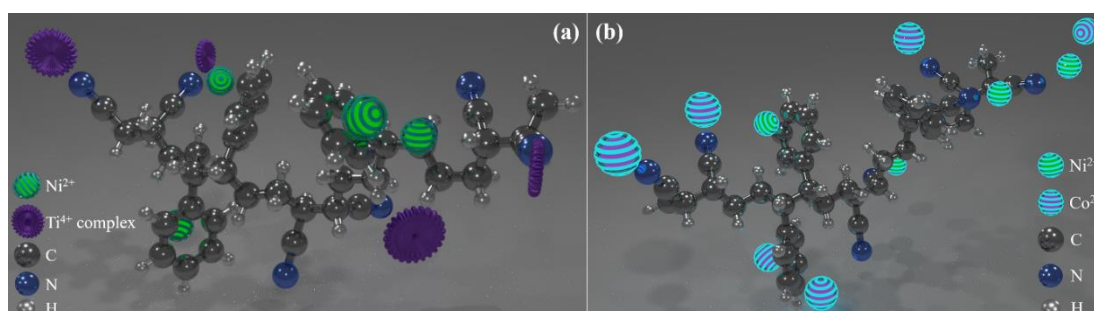
Fig. 2.3 Structural depiction of interaction between (a) SAN/NTO precursors and (b) SAN/NCO precursors.

For NCO precursor sol preparation, 20 w/v% of SAN was first dissolved in DMF by continuously stirring for 4 h, in a stoppered glass vial. Later, a predefined amount of NATH and CATH (*i.e.*, 0.665 g of NATH and 1.335 g of CATH for 2 g of SAN) was added to this solution, such that the inorganic precursor to SAN weight ratio

is 1:1. The solution was stirred vigorously for 12 h to ensure the complete dissolution of inorganic precursors and ensure homogeneity of SAN/NATH/CATH precursor sol. The cationic interactions with the nitrile and benzene functional groups of the SAN are shown in Figure 2.3b. SAN and all acetate inorganic precursors were vacuum oven dried at 343 K for one hour before adding to the DMF to remove moisture.

2.2.2 Fabrication of precursor nanofibers mat

A single spinneret vertical electrospinning unit (V1, E-spin Nano, Physics Equipments Co., Chennai, India) was used to fabricate the precursor nanofibers using two types of collectors (Fig. 2.4a and b). The RDI collector was built in-house, with a fiber collector of dimension ($\varnothing 10$ cm $\times$ 1 cm) of the same weight as the RDR, whereas the RDR collector ($\varnothing 5$ cm $\times$ 13 cm) was procured from Physics Equipment Co., Chennai, India. The stationary RDI collector was used as the static collector to obtain precursor fibers, for comparing that of with rotating collectors. The as prepared precursor sol was loaded to a 10 mL syringe connected with 22 G hypodermic needle, whose beveled tip was chamfered. The syringe containing the sol was loaded to the electrospinning unit as shown in Figure 2.4, and the needle was connected to a positive direct-current (DC) potential.
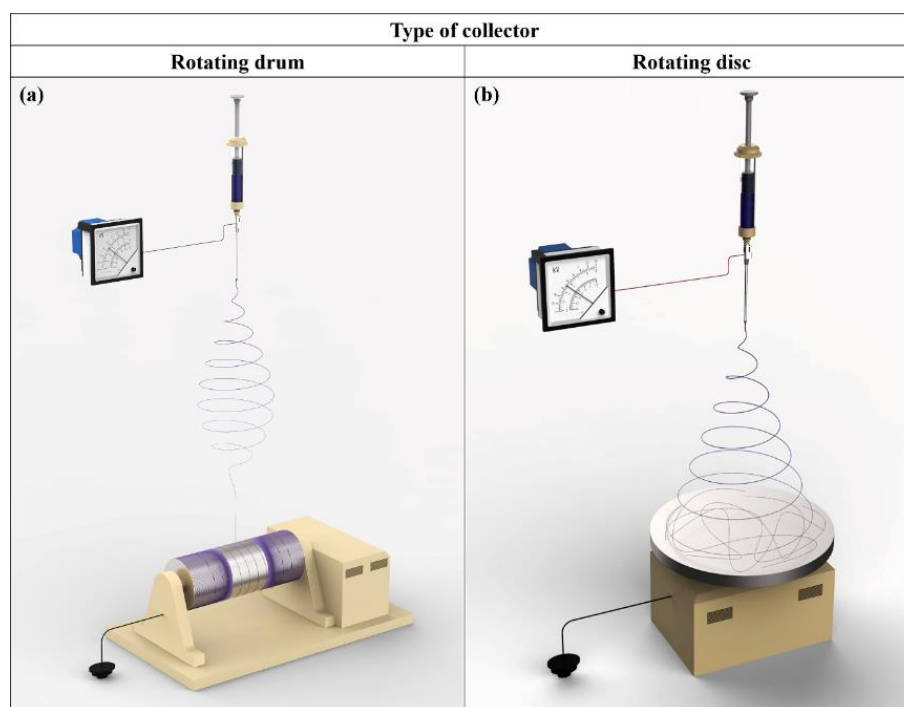
Fig. 2.4 Representation of electrospinning set-up with (a) RDR and (b) RDI collectors.

The optimal electrospinning parameters were fixed based on many trials and previous literature (Senthil et al. 2013) as: spinneret tip to collector distance = 17 cm and flow rate = 1 mL·h^{-1}. The NTO precursor nanofibers were collected on RDR collector at a speed of 2000 rpm and applied voltage of 22 kV. Besides, the rotating speed of both the RDR and RDI was kept at 500 rpm for NCO precursor nanofibers collection at an applied voltage of 25 kV. The variation in the applied voltage to form a stable jet is attributed to the change is charge density at the Taylor cone. It has to be noted that the interaction of cations in precursor sol is different for different inorganic precursors and their composite. Table 2.1 gives the relative electrical conductivity of the solvent (20 mL) in absence and presence of predetermined quantity of inorganic precursors. It is clear that higher conductivity sol needs lower voltage to attain stable jet for defect-free nanofiber formation. Under the optimized parameters, the droplets of the sol produced uniform, continuous and bead-free nanofibers on the electrically grounded collectors. The electrospun fibers were collected for a fixed duration on all the collectors. The precursor fibers were collected on aluminum foil tagged to all types of collector. Later, these precursor fibers were carefully peeled off the foil and pyrolyzed as mentioned in the following section.

Table 2.1: Relative electrical conductivity of inorganic precursor/DMF solutions (20 mL solvent).

Solution	Relative electrical conductivity (µS)
Distilled water	59.2
DMF	36.5
NATH+CATH+DMF	87.7
NATH + Ti(O^{i}Pr)$_4$ + Acetic acid + DMF	104.4

2.2.3 Synthesis of inorganic nanofibers

The precursor fiber mat was peeled out from the aluminum foil tagged to collector surface and placed on a quartz plate. Later, the quartz plate with the precursor fiber mat was fed in to a programmable Muffle furnace (LCR 268, Muffle, Controller-PFU 400,

Indfurr, Chennai, India) for pyrolysis, at a controlled heating rate of 4 K·min^{-1}. NTO precursor nanofibers were pyrolyzed at three different T (*i.e.*, 773, 973, and 1173 K) for *t* = 2 h. And, the NCO precursor nanofibers were pyrolyzed at T = 773 K for three different *t* (*viz.*, 2, 4, and 6 h). The resulting inorganic nanofibers were left in the furnace to anneal till room temperature was reached and then collected for characterization. The selection of T and *t* were based on the thermal analysis, which will be discussed in appropriate chapters.

2.3   MEASUREMENT AND CHARACTERIZATION

2.3.1   Characterization techniques

The micrographs of the precursor and the calcined nanofibers were obtained using SEM (JSM-6380LA, JEOL, Japan). The nanofibers were gold sputtered prior to the imaging (JFC 1600 autofine coater, JEOL, Japan). The fiber diameters were measured for 50 fibers along three different spots of each fiber using software ImageJ (1.51n, National Institutes of Health, USA), and an average of those 150 values is reported for each sample as AFD. Apart from SD in the fiber diameter, the fiber uniformity was estimated as a factor of C_{FU} (Section I.1). The fiber alignment (directionality tool) were measured using directionality tool in software Fiji ImageJ (1.51n, National Institutes of Health, USA) and defined in terms of DoA and DoR as (Cadafalch Gazquez et al. 2017):

$$\text{DoA} = 1 - \text{DoR} = 1 - \left(\frac{dispersion}{90} \right) \tag{2.1}$$

FTIR spectrometer (4200, Jasco, Japan) was used to analyze the infrared active vibrational spectra of SAN, precursor, and inorganic nanofibers in transmission mode (400-4000 cm^{-1}, resolution = 1 cm^{-1}, number of scans = 32). The samples were diluted in 0.1% to 10% in the moisture-free spectra grade potassium bromide (KBr) powder and hydraulically pressed to form transparent wafers for analysis.

Simultaneous TGA/DSC (TGA/DSC-1 STARe System, Mettler Toledo, Switzerland) was used to study the decomposition of SAN and precursor nanofibers at a heating rate of 10 K·min^{-1} in N$_2$ atmosphere at a purge rate of 20 mL·min^{-1}. DTG was plotted using the first derivative of the TGA plot.

FESEM (ULTRA 55, Gemini, Carl Zeiss, Germany) equipped with EDS (X-Max, Oxford instruments, UK) was used to image the grains of the inorganic nanofiber (high-resolution micrographs) and to determine the elemental compositions at a selected area, respectively. The a_{APD} were measured for 150 particles in each sample using ImageJ software.

X-ray diffractometer (DXGE-2P, JEOL, Japan) operating at 30 kV and 20 mA was used to record the XRD patterns of inorganic nanofibers, using Cu K_α radiation of wavelength, $\lambda = 0.154$ nm. The patterns were recorded within a 2θ range of 10-90°, at a scanning rate of 0.5 degrees per minute. The raw XRD patterns were profile fitted using the standard functions in software OriginPro 2016 (Sr1, OriginLab Corporation, USA). The instrumental broadening was accounted for using the bulk silicon sample and subtracted from the measured FWHM to obtain the actual FWHM. The crystallite shape was assumed to be spherical from FESEM and hence, the dimensionless shape factor (κ) was set to 0.9 in crystallite size calculation of samples (Section I.5 and II.3).

SSA and pore volume values of inorganic nanofibers were measured by the BET method. The micropore and mesopore volumes were calculated by DFT and BJH methods using the adsorption-desorption isotherms of N_2, respectively. The adsorption-desorption isotherms were obtained by automated gas sorption system (Autosorb 1C, Quantachrome Instruments, Florida) under high vacuum. The samples were degassed for 5 h at 423 K prior to adsorption-desorption analysis.

HRTEM (JEM 2100, JEOL, USA) was used to image and study the morphological features and crystallite characteristics of inorganic nanofibers at an accelerating voltage of 200 kV. SAED patterns were also recorded with the electron micrographs for the polycrystalline inorganic nanofibers.

XPS was recorded using spectrometer (K-Alpha, Thermo Scientific, USA) employing monochromatic Al K_α radiation (1486.6 eV) was used to obtain survey spectra in the range 0-1350 eV with pass energy of 200 eV for inorganic nanofibers to determine the elemental composition in the sample. High-resolution spectra for Ni *2p*, Co *2p*, Ti *2p*, O *1s*, N *1s*, and C *1s* were recorded with pass energy of 50 eV to resolve the oxidation states of elements present in inorganic nanofibers. For each case, 10 scans

were performed, and the binding energies were measured with a precision of ± 0.1 eV. All binding energies were referenced to the C $1s$ line at 285.0 eV. The photoelectrons were collected at 90° with respect to the sample surface for an analyzed spot of $\varnothing 400$ μm. The base pressure in the XPS analysis chamber was approximately 2×10^{-8} mbar and the deconvolution of the XPS spectra was done by OriginPro 2016 software. The depth profiling was carried out to understand the distribution of different ions within the inorganic nanofibers obtained at different pyrolysis conditions. During depth profiling, the Ar^+ ion bean was sputtered for 25 s to sputter away the sample and attain a new surface at each depth.

The absorption spectra of NCO nanofibers in UV-Vis-NIR region were recorded in diffuse reflectance mode in the range from 200 to 2500 nm using UV-Vis-NIR spectrometer (3600+, Hitachi, Japan).

The PL emission spectra of inorganic fibers were acquired using PL emission spectrometer (Fluoromax-4, Spectrofluorometer, Horiba, France) in the range of 340-620 nm for an excitation of 325 nm. CIE chromaticity diagrams (1931 plot) were plotted by estimating chromaticity co-ordinates using PL spectra in software MATLAB (R2015a, MathWorks, USA).

Raman spectra were obtained for inorganic nanofibers using micro Raman spectrometer (LabRAM HR, Horiba, Japan) in the wavenumber range of 50-1600 cm^{-1} using diode-pumped solid-state laser source with a power of 28 mW and a wavelength of 532 nm. micro-Raman spectrometer (LabRAM HR, Horiba, Japan). Raman spectra were obtained using a diode-pumped solid-state laser source, at a power of 28 mW and a wavelength of 532 nm. Lorentzian function was used to deconvolute Raman spectra using OriginPro 2016 software.

Hall effect measurements and electrical parameters of the inorganic nanofiber mesh (thin layer deposited on 1 cm $\times 1$ cm quartz plate, having 70% porosity as measured from FESEM micrographs and ImageJ software) were obtained using an electromagnet (HEM 150, Polytronic Research, Thane, India) for a magnetic field of 2500 G and the DC probe station (Performance Monitor 5 with Thermal Chuck, Agilent Device Analyzer B1500A, Keysight Technologies, USA) as per NIST (Secula 2010).

VSM (7410, LakeShore Cryotronics, USA) was used to study the isothermal and non-isothermal (ZFC and FC modes) magnetization measurements of NTO nanofibers. The temperatures for non-isothermal magnetization measurements were chosen to be in the range of 20-300 K, *i.e.*, from just below $T_N \sim 23$ K of INTO (Heller et al. 1963; Watanabe et al. 1980) to room temperature. The magnetic hysteresis loops of NCO nanofibers were recorded at $\theta_T = 300$ K, using a VSM (DC SQUID, Quantum design, USA).

2.3.2 Theoretical study

In order to understand the intermediate band-gap and optical characteristics of INTO and SNTO, first-principles DFT calculations were carried out using projector augmented wave method implemented in Vienna ab-initio simulation package (VASP). Generalized gradient approximation (GGA) under Perdew-Burke-Ernzerhof parametrization (PBE) was used for treating the exchange-correlation potential. However, this alone does not remove the ambiguity of electron self-interaction term in DFT. Hence, to prevent unwanted delocalized *d-* and *f-*electrons, onsite Coulomb interaction correction was introduced using GGA+U method (Pontes Ribeiro et al. 2016; Challagulla et al. 2017). A grid of $7 \times 7 \times 7$ Monkhorst Pack k-points was used for reciprocal space sampling. The wave functions were expanded in the plane wave basis with a sufficiently large kinetic energy cut-off of 500 eV. Hellmann-Feynman theorem was used to calculate the forces on each atom. Subsequently, these were used to perform a conjugate gradient structural relaxation until the forces on the atoms reduced to less than 1 meV·Å^{-1}. The electronic band structure and DOS of INTO and SNTO were investigated when their respective unit cells were having optimized structure with minimum total energy. Finally, the optical conductivity was calculated within a range of 0-50 eV using random phase approximation.

2.3.3 Set-ups and methodology used for the electrocatalytic studies of inorganic nanofibers

To study the electrocatalytic behavior of as-prepared inorganic nanofibers, the graphite rods were modified to fabricate WE (*i.e.*, GE) as follows: one end of the rod was glassy polished, whereas, the other end was soldered with insulated wire circuit connections.

The electrode was sealed on the side walls as well as circuit connection ends using Teflon tape to have no current or electrolyte leak.

2.3.3.1 *Bifunctional electrocatalyst for water-splitting by NTO nanofibers*

The electrode prepared using NTO nanofibers was sealed on the side walls as well as circuit connection ends using Teflon tape to have no current or electrolyte leak. The polished end was sonicated in ethanol for an hour and then dried. The electrocatalyst ink having a concentration of 10 mg·mL^{-1} NTO nanofibers and 0.1 mg·mL^{-1} of carbon black (to improve adhesiveness) was prepared by dispersing them in ethanol by ultrasonication for an hour. Similarly, the bare GE was prepared without NTO nanofibers. Later, 1 mL of this electrocatalyst ink was pipetted on the polished surface of the GE and dried in air. After the coated surface is completely dried, 10 µL of 0.5% PVDF solution on DMF was loaded to keep the NTO nanofiber/carbon black deposit in position. The GEs were prepared from NTO nanofibers obtained at pyrolysis soaking temperatures, 773 K, 973 K, and 1173 K.
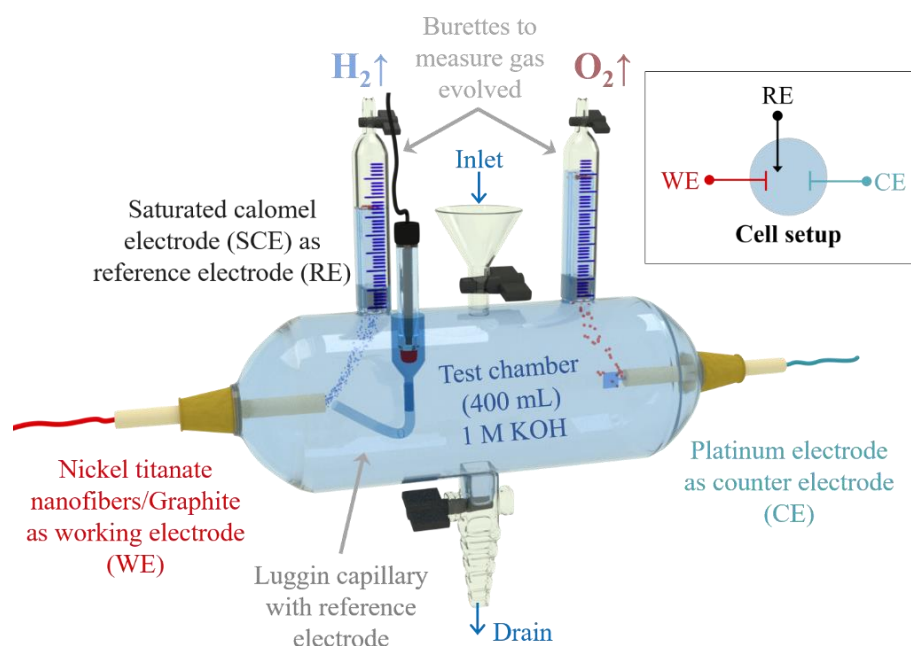
Fig. 2.5 Test set-up used for electrochemical studies of NTO nanofibers.

The electrochemical measurements were performed on an electrochemical workstation (VersaSTAT 3, Ametek Scientific Instruments, USA) with a three-electrode cell set up as shown in Figure 2.5. The cell comprises GE coated with electrocatalyst as WE (effective surface area = 100 mm^2), a platinum foil of same

surface area as CE, and SCE as RE. The SCE was connected through the Luggin's capillary with Agar-KCl salt bridge, to eliminate the error due to Ohmic drop. The GE were submerged for an hour in the electrolyte (N_2 saturated 1 M KOH) before electrochemical studies, to attain equilibrium. The alkaline water electrolysis efficiency of NTO nanofibers obtained at different pyrolysis temperature were analyzed using CV and CP techniques and monitoring the HER and OER kinetics. It must be noted that NTO has natural photocatalytic properties due to its wide range of band-gaps in visible light region. Hence, all the electrochemical measurements were made in the same timeline of 3:00 to 5:00 PM as per Indian standard time, in a closed room environment under a fluorescent lamp.

2.3.3.2 *Multifunctional electrocatalyst for glucose and H₂O₂ sensing, and water-splitting by NCO nanofibers*

In this study, all electrocatalytic studies were carried out using an electrochemical workstation (SP-150, Bio-Logic Science Instruments) with three electrode configuration and test set-up as shown in Figure 2.6 at an ambient environment. The electrolyte and analyte solutions were prepared with Millipore water, which was purged with N_2 for 20 minutes to remove the dissolved oxygen in the solution prior to experiment.
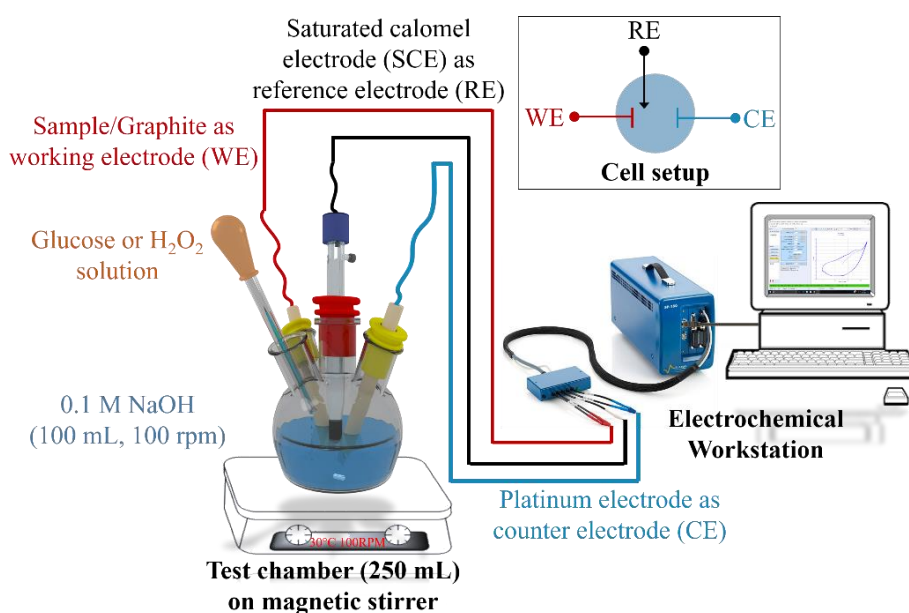
Fig. 2.6 Test set-up used for electrochemical studies of NCO nanofibers.

The GE prepared with NCO nanofibers served as the WE, whereas SCE was used as a reference and platinized platinum as a CE. The catalyst ink was prepared by sonicating 10 mg GL/NCO nanofibers in 1 mL of ethanol. For sensing studies, 40 µL of this suspension was loaded on the polished surface of GE and air dried for 10 minutes, while 1 mL of the catalyst ink was dropped on the polished surface of GE for HER or OER studies. After the deposit dried, 10 µL of 0.5% solution of PVDF in DMF was dropped on the deposit to keep the GL/NCO nanofibers deposit intact on the electrode. The same amount of PVDF/DMF solution alone was loaded on the polished surface of GE to account as bare electrode. The electrode was dried in air for 6 h to ensure that any residual solvents were removed.

The electrodes were submerged in 0.1 M NaOH electrolyte for electrocatalytic sensing application and open-circuit potential was applied for one hour to attain equilibrium before each sensing study. NaOH (1 M) was used as an electrolyte and similar steady state open-circuit potential test was acquired for water-splitting experiments. The electrolyte was continuously stirred at 100 rpm during all electrocatalytic measurements to ensure homogeneity of analyte in electrolyte during sensing, and to avoid the bubbles/gas accumulation on the electrode surface in HER or OER studies. CV, LSV, CA, EIS, and CP responses were acquired to study the electrocatalytic behavior of GL/NCO nanofibers.

PART ONE

ELECTROSPUN NICKEL TITANATE NANOFIBERS

CHAPTER 3

CHAPTER 3

SOME NEW OBSERVATIONS ON THE STRUCTURAL AND PHASE EVOLUTION OF NTO NANOFIBERS
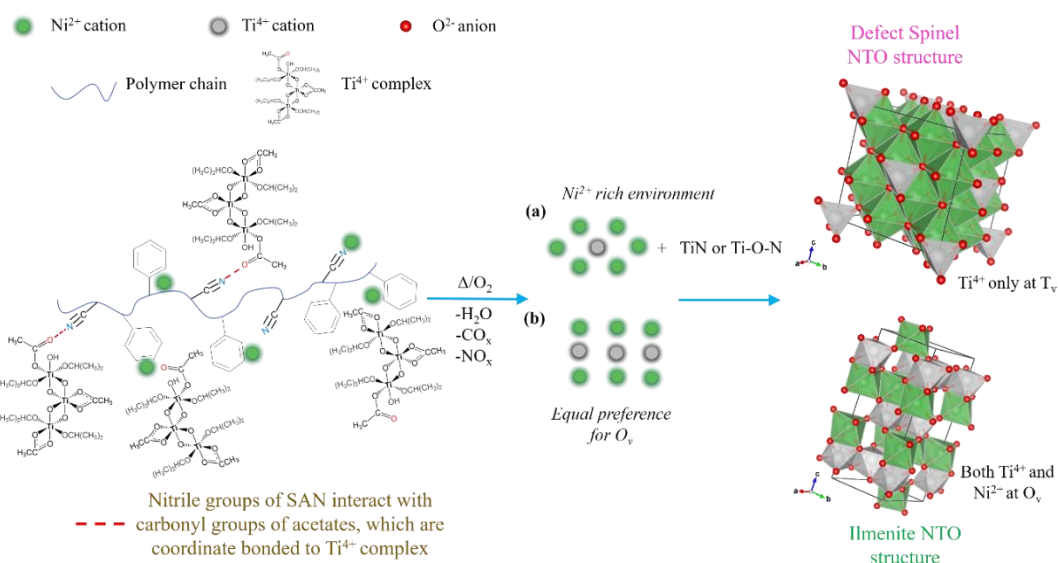
Scheme 3.1 Probable mechanism of SNTO formation.

This chapter reports for the first time the synthesis of NTO nanofibers containing a mixture of INTO and SNTO phases, at an atypical low temperature. Precursor nanofibers produced by sol-gel electrospinning were pyrolyzed at three different temperatures to produce the NTO nanofibers. Thermal analysis along with XPS confirmed the formation of non-crystalline stable phases of TiN and Ti-O-N that restrained the formation of INTO, and the Ni-rich environment pushed the Ti atoms to T_v to form a defective spinel structure. The crystallite size of SNTO was observed to increase as a function of the T above 973 K, as the E_a for coalescence and growth of SNTO was favorable. NTO nanofibers obtained above the T of 973 K exhibited new band gap energy around 2.5 eV in Tauc plot. Oxygen vacancies in these inorganic nanofibers decreased as the T was increased. A hypsochromic shift of 20 nm in the photoluminescence spectra suggested that the material had a Ni^{2+} rich NTO (SNTO).

3.1 RESULTS AND DISCUSSION

3.1.1 Characterization of precursor nanofibers

3.1.1.1 *SEM micrographs*
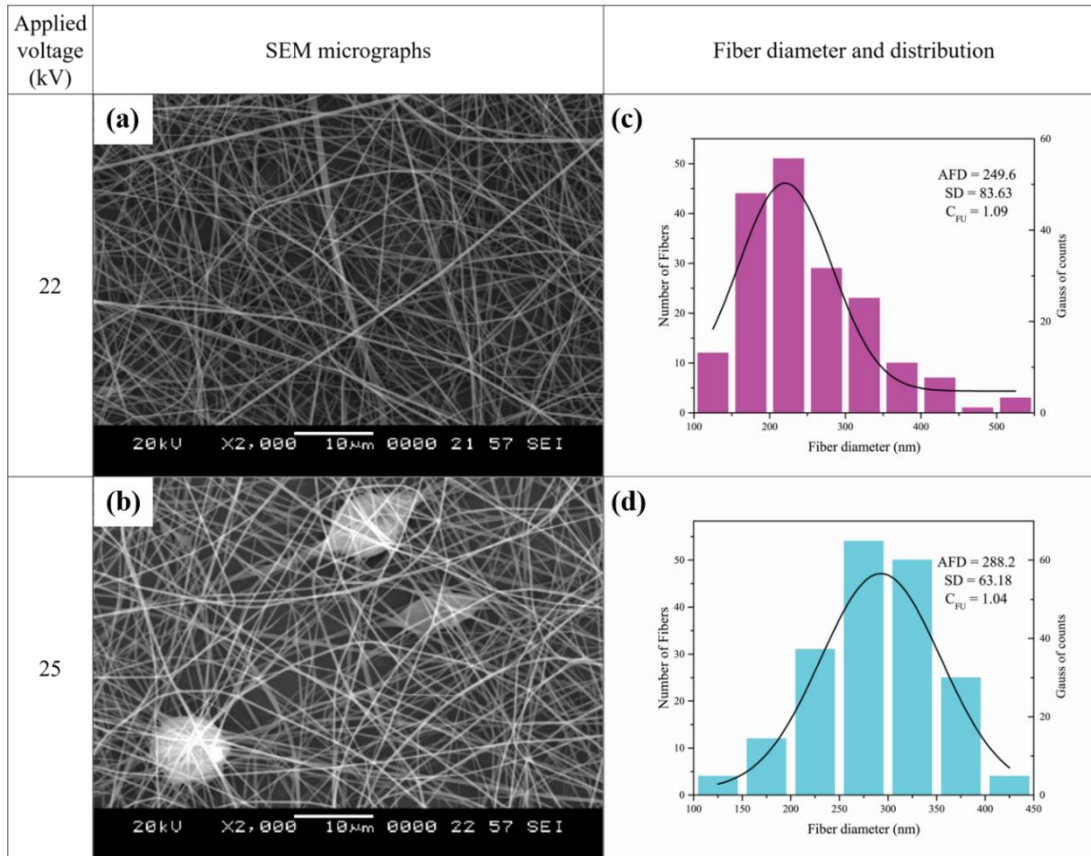
Fig. 3.1 SEM micrographs of precursor nanofiber mat and the corresponding histogram inferring the distribution of fibers developed at two different applied voltages: 22 and 25 kV. AFD and SD are in nm, whereas C_{FU} is a dimensionless number.

Figure 3.1 shows the SEM micrographs of the precursor fibers obtained at two different voltages: 22 and 25 kV. The AFD and SD of the precursor fibers developed at an applied voltage of 22 kV were found to be 250 ± 84 nm and beads-free. A narrow distribution of fibers was observed from the histograms and the C_{FU} for the precursor fibers developed at an applied voltage of 22 kV was determined to be 1.09 (Section I.1). The C_{FU} value close to unity suggests a fairly uniform distribution of the fiber diameter. It is well-established fact in electrospinning process that the increase in voltage,

increases the charge dissipation at the Taylor cone and thus making the jet unstable, which leads to beads formation in the fiber.

3.1.1.2 FTIR spectroscopy

The interaction between SAN and precursor salts plays a major role in the evolution of the pyrolyzed phase morphologically and structurally. FTIR spectra of SAN and precursor fibers (Fig. 3.2) were used to ascertain the possible interactions between the precursor salts and the polymer. A broad peak at 3417 cm^{-1} (O-H stretching) confirms the presence of crystallised water molecules in precursor fibrs from the hydrated nickel acetate. The peaks at 1584 and 1430 cm^{-1} are due to deformation of C=O and C-H in the acetate group, respectively (George and Anandhan 2015b). It is worth noting that, the acetate groups are present in ionised form in nickel acetate, as well as ligand form coordinated to Ti^{4+} in the complex (Fig. 2.2).
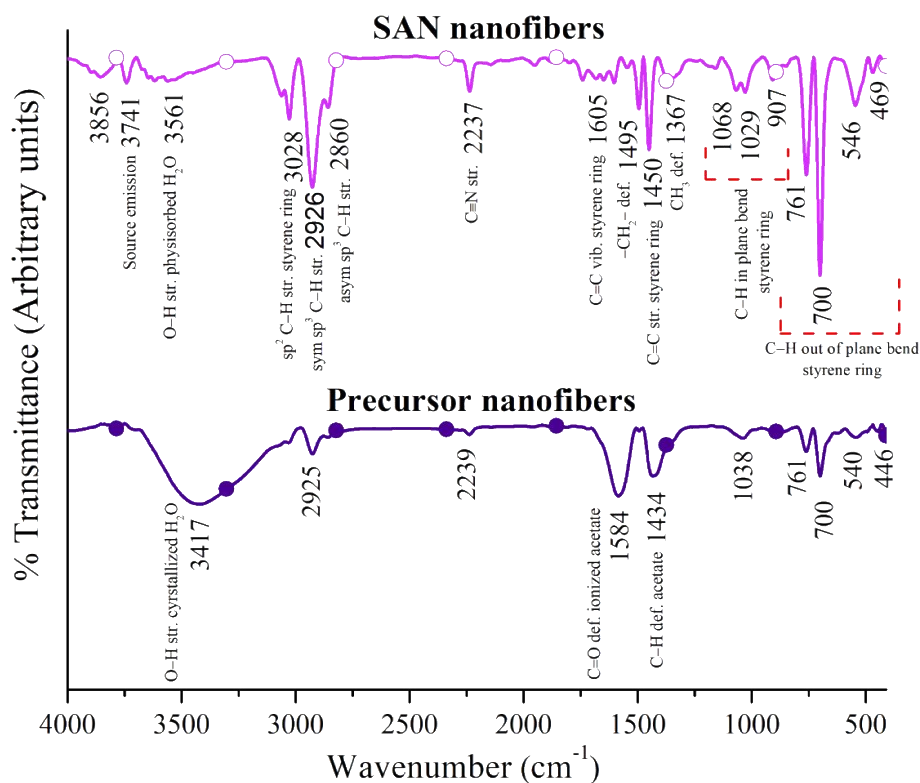
Fig. 3.2 FTIR spectra of SAN and precursor nanofibers.

In earlier study from literature, a doublet peak at 1542 cm^{-1} and 1440 cm^{-1} was reported for the asymmetric and symmetric stretching vibrations of carboxylate group of acetates coordinated to Ti^{4+} as a bidentate ligand (Parra et al. 2008). The remarkable

peak broadening and reduction in the peak intensities indicates the interaction between the functional groups (styrene ring and nitrile) of SAN and the precursor salts, therefore a homogeneous mixing. Also, the functional groups of SAN contribute to the thermal stability of the polymer, which in turn act as structure and morphology supporting organic binder for the crystallite nucleation and growth of the inorganic phases during pyrolysis (George and Anandhan 2015a; George et al. 2015).

3.1.1.3   Thermal analysis

TGA and DTG plots of the precursor fibers in N_2 atmosphere are shown in Figure 3.3. SAN undergoes a complete degradation at 773 K in a single-step (George and Anandhan 2015b; George et al. 2015). The precursor fibers exhibit three step degradations as follows: in the first step, the water molecules from the hydrated salts are removed. In the second step, the degradation of SAN was enhanced and accelerated at a temperature less than 773 K (Section I.2), probably due to the catalytic activity of acetic acid released from the precursor salts at an early stage (Scheirs 2000). In the final step, the residues of the polymer continue to degrade, and the precursor salts react to form NTO at a temperature of 773 K. The expected plausible overall reaction between the precursor salts is shown below (Ni et al. 2009; Vijayalakshmi and Rajendran 2012):

$$Ni\left(CH_3COO\right)_{2(s)} + Ti\left[OCH\left(CH_3\right)_2\right]_{4(s)} + 9O_{2(g)} \rightarrow NiTiO_{3(s)} + 15H_2O_{(g)} + 16CO_{2(g)}$$

$$(3.1)$$
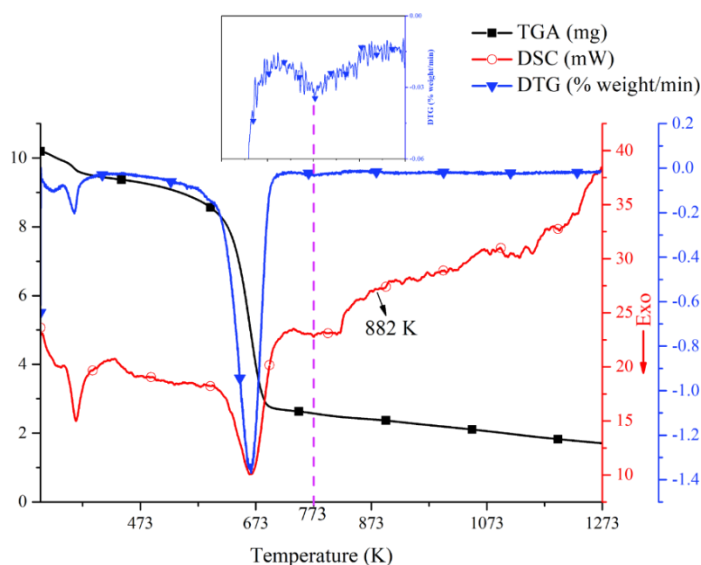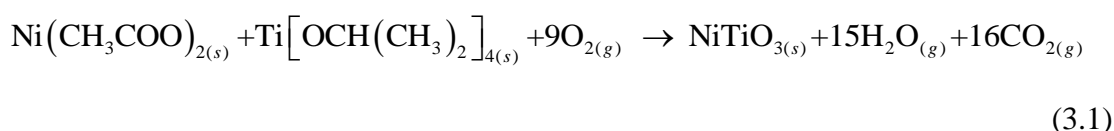
Fig. 3.3 Thermal analysis curves for precursor nanofibers.

DSC trace of precursor fibers is shown in Figure 3.2. It is evident that similar to TGA-DTG plots, the water molecules and organic phases of the precursor fibers were removed with intense exothermic peaks at below 373 K and 673 K, respectively. A small exothermic peak (magnified in the inset Fig. 3.2) at 773 K is the minimum crystallization temperature associated with the nanocrystalline NTO phase formation, which is in good agreement with the value reported around 782 K in literature (Sadjadi et al. 2008). However, it was also reported in other literature that this exothermic peak appeared at a higher temperature, about 880 K for crystalline NTO (Lopes et al. 2009). In the present study, the second exothermic peak observed around 882 K may be due to the phase change occurring in NTO. The new NTO phase formation was also confirmed by XRD and HRTEM analysis at this temperature (see sections 3.1.2.3 and 3.1.2.5). The formation of NTO may be due to the quantum confinement effect, which gives rise to the new phase at a lower temperature when the size of the material is in the nano-scale (Frey and Payne 1996). The DSC plot revealed that there was a serration in peaks, which could be attributed to the reorientation of the lattice and breakdown of the complex structures studied using FTIR and XRD analysis (see sections 3.1.2.2 and 3.1.2.3). The pyrolysis temperatures of precursor fibers were thus chosen based on the major peak changes (shown in Fig. 3.2) from DSC as 773, 973, and 1173 K.

3.1.2   Characterization of NTO nanofibers

3.1.2.1   SEM micrographs

Figure 3.4a-c shows the SEM micrographs of randomly oriented NTO nanofibers obtained at pyrolysis temperatures; 773, 973, and 1173 K, respectively. As degradation removes the organic phases, the fibers shrink during the pyrolysis, and the AFD of NTO nanofibers reduces in comparison with that of the precursor fibers (Fig. 3.4d-f). The nanofiber surface roughness and the size of grains in individual NTO nanofibers increase gradually as a function of T due to the coalescence and growth of the NTO nanoparticles in individual nanofibers (Park and Kim 2009). Besides, the AFD of the nanofibers increased as a function of T. It was observed in earlier work that the concentration of $Ti(O^iPr)_4$ in precursor sol had a minor effect on the AFD of TiO_2/acetic acid/PVP precursor fibers but played a major role in determining the AFD of the pyrolyzed anatase nanofibers. The use of $Ti(O^iPr)_4$, at higher concentrations, is known

to form thicker inorganic nanofibers (Li and Xia 2003). In this study, the concentration of Ti(O^{i}Pr)$_4$ was kept constant in the sol, but still, the AFD increased with an increase in T. The increase in AFD as a function of T suggests that the complex of Ti^{4+} formed in sol with acetic acid did not take part in the conversion reaction completely. Further, this might be the reason for the exothermic peaks observed in DSC after 773 K, undergoing conversion reaction at different temperatures.
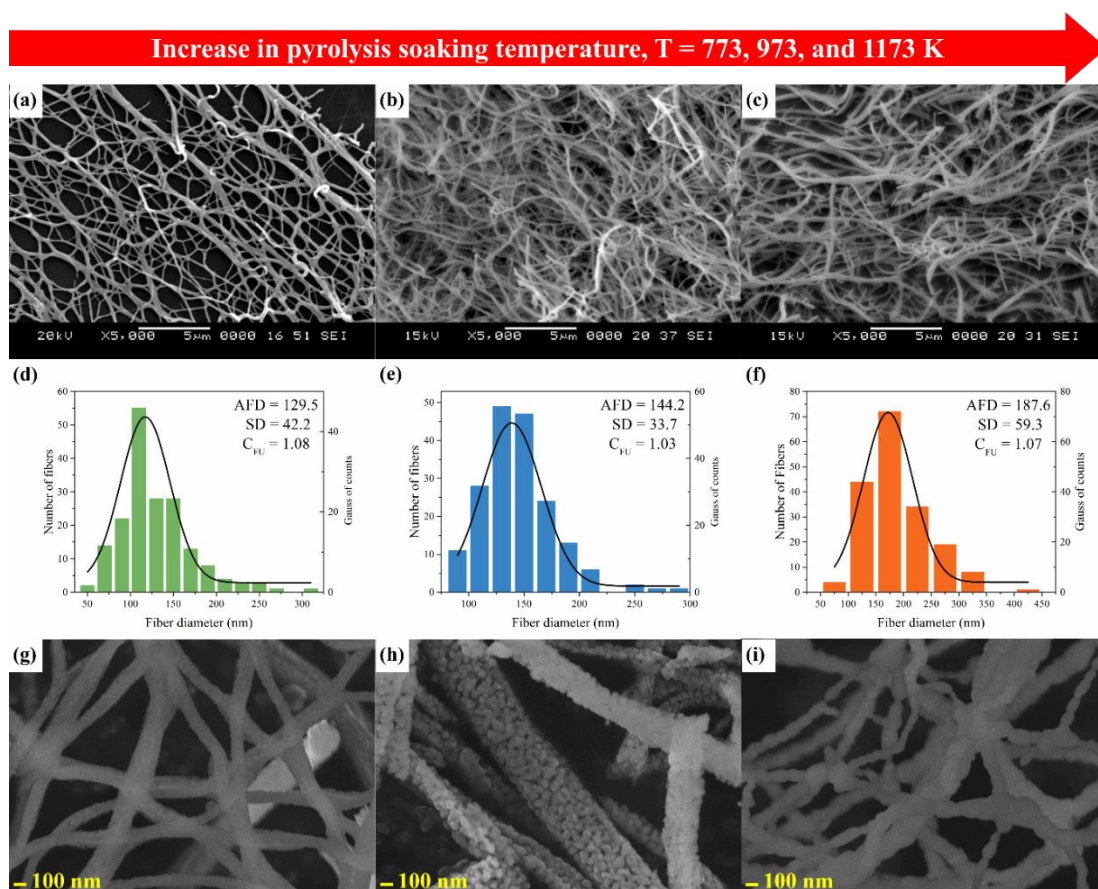
Fig. 3.4 (a-c) SEM micrographs, (d-f) histograms deducing distribution, and (g-i) FESEM micrographs of NTO nanofibers synthesized at different T. AFD and SD are in nm, whereas C_{FU} is a dimensionless number.

The SD, histogram plot, and C_{FU} of the NTO nanofibers were used to find the diameter distribution of the NTO nanofibers for various T (Fig. 3.4d-f). The nanofibers developed at a temperature of 973 K were more uniform. The transformation of particles embedded on nanofibers from mosaic structure to bamboo structure due to thermally driven coalescence and growth of particles can be seen in Figure 3.4g-i.

3.1.2.2 FTIR spectroscopy

The FTIR spectra of NTO nanofiber obtained at different T are shown in Figure 3.5. NTO, are the class of titanate having both nickel and titanium as octahedral partners in the stable INTO structure. The peak 716 cm^{-1} corresponds to the stretching of O-Ti-O in [TiO$_6$] octahedra (meaning Ti in an O$_v$ surrounded by oxygen at octahedron corners) of NTO. The peak at 669 cm^{-1} was for the octahedral Ti-O bending; whereas those at 650, 612 and 536 cm^{-1} correspond to the octahedral Ti-O stretching of INTO. The FTIR spectra exhibited two sharp peaks at 450 cm^{-1} (associated with Ti-O-Ni stretching) and 430 cm^{-1} (octahedral Ni-O stretching, which is also associated with other peaks at 550 cm^{-1} and 566 cm^{-1}). All FTIR absorption peaks are in good agreement with those in the literature (Baraton et al. 1994; Zhou and Kang 2006; Gambhire et al. 2008; Sadjadi et al. 2008; Yuvaraj et al. 2013; Sobhani-Nasab et al. 2015; Johnson et al. 2016). Hence, the FTIR results confirm the formation of NTO without any organic residues in the nanofibers.
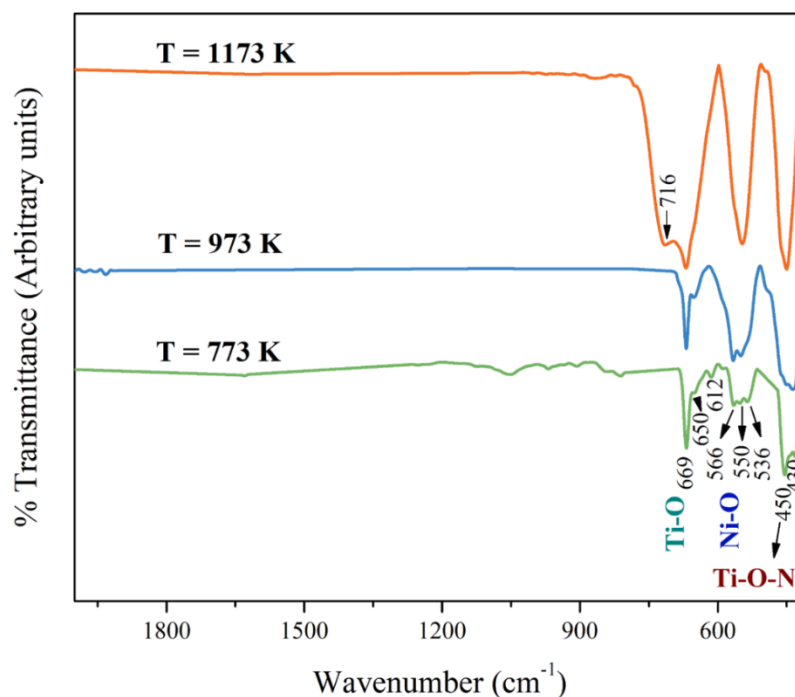
Fig. 3.5 FTIR spectra of NTO nanofibers synthesized at 773, 973, and 1173 K.

As the T increases, the peak intensities also increase and become sharper due to thermally induced particle growth of NTO nanoparticles (George et al. 2015), as seen in FESEM (Fig. 3.4g-i). It should be noted that there are multiple peaks convoluted in

the FTIR spectral peaks and as the T increases, the peak broadening has grown. This kind of spectral change suggests that each sample synthesized at different T had a phase or crystal structure, which is different from the standard INTO structure, and this structural change was thermally driven (Tang et al. 2008; Lemine 2009). In general, the cation positioned in T_v of oxygen has lower wavenumber peak than that of the O_v (Allen and Paul 1995). This is in good agreement with the DSC and FESEM results. The results of XRD, HRTEM, and XPS has to be analysed next, to explain the nature and reason behind such structural change in NTO.

3.1.2.3 XRD analysis

Figure 3.6 shows the XRD patterns of NTO obtained at the pyrolysis temperatures of 773, 973, and 1173 K. The profile fitting of XRD peaks was done by assuming a shape function, Pseudo-Voigt I, which had the best fit for the raw data (inset Fig. 3.6). The profile fitting was carried out to estimate the crystal parameters, crystallite size, and lattice strain of the crystalline phases present in the NTO nanofibers (Section I.3, Table I.1-I.3) (George and Anandhan 2013; Senthil and Anandhan 2014; Minikayev et al. 2015). The XRD peaks of all the samples well-matched with the two distinct polymorphic phases of NTO from the ICDD database (01-076-0334: INTO and 01-084-0297: SNTO). The stable INTO belongs to the rhombohedral crystal system. The characteristic crystallographic peaks of INTO are substantiated at the Bragg's angles of 24.2, 33.2, 35.7, 49.5, 54.1 and 64.2° to the (0 1 2), (1 0 4), (1 1 0), (0 2 4), (1 1 -6) and (3 0 0) planes of reflection, respectively; whereas, the defective SNTO belongs to the cubic crystal system. The SNTO has its characteristic XRD peaks validated for planes of reflection, (3 1 1), (2 2 2), (4 0 0), (5 1 1), (4 4 0) and (6 2 2) at Bragg's angles of 35.7, 37.3, 43.4 57.4, 63.0 and 75.6°. These peaks are the major high-intensity peaks considered for the estimation of crystal variables. The intensity of the peaks increase and the peak broadening decreases with an increase in the T, due to the thermally induced crystallite growth of the particles. The lattice constants, *a* and *c* for reference powder NTO (ICDD files) and NTO nanofibers are measured and shown in Table 3.1. The lattice constants of nanofibers in both the phases are approximately 0.01–0.03 Å less than that of the bulk NTO (ICDD file). This could be due to a significant number of oxygen atoms that are incorporated into the crystal lattice with a few titanium

vacancies (Bläß et al. 2015). The observation is also consistent with the previous assumption that the Ti^{4+} complex is gradually participating in the conversion reaction. The incorporation of oxygen atoms into the lattice in turn enhances the formation of defect SNTO, which are rich in Ni^{2+} and O^{2-}. The wt% of spinel NTO (Table 3.2) was calculated using XRD direct comparison method (Section I.4) and it was observed that the SNTO wt% decreased with increase in T. This suggests the formation of stable INTO, which could also be attributed to the participation of Ti^{4+} complex in forming stable INTO with defective SNTO.
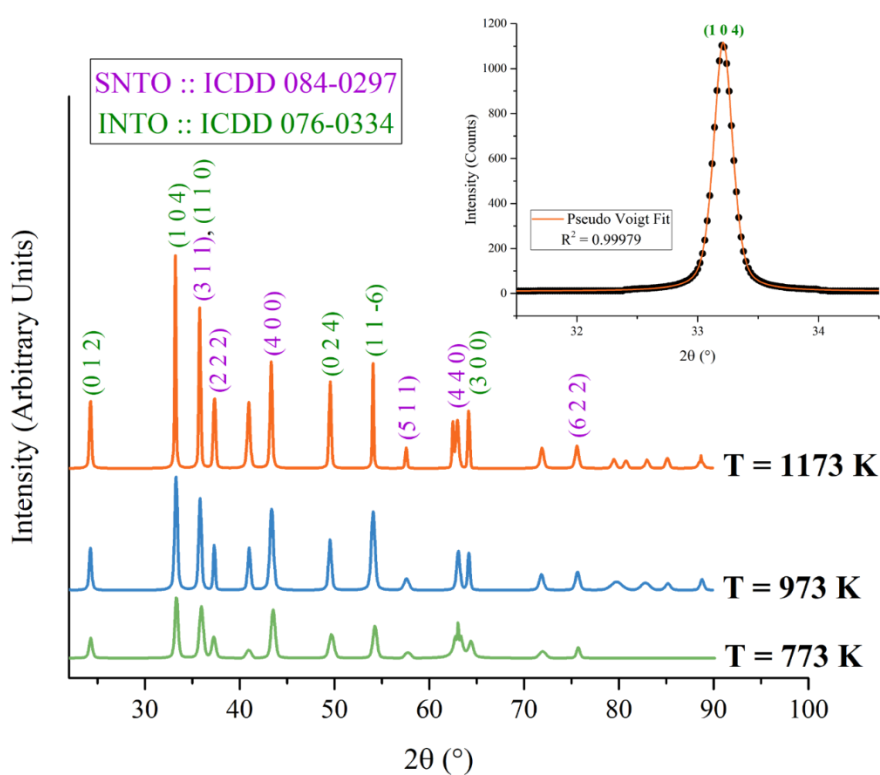
Fig. 3.6 X-ray diffractograms of NTO nanofibers developed at different T compared with ICDD files. The diffraction planes corresponding to different phases are shown in bracket. Pseudo-Voigt function was used to profile fit the peaks for analysis (inset figure).

In case of SNTO, a higher population of Ni^{2+} cations, which have exceptionally higher O_v preference than Ti^{4+} ions, push the few available Ti^{4+} cations (available after the degradation of Ti^{4+} complex) to the T_v while Ni^{2+} cations occupy the majority of the O_v positions. Due to the significant difference in the charge between Ni^{2+} and Ti^{4+}, which are both involved in the spinel structure formation, a high degree of defect

concentration could be anticipated to minimize the crystal-chemical and electrical neutrality constraints for distribution of cations in O_v and T_v. This allocation of cations might lead to distortion in the crystal structure and hence the change in the crystal parameters. However, this is thermodynamically favorable, due to the increase in entropy associated with the formation of cation vacancies, or interstitial atoms/ions, or both. Such a stable structure was indeed predicted and found at high temperatures (1573–2023 K) (Armbruster and Lager 1981; Lager et al. 1981; de Graef et al. 1985; Muan 1992). The difference here is that, the spinel phase of NTO seen in the present work was found in the temperature range of 773 to 1173 K, which is significantly lower compared to these prior works. This low-temperature stability would be promoted by a remarkable increase in entropy during the formation of such defect phase, which could either be due to the formation of another robust and stable phase with remaining Ti^{4+} (creating cation vacancies) or a decrease in activation energy for an interstitial atom/ion to occupy crystal space (voids or lattice sites).

Usually, nanoparticles have slightly higher lattice parameters compared to microcrystallites due to the high degree of disorder in the nanocrystallite. Surprisingly, in this study, it was observed that the lattice parameters, a (crystal length along crystal axis a), were approximately 0.01-0.03 Å less than the reference powder NTO (ICDD file) crystallites. The lattice parameter c (crystal length along crystal axis c), and the rhombohedrality (c/a) were also determined to be approximately 0.007-0.03 Å, and 0.005-0.008 Å respectively greater than that of the reference powder NTO (ICDD file). This kind of lattice distortion is possible only when a foreign atom/ion has been doped into the crystal lattice (Fang et al. 2005). Further, the crystal rhomohedrality in INTO, c/a, increases as the crystallite size increases with increasing T, which also translates to distortion of the volume of the unit cell. These dimensional changes are the result of a decrease in the internal stress/strain (Arlt 1990; Chattopadhyay et al. 1995; Randall et al. 1998), which are all evident from Table 3.1 and 3.2. The crystallite size and lattice strain were calculated using the Williamson-Hall plot analysis (Section I.5, Fig. I.2). The results of characterization by EDS, and XPS would reveal the type and nature of doped or interstitial element. From Table 3.2 and 3.3, it can be noted that the SNTO has a favorable increase in crystallite size and a slight increase in lattice strain (higher

degree of defects) as a function of T. The crystallite and particle size increase because of the increased diffusion of ions across the crystallite/particle boundary with rise in T. As the crystallite size attains its critical value, the surface energy decreases and diffusion of ions becomes negligible (Park and Kim 2009). This controlled diffusion pattern leads to a deficiency of Ti^{4+} ions. Therefore, the INTO, which has no sufficient Ti^{4+} ions to form, exhibits a slower increase in crystallite size, caused only by thermally driven growth. On the contrary, the Ni^{2+} rich spinel phase with few available Ti^{4+} ions, exhibits a greater increase in crystallite size as a function of T.

Table 3.1: Lattice parameters of SNTO and INTO in NTO nanofibers developed at different T.

Crystal structure	Theoretical lattice parameter (Å)	Lattice parameter at different T (K)			Activation energy for crystallite growth, E_a (kJ·mol^{-1})
		773	973	1173	
SNTO	$a = 8.3416$	8.3158	8.3282	8.3341	34.96
INTO	$a = 5.0274$	5.0028	5.0164	5.0146	5.77
	$c = 13.7830$	13.7539	13.7804	13.7899	
	$c/a = 2.7416$	2.7492	2.747	2.7499	

Table 3.2: SNTO wt% and crystallite size estimated for SNTO/INTO nanofibers developed at different T.

T (K)	SNTO (wt%)	Crystallite size, D (nm)					
		Scherrer equation			Williamson-Hall plot		
		SNTO	INTO	Overall	SNTO	INTO	Overall
773	43.95	20.13	17.99	19.06	13.01	24.20	17.04
973	41.67	21.98	25.34	23.66	38.63	24.33	32.25
1173	37.46	29.43	39.07	34.25	83.54	33.75	57.07

Table 3.3: Lattice strain obtained for SNTO/INTO nanofibers developed at different T.

T (K)	Lattice strain (ε) (%)			Average particle size measured from HRTEM (nm)
	SNTO	INTO	Overall	
773	-0.00177	0.00142	-2.6E-4	16.95 ± 4.24
973	0.00178	-5.9E-5	0.00115	24.64 ± 5.97
1173	0.0019	-3.1E-4	0.00117	91.54 ± 31.87

An Arrhenius model can be used to describe the influence of temperature on crystallite size (Senthil and Anandhan 2014):

$$D = A_0 \exp\left(\frac{E_a}{RT}\right), \tag{3.2}$$

where D is the crystallite size, A_0 is the pre-exponential factor, E_a is the activation energy for ionic diffusion across the crystallite boundary, R is the universal gas constant, and T is the absolute temperature of pyrolysis. From the plot of $\ln(D)$ as a function of $1/T$ shown in Figure 3.6, E_a for the crystallite growth of SNTO and INTO were obtained as a slope of linear fit (Table 3.1). The activation energy for the overall phase crystallite growth was 22.55 kJ·mol⁻¹, while the activation energy for pure INTO has been observed to be 8.84 kJ·mol⁻¹ (Lin et al. 2006). The activation energies for pure INTO have been reported with different Ni:Ti molar ratios. For Ni:Ti molar ratios of 1:3, 1:1, and 3:1, the E_a values were 37.17, 35.08, and 24.93 kJ·mol⁻¹, respectively. These values indicate that as there is an increase in Ni:Ti ratio, the E_a of the crystal growth decreases and is assisted by diffusion. From the present study, it is clear that the E_a of INTO (kJ·mol⁻¹) was lower than that of spinel NTO (34.96 kJ·mol⁻¹). This result suggests that a significant amount of free Ni2+ ions (above Ni:Ti = 3:1) was present during the conversion reaction. This further confirms the deficiency of Ti^{4+} ions due to the formation of Ti^{4+} complex as noted in the XRD analysis. The presence of excess Ni^{2+} ions is indeed responsible for the SNTO formation (Armbruster and Lager 1981;

Lager et al. 1981; de Graef et al. 1985; Muan 1992). Further, from Figure 3.6, it was observed that above 886 K, the slope of the plot for SNTO decreases below that of INTO. In other words, E_a decreases for spinel phase above 886 K, and more of spinel NTO crystallite grows significantly. These trends are consistent with the values of crystallite size obtained using Williamson-Hall plot. The impressions of this structural change are also manifested in the DSC peak near 882 K (Fig. 3.2).
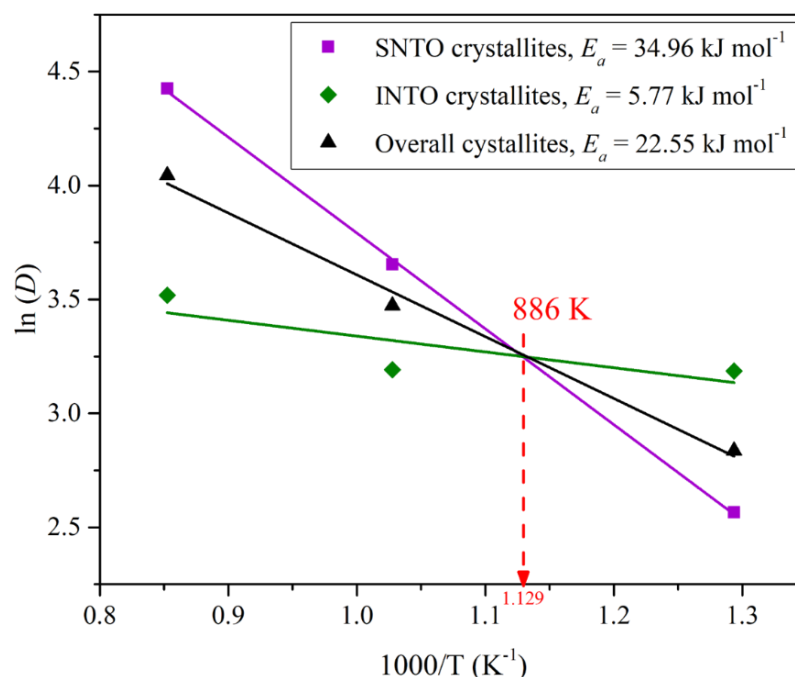
Fig. 3.7 Plot of $\ln(D)$ versus $1/T$.

3.1.2.4 EDS analysis

The FESEM-EDS enables the approximate estimation of the atomic and mass ratio of Ni, Ti and O present in the NTO fibers after pyrolysis. Table 3.4 lists the mass and atomic percentage of the elements corresponding to different temperatures. According to the molecular structure of SNTO and INTO, the theoretical mass and atomic percentage of Ni, Ti, and O were also calculated (Table 3.4). It is evident from Table 3.4, that as the T was increased the mass and atomic percentage of Ni, Ti, and O were close to their theoretical values of SNTO. This suggests that an increase in T favored the formation of the SNTO and enhanced the crystallinity of NTO grains.

Table 3.4: EDS results of SNTO/INTO nanofibers obtained at various T.

Element	Mass percentage (%)					Atomic percentage (%)				
	T (K)			Theoretically calculated		T (K)			Theoretically calculated	
	773	973	1173	SNTO	INTO	773	973	1173	SNTO	INTO
Ni	38.4	35.6	56.3	61.3	37.9	24.8	23.6	33.9	35.8	20
Ti	34.0	37.3	20.4	13.1	30.9	9.4	10.5	15.0	9.4	20
O	27.4	27.0	23.2	25.5	31.0	65.7	65.7	51.0	54.7	60

3.1.2.5 HRTEM results

The HRTEM micrographs of NTO nanofibers obtained at different T are shown in Figure 3.8a-c. The mosaic structure of the nanofiber reveals numerous grains that are held together with mesoporous cavities between them. The resulting high surface area and adsorption capabilities make NTO nanofibers a candidate material for catalysis or sensor applications. Figure 3.8d-f revealed the polycrystalline nature of NTO nanofibers formed during the pyrolysis, where contiguous crystallites had distinct planes of orientation. The lattice fringes corresponding to the planes of both SNTO (dark yellow) and INTO (light yellow) are seen with different colored marking. The SAED patterns of the three samples are shown in Figure 3.8g-i, which were indexed to the planes of diffraction that correspond to NTO. The diffraction planes corresponding to both SNTO (blue) and INTO (green) were obtained. Further, although it is well-known that HRTEM particle size analysis is approximate, it was observed from Table 3.3 that the average particle sizes of the NTO at pyrolysis temperatures 773, 973, and 1173 K were in close agreement with the crystallite size calculated using Williamson-Hall plot (Table 3.2 and 3.3). It must be noted that the nanoparticles are polycrystalline in nature and might have more than one crystallite in each grain.
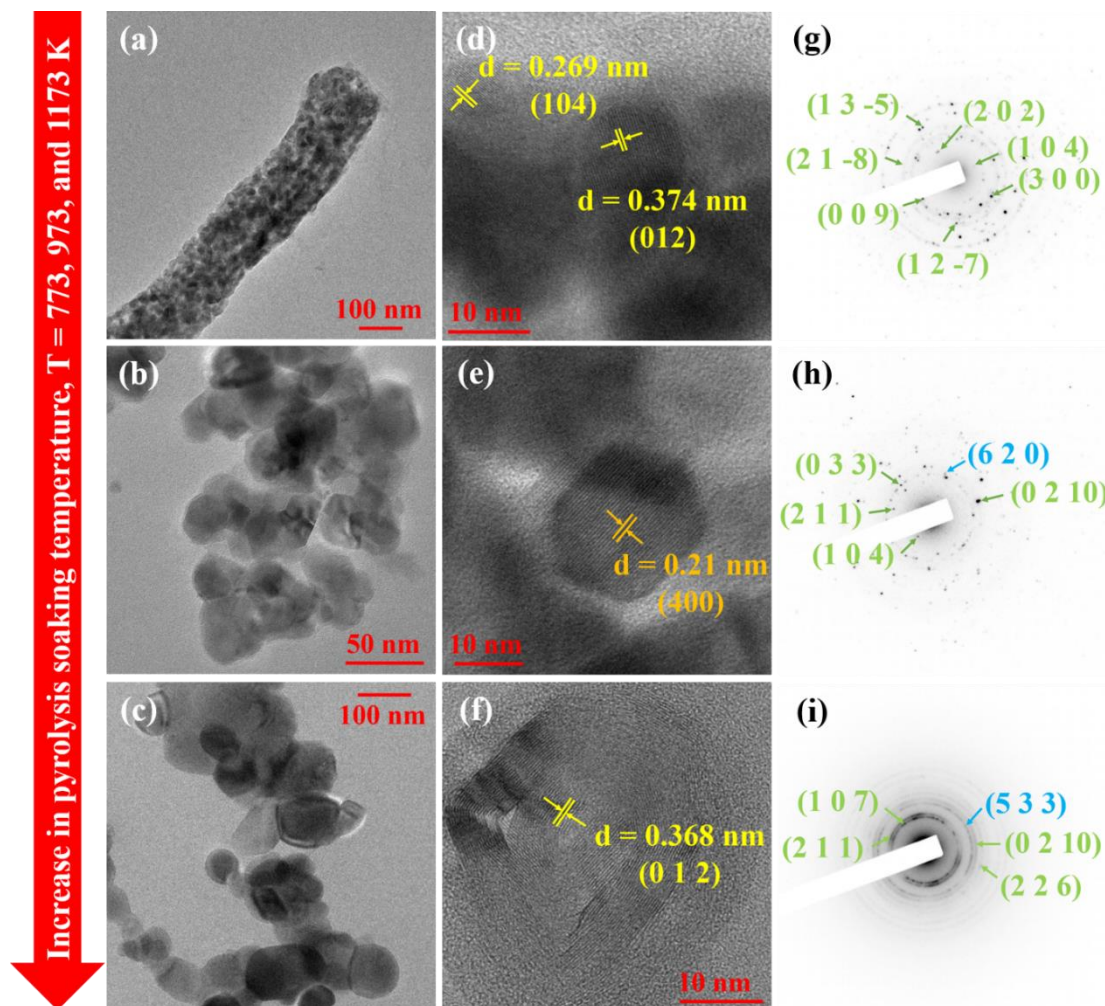
Fig. 3.8 (a-c) HRTEM micrographs, (d-f) high-resolution image showing the lattice fringes and the *d*-spacing corresponding to crystal planes, and (g-i) SAED patterns of SNTO and INTO.

3.1.2.6 SSA and porosity analysis

The SSA for NTO nanofibers developed at 773, 973, and 1173 K were measured by BET method using N_2 adsorption-desorption isotherms (Table 3.5). The SSA of nanofibers were calculated theoretically assuming that NTO fibers are smooth, and the length of each nanofiber is 100 μm (Section I.6). The measured experimental SSA values of NTO nanofibers were higher than the theoretically calculated ones. Therefore, it could be concluded that the combined electrospinning (macropores due to interconnected fibers) and sol-gel (micro and mesopores due to constrained crystal growth in nanoparticles) process has enhanced the porosity in the material improving the SSA of NTO nanofibers compared to the literature (Lin et al. 2006; Lopes et al.

2009; Ni et al. 2009; Mohammadi and Fray 2010; George and Anandhan 2013). From Table 3.5, it is clear that as the T increases the SSA decreases, which is in line with the average crystallite and particle size measurements from XRD and HRTEM. As the T increases, both the crystallite and particle size increase due to coalescence and growth, which reduces SSA. It could be seen that there is a sudden decrease in SSA of NTO nanofibers developed at T = 973 K compared with that of T = 773 K. This abrupt change is closely related to DSC peak change above 882 K, and spinel phase crystallite growth (Table 3.2), suggesting a crystal reorientation as the mesopore volume decreases from 0.11953 cc·g⁻¹ (for 773 K) to 0.00466 cc·g⁻¹ (for 973 K). Further, such changes in SSA could also be attributed to the critical doping concentration of the foreign element (Wang et al. 2005; Ganesh et al. 2012). It was observed that as the T was increased from 973 to 1173 K, there was a significant increase in crystallite size with an appreciable increase in SSA. This might be due to the pores induced during the crystallographic phase change of the NTO and increase in the fiber diameter, simultaneously.

Table 3.5: Surface area and band gap energy analysis of SNTO/INTO nanofibers obtained at different T.

T (K)	Surface area ($m^2 \cdot g^{-1}$) Theoretical	BET method	Total pore volume ($cc \cdot g^{-1}$)	Mesopore volume by BJH method ($cc \cdot g^{-1}$)	Band gap calculated using Tauc's plot, E_{bg} (eV)			
773	6.05	166.7	0.1744	0.11953	--	--	2.55	2.67
973	5.43	10.14	0.00121	0.00466	--	2.50	2.53	--
1173	4.18	22.91	0.01534	0.01578	2.40	2.49	2.57	--

3.1.2.7 XPS analysis

To understand the phenomenon of defective phase formation (SNTO) of NTO nanofibers, the binding energies of plausible foreign elements present either as a dopant or new phase were studied using XPS spectra. Figure 3.9a-i shows the high-resolution XPS spectra of the elements O, N, and C. As per literature, the peak corresponding to lattice O of NTO has been noted at 530.3 eV (Varga et al. 2012; Bellam et al. 2015).

The bathochromic shift in the peak to 529.27 eV (Fig. 3.9a and b) and 529.43 eV (Fig. 3.9c), as observed in the present study is the evidence for the O deficiency in the lattice either through doping or substitution. Further, an additional peak at 528.93 eV in Figure 3.9c confirms a different kind of lattice O due to the change of crystal structure (Kwon et al. 2014). This peak might be due to a highly defective lattice O as the bathochromic shift is significant (close to O corresponding to NiO 528.9 eV) and hence it represents lattice O of spinel NTO, where Ni^{2+} cation and O^{2-} anion are abundant and closely packed. The peaks at 531.85 eV and 531.65 eV correspond to N-substituted titanium oxide or titanium oxynitride (TiON). It has been reported earlier that as TiON undergoes reduction, there is a corresponding bathochromic shift in the XPS spectra from 531.9 eV ($TiO_{0.74}N_{0.09}$) to 531.6 eV ($TiO_{0.08}N_{0.63}$) (Kuznetsov et al. 1992). This observation is in line with the present study (Fig. 3.9a-c) suggesting that as the T increases, oxidation of TiON becomes challenging and thus Ti^{4+} cation deficient SNTO was formed. In other words, the reduction of TiON (increase in N doping concentration and decrease in O due to substitution) leads to stable titanium nitride (TiN), which in turn gives rise to Ni^{2+} cation rich SNTO structure. This explanation is in good agreement with the spinel phase growth of XRD and EDS analysis. A small shoulder at 534.37 eV (Fig. 3.9a and b) corresponds to the O of nickel carbonyl [Ni(CO)$_4$] (Barber et al. 1972), which could be formed in the process of nickel acetate decomposition, before it forms NTO.

Figure 3.9d-f shows the N *1s* high-resolution XPS spectra of NTO nanofibers. The peaks at 396.63, 396.52, 398.29, 398.30, and 398.15 eV are characteristic of substitutional nitrogen (N-doped TiO$_2$), TiON and TiN (Kuznetsov et al. 1992; Asahi et al. 2001; Diwald et al. 2004; Vesel et al. 2006; Chen and Burda 2008). The bathochromic shift in Figure 3.9f suggests a higher extent of reduction of TiON and TiN at higher T. In the carbon C *1s* spectra (Fig. 3.9g-i), the peak around 284 eV corresponds to the graphitic or free carbon (Filik et al. 2003; Pan et al. 2007). Whereas, the peaks at 285.5, 287.6, and 291.97 eV are assigned to carbon atoms containing different oxygen moieties (Okpalugo et al. 2005; Datsyuk et al. 2008). These carbon species might be from the residue of SAN pyrolyzed at high temperature. Further, pure

residual carbon helps as a medium for charge or ionic transport (George and Anandhan 2015b).
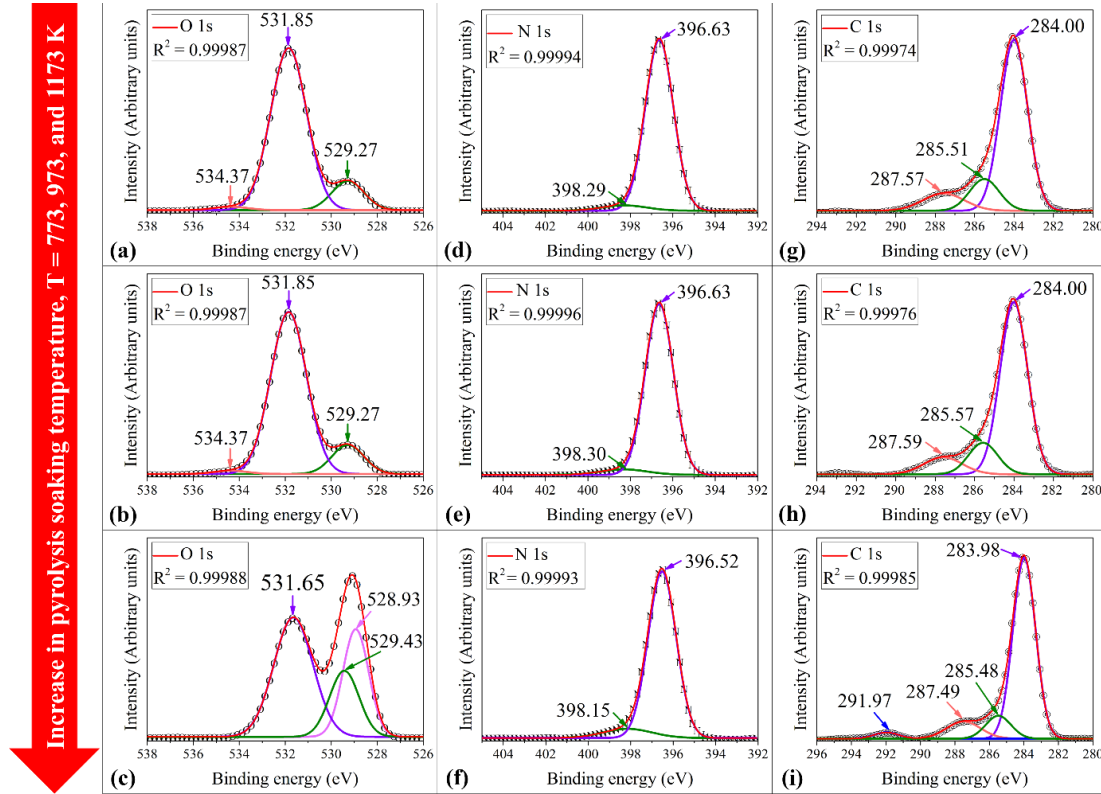
Fig. 3.9 High-resolution XPS spectra of O *1s*, N *1s*, and C *1s* for NTO nanofibers developed at three different T: (a, d, and g) 773 K, (b, e, and h) 973 K, and (c, f, and i) 1173 K.

3.1.3 Optical spectroscopy

3.1.3.1 UV-Vis-NIR spectroscopy

Figure 3.10a shows the UV–Vis–NIR Spectra for the NTO nanofibers developed at three different temperatures, T. The broad absorption edge corresponding to $O^{2-} \rightarrow Ti^{4+}$ (optical band charge transition) is found to be narrowed. From prior literature, this is possible by an increase in substitutional doping of either N or Ni into TiO_2 particles (Diwald et al. 2004; Hyun Kim et al. 2006; Chen and Burda 2008; Ganesh et al. 2012). In this study, on one hand, Ni-doped TiO_2 could be considered equivalent to a SNTO, where the interaction between the O^{2-} and Ti^{4+} is suppressed due to Ti^{4+} deficiency, as the T increased. On the other hand, the presence of TiN or TiON is also possible as seen in XPS results, which would hinder the interaction between the O^{2-} and Ti^{4+}. The latter

could therefore have the same impression as Ni-doped TiO_2. For fibers pyrolyzed at 973 K and 1173 K, two absorption bands around 445 nm and 512 nm are observed in the visible range, due to the crystal field splitting of NTO. The field splitting is such that the $3d^8$ band associated with Ni^{2+} ions splits up into two sub-bands at about 490 nm and 560 nm, which corresponds to $Ni^{2+}_{(Ov)} \rightarrow Ti^{4+}$ CT bands. The increase in intensities of the peaks corresponding to these CT bands in the visible light region with increase in T suggests the high possibility of CT. The crystallite growth of NTO with higher T having $Ni^{2+}_{(Ov)}$ rich atmosphere especially favors such interactions (Qu et al. 2012; Wang et al. 2013a). The least absorption was observed in the range of 550-600 nm of the spectrum, which corresponds to a greenish-yellow region of visible light, indicating the color of the synthesized NTO nanofibers. Further, two broad peaks ranging from 600 to 1000 nm and 1000-1400 nm were observed, whose intensities increased as a function of T. This could be due to d-d transitions from the Ni^{2+} cations in the O_v environment corresponding to $^3A_{2g}(F) \rightarrow {}^3T_{1g}(F)$ and $^3A_{2g}(F) \rightarrow {}^3T_{2g}(F)$, respectively (Biswas et al. 2008).

Assuming the NTO nanofibers as crystalline semiconducting oxides, the intercept of the linear part in Tauc plot of $(\alpha h\upsilon)^2$ versus $h\upsilon$ (Fig. 3.9b) was calculated to estimate the band gap energy (E_{bg}) values of the NTO nanofibers developed at different T. Here, α is the absorption coefficient, h is *Planck's* constant and υ is the frequency of the photon (Senthil and Anandhan 2014). The multiple band gap energies in the individual sample could be attributed to the different crystal structure as well as phases of materials present in the NTO nanofibers. The obtained E_{bg} values are shown in Table 3.5. The values are higher than that of the bulk NTO (E_{bg} = 2.18 eV), due to quantum confinement effect (Qu et al. 2012; Vijayalakshmi and Rajendran 2012). The E_{bg} values ranging from 2.53 to 3.05 eV are in good agreement with the literature values for Ni-doped TiO_2 and INTO (Hyun Kim et al. 2006; Chen and Burda 2008; Ganesh et al. 2012). However, as reported earlier (Diwald et al. 2004; Bellam et al. 2015), N-doping in TiO_2 and NTO would introduce a band gap ranging from 2.4 to 2.5 eV, which is seen at pyrolysis temperatures of 973 K and 1173 K in this study. The absence of E_{bg} above 3 eV for NTO nanofibers developed at 773 K as well as the role

of SNTO in the formation of multiple band gap energies needs further investigation. Meanwhile, it is evident from the E_{bg} values that such small and multiple band gap energies in a material would enhance its photocatalytic property. Various research groups have reported that INTO, which has an enhanced visible light response photocatalytic property has been used for the elimination of organic contaminants and water splitting for oxygen evolution (Shu et al. 2008; Tahir et al. 2009; Yuan et al. 2012).
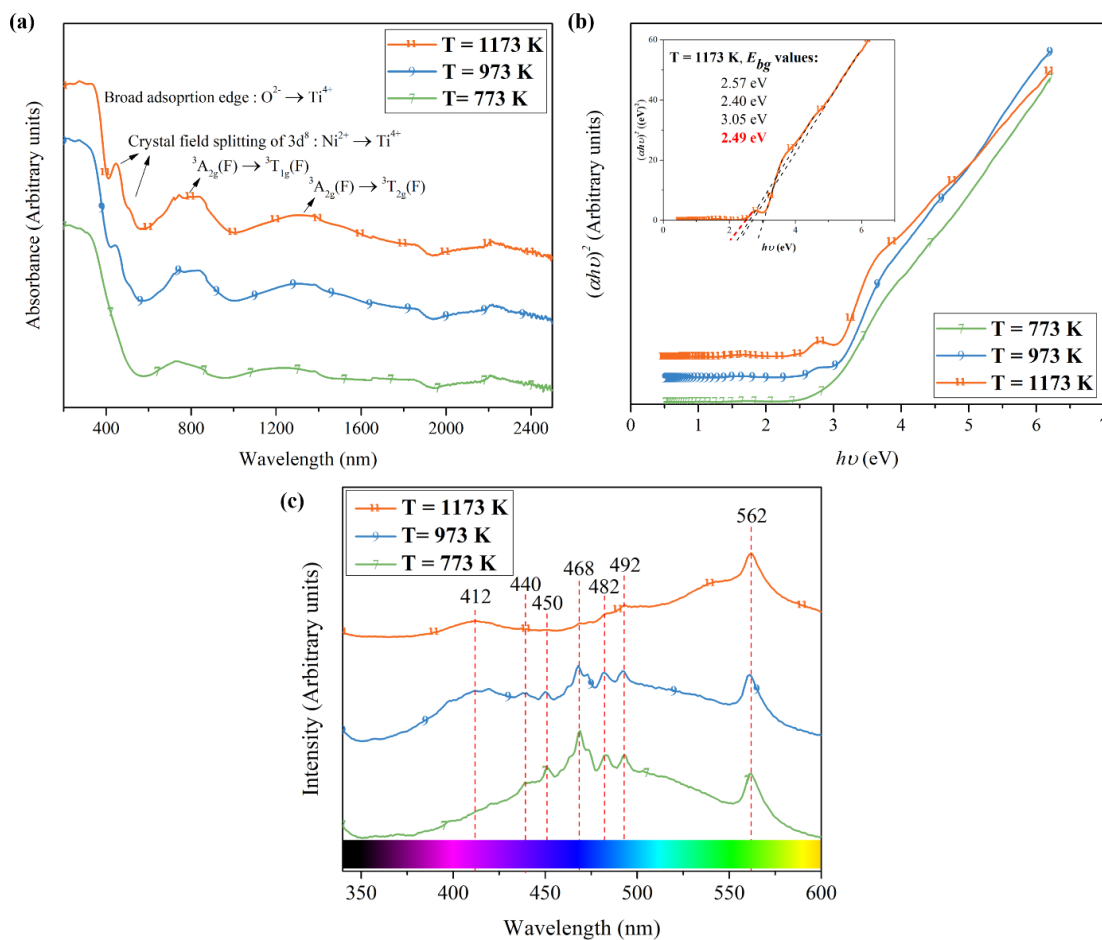
Fig. 3.10 (a) UV–Vis–NIR spectra, (b) Tauc plots (inset: intercept drawn to linear portions to calculate E_{bg}), and (c) PL spectra of NTO nanofibers developed at different T.

3.1.3.2 PL spectroscopy

Figure 3.10c shows the PL spectra of NTO nanofibers developed at different T. The competition among electron-hole separations, electron-phonon scattering, and electron-

hole recombination are the result of PL spectra, which are attributed to self-trapped excitons, oxygen vacancies and surface states (defects). The peaks around 480 nm found here are associated with the intrinsic CT from Ti^{4+} ion to oxygen ion in complex octahedra $[TiO_6]^{8-}$ (Tripathi et al. 2015). Such intrinsic defects act as luminescent centers that can form defect levels located highly in the gap, trapping electrons from the valence band to contribute to the luminescence in the visible region (blue) as seen in this study. Such visible emissions could also be caused by the Ti vacancies introduced by Ni doping. The peaks around 460 nm found here are due to the characteristics of the traps present in the nanoparticles (Vijayalakshmi and Rajendran 2013; Tripathi et al. 2015). The PL emission around 440 nm could be attributed to electron transition mediated by defects levels in the band gap, such as oxygen vacancies. The emission peaks were in good agreement with the INTO observed from the literature (Vijayalakshmi and Rajendran 2013). The PL emission peak around 562 nm corresponds to the color of the material, which showed an hypsochromic shift to greenish-yellow region from the yellow region (580 nm) (Wang et al. 2013a). This could be due to the presence of Ni^{2+} rich environment in SNTO nanofibers (Wang et al. 2003). It was observed that the intensities of the PL emission peaks decrease as a function of the T, which indicates the efficient suppression of electron-hole recombination rate upon increase in spinel NTO crystallite size and coalescence of particles (Qu et al. 2013; Zeng et al. 2016).

3.1.4   Probable mechanism of SNTO formation

Figure 3.11 shows a schematic representation of the mechanism of SNTO formation. The Ti^{4+} complex (see Fig. 2.2), which was supposed to yield TiO_2 on pyrolysis (Parra et al. 2008), interacts with nitrile groups of SAN as evidenced by FTIR (George et al. 2015). Above 693 K, nitriles are released from SAN degradation and this free nitrile continues to interact with the carboxylate of acetate coordinated to Ti^{4+} complex. Currently, there is substantial literature that confirms the formation of stable TiON (O and N are of variable composition) especially in oxygen bearing precursor systems (Li et al. 2001; Kaskel et al. 2003; Kawano et al. 2003). Further, in the presence of carbon or carbon monoxide, sub-products of SAN undergo thermal cracking, and the conversion rate of oxide to TiN is enhanced significantly (Drygaś et al. 2006). This

mechanism is known as *carbothermal reduction*. Once the stable TiN is formed, the system is left with only a few Ti^{4+} cations, which take part in NTO formation. Now, the system is left out with a non-stoichiometric ratio of Ni:Ti to form INTO. Hence, the Ni^{2+} cation rich atmosphere in the system forces the Ti^{4+} cations to occupy T_v while they preferentially occupy O_v forming a defective non-stoichiometric SNTO.
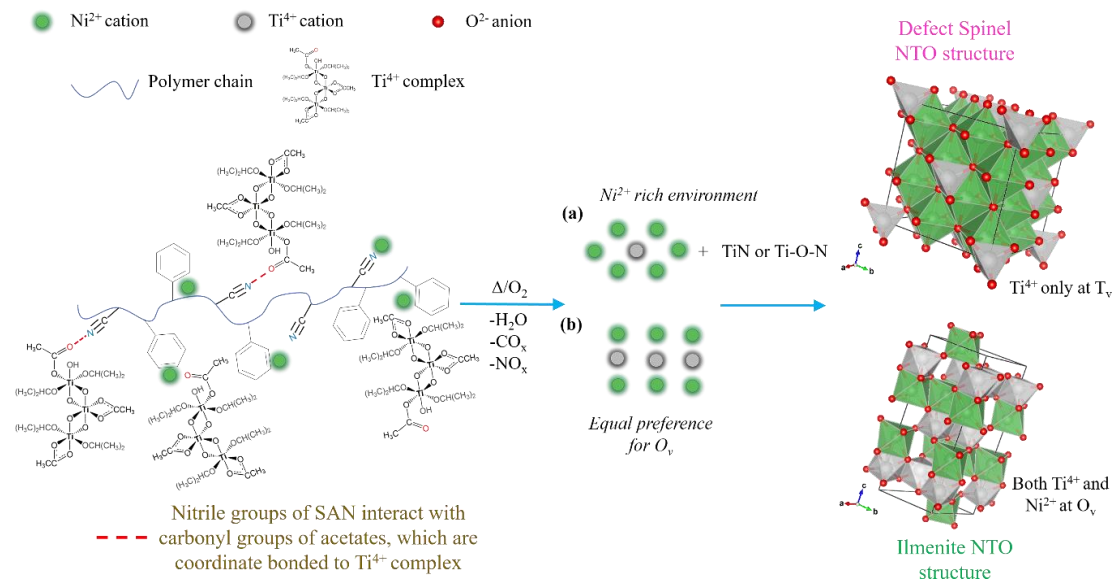
Fig. 3.11 Schematic depicting the mechanism of SNTO formation.

As the T and *t* increases, conditions for *carbothermal reduction* are more conducive, which in turn favors the formation of SNTO with TiN getting oxidized. Thus, the importance of SAN, polymeric binder is most relevant in this fabrication of NTO nanofibers as none of the other synthesis techniques including sol-gel assisted electrospinning with different polymeric binder could yield SNTO (Armbruster and Lager 1981; Muan 1992; Lin et al. 2006; Gambhire et al. 2008; Sadjadi et al. 2008; Lopes et al. 2009; Ni et al. 2009; Mohammadi and Fray 2010; Varga et al. 2012; Vijayalakshmi and Rajendran 2012; Yuvaraj et al. 2013; George and Anandhan 2014a; Nguyen-Phan et al. 2014). Further, at the end of pyrolysis most of the TiN and TiON could be consumed to take part in crystallite growth of NTO and this could have led to minute and disordered phases of TiN and TiON. Hence, this could be a reason why TiN and TiON were not detected in any characterization technique other than XPS. Their non-crystallinity may be due to the randomness (disorder) in the copolymer, as nitrile (C≡N) groups are randomly distributed in SAN.

3.2 SUMMARY AND CONCLUSIONS

In summary, NTO nanofibers were successfully synthesized by sol-gel assisted electrospinning method, using SAN as the polymeric binder. The nanofibers were embedded with defective non-stoichiometric SNTO. These SNTO/INTO composite nanofibers were formed due to *carbothermal reduction* occurring between Ti^{4+} complex and nitrile group of the SAN. The increase in crystallite size of defective spinel phase was thermally driven due to the simultaneous formation of TiN or TiON during the process. The molecular level mixing and interaction of the precursor materials with SAN seems to be the significant factor allowing SNTO formation at a relatively low temperature. It also avoids severe coalescence giving rise to enhanced porosity and high surface area of the material, which is not achieved when these materials are synthesized by conventional methods. The results presented here suggest a potentially new method for stabilizing the defective SNTO, which would be otherwise metastable at room temperature, and may therefore be difficult to prepare or access.

The UV-Vis-NIR spectra showed different absorption peaks in the presence of Ni^{2+} abundant environment. Further, the PL spectra showed a hypsochromic shift with the color of the material, which has a peak at the greenish region attributed to the presence of excess Ni^{2+} phase (SNTO). Fluorescence peaks were also observed in the blue region due to the defects formed at low T. The intensity of the PL spectra decreased as the defects decreased with an increase in the T. The nature of the different absorption peaks makes the material a promising candidate for solar energy and light source peaking as its effective wavelength is below 560 nm. The enhanced porosity and photo-generated electron-hole pairs due to the presence of defects boosts the photo-catalytic property of the NTO, which enables its use in photo-oxidation of water. The material has to be investigated further for electrical, magnetic and shape memory properties to understand the implications of crystal defects and polymorphism, as all the physical and chemical properties of materials depend on the crystal structure of the phases present in it.

CHAPTER 4

CHAPTER 4

POLYMORPH NICKEL TITANATE NANOFIBERS AS BIFUNCTIONAL ELECTROCATALYST TOWARDS HYDROGEN AND OXYGEN EVOLUTION REACTIONS
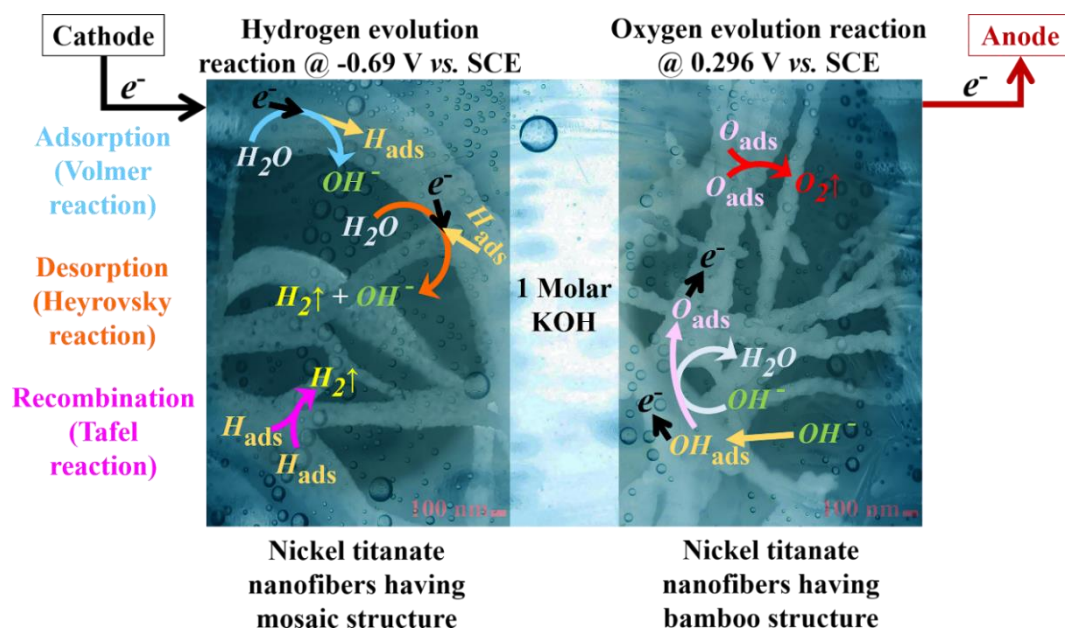
Scheme 4.1 Probable mechanism of water-splitting in presence of NTO nanofibers.

The SNTO/INTO composite nanofibers synthesized using sol-gel assisted electrospinning followed by pyrolysis at T (viz., 773, 973, and 1173 K) in previous chapter were used for determining the electrocatalytic activity of NTO nanofibers for alkaline water-splitting in this chapter. Producing pure H_2 and O_2 to sustain the renewable energy sources with minimal environmental damage is a key objective of photo/electrochemical water-splitting research. Metallic Ni-based electrocatalysts are expensive and eco-hazardous. This has rendered the replacement or reduction of Ni content in Ni-based electrocatalysts a decisive criterion in the development of bifunctional electrocatalytic materials. The highly defective SNTO manifests properties similar to the metallic Ni and favors H_2 evolution through HER by adsorbing more H^+ ions on active sites. In contrast, the INTO favors O_2 discharge. These results are explained based on the morphology of the NTO nanofibers. The mosaic structure, which

has higher porosity and greater SNTO content shows excellent HER performance. On the contrary, the large bamboo structured NTO nanofibers, which has lesser porosity and SNTO content, cage the bigger (OH)ads ions at its catalytic sites to facilitate OER performance.

4.1   RESULTS AND DISCUSSION

4.1.1   FESEM-EDS and HRTEM analysis

The FESEM-EDS images (Section I.7) unveils the morphology, structure and selected area stoichiometry of the NTO nanofibers. The mosaic structure possesses higher surface area and porosity at lower T (773 K and 973 K), which promotes the diffusion of electrolytes; whereas the bamboo structure of NTO nanofibers obtained at 1173 K enable fast CT during electrocatalysis. The molar ratio of Ni/Ti (~ 2.2) from EDS spectra suggests the non-stoichiometric phase present in the system. The mechanism for formation of this defective phase (*i.e.*, SNTO) has been discussed in Chapter 3 (Section 3.1.4). It must be noted that apart from point defects, dislocations in the crystallite act as active sites for electrochemical reactions. The D of both INTO and STNO present in the nanofibers were calculated by the XRD patterns *via* Williamson-Hall plot as in Chapter 3 (Section 3.1.2.3).

Table 4.1: Crystallite size and dislocation density estimated for NTO nanofibers developed at different T.

T (K)	Crystallite size obtained from Williamson-Hall plot, D (nm)		Dislocation density, ρ_D ($\times 10^{11}$ cm^{-2})	
	INTO	SNTO	INTO	SNTO
773	24.20	13.01	1.71	5.91
973	24.33	38.63	1.69	0.67
1173	33.75	83.54	0.88	0.14

The crystallite size thus estimated was used to calculate the ρ_D in NTO nanofibers by following equation (Aytimur et al. 2013):

$$\rho_D = \frac{\tau}{D^2}, \tag{4.1}$$

where τ is a factor ($\tau = 1$ for minimum dislocation density). The dislocation densities for INTO and SNTO of nanofibers obtained for different T are tabulated in Table 4.1. The ρ_D decreases with increase in T. This influences the electrochemical reactions, because the CT resistance decreases with increase in ρ_D (Rafiee et al. 2013). This suggests that samples obtained at 773 K are more active for electrolysis.
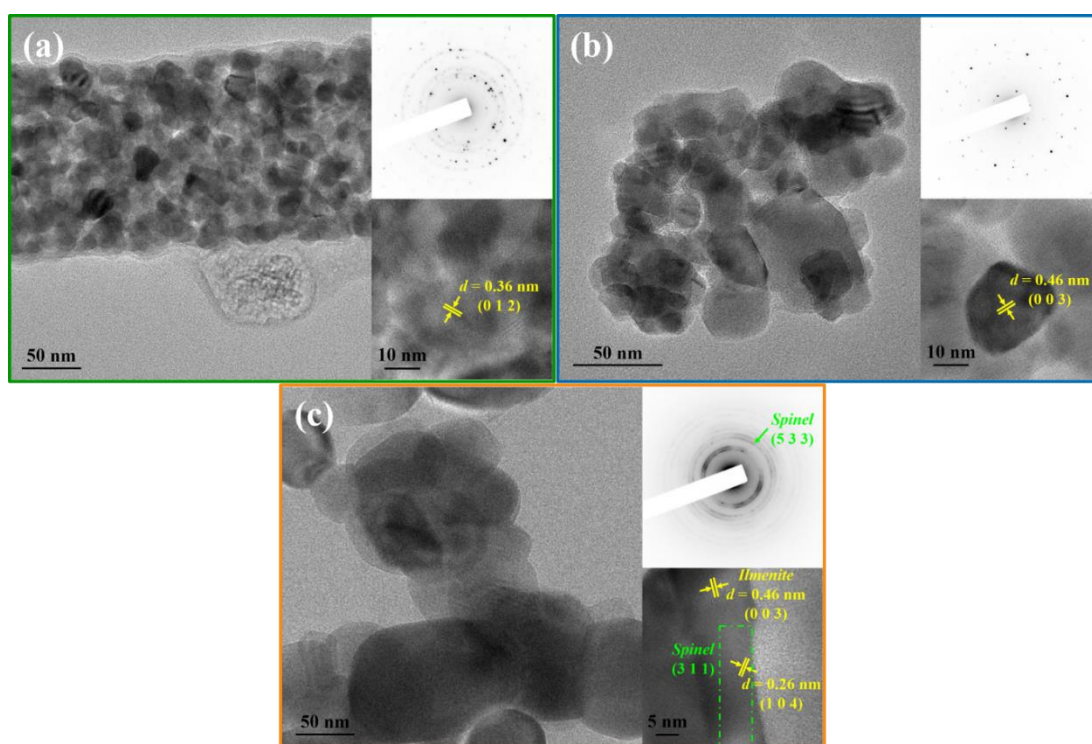
Fig. 4.1 HRTEM micrographs of NTO nanofibers obtained at different T: (a) 773 K, (b) 973 K, and (c) 1173 K. Inset figures are the lattice fringes and indexed SAED patterns of the polycrystalline NTO nanofibers in corresponding samples.

HRTEM micrographs of NTO nanofibers obtained at different T are shown in Figure 4.1. The NTO grains obtained from pyrolysis at 773 K (Figure 4.1a) are loosely packed in contrast to the dense grains obtained at higher T (973 K and 1173 K, Figure 4.1b, c). Figure 4.1 also reveals the polycrystalline nature of the NTO grains as seen from SAED patterns with lattice fringes indexed correspondingly to INTO and SNTO.

At close inspection it can be observed that the NTO grains transform their shapes from irregular ellipsoidal to regular polygon with increase in pyrolysis temperature.

4.1.2 Raman spectroscopy

The Raman spectra of NTO nanofibers obtained at different T are shown in Figure 4.2. For INTO structure with C_{3i}^2 symmetry and $R\overline{3}$ space group, all the ten Raman active modes ($5A_g + 5E_g$) are observed in the range of 150-800 cm^{-1} (Bellam et al. 2015; Ruiz-Preciado et al. 2015). These peaks are characteristic peaks of INTO and the same are assigned for NTO nanofibers in present study, especially NTO nanofibers obtained at higher pyrolysis temperature. The well-defined peaks at higher T are due to the structural order, as the intensity of the peak is function of scattering efficiency of the material. Hence, the ambiguous peaks were noticed for NTO nanofibers obtained at 773 K having high structural disorder. However, the peak around 773 cm^{-1} remain unassigned even with both experimental (Ruiz-Preciado et al. 2015) and theoretical (nanocrystallite) (Preciado et al. 2015) studies until the present study. Here, from the previous study on SNTO (Chapter 4) and by comparing the Raman spectra of spinel structures (D'Ippolito et al. 2015), thus suggest that this peak belongs to Raman mode of A_{1g} for SNTO. Furthermore, this also corroborates the presence and existence of SNTO phase in nanofibers.
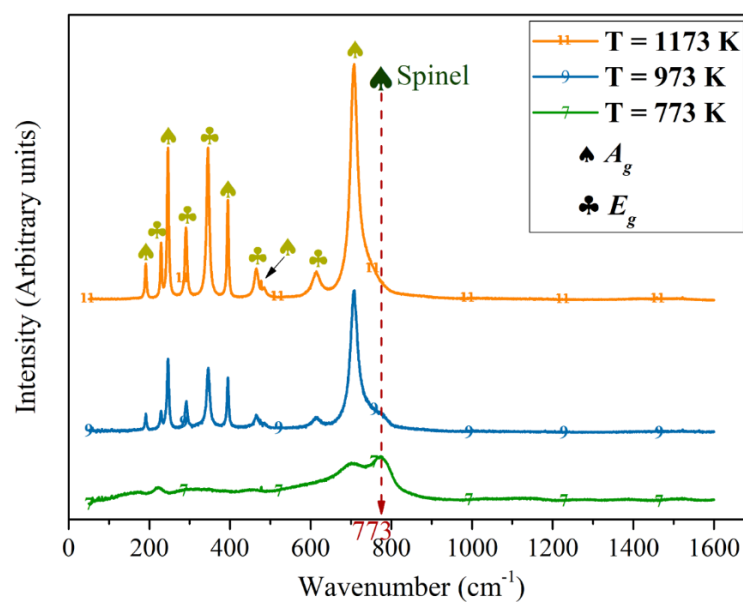
Fig. 4.2 Raman spectra NTO nanofibers obtained at different T.

4.1.3 CIE plot from PL spectroscopy

The CIE 1931 plot obtained for the PL spectra (Chapter 3, Section 3.1.3.2) in Figure 4.3. The CIE plot shows a noteworthy shift of NTO nanofibers with increase in T, which demonstrate amalgamation of additional oxygen to the system.
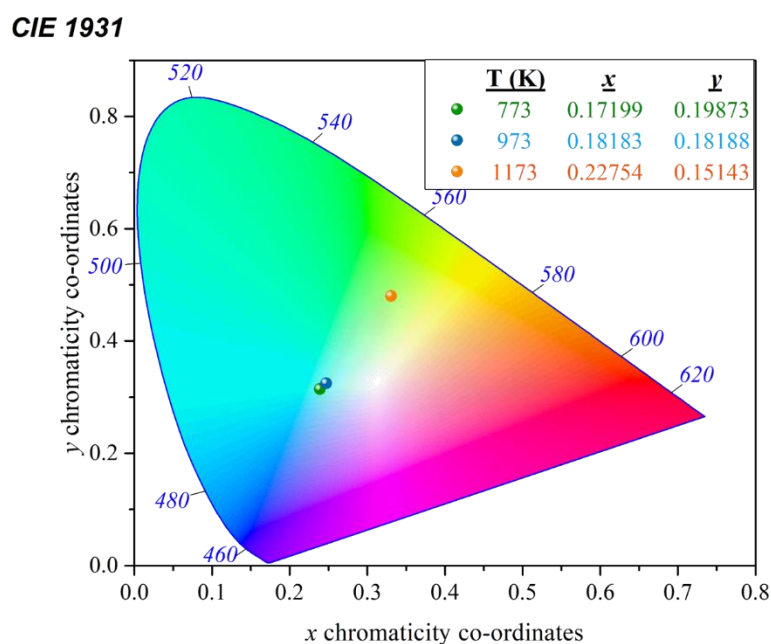
Fig. 4.3 CIE 1931 chromaticity diagram from PL spectra for NTO nanofibers developed at different T.

4.1.4 DFT analysis

The structural and physical properties of various ilmenite type titanates are studied theoretically using DFT analysis (Pontes Ribeiro et al. 2016; Yoshimatsu et al. 2017). To have the additional insight of the NTO phases (INTO and SNTO) over the competing band gaps for electrocatalyst or photocatalyst phenomena, the CB and VB were estimated by first principles DFT calculations. Figure 4.4a and b shows the DOS of INTO and SNTO, respectively. Apart from multiple band gaps mentioned in previous study ranging from 2.4-2.7 eV (Chapter 3, Section 3.1.3.1), two new band gaps were observed from the electronic structure calculations, *i.e.*, 1.07 eV and 1.56 eV for INTO. And, 0.3 eV and 0.81 eV intermediate narrow band gaps were obtained for SNTO. The former 1.56 eV of INTO can be attributed to the absorbance peak for the $^{3}A_{2g}(F) \rightarrow {}^{3}T_{2g}(F)$ due to Ni^{2+} *d-d* transitions (as seen from Figure 3.10a). The latter,

1.07 eV of INTO and 0.81 eV of SNTO to $^3A_{2g}(F) \rightarrow {}^3T_{1g}(F)$ and its shoulder peak, which confirms the theoretical band gap is close to the value obtained from that of the experiments. The pseudo band gaps around 0.3 eV or sometimes less than ~1.5 eV are due to hybridization of strong covalent character Ni-O bonds, which is believed to hinder the $Ni^{2+} \rightarrow Ti^{4+}$ CT (M. Banerjee et al. 2015; Rawool et al. 2018). These transitions are in visible and infrared light region, and hence suggest the photocatalytic behavior of the nanofibers. For both INTO and SNTO phases, the VB is primarily fabricated of Ni *3d*, and CB of Ti *3d*, whereas there are additional sub-bands for both the phases above VB minima and below CB maxima. This result of INTO is in contrary to the DOS obtained in literature, where VB is predominant by O *2p* orbitals (Li et al. 2016a), whereas comparable to the other literature (Xin et al. 2014; M. Banerjee et al. 2015; Preciado et al. 2015).
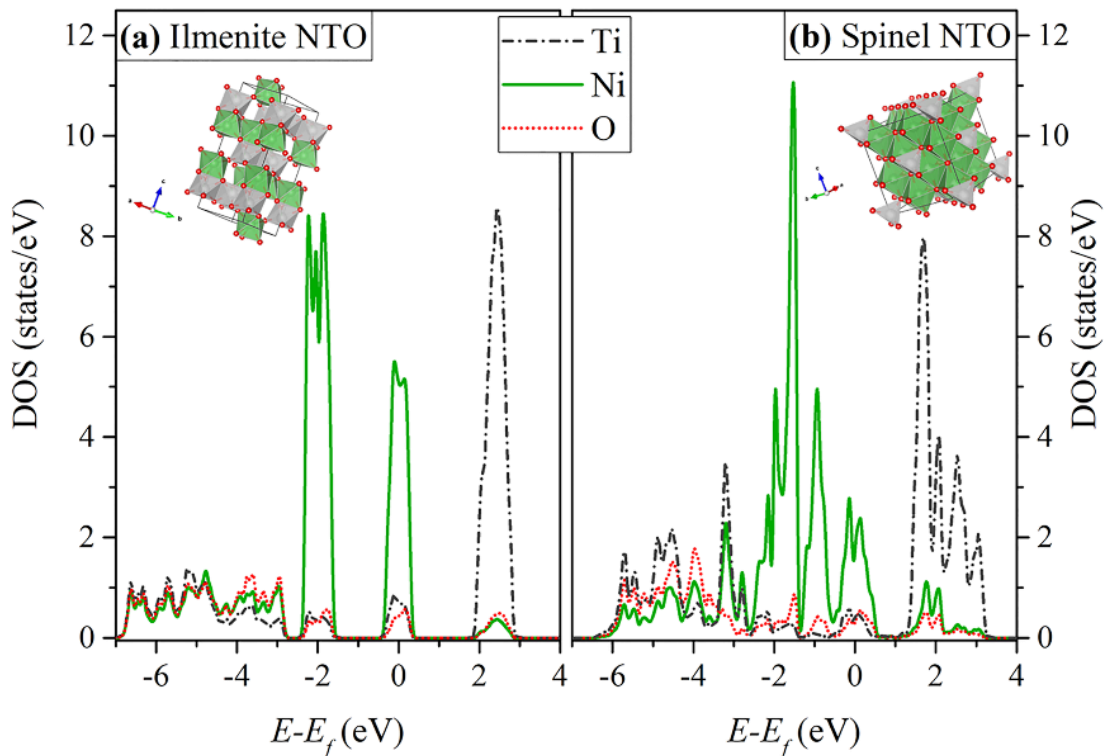
Fig. 4.4 DOS calculated by DFT analysis for (a) INTO and (b) SNTO. Inset figures are the corresponding unit cells of INTO and SNTO phases.

The band structure of INTO and SNTO in Figure I.6a and b, conveys that the SNTO is semi-metallic nature with closet to Fermi level being completely occupied.

However, unoccupied states are seen in VB or high CB. This can be attributed to highly defective phase of SNTO having oxygen vacancies or possibility of existence of intermetallic connection (Ni-O-Ti-O-Ni) as previously reported (Pontes Ribeiro et al. 2016). However, such states have been confirmed with NCO and NiO/TiO$_2$ DFT study, where favors in electrochemical redox reaction as communicative media for charge-transfer (CT) and water absorption (Zhao et al. 2016; Naik et al. 2017). If such semi-metallic/metallic states exists with the INTO, it has also been proven to increase the efficiency of catalyst for electrochemical water-splitting (INTO/Ni), experimentally (Dong et al. 2017).
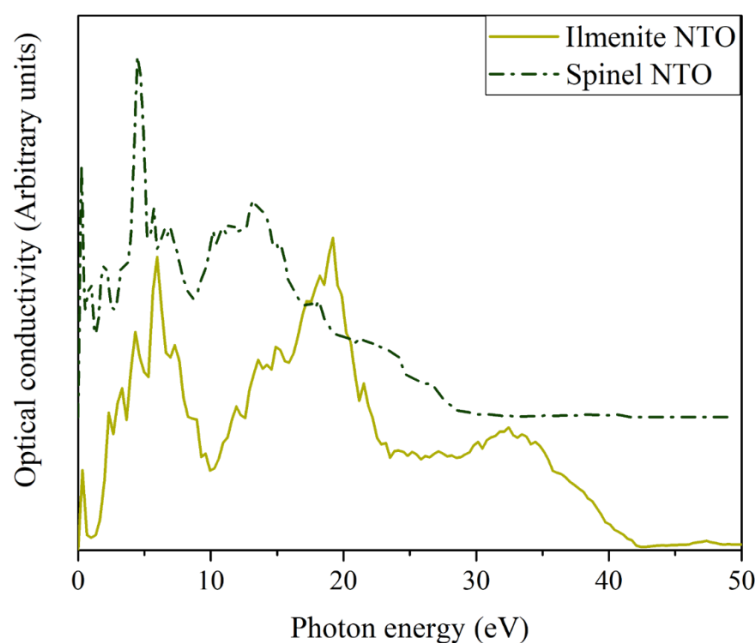
Fig. 4.5 Comparison of optical conductivity of INTO and SNTO acquired by DFT analysis.

The optical conductivity of the INTO and SNTO were estimated from DFT analysis are shown in Figure 4.4 ranging 0 to 50 eV. The peaks below 50 eV belong to the UV-Vis light assisted inter-band transitions in the material. The hyperchromic effect for both INTO and SNTO is observed in the range of 4-7 eV due to the CT interactions in respective material. The optical conductivity reaches maxima at 4.46 eV and 5.96 eV for SNTO and ITNO, respectively. This suggests they are promising photocatalyst and electrocatalyst. A second maxima peak is observed for INTO around 19.21 eV, which decreases and shifts to lower energy (13.15 eV) in case of SNTO. This indicates that

INTO is more optically conductive to the incident photons of higher energies. The bathochromic shift in SNTO can be attributed to the smaller band gaps or rich Ni ion concentration (Amin et al. 2011, 2012). The overall picture of variation in the peaks of optical conductivity concludes the change in the band gaps of INTO and SNTO, expressing different behavior for incident photons.

4.1.5   XPS depth profiling

XPS studies were performed to confirm the elemental composition and valence states of elements present in NTO nanofibers developed at different T (Section I.9). The XPS depth profiling was carried out to understand the anatomy of NTO nanofibers obtained at 773 K (Figure 4.6), which seem to possess high structural disorder compared to the other two samples. Figure I.7a shows wide scan XPS spectra of NTO nanofibers synthesized at different T, and Figure 4.6a shows the XPS survey spectra of NTO nanofibers obtained at surface and two different depths of NTO nanofibers developed at T = 773 K. Both the survey spectra Figure I.7a and 4.6a confirms the presence of C, O, Ti, and Ni elements (Yang et al. 2014a; Dong et al. 2017) distributed non-homogeneously over the NTO nanofibers (ratio of intensity of respective elements is not equal to one) (Subramanya et al. 2015). The deconvoluted high-resolution spectra of Ni $2p$, Ti $2p$, and O $1s$ (Figure I.7b-d) confirms the formation of INTO, which is in good accordance with literature (Qu et al. 2012; Yang et al. 2014a; Dong et al. 2017). The presence of defective O^{2-} (Figure I.7b) even in XPS depth profiling (Figure 4.6b) suggests that these are not oxygen moieties or absorbed surface oxygen compounds, whereas distributed over bulk sample. This observation indeed helps in predicting the presence of SNTO in the NTO nanofibers.

The high-resolution Ni $2p$ spectra observed in all samples as shown in Figure I.7c and 4.6c, suggests the presence of typical O_v Ni^{2+} ions (characteristic $2p$ spin orbital splitting separated by ~17.3 eV) in both INTO and SNTO (Yang et al. 2014a). It has to be noted that the Ni^{2+} ions in both crystal structures remain in O_v (Chapter 3). The hypsochromic shift in Ni $2p$ spectra of Ni^{2+} ions present in SNTO is attributed to the subtle change in ion charge by oxidation, *i.e.*, $Ni^{2+\delta}$, which promote stability of non-stoichiometry SNTO having oxygen deficiency (Braski et al. 1994). Furthermore, Figure 4.6c shows the existence of Ni^0 ($2p_{3/2}$ ca. 852.3 eV and $2p_{1/2}$ ca. 869.4 eV) (Dong

et al. 2017) after Ar^+ ion sputtering during XPS depth profiling. This is ascribed to metallic Ni, which are formed due to the reduction of high valence Ni ions during Ar^+ ion bombardment (Leinen D. et al. 2004).
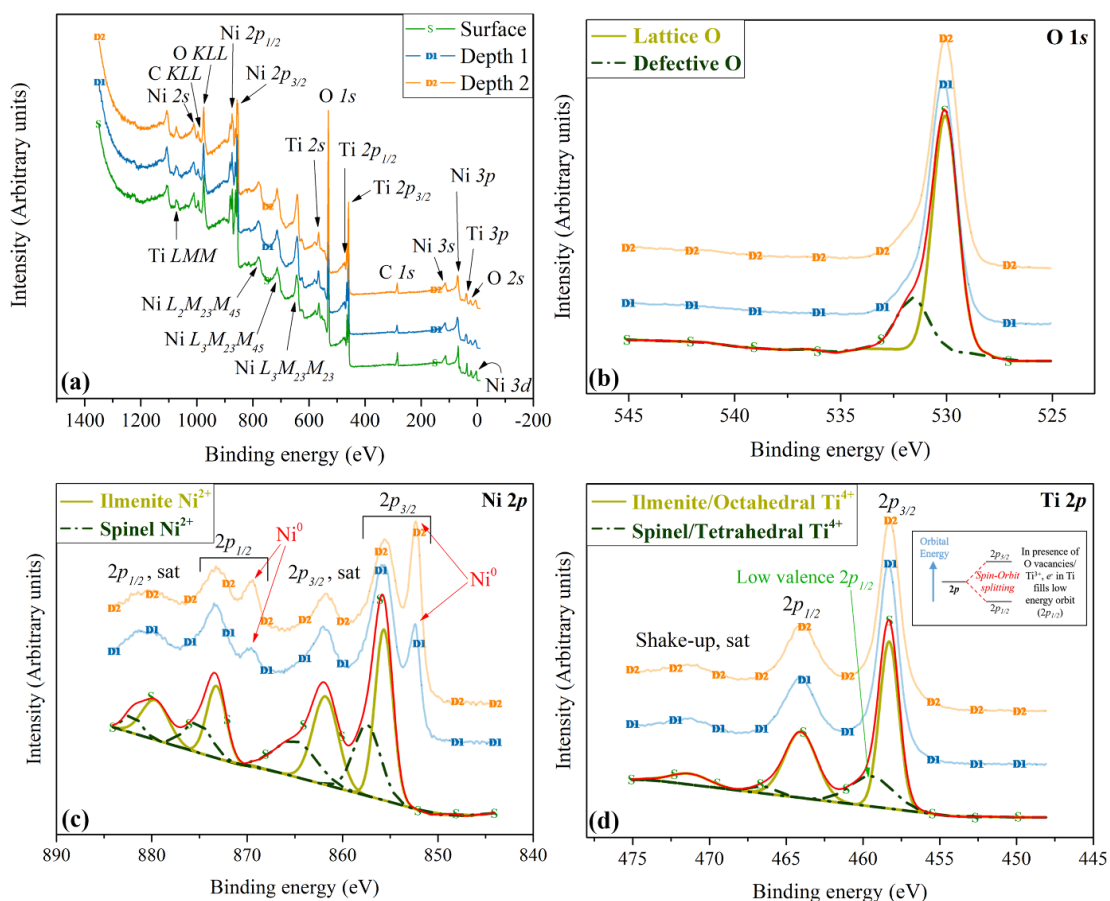
Fig. 4.6 XPS depth profiling analysis of NTO nanofibers obtained at T = 773 K: (a) survey spectra, (b) high-resolution spectra for O *1s*, (c) high-resolution spectra for Ni *2p*, and (d) high-resolution spectra for Ti *2p* (inset figure: spin-orbit splitting for Ti^{3+} ion).

It is well-known that the Ti^{4+} ions occupy only the O_v in INTO, and T_v in SNTO (Chapter 3). The O_v and T_v located Ti^{4+} ions are easily distinguished in the high-resolution XP spectra of Ti *2p* (Figure I.7d and 4.6d), which is consistent with the literature.(Capel-Sanchez et al. 2000; Arillo et al. 2001) However, the presence of $Ti^{4-\delta}$ may be due to (i) charge neutrality in non-stoichiometry SNTO, (ii) the reduction to low valent ion during XPS depth profiling, which is negligible due to low concentration of Ti ions in SNTO (Ni:Ti ~3.8) (Varga et al. 2012), or (iii) partial reduction of Ti^{4+}

ions during Ar$^+$ ion etching (Leinen D. et al. 2004). Besides, the peak representing $2p_{1/2}$ Ti$^{4-\delta}$ ion due to oxygen deficiency (Bharti et al. 2016), might have been convoluted with tetrahedral $2p_{3/2}$ Ti^{4+} ions. It must be noted that $2p_{1/2}$ Ti$^{4-\delta}$ ion have lower orbital energy than $2p_{3/2}$ Ti$^{4-\delta}$ (inset Fig. I.7d and 4.6d) and hence the partial reduction in ionic charge is fulfilled by addition of electrons to lower valence. This clarifies the absence of $2p_{3/2}$ Ti$^{4-\delta}$ peak in Ti $2p$ XP spectra of the samples. These results further corroborate the presence of SNTO in NTO nanofibers.

4.1.6 Bifunctional electrocatalyst for water-splitting

4.1.6.1 HER

The electrocatalytic HER of NTO/GE nanofibers in alkaline medium was studied *via* CV and CP methods, and electrocatalytic parameters were evaluated by Tafel plots. In electrochemistry, HER is comprehensively studied through its ease in producing pure hydrogen gas. The protons from the electrolyte are adsorbed on the active sites of the electrocatalyst surface (cathode) through HER and receive electrons to form chemisorbed hydrogen atoms, which later disengage as hydrogen gas (Ullal and Hegde 2014; George et al. 2015; Subramanya et al. 2015). In this regard, CV analysis is a well-established technique to comprehend the thermodynamics of redox reactions and kinetics of adsorption process. Besides, the CP analysis is a basis for evaluating the material stability, where a definite controlled current is applied between electrodes (three electrode system) as the redox reactions occur at the active sites of the working electrode.

Figure 4.7 shows the results of the CV analysis for HER. For all working electrodes during HER, CV analysis was conducted in a negative potential range (0 to -1.6 V) with 50 cycles under 1 M KOH. The optimal scan rate for the HER efficiency of NTO/GE was selected based on the CV tests of NTO nanofibers obtained at T = 773 K at different scan rates (5, 25, 50, and 100 mV·s^{-1}) (George et al. 2015). The maximum peak current attained after equilibrium was observed for the scan rate of 100 mV·s^{-1} for the stable cycle. Hence, CV analysis for all working electrodes were performed at this scan rate. Furthermore, the peak current at -1.6 V decreased sequentially for each sample during 50 cycles of CV analysis until it attained an equilibrium and became constant for the rearmost cycles. This retarding peak current within 50 cycles is

attributed to the increase in resistance instituted by the hydrogen bubbles formed on the NTO/GE surface. Later, these hydrogen bubbles stabilize once they attain equilibrium in the formation and detachment of hydrogen gas, which leads to constant peak current for hindmost cycles. From Figure 4.7 and Table 4.2, it is found that the least peak current was observed for NTO/GE obtained at T = 773 K. This highest electrocatalytic activity of NTO nanofibers synthesized at T = 773 K is attributed to the high surface area, morphology and defective active sites (especially from non-stoichiometric SNTO), which will be further discussed in Section 4.1.6.3. The onset potential for HER was measured from CV plots and tabulated in Table 4.2.
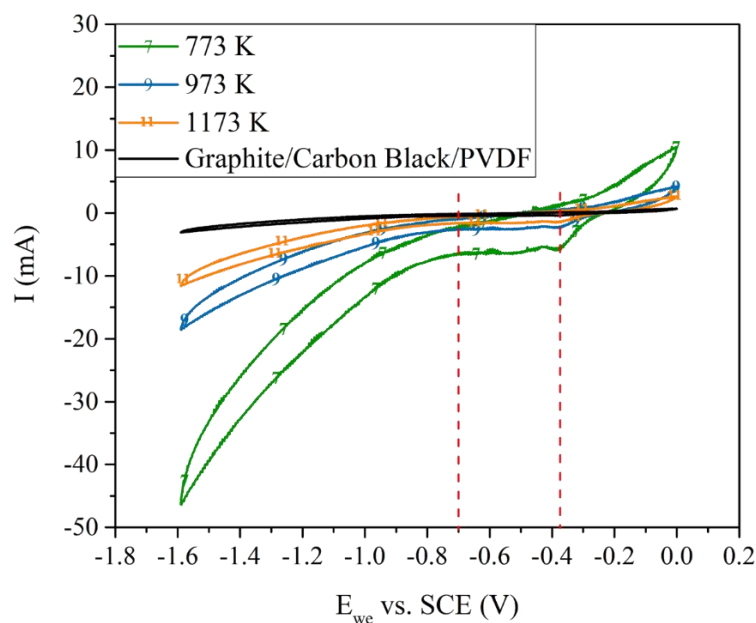
Fig. 4.7 CV curves for HER analysis using NTO/GE developed at different T.

The typical operating current densities for the conventional low pressure alkaline electrolyzers in industry range from -100 to -300 mA·cm^{-2} (Subramanya et al. 2015). To evaluate the electrocatalytic behavior of the electrodes, CP analysis was monitored at a constant current density applied over sufficient period. The CP analysis for the liberation of hydrogen on NTO/GE electrodes were obtained at a constant current of -300 mA for a period of 1800 s. This optimal stable current for hydrogen gas evolution was fixed after measuring the amount of hydrogen gas evolved using NTO/GE obtained at T = 773 K at different applied currents (Section I.10). Furthermore, by measuring the amount of hydrogen gas evolved for the initial 300 s, the electrocatalytic activity of all

the NTO/GE electrodes obtained at different pyrolysis temperatures was estimated. The nature of CP plots is shown in Figure 4.8 for all the working electrodes and the inset Figure 4.8 shows the volume of hydrogen gas evolved on the corresponding working electrode for the initial 300 s. The production of hydrogen gas is maximum for the NTO/GE obtained at T = 773 K. This result is an evidence for the best electrocatalytic activity of NTO/GE obtained at T = 773 K for HER in present study.

Table 4.2: HER and OER parameters of NTO nanofibers developed at T. T_v: Tetrahedral void and O_v: Octahedral void.

T (K)	Cathodic peak current at 1.6 V (mA)	Onset potential of H₂ evolution, E_{we} vs. SCE (V)		Anodic peak current at 0.75 V (mA)	Onset potential of O₂ evolution, E_{we} vs. SCE (V)	
		Ti in T_v	*Ni in O_v*		*Ti in T_v*	*Ni in O_v*
773	-46.4	-0.37	-0.69	42.6	0.19	0.382
973	-18.5	-0.38	-0.74	125	0.19	0.336
1173	-11.6	-0.38	-0.82	211	0.18	0.296
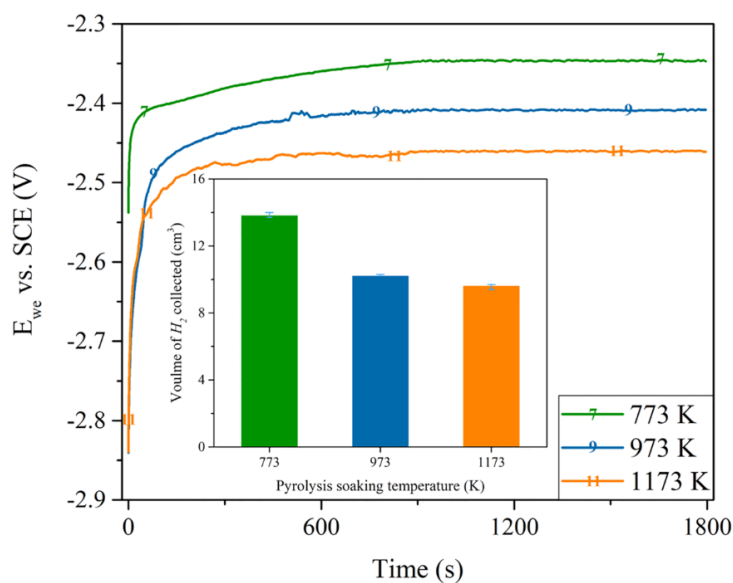
Fig. 4.8 CP stability responses attained by NTO/GE developed at different T, for HER. Inset figure: H₂ liberated for 300 s for corresponding NTO/GE.

4.1.6.2   OER

Similar to HER, the NTO/GE developed at different T were evaluated for their electrocatalytic behavior in OER. For OER, the CV analysis were conducted in the positive potential window of 0 to 0.75 V at scan rate of 100 mV·s^{-1}. The onset potential for incessant liberation of oxygen gas was recorded from the CV plots. From Figure 4.9 and Table 4.2, it was determined that the NTO/GE obtained at T = 1173 K showed the supreme electrocatalytic behavior with the least onset potential of 0.296 V towards OER.
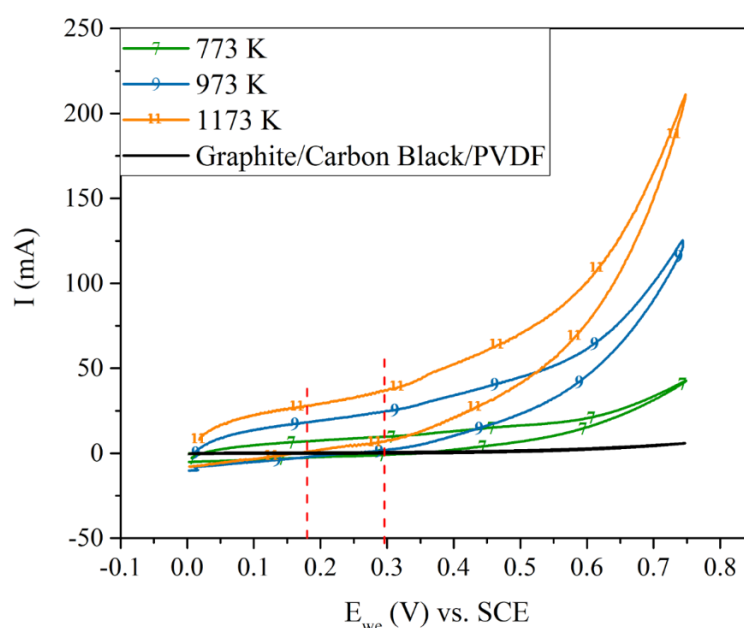
Fig. 4.9 CV curves for OER analysis using NTO/GE developed at different T.

The stability and competence of NTO/GE for OER was also studied using CP analysis. The optimal operating current density for OER was chosen on similar grounds as HER (Section I.11), but with a positive current value, *i.e.*, +300 mA for a time interval of 1800 s. When this current was applied, the potential was found to decrease drastically as shown in CP plots (Figure 4.10), until it reached an equilibrium potential, where OH$^-$ oxidizes to O$_2$. At this equilibrium, the oxygen gas bubbles forming at the active site of the NTO nanofiber surface and ones that are escaping attain steadiness, which keeps the potential stable throughout the experiment.
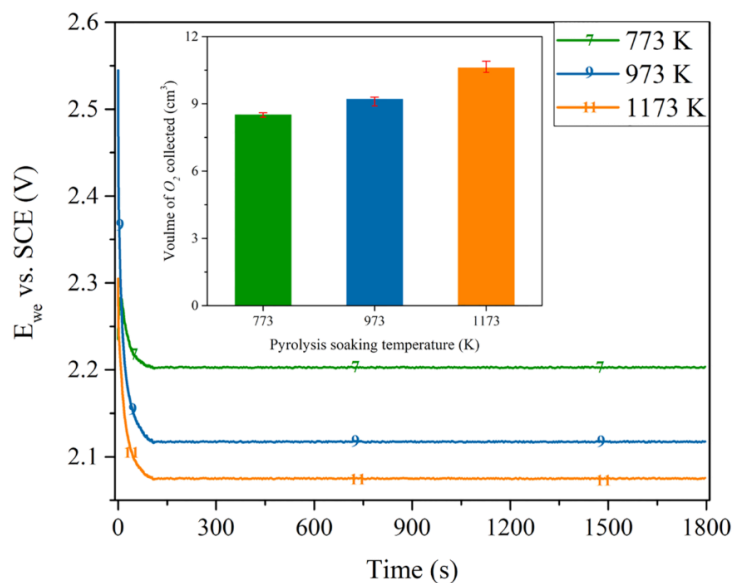
Fig. 4.10 CP stability responses attained by NTO/GE developed at different T, for OER. Inset figure: O_2 liberated for 300 s for corresponding NTO/GE.

The relative volume of oxygen gas evolved in 300 s for NTO/GE, corresponding to different pyrolysis temperature is shown in the inset Figure 4.10. The NTO/GE obtained at T = 1173 K exhibited the least onset potential for oxygen gas liberation, in contrast to that observed for hydrogen gas liberation. This observation shows that the NTO/GE obtained at T = 1173 K was a more efficient electrocatalyst for OER. In other words, NTO/GE obtained at T = 1173 K possesses the highest electrocatalytic efficiency, presumably due to adsorption of more OH$^-$ ions on active sites of the surface from electrolyte. This can be understood by the large crystallite size of NTO nanofibers obtained at T = 1173 K, which favors the colonization of the large OH$^-$ ions on the active sites though it is not the recommended material for HER (due to low surface area and lesser defective active sites), as discussed previously. On the other hand, the NTO/GE obtained at T = 773 K displays the minimum electrocatalytic competence for OER due to lack of surface activity towards OH$^-$ ions adsorption. Therefore, it could be concluded that the electrocatalyst surface favoring the anodic reaction has a hostile outcome on the cathodic reaction and *vice versa*.

4.1.6.3 *Tafel polarization plot*

The electrocatalysts prepared under different T are analyzed for their kinetic behavior using Tafel polarization plot. The Tafel plot of NTO/GE electrodes were obtained by

linear sweep voltammetry at a scan rate of 5 mV·s⁻¹. The b for both the HER and OER were determined from Tafel plot (Figure 4.11) and tabulated in Table 4.2. In alkaline medium, HER in general trails through two different mechanisms either as Volmer-Tafel (Equation 4.2 and 4.3) or Volmer-Heyrovsky (Equation 4.2 and 4.4) process (Subramanya et al. 2015).

The Volmer reaction by electrochemical hydrogen atom adsorption is written as:

$$H_2O + M + e^- \leftrightarrow M - H_{ads} + OH^- \tag{4.2}$$

and the Tafel reaction by chemical desorption as:

$$2M - H_{ads} \leftrightarrow 2M + H_2 \uparrow \tag{4.3}$$

The Heyrovsky reaction by electrochemical desorption is:

$$M - H_{ads} + H_2O + e^- \leftrightarrow M + OH^- + H_2 \uparrow \tag{4.4}$$
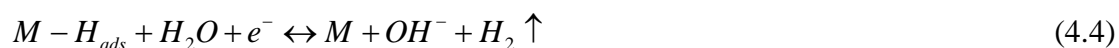
Both Volmer-Tafel and Volmer-Heyrovsky processes involve the H_2O molecule adsorption, and its electrochemical reduction to adsorbed H atom (H_{ads}) and OH^- ion. Later, the OH^- ion is desorbed to electrolyte to create fresh surface and active H_{ads} intermediate in formed to liberate H_2 (Subramanya et al. 2015). Generally, depending upon the b_c, the rate-determining step is Volmer (b_c >100 mV·dec⁻¹), Heyrovsky (b_c about 40 mV·dec⁻¹), or Tafel (b_c about 30 mV·dec⁻¹) (Conway and Tilak 2002). In case of electrochemically activated WE, the Volmer-Heyrovsky mechanism is facile and the rate-determining step is a mixed process (Choquette et al. 1990). The b_c for NTO/GE obtained at T = 773 K is close to Volmer-Heyrovsky mechanism and best suitable for HER compared to NTO/GE obtained at T = 973 K and T = 1173 K. It was observed that the Ni-based materials hold suitable binding energy for H_{ads} close to Pt, though the electrocatalytic activity for HER is less compared with Pt/C.(Dong et al. 2017) Table 4.2 shows that the performance of HER activity (*i.e.*, b_c) of the NTO/GE nanofibers is better than values reported earlier in literature, which falls near to Pt/C, especially for NTO/GE obtained at T = 773 K. This is attributed to the (i) uniform compositions of

INTO and SNTO as seen from XPS, and (ii) synergetic kinetics of INTO/SNTO, where the defective SNTO behaves similar to a pure metallic Ni as seen from DFT analysis.
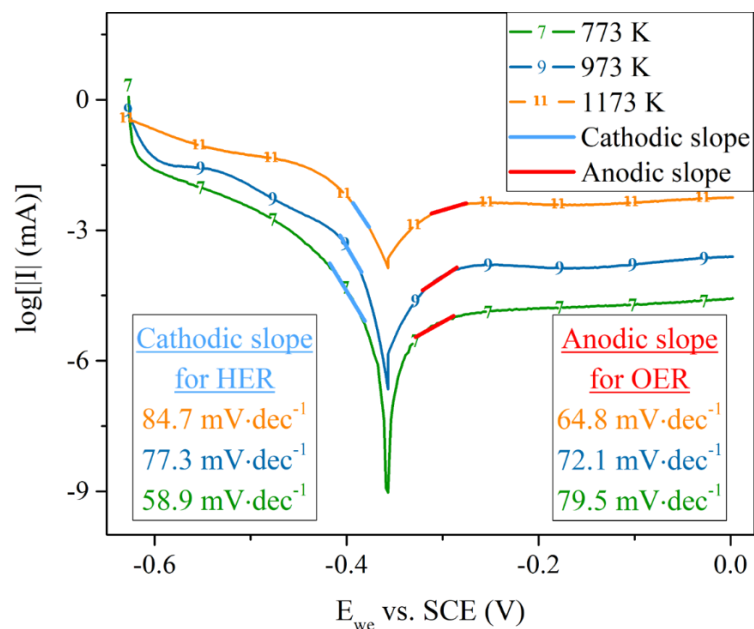
Fig. 4.11 Comparison of Tafel polarization plots and slopes, for HER and OER, of NTO/GE developed at different T.

It has been reported that pure Ni has favorable active site for H_{ads}, whereas INTO favors the absorption of OH^- ions, which also occupy the active sites of H_{ads} in INTO (Subramanya et al. 2015; Dong et al. 2017). Furthermore, the NTO nanofibers obtained at T = 773 K has greater porosity (HRTEM, Figure 4.1) compared to those obtained at 1173 K. This suggests that ease of adsorption of large OH^- ions onto the active surface and follow OER process. Hence, the synergetic effect of both structural factor and compositional distribution contributes to the respective HER and OER process. It has also been reported that the presence of Ti^{4+} ions in INTO is advantageous to improve the stability of the electrocatalyst in case of INTO/Ni. However, the role of Ti^{4+} ions in INTO/STNO composite nanofibers can be attributed to (i) the stability of INTO for OER process in forming a stoichiometric phase (Dong et al. 2017) and (ii) low valence Ti ions as seen from XPS in STNO apart from forming a defective non-stoichiometric phase, may also help in HER process (Zuo et al. 2010; Lu et al. 2015; Swaminathan et al. 2016). These observations are in good agreement with the HER and OER results obtained by CV analysis, where the NTO/GE consisting less STNO (Table

3.2, Chapter 4), shows up more OER activity and *vice versa*. The performance of OER activity is highest for NTO/GE obtained at T = 1173 K, having least b_a. The b_a values (Table 4.2) obtained for NTO nanofibers are akin to the values in literature as well as better than the commercial used material, like RuO_2 (Dong et al. 2017), suggest the complimentary OER kinetics of NTO nanofibers. In general, the OER mechanism in alkaline solution for active sites represented as Λ on the surface of electrocatalyst is as given by (Dong et al. 2017; Anantharaj et al. 2018; Li et al. 2018):

$$\Lambda + OH^- \leftrightarrow \Lambda - OH^- + e^- \tag{4.5}$$

$$\Lambda - OH^- + OH^- \leftrightarrow \Lambda - O + e^- + H_2O \tag{4.6}$$

$$\Lambda - O + OH^- \leftrightarrow \Lambda - OOH + e^- \tag{4.7}$$

$$\Lambda - OOH + OH^- \leftrightarrow \Lambda - O_2 + e^- + H_2O \tag{4.8}$$

$$\Lambda - O_2 \leftrightarrow \Lambda + O_2 \tag{4.9}$$

Furthermore, in Figure 4.7 and 4.9, the presence of two onset potential can be attributed to the activation of two different ions (Ni in O_v and Ti in T_v) at active sites (Rasiyah et al. 1982; Rasiyah and Tseung 1983) from the respective favorable phases. On second onset potential, the Ni rich active sites are activated, which increase the current output as seen from HER and OER CV plots. Overall, the analysis concludes that the NTO/GE obtained at T = 773 K is an excellent cathodic electrode for electrolysis in alkaline medium. In addition, the NTO/GE obtained at T = 1173 K outperforms as an anode for the same electrolysis process. Hence, these NTO nanofibers based NTO/GE electrodes have a huge potential as candidate materials for large scale production of H_2 and O_2 by water-splitting process.

Table 4.3: Comparison of synthesis, morphology, HER, and OER parameters with some reported mono/bifunctional electrocatalysts.

Synthesis of material	Type of electrode (*Electrocatalyst morphology*)	Onset potential of H₂ evolution (V vs. SCE)	Onset potential of O₂ evolution (V vs. SCE)	Tafel slope for HER (mV·dec⁻¹)	Tafel slope for OER (mV·dec⁻¹)	Electrolyte	Reference
Sol-gel assisted electrospinning followed by pyrolysis for t = 2 h	NTO nanofibers/GE, obtained at T = 773 K and t = 2 h (*Mosaic structured nanofiber*)	-0.69 or -0.446 vs. RHE or -0.653 vs. RHE@10 mA·cm⁻²	0.382 or 0.626 vs. RHE or 0.554 vs. RHE@10 mA·cm⁻²	58.9	79.5	1 M KOH	Present work
	NTO nanofibers/GE, obtained at T = 973 K and t = 2 h (*Mosaic structured nanofiber*)	-0.74 or -0.496 vs. RHE or -1.020 vs. RHE@10 mA·cm⁻²	0.336 or 0.58 vs. RHE or 0.304 vs. RHE@10 mA·cm⁻²	77.3	72.1		

	NTO nanofibers/GE, obtained at T = 773 K and t = 2 h *(Bamboo structured nanofiber)*	-0.82 or -0.576 vs. RHE or -1.263 vs. RHE@10 mA·cm^{-2}	0.296 or 0.54 vs. RHE or 0.266 vs. RHE@10 mA·cm^{-2}	84.7	64.8		
Sol-gel assisted electrospinning followed by pyrolysis for t = 4 h	NCO nanofibers/GE, obtained at T = 773 K *(Mosaic structured nanofiber)*	-0.781 or -0.537 vs. RHE or -0.914 vs. RHE@10 mA·cm^{-2}	0.491 or 0.735 vs. RHE or 0.855 vs. RHE@10 mA·cm^{-2}	37.6	67.0	1 M NaOH	Chapter 8 of this thesis
Sol-gel assisted electrospinning followed by	Co$_3$O$_4$ nanofibers/GE, obtained at T = 773 K	-1.26 or -1.016 vs. RHE	0.54 or 0.784 vs. RHE	-	-	1 M KOH	(George et al. 2015)

pyrolysis for t = 2 h	*(Bamboo structured nanofiber)*						
Precipitation method followed by pyrolysis for t = 6 h (1173 K) and reduction for 2 h	INTO/Ni, obtained using reduction atmosphere of 723 K *(Villiform structured nanosheets)*	-0.05 vs. RHE or -0.196 vs. RHE@10 mA·cm^{-2}	1.5 vs. RHE or 1.566 vs. RHE@10 mA·cm^{-2}	118	62.2	0.1 M KOH	(Dong et al. 2017)
Reverse microemulsion method for 27 h (383 K) followed by pyrolysis for t = 2 h	NiO/TiO$_2$/GE, obtained at T = 773 K *(Monolayer nanosheets)*	-	1.55 vs. RHE@10 mA·cm^{-2}	-	52	1 M KOH	(Zhao et al. 2016)

Solid-state reaction followed by pyrolysis for t = 1 h	Ni$_2$P/GE, obtained at using N$_2$ atmosphere of 523 K *(Nanoparticles)*	-0.221 vs. RHE@10 mA·cm^{-2}	1.45 vs. RHE or 1.52 vs. RHE@10 mA·cm^{-2}	-	47	1 M KOH	(Stern et al. 2015)
Electrodeposition followed by selenization (Graphene/Ni mesh by chemical vapour deposition)	NiSe/Graphene/Ni mesh *(Nanowalls)*	-	1.6 vs. RHE or 1.66 vs. RHE@10 mA·cm^{-2}	-	83.4	1 M KOH	(Li et al. 2016b)
Hydrothermal synthesis for 8 h	NiCo$_2$S$_4$/Ni foam, obtained at 393 K *(Nanowires)*	-0.21 vs RHE or -0.310 vs. RHE@10 mA·cm^{-2}	1.5 vs. RHE or 1.57 vs. RHE@10 mA·cm^{-2}	58.9	40.1	0.1 M KOH	(Sivanantham et al. 2016)
Solvothermal process followed by	Hierarchical NCO/Ni foam,	-0.110 vs. RHE@10 mA·cm^{-2}	1.52 vs. RHE@10 mA·cm^{-2}	49.7	53.0	1 M NaOH	(Gao et al. 2016)

pyrolysis for t = 2 h	obtained T = 623 K (*Hollow microcuboids*)						
Thermal decomposition process for 2.5 h	Ni_2P /GE, obtained T = 593 K (*Hollow and Solid nanocrystals*)	-0.088 vs RHE or -0.124 vs. RHE@10 mA·cm^{-2}	-	53.0	-	0.5 H_2SO_4	(Pan et al. 2015)
Hydrothermal process followed by pyrolysis for t = 2 h (573 K) and hydrogenation for 3 h	Ni@NiO/Ni foam, obtained using reduction atmosphere of 473-573 K (*Core shell Nanosheets*)	-0.07 vs RHE or -0.149 vs. RHE@10 mA·cm^{-2}	-	69	-	1 M KOH	(Yan et al. 2015b)
Hydrothermal process	$TiN@Ni_3N/Ti$ foil,	-0.015 vs RHE or	1.52 vs RHE or	42.1	93.7	1 M KOH	(Zhang et al. 2016)

followed by pyrolysis for t = 3 h (823 K) and ammonization for 2 h	obtained using ammonia atmosphere of 1073 K *(Myriophyllum-like nanowires)*	-0.021 vs. RHE@10 mA·cm^{-2}	1.58 vs. RHE@10 mA·cm^{-2}

$E_{RHE} = E_{SCE} + 0.244$ V, Onset potential of HER = overpotential + 0 V, Onset potential of OER = overpotential + 1.23 V, GE: nitrogen doped- rGO/graphite electrode.

4.2   SUMMARY AND CONCLUSIONS

The mosaic structured NTO nanofibers (especially developed at T = 773 K), which consist of high amount of SNTO and small crystallite size in comparison to the bamboo structure (developed at T = 1173 K), show superior electrocatalytic activity for HER. The bamboo structured NTO, which have lesser amount of SNTO and larger crystallite size, show dominance towards OER. The HER and OER performance of the different NTO structures may be understood based on (i) the rational affinity of H^+ ions towards SNTO and the large number of OH^- ions adsorption at INTO (ii) the favorable composition of INTO and SNTO in different NTO nanofibers, and (iii) the conducive morphology for the diffusion of electrolyte to reach the preferred mating active sites. The NTO nanofibers obtained at T = 773 K exhibits higher electrocatalytic activity for HER and is promising as a good cathode material for alkaline water-splitting. Besides, the one that is tailored at T = 1173 K outperforms as anode, with effective OER performance. In summary, SNTO/INTO nanofibers have wide potential as photo/electrochemical catalysts in water-splitting and other photo/electrocatalyst assisted applications.

CHAPTER 5

CHAPTER 5

MAGNETIC BEHAVIOUR OF POLYMORPH COMPOSITE NICKEL TITANATE NANOFIBERS
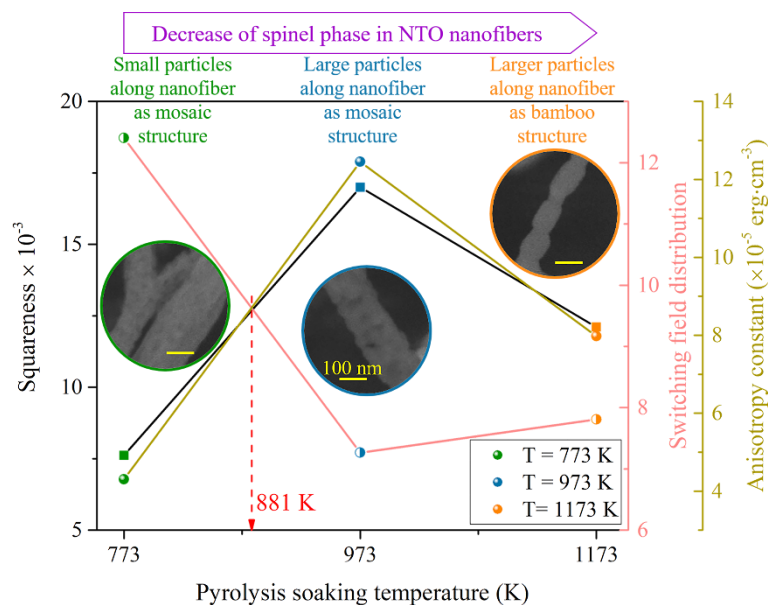
Scheme 5.1 Variation in magnetic parameters with NTO nanofiber morphology as a function of T.

In this chapter, the magnetic behavior of as-synthesized polymorph (SNTO/INTO) composite nanofibers of NTO in Chapter 3 was studied at isothermal (θ_T = 20, 50, and 300 K) and non-isothermal conditions (θ_T varying between 20 K and 300 K at constant H of 500 G). The magnetic parameters such as H_c, M_r, and M_s were found to be strongly dependent on T. This is presumably due to the synergetic effect of SNTO/INTO exchange coupling, structural defects in crystallites, long range ordering in the nanoparticles/nanofibers and the morphology of NTO nanofibers (function of T). The highest H_c (342.44 G at θ_T = 300 K) and M_r (0.0306 emu·g^{-1} at θ_T = 20 K) were observed for NTO nanofibers developed at T = 973 K, which have mosaic structured morphology with SNTO and INTO crystallite sizes of ~39 nm and ~24 nm, respectively, and the highest K (~1.2 × 10^4 erg·cm^{-3}). On the other hand, the highest M_s (5.3 emu·g$^-$

[1] at $\theta_T = 20$ K) and SFD = 12.4 was observed for mosaic structured NTO nanofibers having smaller crystallites (~13 nm and 24 nm for SNTO and INTO, respectively, with high inter-particle distance and high porosity) developed at T = 773 K, which is also rich in SNTO content. The correlation between the variation in magnetic features and structural-morphological change of NTO nanofibers was studied as a function of T.

5.1 RESULTS AND DISCUSSION

5.1.1 Morphological and structural features

The AFD and the arrangement of NTO nanoparticles (which were imbedded in the NTO nanofibers) of NTO nanofibers substantial changed as a function of T as seen from Figure 3.4, Section 3.1.2.1 of Chapter 3. The small NTO nanoparticles were distributed along the NTO nanofibers developed at T = 773 K (Fig. 3.4g), whereas these nanoparticles coarsened with increase in T to 973 K (Fig. 3.4h). These two samples form a mosaic structure with NTO nanoparticles creating high porosity (Section 3.1.2.6) along the NTO nanofiber. At T = 1173 K (Fig. 3.4i), the nanoparticles coarsen further to form bamboo structure with many larger particles connected to each other, reducing the porosity in the nanofiber (Section 3.1.2.6). It is also noted that the structural as well as stoichiometry defects are reduced at higher T from Chapter 3 and 4.

5.1.2 Isothermal VSM analysis

Figure 5.1 shows the isothermal hysteresis loops (M - H curves) at $\theta_T = 300$ K of NTO nanofibers developed at different T. The inset Figure 5.1 shows narrow loops for all the three samples, indicating the presence of weak FM at $\theta_T = 300$ K. Furthermore, Figure 5.1 also suggests a significant difference in the magnetic parameters of NTO nanofibers developed at different T. The magnetic parameters such as H_c, M_r, and M_s were measured and tabulated in Table 5.1 for $\theta_T = 300$, 50, and 20 K. The data in graphical form is depicted in Figure 5.2. It is observed that the H_c increases with respect to increase in θ_T in all samples, while it had its highest value for the sample with T = 973 K at each individual θ_T value (Fig. 5.2a). The magnetic, crystallite, and morphological parameters of nanofibers of other oxides such as NCO, NiO, and Co_3O_4, prepared

earlier by similar techniques are compared with NTO nanofibers developed in the present study in Table 5.1 and Table 5.2.
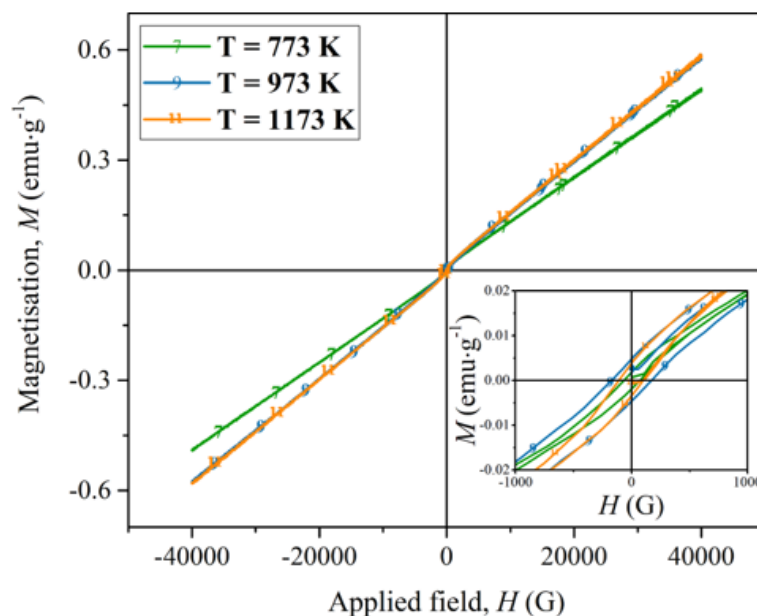
Fig. 5.1 Hysteresis curve obtained at $\theta_T = 300$ K for NTO nanofibers developed at T = 773, 973, and 1173 K.

In Figure 5.2b, it is seen that the M_r values decrease with respect to increase in θ_T, however, the highest values were still observed for the sample with T = 973 K. Figure 5.2c shows that there is a significant decrease in the M_s with decrease in θ_T for all the three samples, but at each θ_T, the M_s is nearly the same for the samples with T = 973 K and 1173 K. The earlier study has confirmed the absence of metallic Ni or Ti phases through XRD (Section 3.1.2.3) and XPS (Section 4.1.5 and I.9) analyses. Therefore, the magnetic parameters measured here are representative of the INTO and SNTO phase mixture in the NTO nanofibers. The net magnetic property of NTO nanofibers is the synergetic effect of AFM INTO, FM SNTO, as well as the morphological features of NTO nanofibers. The existence of weak FM due to discrete regions of AFM and FM phases in other mixed transition metal oxides, has been reported earlier (Troyanchuk et al. 2003). The anomalous increase in H_c with an associated decrease in M_r with θ_T has been observed in INTO by (Modak et al. 2018).

This was supposedly due to the layered hexagonal planar structure of Ni ions in NTO, as explained next.
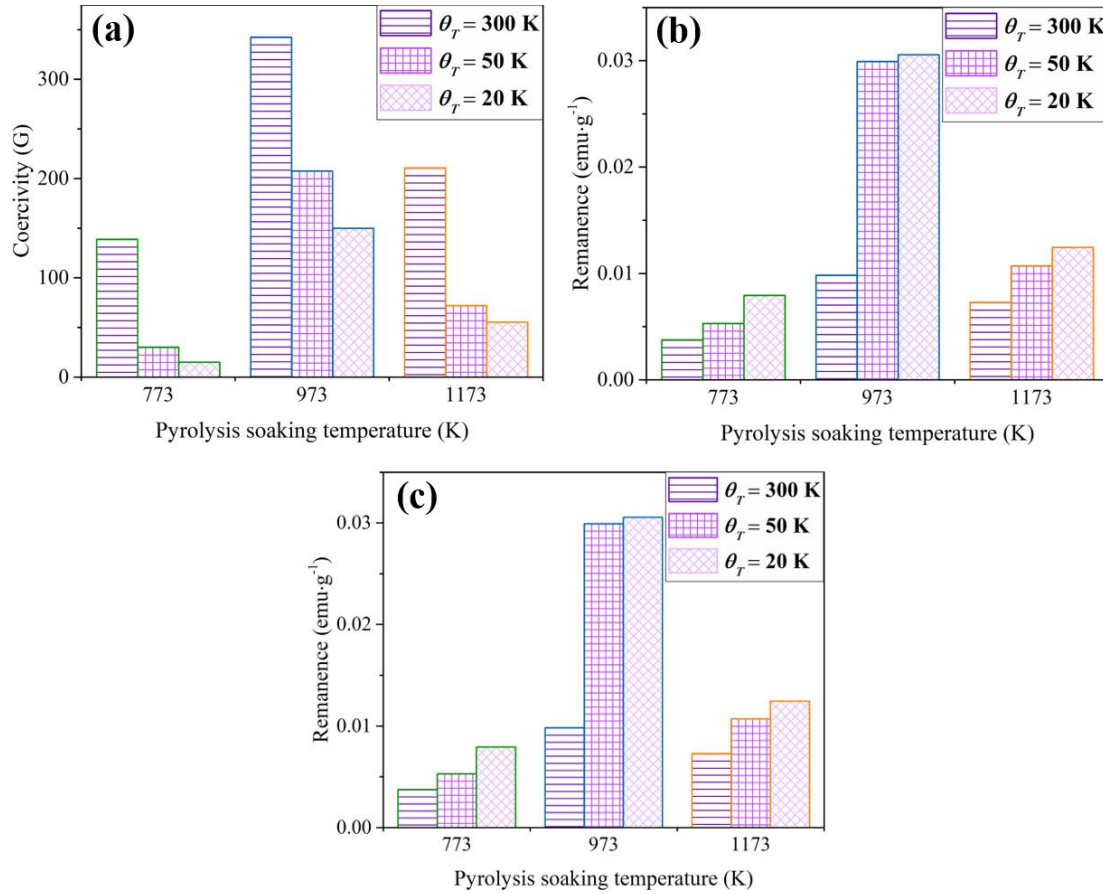
Fig. 5.2 Comparison of (a) coercivity: H_c, (b) remanence: M_r, and (c) saturation magnetization: M_s obtained at different θ_T (20, 50, and 300 K) for NTO nanofibers developed at T = 773, 973, and 1173 K.

Table 5.1: Magnetic parameters measured at different θ_T for NTO nanofibers of the present study and other oxides in earlier literature synthesized at different pyrolysis conditions.

Materials	Pyrolysis soaking conditions	D (nm)	Average fiber/(particle) diameter (nm)	θ_T (K)	H_c (G)	M_r (emu·g⁻¹)	M_s (emu·g⁻¹)	Reference
NTO composite nanofibers prepared by sol-gel assisted electrospinning and followed pyrolysis	T = 773 K, t = 2 h	17.0	130 (16.9)	300	138.9	0.0038	0.49	Present study
				50	30.0	0.0053	2.3	
				20	15.0	0.0079	5.3	
	T = 973 K, t = 2 h	32.3	144 (24.6)	300	342.4	0.0098	0.58	
				50	207.5	0.0299	1.84	
				20	149.8	0.0306	2.9	
	T = 1173 K, t = 2 h	57.0	188 (91.5)	300	210.8	0.0073	0.6	
				50	72.1	0.0107	1.99	
				20	55.2	0.0125	3.03	
NCO nanofibers prepared by similar technique	T = 773 K, t = 2 h	16.2	117	300	550.3	0.2964	4.11	Chapter 9 of this thesis
	T = 773 K,	14.4	268	300	393.6	0.0975	4.06	

	$t = 4$ h							
	T = 773 K, $t = 6$ h	16.7	283	300	119.9	1.2438	9.8	
NiO nanofibers prepared by similar technique	T = 773 K, $t = 2$ h	43.5	135	300	97.7	0.472	-	(George and Anandhan 2014b)
	T = 873 K, $t = 2$ h	50.5	104	300	107.3	0.0429	-	
	T = 973 K, $t = 2$ h	63.9	88	300	150.3	0.0366	-	
Co$_3$O$_4$ nanofibers prepared by similar technique	T = 773 K, $t = 2$ h	19.8	126	300	91.4	0.0658	-	(George 2015; George and Anandhan 2015a)
	T = 873 K, $t = 2$ h	22.3	101	300	91.5	0.050	-	
	T = 973 K, $t = 2$ h	31.5	96	300	90.8	0.037	-	
NTO microcrystals prepared by simple molten salt technique	T = 1123 K, $t = 10$ h	70	(238)	300	157	0.209	-	(Yuvaraj et al. 2013)
				100	216	0.321	-	
				15	155	0.545	-	
				5	168	0.561	-	

Table 5.2: Comparison of squareness (S), switching field distribution (SFD), and anisotropy constant (K) for $\theta_T = 300$ K of NTO and NCO nanofibers developed at different pyrolysis conditions. Curie constant (C) and Weiss temperature (θ_w) for NTO nanofibers developed at T = 773, 973, and 1173 K.

Materials	Pyrolysis conditions	S	SFD	$K \times 10^{-4}$ (erg·cm^{-3})	$C \times 10^{-4}$ [emu·K·(G·g)$^{-1}$)]	θ_w (K)
NTO nanofibers	T = 773 K, t = 2 h	0.008	12.4	0.43	1.53	-20.6
	T = 973 K, t = 2 h	0.017	7.3	1.25	2.90	-97.2
	T = 1173 K, t = 2 h	0.012	7.8	0.79	3.72	-137.9
NCO nanofibers prepared by similar technique (Chapter 9 of this thesis)	T = 773 K, t = 2 h	0.072	10.9	1.42	-	-
	T = 773 K, t = 4 h	0.024	23.7	1.00	-	-
	T = 773 K, t = 6 h	0.127	7.8	0.74	-	-

The major factors that affect H_c are: (i) magnetocrystalline anisotropy, (ii) shape anisotropy, and (iii) the exchange coupling at the interface between FM-AFM regions. Among these, (ii) and (iii) are particularly relevant to the present system. The shape anisotropy here arises from the nanoparticle/nanofiber morphology. As mentioned the sample with T = 973 K has a mosaic structure with larger crystallites and less porosity. The anisotropy in this sample will be more compared to the rod-like bamboo structured sample of T = 1173 K, as the former tends to behave similar to nanosheets or thin films (Vranješ et al. 2014; Kumar et al. 2018). Therefore, the H_c and M_r is higher in NTO nanofibers developed at T = 973 K. Although the sample with T = 773 K also possesses the mosaic structure, it has much smaller crystallite size and a highly porous structure, which leads to lack of magnetic ordering, thus resulting in lower H_c and M_r (Thakur et al. 2013).

The T_N for INTO has been determined to be near 23 K (Heller et al. 1963; Watanabe et al. 1980). Below θ_T = 23 K, the in-plane ordering of the Ni moments is FM, while ordering across the planes is AFM. Above θ_T = 23 K, the coupling between the hexagonal planes of Ni^{2+} in INTO is very week. So, the FM hexagonal Ni^{2+} planes remain uncorrelated with each other. Therefore, the surface moments on the larger particles make a transition from a canted AFM state with net moment to many uncorrelated 2D FM planes. In other words, above θ_T = 23 K, the surface of each magnetic nanoparticle may be seen as a collection of many FM planes, each of which might be blocked along its own anisotropy axis. This results in the anomalous increase in H_c with increase in θ_T. Ordinarily, a decrease in H_c with θ_T would have been expected in INTO on the basis of the core-shell nanostructure model.(Yuvaraj et al. 2013) According to this theory, a higher magnetic field would be required to flip the strong AFM spin interaction between cations (Ni^{2+}-Ni^{2+}) in the core, which are aligned in antiparallel fashion. In the present case, the highest H_c observed at θ_T = 300 K is because of the uncompensated spins in the shell surface increase, breaking their AFM interaction with core spins. Furthermore, among the three samples developed at different T, the high value of H_c observed for the sample developed at T = 973 K

suggests that the AFM coupling strength is the strongest in these nanoparticles, which may be due to the presence of large crystallites of INTO with less porosity or the large defective crystallites of SNTO, as spinel phase is normally FM, compared to sample developed at T = 773 K. In addition, this sample at T = 973 K also behaves similar to a thin film with high shape anisotropy unlike rod-like (bamboo) structure of sample at T = 1173 K, which contributes to high H_c in samples developed at T = 973 K (Kumar et al. 2018).

FM contribution is also caused by creation of F-centers in oxygen vacancy. The electron orbital trapped near a vacancy by polaronic effect has a large radius and can overlap with the d-orbitals of the neighboring magnetic ions to form an F-center BMP in NTO nanofibers (Typek et al. 2016; Kumar et al. 2018). This phenomenon depends on temperature and can significantly influence the H_c of the material based on its T. It is known that M_r is also related to temperature through the electronic structure of the material. The M_r increases with the number of $3d$ unpaired electrons. At higher T, the defective SNTO crystallites are larger in size with more cationic defects in presence of oxygen rich environment (Kumar et al. 2017), which in turn means more unpaired electrons in the form of Ni^{3+} cations. This causes the M_r to increase in the NTO nanofibers developed at higher T (Sangaletti et al. 2006). In addition, the least M_r at T = 773 K or the slight decrease in M_r from T = 973 K to T = 1173 K can be attributed also to the existence of uncompensated spin from surface of nanoparticle and spin canting effect due to the morphological change in the material (Varga et al. 2015b; Kumar et al. 2018). These phenomena also suggest a weak FM response in the material, which leads to decrease in H_c for T = 773 K and 1173 K as seen from Table 5.1. The variation in M_s is attributed to super-exchange interactions, crystallinity, particle size and surface AFM oxidation (Umeshbabu et al. 2015). First, the super-exchange d-d interactions between the neighboring atoms may be responsible for the relatively higher values of M_s in case of NTO nanofibers developed at T = 773 K (lattice parameters are the least in this material, Table 3.1, Section 3.1.2.3). These nanofibers also have the maximum concentration of the SNTO phase (Table 3.2), in which the Ni-Ni inter-

cationic distance is the closest, favoring the super-exchange *d-d* interactions (Bahadur et al. 2012; Vranješ et al. 2014). Thus, NTO nanofibers developed at T = 773 K possess higher values of M_s. Furthermore, at lower θ_T when distance between cations is less, the spins are repelled, and orient themselves in an antiparallel fashion. This results in increase in number of uncompensated spins in the shell (core-shell model) of nanoparticles, which breaks their AFM interaction in the core spin causing spin disorder in material (Yuvaraj et al. 2013). Hence, higher value of M_s (Fig. 5.2c) and magnetization (Fig. 5.4, Section 5.1.3) is observed for the lease T or θ_T.

In summary, the variation in the magnetic parameters in NTO nanofibers can be understood by a combination of the following effects: (i) exchange interaction between cationic (Ni and Ti) atoms within the SNTO and INTO crystal/crystallite, (ii) ordering of the SNTO and INTO crystallites having exchange interaction within the nanoparticle, and (iii) long-range ordering of nanoparticles having exchange interaction along the NTO nanofiber.

The S, SFD, and K were calculated and are tabulated in Table 5.2 for θ_T = 300 K, using the following relations (McHenry et al. 1995; Sontu et al. 2015):

$$S = \frac{M_r}{M_s},$$
(5.1)

where M_s is the saturation magnetization obtained from the hysteresis loop,

$$SFD = \frac{\Delta H}{H_c},$$
(5.2)

where ΔH is the FWHM of the curve $\frac{dM}{dH}$, and

$$K = \frac{\mu_0 H_c M_s}{2},$$
(5.3)

where μ_0 is the permeability constant. Figure 5.3 shows the change in S, SFD, and K as a function of morphological change in NTO nanofibers (*viz.*, T). The NTO nanofibers with the least crystallite/particle size, and the highest porosity (refer Chapter

3) with mosaic structure (T = 773 K) exhibits the least S and K, but the highest SFD. On the contrary, the large crystallite/particle sized NTO nanofibers with similar mosaic structure (T = 973 K) have much higher S and K, and the least SFD. The values of S and K again reduce, while the SFD increases (Fig. 5.3), when the crystallite/particle size increase further in the bamboo structured NTO nanofibers (T = 1173 K) having the less porosity.
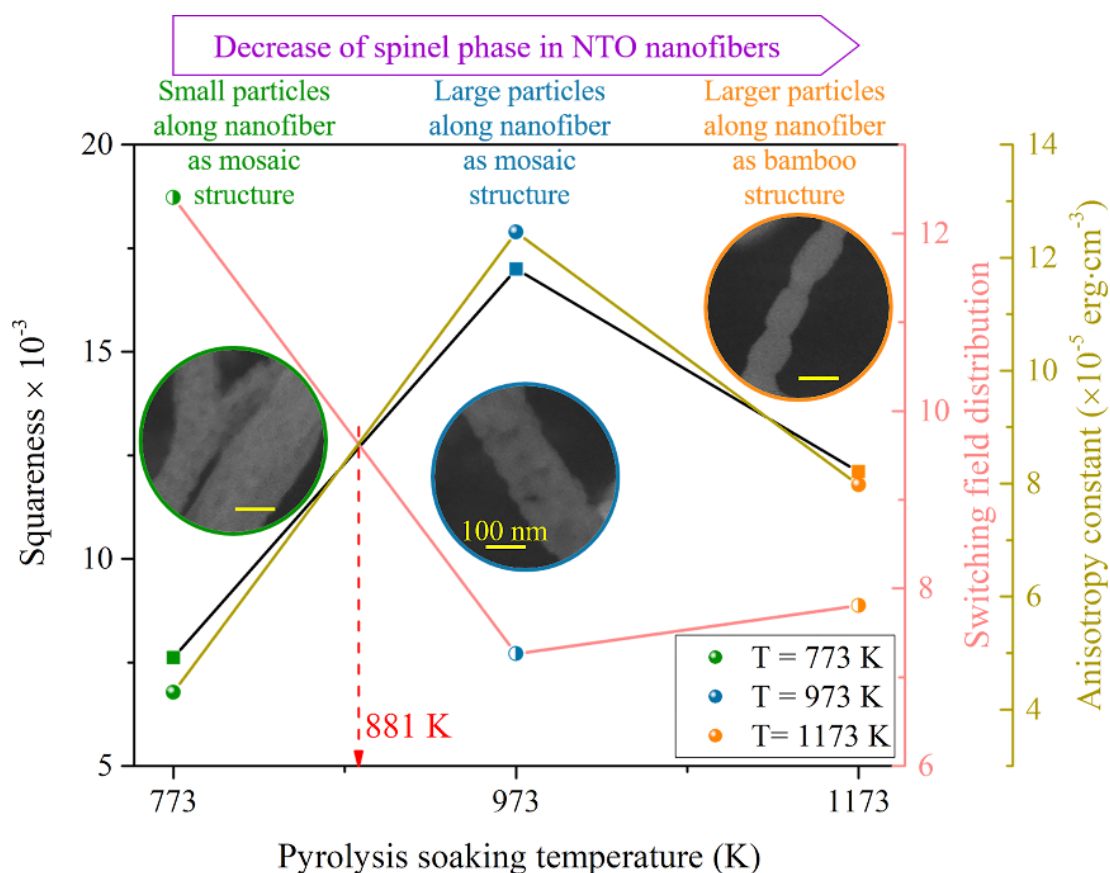
Fig. 5.3 Morphology-magnetic property correlation of NTO nanofibers developed at T = 773, 973, and 1173 K.

5.1.3 Non-isothermal VSM analysis

Figure 5.4 represents the ZFC-FC plots recorded for H of 500 G for the NTO nanofibers developed at different T. The secondary y-axis in Figure 5.4 is the FC derived χ^{-1} plotted against θ_T. The ZFC-FC plot suggests that both the T_B (magnetization maxima of ZFC mode) and T_N (θ_T above which AFM to paramagnetic transition of the material occurs) lies below 20 K. It was reported earlier that T_N shifts

to lower value (14.9 K) when the D of NTO was decreased from bulk (~ 23 K) (Yuvaraj et al. 2013). The influence of off-stoichiometry of NTO on the T_N was reported in literature and it linearly increases with increase in Ni content, which leads to stronger AFM ordering (Varga et al. 2015b). This suggests the higher T_N value for nanofibers developed at T = 773 K, which is rich in SNTO. It has to be noted that the bigger the particle, the higher the T_B (Typek et al. 2016). It is also observed that the magnetization is highest for NTO nanofibers obtained at T = 773 K. This can be attributed to the uncompensated FM layers of INTO on the surface of the nanoparticles or the super-exchange d-d interactions as explained earlier.
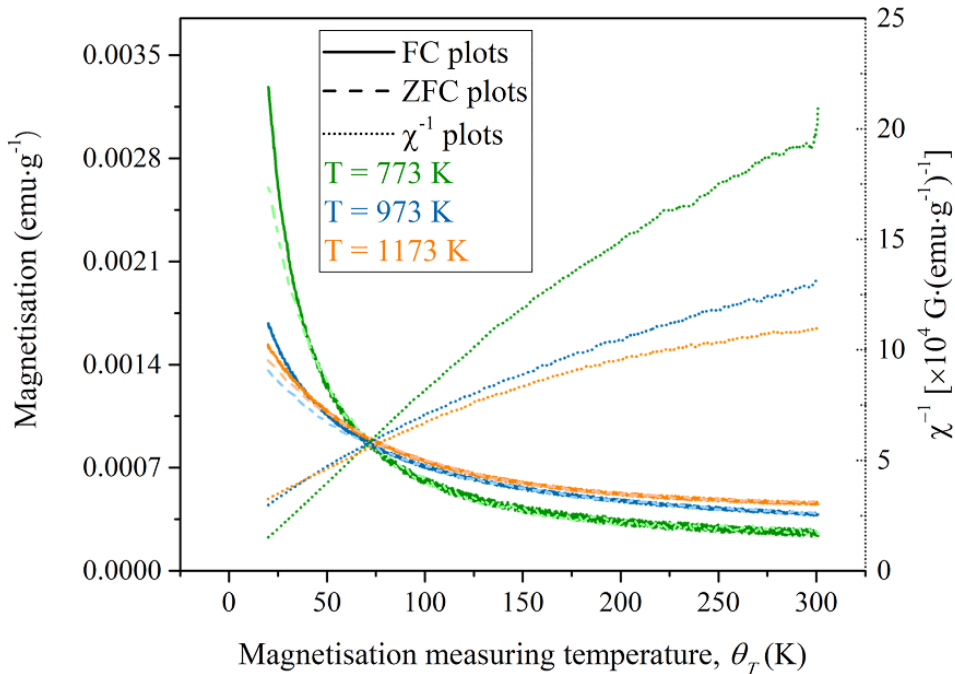
Fig. 5.4 ZFC-FC and χ^{-1} plots of NTO nanofibers developed at T = 773, 973, and 1173 K.

The overall pattern of the θ_T dependence of χ^{-1} pictured in Figure 5.4 suggests the existence of magnetic ordering in the NTO nanofibers. Further, it was reported in earlier literature that the INTO/NiO nanoparticles had no appreciable ZFC-FC splitting in magnetization at H = 500 G in the range of θ_T = 10 to 300 K (Modak et al. 2018). However, below 50 K a bifurcation in ZFC-FC curve was observed even though there was no difference above 50 K. The bifurcation of FC and ZFC below 50 K originates from the pores in the NTO nanofiber. The disorder and frustration in porous

nanomaterial lead to disruption in magnetic coupling and a state of dilute magnet emerges in the nanoparticles embedded in pores (Lee et al. 2013b), as in the NTO nanofibers here. The negative intercept in the θ_T-axis indicates the presence of AFM coupling in the study material (Yuvaraj et al. 2013; Typek et al. 2016). The θ_w and hence the AFM coupling is larger in NTO nanofibers developed at higher T.

The behavior of χ^{-1} vs. θ_T may be analyzed in the light of the Curie-Weiss law, *i.e.*,

$$\chi^{-1} = \left(\frac{1}{C}\right)\theta_T - \left(\frac{\theta_w}{C}\right), \tag{5.4}$$

where C and θ_w are Curie constant and Weiss temperature, respectively. The Curie-Weiss plot in Figure 5.4 suggests that a linear extrapolation of the curves of T = 773, 973 and 1173 K to χ^{-1} = 0 will meet the θ_T-axis on its negative side indicating an effective AFM interaction (Typek et al. 2016; Modak et al. 2018). Furthermore, the nonlinear behavior of χ^{-1} vs. θ_T in this regime suggests that material at these temperatures consists of paramagnetic moments too. It is worth noting that the AFM interaction weakens with increasing T. The linear fit as per the Curie-Weiss law also helps in extracting the C from the inverse of the slope and the θ_w from the y-intercept. The extracted values are tabulated in Table 5.2. It has to be noted that C is expressed in units of emu·K·(G·g)$^{-1}$ as the density of the composite material is not accurately known. The negative sign of θ_w indicates that magnetic interaction should be AFM (Yuvaraj et al. 2013). The C_m and θ_w for the single crystal INTO have been measured previously in the literature as 2 emu·K·mol^{-1} and -58 K, respectively at θ_T in the range of 4.2 to 300 K and H of 2.85 kG, when synthesized by floating zone method (Watanabe et al. 1980). Along similar lines, the polycrystalline INTO prepared by respective melts (Van Uitert et al. 1964), precipitation-decomposition-sintered-quenching (Harada et al. 2016), solid solution-annealing (Stickler et al. 1967), and simple molten salt (Yuvaraj et al. 2013) techniques showed a θ_w of -36 K (θ_T = 1.4-300 K, H = 15.3 kG), -14 K (θ_T = 250-380 K, H = 1 kG), -13 K (C_m = 1.26

emu·K·mol^{-1}, θ_T = 4.2-300 K, H = 7320 G), and -6.2 K (C_m = 2.76 emu·K·mol^{-1}, D ~70 nm, θ_T = 2-300 K, H = 10 kG), respectively. These values of θ_w are comparable with the θ_w = -20.6 K (θ_T = 20-300 K, H = 500 G) obtained for sample T = 773 K in the present study. In sharp contrast, values of θ_w around -170 K and -200 K, based on experimental and theoretical work have also been reported in literature (Fennie 2008; Varga et al. 2013). These are close to the θ_w obtained values in the present study for the sample with T = 973 K and 1173 K. The considerable variation in θ_w can be attributed to the morphological change and exchange coupling of FM-AFM domains in NTO nanofibers. Further investigation is required with measurements below θ_T = 20 K to understand the FM and AFM transition kinetics of the composite NTO nanofibers.

5.2 SUMMARY AND CONCLUSIONS

In conclusion, it is noted that the FM-AFM exchange coupling between SNTO and INTO has a vital role in tailoring the magnetic properties of NTO composite nanofibers due to the presence of electronic structural defects. The peculiar morphology of nanoparticles/nanofibers in the NTO composite nanofibers contribute to the shape anisotropy and surface irregularities, which influence the magnetic parameters. Apart from the morphology, the relative concentration of SNTO/INTO phases, porosity, and the long-range ordering in the FM-AFM exchange coupling (also function of T) along the NTO nanofibers also determine the magnetic behavior of the material. Due to the semiconducting nature of NTO in presence of defects and weak FM at room temperature, SNTO/INTO composite nanofibers could find potential uses in soft magnets, magnetic sensors, and in advanced devices such as multiferroics and spintronics.

PART TWO

ELECTROSPUN NICKEL COBALTITE NANOFIBERS

CHAPTER 6

CHAPTER 6

SYNERGISM OF FICTITIOUS FORCES ON NICKEL COBALTITE NANOFIBERS: ELECTROSPINNING FORCES REVISITED
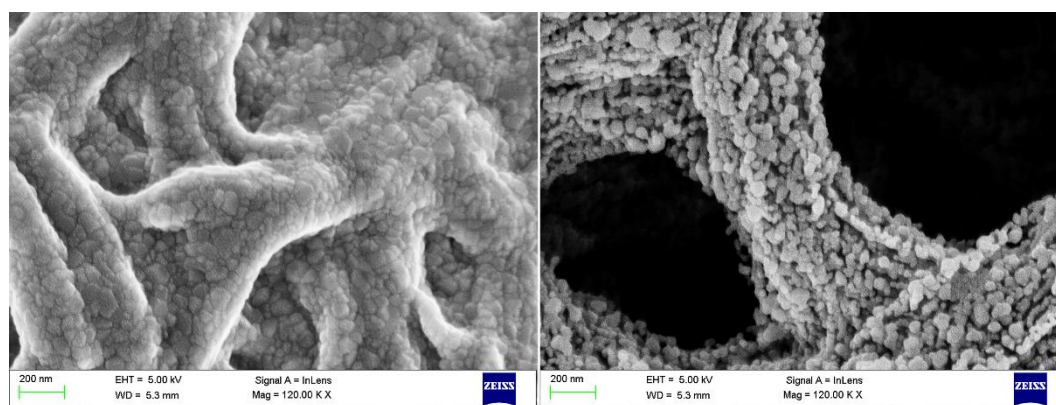
Nickel cobaltite nanofibers obtained using rotating drum collector

Nickel cobaltite nanofibers obtained using rotating disc collector

Scheme 6.1 Morphological changes observed by modifying relevant electrospinning forces.

In this chapter, the randomly oriented nanofibers of NCO were fabricated using sol-gel electrospinning followed by pyrolysis. The precursor fibers were collected on RDI and RDR collectors. Variable fictitious forces produce continuous deflection at each fiber landing position on the RDI collector, which subjects the nanofibers to non-bundling. On the other hand, in the case of the RDR collector, the fictitious forces act just at the surface, and these forces merely cause slip of the fibers along the rotational axis of the RDR. This slip along with the retained Columbic charges on the surface of the fibers produces fiber bundling, which affects the morphological and structural properties of the NCO nanofibers obtained by pyrolyzing the precursor fibers. The use of the RDI collector in sol-gel electrospinning is a simple and optimal method of fabricating precursor nanofibers, which yields non-agglomerated and impurity-free inorganic nanofibers.

6.1 RESULTS AND DISCUSSION

6.1.1 SEM micrographs

6.1.1.1 Precursor nanofibers
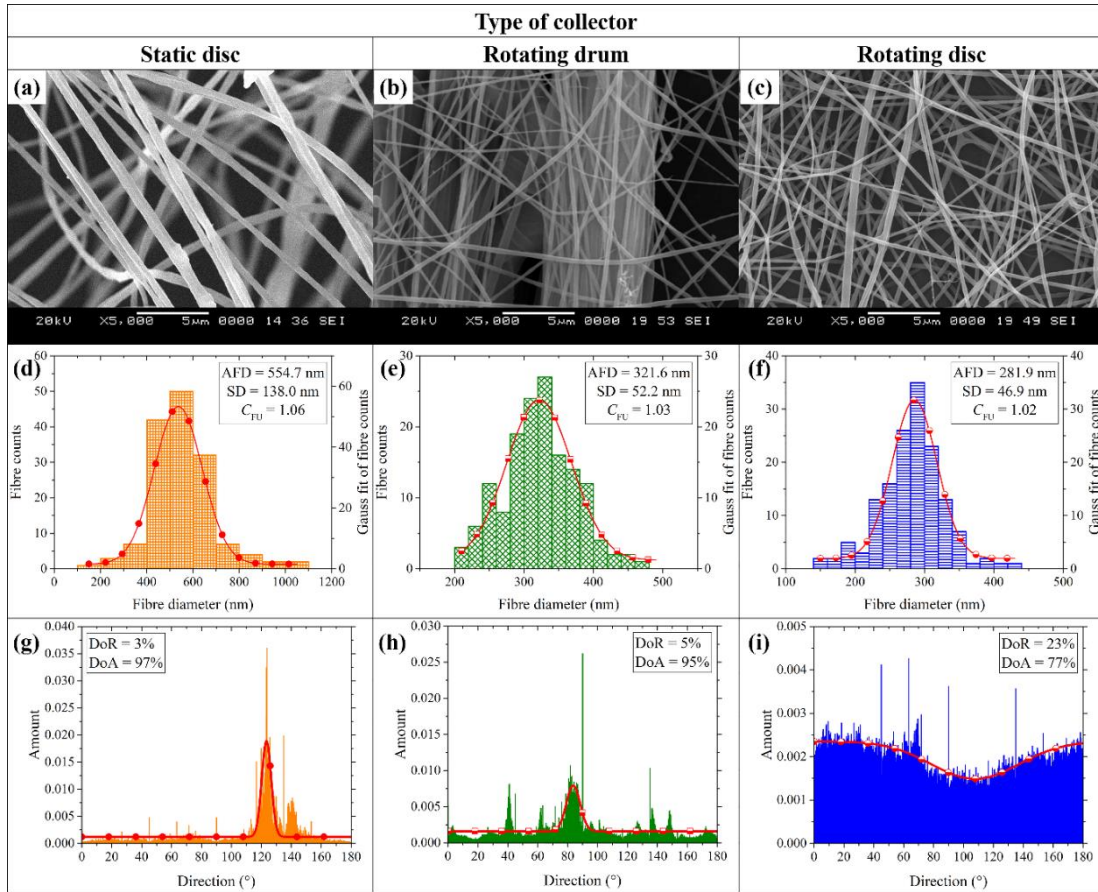
Fig. 6.1 SEM micrographs of the precursor nanofibers fabricated using three different types of collectors, and the corresponding histograms inferring AFD±SD, C_{FU}, DoR, and DoA; for three different types of collectors.

The diameter and alignment of the precursor nanofibers are affected by the electrostatic interactions of the surface cations on the fiber during whipping, and the mechanical drawing of the fiber by the collector. Accordingly, from Figure 6.1, the AFD and SD of the precursor nanofibers are observed to be the least for the RDI collector. Conversely, the larger AFD and SD values of the fibers from the static collector are due to the role of the mechanical drawing process of the rotating collectors (Fig. 6.1a and d). However, the alignment of nanofibers in the static collector is a result of fiber bundling during spinning due to the increase in conductivity of the sol. This causes an

insufficient stretching of nanofibers during whipping, resulting in high values of SD and C_{FU} in the static collector, which indicates non-uniformity in the fiber diameter. Hence, the precursor fibers obtained using the static collector exhibit a high degree of fiber alignment. From Figure 6.1g and h, it was observed that the DoA of RDR_p was less in comparison with that of the static collector. This could be due to the slip caused during the winding of fibers onto the surface of the RDR collector, which is also evident from the SD and C_{FU} of the fibers. Further, the DoA, AFD, SD, and C_{FU} of fibers spun on the RDI were found to be the least (Fig. 6.1f and i), which are the essential parameters to form non-agglomerated, ultrathin pyrolyzed fibers. The least DoA and high DoR in RDI_p were presumably due to the action of fictitious forces, which are discussed in detail in Section 6.1.4.

6.1.1.2 Pyrolyzed nanofibers

Figure 6.2a and b show the electron micrographs of pyrolyzed nanofibers obtained from the RDR and RDI collectors. The pyrolyzed fibers obtained from the RDR collected fibers were found to have larger AFD and SD values than their precursor fibers (Fig. 6.1e) due to the acute agglomeration of well-aligned adjacent nanofibers. This in turn increases the C_{FU} (Fig. 6.2c), and thus decreases the fiber uniformity. However, in the case of the RDI collector, the DoR of fibers increased up to 14% due to the thermally induced wrinkling of agglomerated fibers during the pyrolysis as the precursor fibers shrink, liberating organic volatiles. From Figure 6.2d, the AFD and SD of the RDI_c nanofibers were found to be lower than their RDI_p. This observation implies that the fibers did not agglomerate much and retained their morphology even after pyrolysis. However, the increase in C_{FU} of the RDI_c nanofibers suggests the unavoidable agglomeration and segregation (by diffusion) during the pyrolysis, which are significantly less compared to that of the RDR_c nanofibers. Here, an increase in DoR of about 11% was calculated, which is due to the thermally induced fiber wrinkling; this might be due to the increased intersection of nanofibers deposited on the RDI collector. The randomly oriented fibers tend to have a large number of intersections with other fibers as compared to the aligned ones (Fig. 6.1b and c), which could constrain the wrinkling of precursor nanofibers during the pyrolysis. Hence, the pyrolyzed nanofibers obtained using the RDI collector have the smallest AFD and SD,

and comparatively better fiber uniformity. This plays a significant role in the structural and functional properties of the inorganic nano-fibrous material.
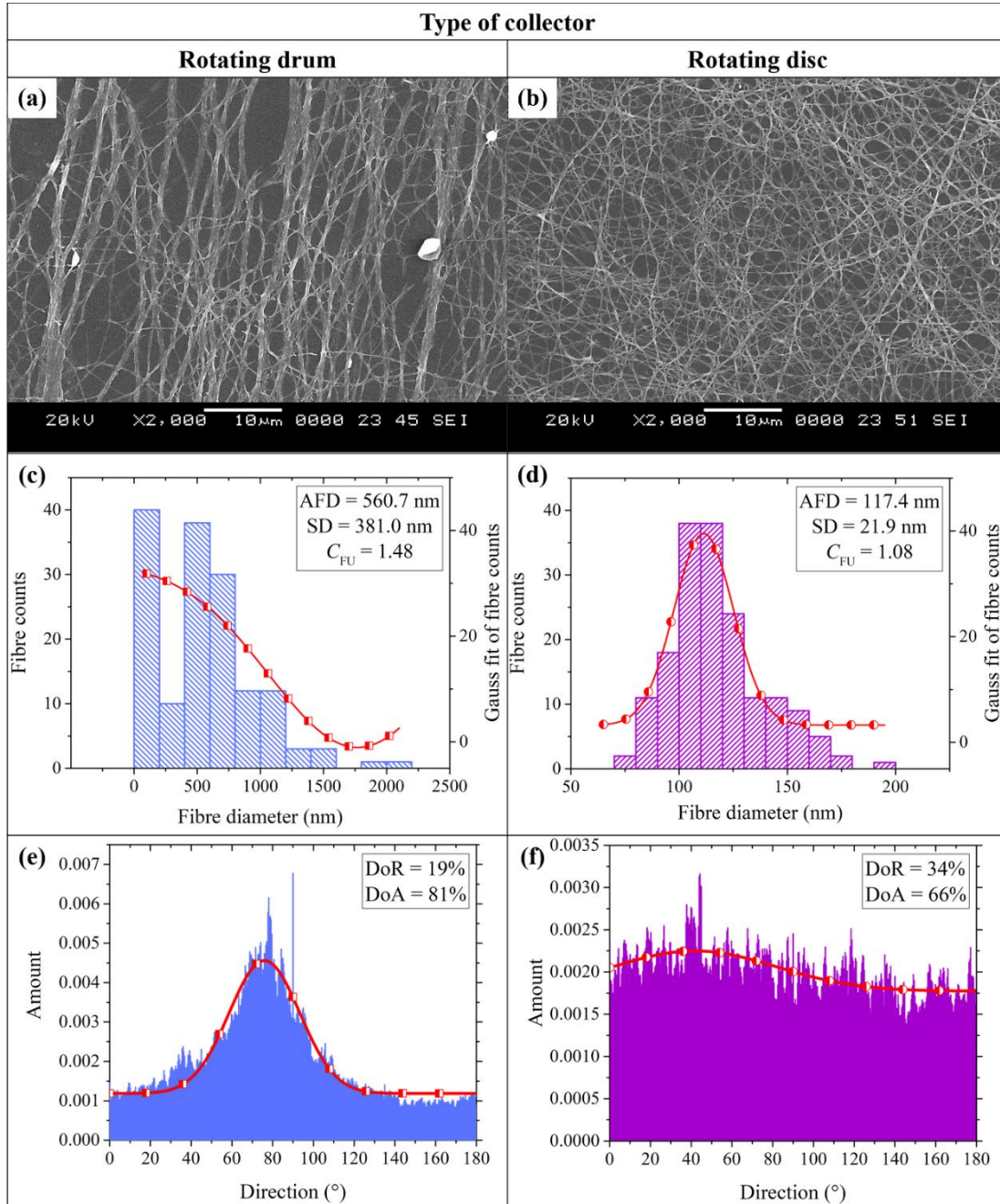
Fig. 6.2 SEM micrographs of RDR$_c$ and RDI$_c$ nanofibers, and the corresponding histograms inferring AFD±SD, C_{FU}, DoR, and DoA.

The SSA values of the RDR$_c$ and RDI$_c$ nanofibers are tabulated in Table 6.1. The increase in the surface area of the RDI$_c$ nanofibers is attributed to the reduction in

their AFD and porous morphology due to the NCO nanoparticles embedded along the nanofibers. These values are comparable with the NCO based nanofibers/nanobelts reported hitherto in the literature (Li et al. 2013b; Huang et al. 2016). The improved SSA of the RDI_c nanofibers is expected to improve their functional properties such as electrocatalytic performance.

Table 6.1: SSA and crystallite parameters of RDR_c and RDI_c nanofibers.

Type of collector	SSA $(m^2 \cdot g^{-1})$	Phase	Scherrer equation	Williamson-Hall plot	
			Crystallite size, D (nm)	Crystallite size, D (nm)	Microstrain, ε (%)
RDR	10.1	NCO	13.44	18.29	0.184
		$NiCoO_2$	15.12	15.89	0.024
RDI	24.0	NCO	12.65	18.34	0.222

6.1.2 FESEM analysis

High-resolution FESEM micrographs of the inorganic nanofibers (Fig. 6.3) were examined to observe the nanoparticle morphology along the pyrolyzed nanofibers obtained using both the RDR and RDI collectors. In the case of the RDR_c nanofibers, the nanoparticles are densely packed and agglomerated, leading to less macro porosity. However, the RDI_c nanofibers have a highly porous structure with well-distinguished near-spherical nanoparticles, decorated similar to a cephalopod limb along the fiber. This could make the RDI_c nanofibers a potential candidate for catalytic applications. Furthermore, the morphological changes observed in the RDR_c and RDI_c nanofibers are functions of the fictitious forces acting on their respective precursor fibers, which form a subset of the electrospinning process parameters. This suggests that the use of the RDI collector might be extended to metal oxide nanofibers of other transition metals as well.
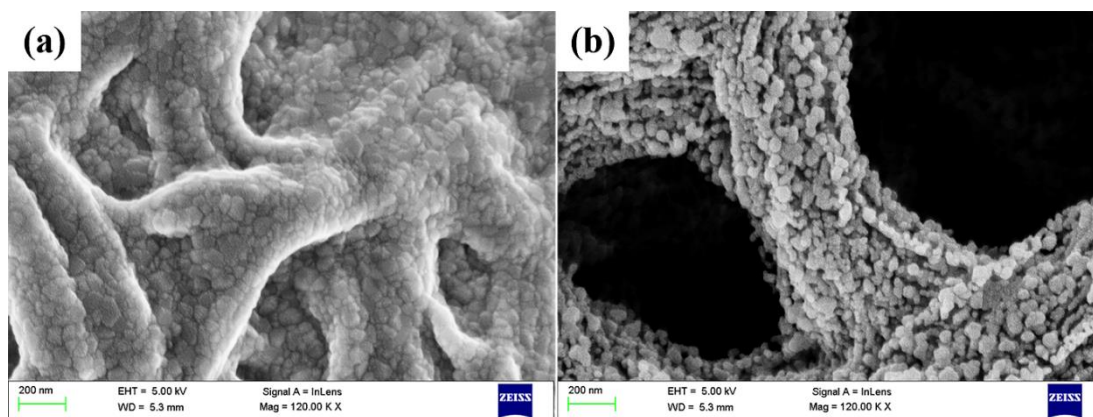
Fig. 6.3 High-resolution FESEM micrographs of RDR$_c$ and RDI$_c$ nanofibers, showing NCO nanoparticles embedded along the nanofibers.

6.1.3 Structural characterization of the inorganic nanofibers

6.1.3.1 XRD analysis
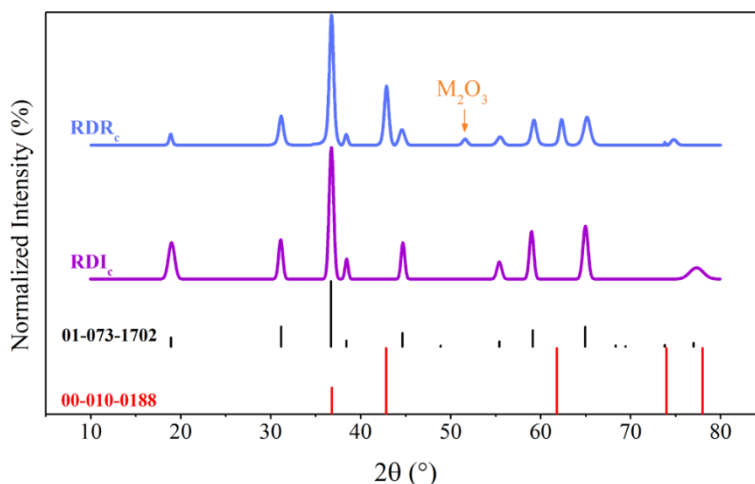
Fig. 6.4 XRD patterns of RDR$_c$ and RDI$_c$ nanofibers, with ICDD reference patterns of NCO (01-073-1702) and NiCoO$_2$ (00-010-0188).

In Figure 6.4, XRD patterns obtained for both the RDR$_c$ and RDI$_c$ nanofibers revealed the presence of crystalline NCO indexed to the ICDD file no. 00-073-1702. In the case of the RDR$_c$ nanofibers, the presence of crystalline NiCoO$_2$ was observed, which matches with the ICDD file no. 01-010-0188. Further, the presence of an additional peak at ~51.5° with some coinciding peaks of NCO hints at the formation of crystalline M$_2$O$_3$ in the RDR$_c$ nanofibers. The cation M represents both Ni (ICDD file no. 00-014-

0481) and Co (ICDD file no. 00-002-0770) ions. The formation of $NiCoO_2$ and M_2O_3 may be attributed to a two-stage redox reaction.

When the fibers agglomerate in the RDR_p nanofibers during pyrolysis, the sub-products are probably entrapped within the fiber along with NCO particles to a greater extent. At this stage, *carbothermal/NO$_x$ reduction* of NCO takes place in the presence of by-products of the precursor to form $NiCoO_2$, Ni^0, and Co^0 (Nissinen et al. 2003; Reddy et al. 2014; Wang et al. 2015a; Alegre et al. 2017; Zhang et al. 2017b). Subsequently, Ni^0 and Co^0, in the presence of excess oxygen due to the entrapment of oxygen bearing groups like acetate from the precursor, give Ni_2O_3 and Co_2O_3. Hence, the overall redox reaction can be written as:

$$3NiCo_2O_4 \xrightarrow{\Delta/O_2/C/CO/NO_x} NiCoO_2 + Ni_2O_3 + Co_2O_3 + CO_y + NO_z \tag{6.1}$$
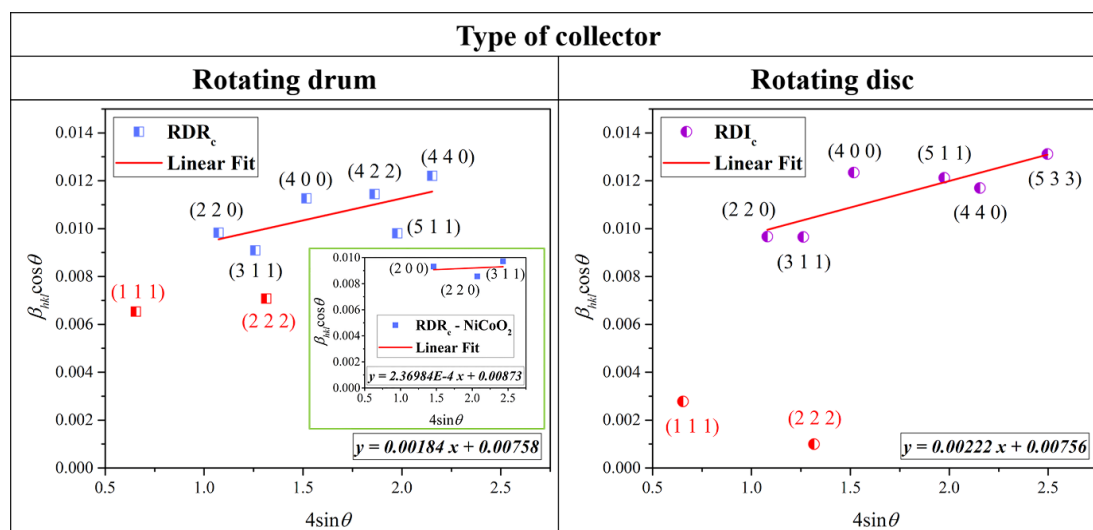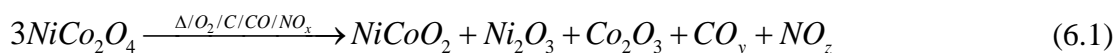
Fig. 6.5 Williamson-Hall plot of RDR_c and RDI_c nanofibers for the NCO peaks. Inset figure: Williamson-Hall plot for the $NiCoO_2$ peaks.

The Scherrer equation and the Williamson-Hall plot (Fig. 6.5) were used to measure the crystallite size (D) and microstrain (ε) in both the RDR_c and RDI_c nanofibers, and the values are tabulated in Table 6.1. The Scherrer equation does not account for the thermally induced microstrain in the crystal lattice and hence, the Williamson-Hall plot is more appropriate for finding the crystallite size. It was observed that there is no significant change in the crystallite size of NCO in both the RDR_c and RDI_c nanofibers. However, the lattice strain is marginally higher in the RDI_c than RDR_c

nanofibers. In comparison, the NiCoO₂ lattice has almost no strain. This suggests the formation of NiCoO₂ from NCO crystals. Also, it is a well-known fact that nanostructures have more lattice strains due to defects. Since RDI$_c$ has an overwhelming population of well-defined NCO particles in comparison with that of the RDR$_c$ nanofibers, the crystallites in the former could be under high lattice strain.

6.1.3.2 Raman analysis
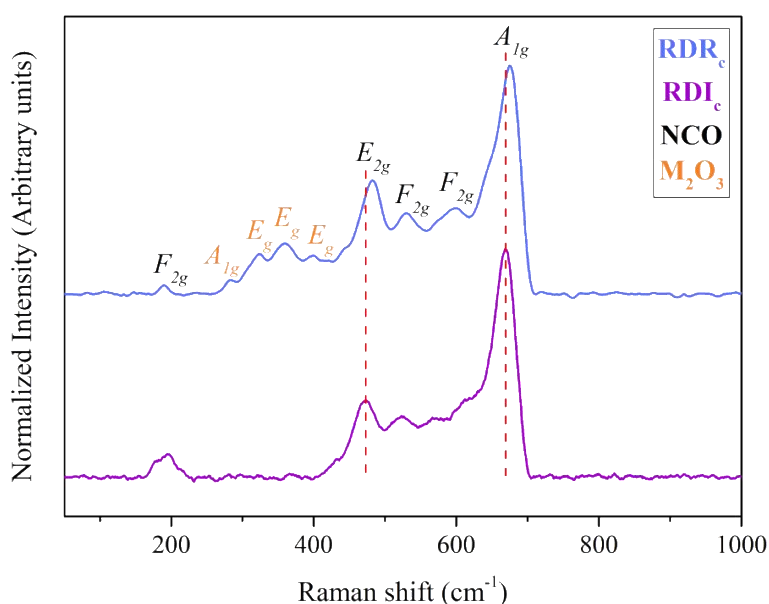
Fig. 6.6 Raman spectra of RDR$_c$ and RDI$_c$ nanofibers.

To understand the presence of the non-crystalline phase of oxides in the pyrolyzed nanofibers, Raman spectra were obtained for both the RDR$_c$ and RDI$_c$ NCO nanofibers (Fig. 6.6). Five Raman active modes ($A_{1g} + E_{2g} + 3 F_{2g}$) were observed for both the RDR$_c$ and RDI$_c$ nanofibers, confirming the crystalline phase of NCO (Venkatachalam et al. 2017). A broad shoulder peak was observed at ~650 cm⁻¹, which suggests the formation of the amorphous phase of NCO (Gouadec and Colomban 2007). It has been reported that a broad peak at ~530 cm⁻¹ is a distinct characteristic feature of NiCoO₂ in the literature (Leng et al. 2016). However, this peak coincides with the F_{2g} peak of NCO and remains indistinguishable. Further, in the case of the RDR$_c$ nanofibers, four broad peaks in the range of 250-400 cm⁻¹ were observed. These peaks also appear in the Raman spectra of M₂O₃ structures such as Cr₂O₃ and Fe₂O₃, as per the literature (Beattie and Gilson 1970; Shim et al. 2004). As no specific study on the Raman spectra

of Ni_2O_3 and Co_2O_3 is available, and, since the Raman signature is a structural property of the material, thus ascribe the observed Raman peaks to Ni_2O_3 and Co_2O_3 formed in the RDR_c nanofibers.

It has been observed in the literature that nanocrystallites confine optical phonons within them, if the surrounding medium (amorphous phases) of nanoparticles does not support the vibrational wave numbers in the material. As the nanoparticle size reduces, the amorphous phase increases (as there is an increase in crystallite boundary area) and the electron-phonon interaction decreases, leading to broadening and shifting of the peaks. Hence, the vibrational spectrum of the nanoparticles deviates from that of their bulk counterparts. Raman spectroscopic investigations of such nanoparticles (typically less than 10 nm) have revealed such shifts in the Raman peaks along with asymmetric broadening (K. Arora et al. 2007). From Figure 6.6, it is evident that the peaks of NCO ($A_{1g} + E_{2g} + 3F_{2g}$) have not only shifted, but also, asymmetric broadening is observed for all the F_{2g} peaks. This suggests that the RDI_c nanofibers are made of pure NCO nanoparticles of higher porosity and smaller size when compared with the RDR_c nanofibers.

6.1.4 Mechanism of fiber morphology evolution

From the SEM micrographs (Fig. 6.1c and e), it was observed that a larger DoR in the fiber orientation has been generated for RDI_p even though the speed of rotation of both the collectors was fixed at 500 rpm. All the synthesis parameters were kept constant for both the RDI_p and RDI_p nanofibers. The variation in the randomness of fiber orientation and AFD in both the RDR and RDI collectors can be explained in the light of physical forces governing the motion of the jet.

6.1.4.1 Effect of time of flight of the fiber

The velocity of a fiber (v) arriving at the collector can be calculated using the following equation (Wang et al. 2006b):

$$t_f = \left(\frac{4w}{100\pi\rho v} \right) \times \frac{1}{d_{AFD}^2}, \tag{6.2}$$

where w is the weight, ρ is the density, and d_{AFD} is the AFD. The time t_f represents the time of flight of the fiber to reach the collector. Now, considering the equivalent fibers landing at the two different collectors, the time of flight of a fiber landing on the RDI collector is more than that taken by a fiber depositing on the RDR collector as the AFD is less for the former, as calculated earlier from the SEM micrographs (Fig. 6.1b and c). This suggests that the increase in the time of flight of a fiber increases the drawing process of the fiber due to Columbic forces during whipping before it reaches the collector. Hence, fibers are wound faster along the RDR collector without much drawing effect as they enter the collector parallel to the axis of whipping (Fig. 2.4 and 6.7a). On the other hand, in the RDI collector, the fibers are pulled in the direction of whipping, which provides more scope for fiber drawing; which, in turn, produces fibers with lower AFD values.
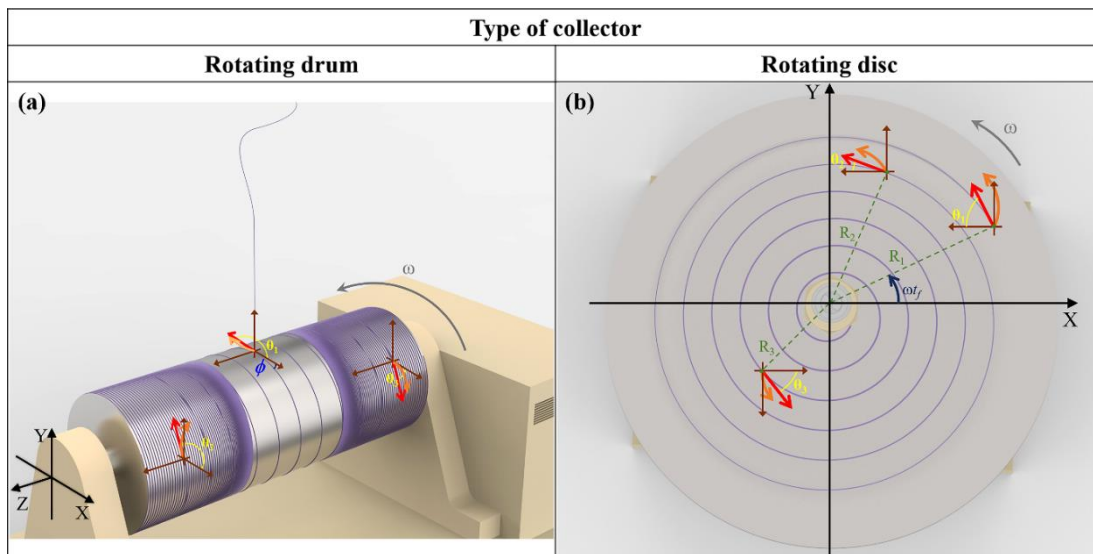
Fig. 6.7 Fictitious force body diagram at time of fiber element landing on (a) RDR and (b) RDI collectors, at different positions. Coriolis deflection makes the fiber take a curved path at each position (orange color).

6.1.4.2 Synergism of fictitious forces on the fiber

Using a rotating frame of reference for the coordinate system, the governing equations of the system may be described by the continuity equation (Padron et al. 2011; Wan et al. 2011):

$$\nabla \cdot u = 0 , \tag{6.3}$$

where u is the relative velocity of the fiber jet per unit mass at the collector position (say, R) and the relevant momentum balance equation may be written as:

$$\frac{\partial u}{\partial t_f} + (u \cdot \nabla)u = -\frac{\nabla P}{\rho} + \frac{\nabla T}{\rho} + E(q) + \Gamma(\varphi) + g - \Omega \times (\Omega \times R) - 2\Omega \times u \,, \tag{6.4}$$

where P is the pressure, ρ is the density of the fiber material, T is the stress tensor, E is the applied electric field, which is a function of Columbic charge (q) in the nanofiber, Γ is the ambient environment, which is a function relative humidity (φ), g is the gravity effect, Ω is the angular velocity of the collector and R is the position vector describing the fiber position on collector. For both the RDR and RDI collectors, the first five terms on the right-hand side of Equation 6.4 remain the same and thus, the last two terms additionally affect the acceleration of the fiber on the collector.

The centrifugal acceleration term, $-\Omega \times (\Omega \times R)$, arises due to the rotation of the collector; and the Coriolis acceleration $(-2\Omega \times u)$ arises due to the non-inertial frame of reference as the fiber rotates on its own axis relative to the collector rotation. The angular velocity vector, Ω, is pointed along the axis of rotation of the collector using the *right-hand rule* (Fig. 6.7a and b) and its magnitude is given by:

$$|\Omega| = \frac{\mathrm{d}\theta}{\mathrm{d}t_f} = \omega(t_f) \,, \tag{6.5}$$

where θ is the angle made by the trajectory in the inertial frame of reference (local frame) of the fiber element. This trajectory is a straight line along the tangential path of fiber rotation. The position of the fiber element in (X,Y) coordinates for a given time of flight, t_f, is given by:

$$R_i(t_f) = vt_f(\cos\theta, \sin\theta) \,, \tag{6.6}$$

where v is the actual velocity of the fiber element. Now in collector frame of reference, the XY axes rotate with an angular velocity of ω, so the trajectory is a non-linear curved path and expressed as:

$$R(t_f) = vt_f(\cos(\theta - \omega t_f), \sin(\theta - \omega t_f)) \tag{6.7}$$

Equation 6.7 represents the deflection of the fiber element from its actual position on the collector. This deflection is a function of time of flight, position and velocity of the fiber element. Hence, with different combinations of R, θ, and t_f, a wide range of various deflected trajectories are created along the variable radius of RDI. This wide range of deflected trajectories creates more randomness in the nanofibers collected on the RDI collector.

Furthermore, from Equation 6.7, for a given position (R, θ) and velocity (v), the deflection experienced by the fiber is directly proportional to the time of flight, t_f. In other words, with an increase in the time of flight of the fiber, the deflection of the fiber path on the collector is increased. And this helps in further drawing of the fiber before it lands on the collector, which in turn leads to a decrease in AFD. This is in agreement with the observation drawn from Section 6.1.4.1.

Using Equations 6.5 and 6.7, the centrifugal acceleration on the nanofiber can be expressed as (New World Encyclopedia contributors 2017) :

$$-\Omega \times (\Omega \times R) = \omega^2 vt_f \left[\cos(\theta - \omega t_f), \sin(\theta - \omega t_f)\right] = \omega^2 R(t_f) \tag{6.8}$$

and the *Coriolis* acceleration is expressed as follows:

$$-2(\Omega \times u) = 2\omega v \left[\sin(\theta - \omega t_f), -\cos(\theta - \omega t_f)\right] - 2\omega^2 R(t_f) \tag{6.9}$$

Comparing Equations 6.8 and 6.9, the Coriolis acceleration opposes the centrifugal acceleration, and the net effect has two components, namely, $-\omega^2 R(t_f)$ corresponding to the circular motion at $R(t_f)$ (inward component directed towards the center of rotation) and a perpendicular component $2\omega v \left[\sin(\theta - \omega t_f), -\cos(\theta - \omega t_f)\right]$ that is a function of the actual velocity of the fiber (v). Hence, the fiber in the RDI

collector experiences a circular motion with an additional velocity perpendicular to its actual velocity. This increased velocity, in turn, decreases the AFD of the fiber.

In the case of the RDR collector (Fig. 6.7b), the non-inertial frame of reference of the fiber rotates only about a fixed distance (R = radius of the drum) around the axis of rotation in the inertial frame XY. Hence, the Coriolis deflection of Equation 6.7 results in slip (wind-on angle, ϕ) of fibers during the winding of fiber on the rotating drum, and the constant Coriolis accelerations (as R is fixed for RDR) are tangential to the motion of the fiber, which creates a spiral path around the drum collector (Barr 1960; Wolf and Schwarz 1991). The mathematical formulations and the effect of this slip have been discussed elsewhere in the literature (Fraser et al. 1992; Xiang Ming Kong et al. 1999). The net effect is that it bundles up the fibers on the rotating drum to a large extent, and this effect will be greater with increasing speed of the rotation of the drum collector. Thus, the fictitious forces play a vital role in reducing the fiber orientation and fiber diameter of the nanofibers. In other words, these fictitious forces affect the morphology of the precursor nanofibers. This also helps in reducing agglomeration of inorganic nanofibers during pyrolysis to attain least AFD, defect-free, uniform, and porous inorganic nanofibers. Also, it helps in eliminating the formation of impurities due to phenomena such as phase separation.

6.2 SUMMARY AND CONCLUSIONS

RDI$_c$ fibers were uniform and less oriented with an AFD of ~117 nm. The fictitious forces played a remarkable role in the formation of high degree randomly oriented fibers (DoR = 34%) in case of the RDI collector, and the effect was revisited in detail. The proper choice of collector must be made depending on the desired morphology and properties of the inorganic nanofibers to be fabricated using sol-gel assisted electrospinning. Less agglomerated and impurity-free NCO nanofibers were obtained using the RDI collector, which had near-spherical NCO nanoparticles decorated along the nanofiber similar to the suckers of a cephalopod limb, with a high porosity. The physics discussed here may possibly be extrapolated to other metal oxide nanofibers of the first-row transition metals for tailoring their structural and functional properties.

CHAPTER 7

CHAPTER 7

A MECHANISTIC STUDY ON THE STRUCTURE FORMATION OF NICKEL COBALTITE NANOFIBERS DECORATED WITH IN SITU FORMED GRAPHENE-LIKE STRUCTURES
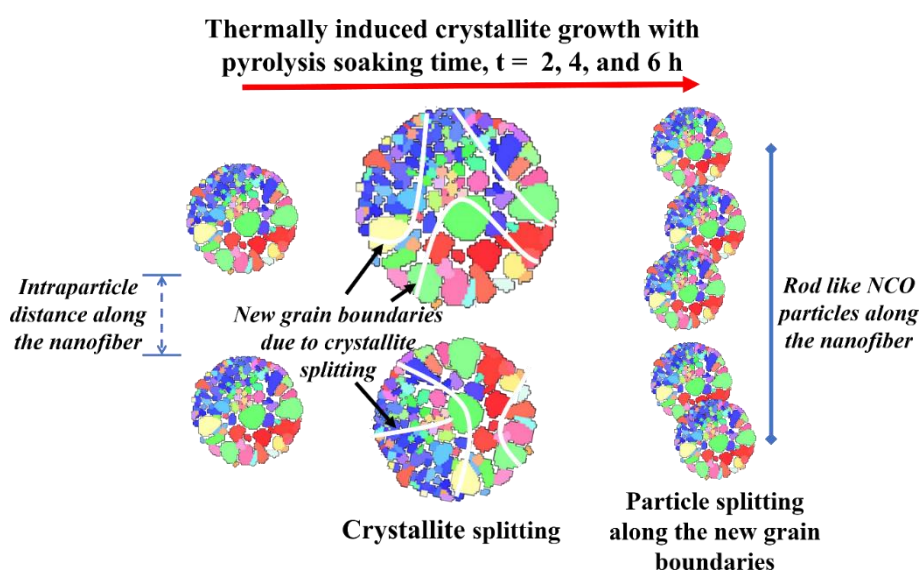
Scheme 7.1 Probable mechanism of crystallite and particle splitting in NCO nanofibers with increasing *t*.

In this chapter, the defect-free precursor nanofiber mats obtained from previous study (Chapter 6) were pyrolyzed at 773 K at three different t: 2, 4, and 6 h. The SAN present in the precursor nanofibers caused morphological changes in the NCO nanofibers during their thermochemical degradation. Consequently, fractal aggregates of NCO nanoparticles were formed along the length of the nanofibers. X-ray photoelectron spectroscopy (XPS) revealed both +2 and +3 oxidation states for Ni and Co, with spinel crystal defects due to oxygen rich atmosphere. XPS, high-resolution transmission microscopy, and optical analysis showed GL structures embedded within the NCO nanofibers. With increase in t, the morphology of the NCO particles markedly changed from spherical to rod-like. Thus, propose a mechanism for the morphological change of NCO nanoparticles on the basis of crystallite splitting accompanied by particle splitting and reordering.

7.1 RESULTS AND DISCUSSION

7.1.1 Characterization of precursor nanofibers

The optimal and uniform RDI$_p$ nanofibers, which were less oriented with an AFD of ~117 nm obtained from previous study (Chapter 6) were used in this study.

7.1.1.1 FTIR spectroscopy

The FTIR spectrum in Figure 7.1 corresponding to the SAN nanofibers is in good agreement with the earlier literature (Senthil et al. 2013). The interaction of precursor salts with the polar groups of the SAN (nitrile at 2239 cm^{-1} and aromatic ring of styrene at 1607 cm^{-1} and 1450 cm^{-1}) are represented by the reduction in peak intensity and peak broadening, respectively. Hence, a uniform sol-gel precursor nanofiber prevails. In other words, the precursor nanofiber is homogenous and this in turn yields uniform phase during pyrolysis. Further, the nucleation and growth of inorganic crystallites are dependent on thermal stability (function of functional groups) of the polymeric binder as they act as a structural and morphological supporting elements during pyrolysis (George and Anandhan 2015b; George et al. 2015).
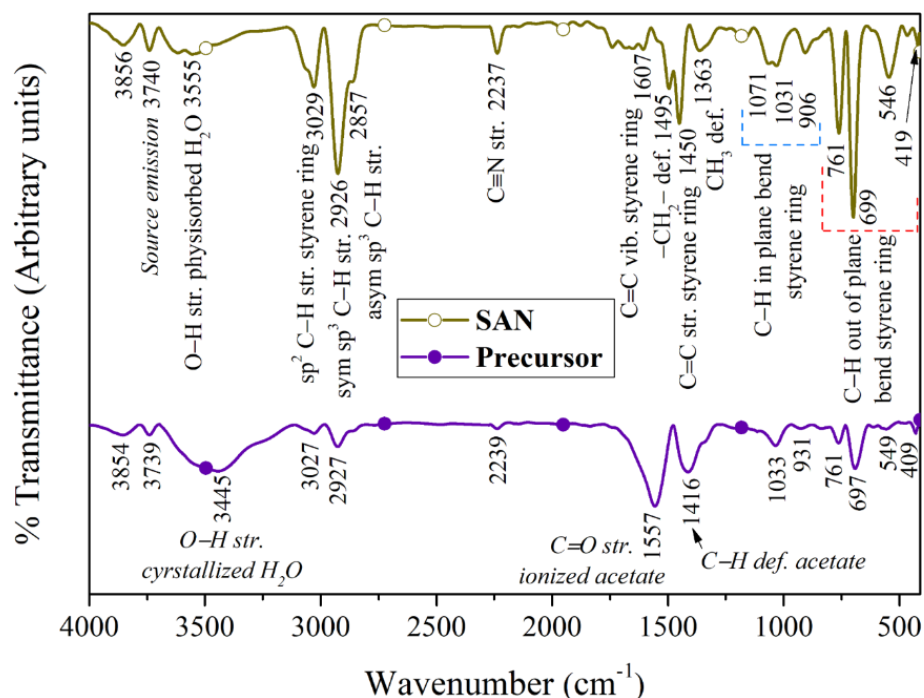
Fig. 7.1 FTIR spectra of SAN nanofibers and precursor nanofibers.

7.1.1.2 Thermal analysis

TGA plot of the polymeric binder SAN and precursor nanofibers are shown in Figure II.1 (Section II.1). It depicts the complete degradation of SAN in one step at 737 K, whereas the precursor undergoes multi-step degradation. The major weight loss of the precursor nanofibers occurs around 699 K due to the release of acetic acid, which accelerates the degradation of SAN, and causing it to occur at a lower temperature than that of pristine SAN nanofibers (George and Anandhan 2015b; George et al. 2015). There is also a secondary weight loss in the precursor nanofibers from 776 to 885 K, which may lead to residual carbon compounds having sp^2 hybridization, as in reduced graphene oxide (Yao et al. 2012). However, the exact form of carbon needs further investigation.
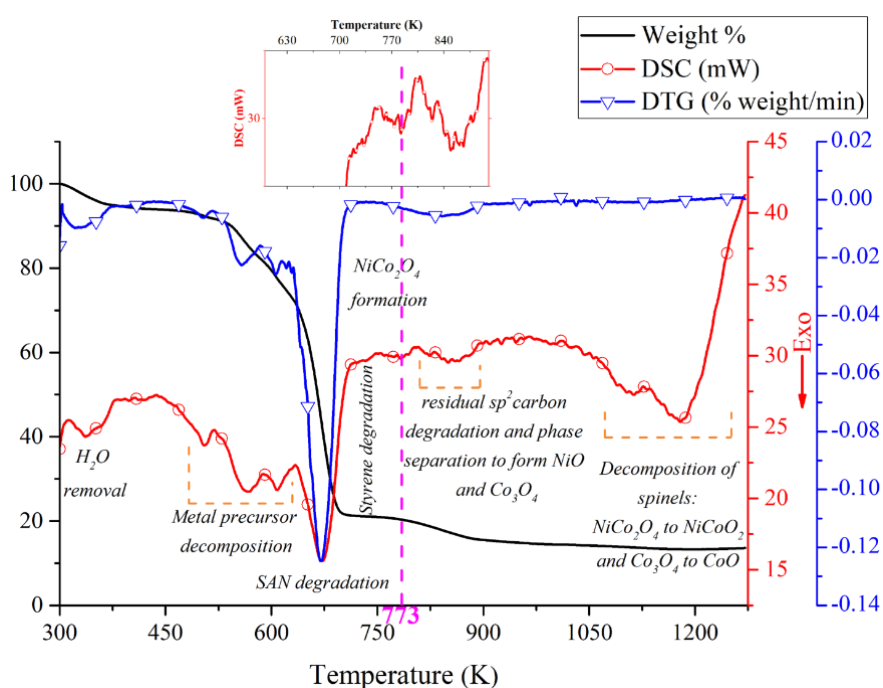
Fig. 7.2 Thermal analysis curves for precursor nanofibers.

Figure 7.2 shows the DSC, TGA, and DTG traces of precursor nanofibers in flowing N_2 environment. The peak at 375 K is due to removal of water molecules from the salts in nanofibers. Between 450 to 600 K, the metal precursor is known to eliminate acetic acid to form hydroxides and lose some organic compounds to form metal carbonates (De Jesus et al. 2005; M. Barakat et al. 2009). Further, the metal precursor residues along with the polymeric binder, SAN, undergoes extensive degradation

around 670 K and all major organic volatiles are removed (George and Anandhan 2015b; George et al. 2015). However, a small shoulder peak corresponding to the degradation of styrene group at 733 K is seen in the plot (Xue and Wilkie 1997). It has to be noted that this delayed degradation of styrene group makes it a structural support for the nucleation and growth of the oxides, and as a source for the formation of residual carbon compounds in the system (George and Anandhan 2015b; George et al. 2015).

A broad peak at 773 K can be attributed to the formation of single-phase NCO. This temperature varies with synthesis techniques and process parameters, but is consistent with values reported previously (Lapham and Tseung 2004; Cui et al. 2008; Jadhav et al. 2014; Babu et al. 2015). The peak in the range 800 to 900 K corresponds to the phase separation of NCO to NiO and Co_3O_4, which is also consistent with prior literature (Cabo et al. 2009; Kuboon and Hu 2011). Some reports instead suggest that this broad peak could be due to the thermal degradation of carbon skeleton from graphene oxide in the absence or presence of NiO and/or Co_3O_4 (Xu et al. 2008; Qiang Chen and Wang 2010; Kottegoda et al. 2011; Yao et al. 2012; Mahmood et al. 2013). It is a well-established fact that Ni and/or Co compounds are good catalysts for the formation of polyaromatic or GL structures from polymers. The peaks above 1050 K are the source of complete phase transformation from a decomposing spinel, *i.e.*, NCO to NiO, Co_3O_4, and $NiCoO_2$; and Co_3O_4 to CoO due to the loss of excess oxygen from the spinel (Lapham and Tseung 2004). Hence, based on thermal analysis, the pyrolysis temperature of nanofibers was chosen to be 773 K to form a single phase of NCO nanofibers. And, an isochronal time scale was adopted to study the effect for pyrolysis soaking such as, $t = 2$, 4, and 6 h.

The kinetics of crystallites growth during pyrolysis is dependent on the soaking temperature and time (Choi et al. 2011; Park et al. 2011; Xia et al. 2012). The crystallite growth for isothermal pyrolysis follows a phenomenological parabolic kinetic equation (Stráská et al. 2015):

$$D^n - D_0^n = tA = tA_0 \exp\left(-\frac{E_a}{RT}\right), \tag{7.1}$$

where D_0 and D are the initial and instantaneous crystallite sizes, A is the rate constant, A_0 is the pre-exponential factor, E_a is the activation energy for the crystallite growth, R is the universal gas constant, T is the absolute pyrolysis temperature and n is the crystallite growth exponent. For classical crystallite growth in a single-phase system, $n \sim 2$. In the presence of solutes and pores, it ranges between 3 and 4. To find the E_a for crystallite growth and D_0 of the NCO (Table II.2, Section II.3.4), as per the standard model for normal crystallite growth and crystallite boundary migration, $n = 2$ was assumed. It has to be noted that, the E_a for crystallite growth in size-strain plot from t = 2 to 4 h has a positive value, which suggests that energy is liberated due to crystallite size reduction. Such a phenomenon is possible either when there is a phase separation by diffusion of ions out of the system or increase in the total area of crystallite boundary.

7.1.2   Characterization of NCO nanofibers

7.1.2.1 *Morphology of NCO nanofibers and fractal nature of NCO particle aggregates*

The AFD and SD of NCO nanofibers increased as a function of *t* (Fig. II.2, Section II.2). The nanofibers (Fig. 7.3) tend to transform from hollow rods to ribbon or belt like structure due to thermally induced fiber opening up during pyrolysis (see Section 7.1.4.2). Figure 7.3a-c, show the FESEM micrographs of NCO particles grown along the rough NCO nanofibers at different *t*. NCO nanoparticles that are nearly spherical with rough surface and edges, (Fig. 7.3a and b) transform to cluster rod-like structures in Figure 7.3c. This is because the diffusion is spatially confined along the nanofiber and the NCO nanoparticles undergo agglomeration along the fiber axis. The NCO nanofibers are composed of several connecting primary particles. These NCO nanoparticles have wide range of sizes, irregular shapes, and variations in their compactness and apparent densities as shown in Figure 7.3a-c. Since NCO nanofibers are clusters of particles obtained by diffusion-limited process, these agglomerates can be treated as fractal-like structures. Their irregularities can be explained in terms of the fractal dimension (D_f) (de Martín et al. 2014; Patil et al. 2015). The number of primary particles (N_P) in an agglomerate can be estimated in terms of D_f as:

$$N_P \approx \left(\frac{d_{AFD}}{a_{APD}} \right)^{D_f}, \tag{7.2}$$

where d_{AFD} is the AFD of the NCO nanofiber, and a_{APD} is the average NCO nanoparticle diameter. In the present study, the values of D_f as 2.5 (for spherical NCO nanoparticles at $t = 2$, 4, and 6 h) and 1.8 (for rod-like NCO nanoparticles at $t = 6$ h), were assumed respectively. These assumptions of D_f was based upon the particle-cluster, and cluster-cluster diffusion limited agglomeration models (de Martín et al. 2014; Patil et al. 2015).
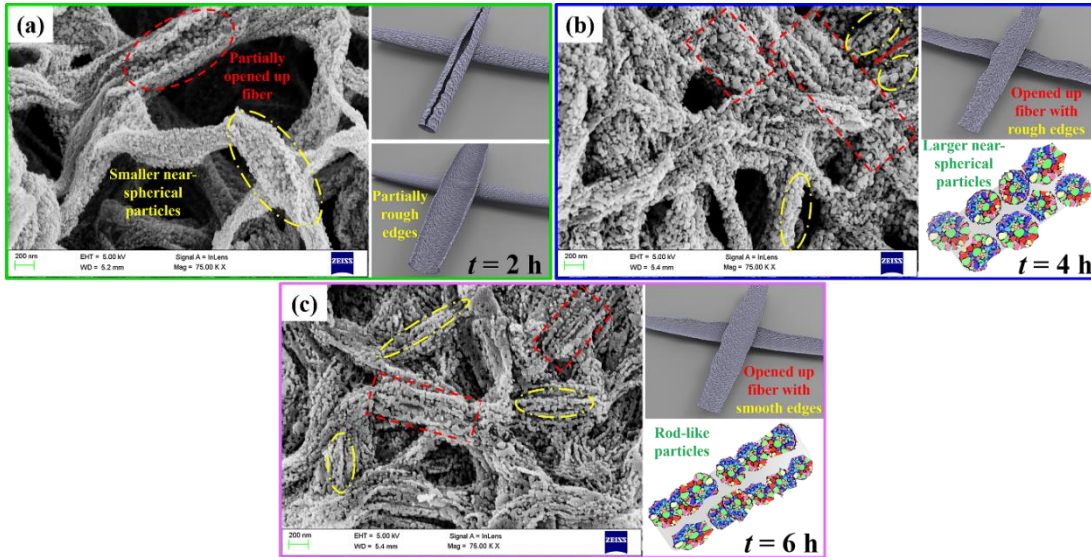
Fig. 7.3 FESEM micrographs of NCO nanofibers, and the corresponding schematic of NCO nanofibers and nanoparticles morphologies (inset figures) synthesized at 773 K for different $t = 2$, 4, and 6 h.

The N_P was estimated using Equation 7.2 and is tabulated in Table 7.1. When D_f is 2.5, and for an d_{AFD} value equal to the measured AFD or a random value (say 100 nm), the N_P increases with t. On the other hand, when D_f is 1.8 as in case of rod-like structure ($t = 6$ h), the N_P is nearly same as for the spherical primary particles of $t = 4$ h. This suggests that there is a thermally driven growth and agglomeration of the same spherical particles at $t = 4$ h to form rod-like particles at $t = 6$ h, along NCO nanofibers. The fine particles are expected to grow and agglomerate within the NCO

nanofibers due to the spatial confinement, and pyrolysis soaking has significantly enhanced the fusion of solid NCO nanoparticles, resulting in voids between the particles of NCO nanofibers. This is in good agreement with the XRD and porosity measurements to be discussed in Section 7.1.2.3 and 7.1.2.5, respectively. The fractal-like structure of the agglomerates plays a vital role in the performance and properties of the material. The anisotropic shapes in the NCO nanofibers could be probably due to various factors such as coupling of magnetic dipoles of the particles, which can affect the fractal dimensions (Niklasson et al. 1988).

Table 7.1: Particle parameters of NCO nanofibers synthesized at t = 2, 4, and 6 h.

t (h)	Average particle size measured from FESEM (nm)	Average particle size measured from HRTEM (nm)	Average number of particles from D_f = 2.5 (D_f = 1.8)	
			d_{AFD} = AFD	d_{AFD} = 100
2	56.15 ± 3.73	20.14 ± 5.48	6	4
4	71.74 ± 2.34	26.56 ± 7.49	27	3
6	46.58 ± 2.80	24.83 ± 7.59	91 (26)	7 (4)

7.1.2.2 FTIR spectroscopy

Figure 7.4 shows the FTIR peaks of NCO nanofibers synthesized at different t: 2, 4, and 6 h. The peaks at 652 and 560 cm^{-1} are the characteristic peaks of spinel structure. These are the transverse optical modes of vibration attributed to metal-oxygen stretching of divalent cations (Ni^{2+}, Co^{2+}) positioned at T_v, and the trivalent cation in O_v (Co^{3+}, Ni^{3+}), respectively (George and Anandhan 2013; Zhou et al. 2015; Trivedi and Prasad 2017). The positions of cations are still inconclusive in literature, as NCO exhibits inverse spinel behavior in some cases, where the Ni cations occupy only T_v, and the Co cations are equally distributed over O_v and T_v (Iliev et al. 2013). However,

the presence of all the cations mentioned above have been confirmed through XPS analysis, this will be discussed in Section 7.1.2.6.
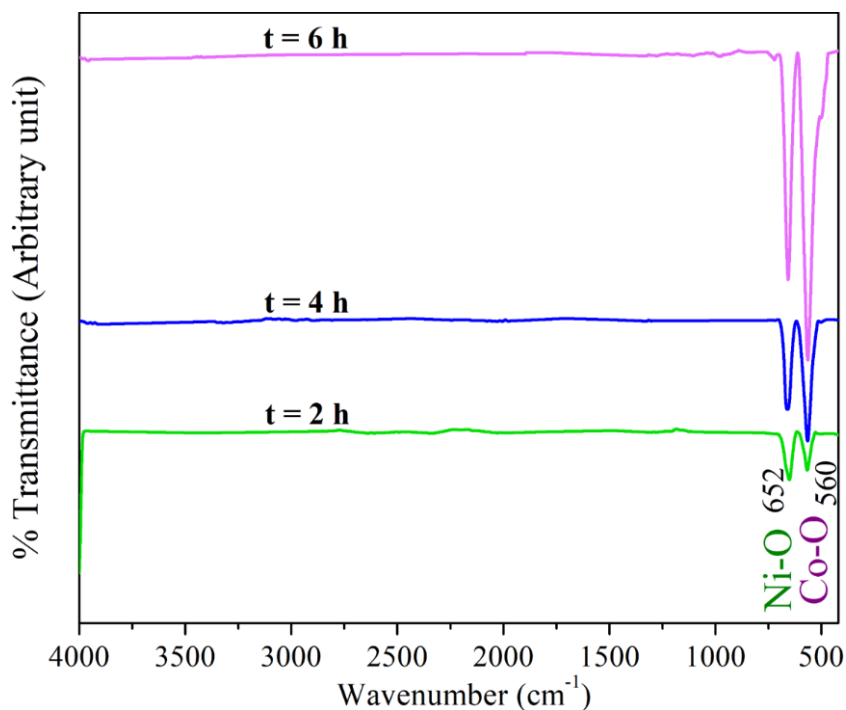
Fig. 7.4 FTIR spectra of NCO nanofibers synthesized at $t = 2$, 4, and 6 h.

It was observed that there are no peaks corresponding to organic phases, suggesting the complete elimination of organic volatiles unlike the residual carbon compounds found in thermal analysis (Section 7.1.1.2). However, ~23 wt% of elemental carbon was observed in the sample with $t = 2$ h through EDS (Figure II.3, Section II.2.2). The is attributed the sensitivity of the FTIR spectroscopy, which is limited as the sample is diluted with KBr in the ratio 1:100 to form transparent pellets for FTIR analysis.

7.1.2.3 XRD analysis

Figure 7.5 shows the XRD patterns of NCO nanofibers obtained at t. Except for the two typical diffraction peaks corresponding to NiO, arising due to phase separation at $t = 8$ h, all the other diffraction peaks belong to spinel NCO. The peaks were indexed to the reflection planes of the standard peaks of ICDD file no. 01-073-1702 (crystal system: cubic and space group: *Fd-3m*). The profile fitting of the raw XRD data was done using Pearson VII function. This would help in estimating the lattice parameters, crystallite

size, and lattice strains in the crystalline phases present in pyrolyzed NCO nanofibers (Table 7.2 and 7.3, Table II.1, and Fig. II.4 of Section II.3). Increase in peak intensities with t, can be attributed to densification of crystallites of NCO. At $t = 8$ h, the peak shift towards higher Bragg angles is seen, and these XRD patterns matches with the ICDD file no. 01-073-1701, which suggests the presence of Co_3O_4 spinel. The peak around 43.2° for $t = 8$ h corresponds to NiO (ICDD file no. 01-073-1523). Therefore, this suggests the phase separation above $t = 8$ h. Hence, the samples obtained at this soaking time were not further analyzed.
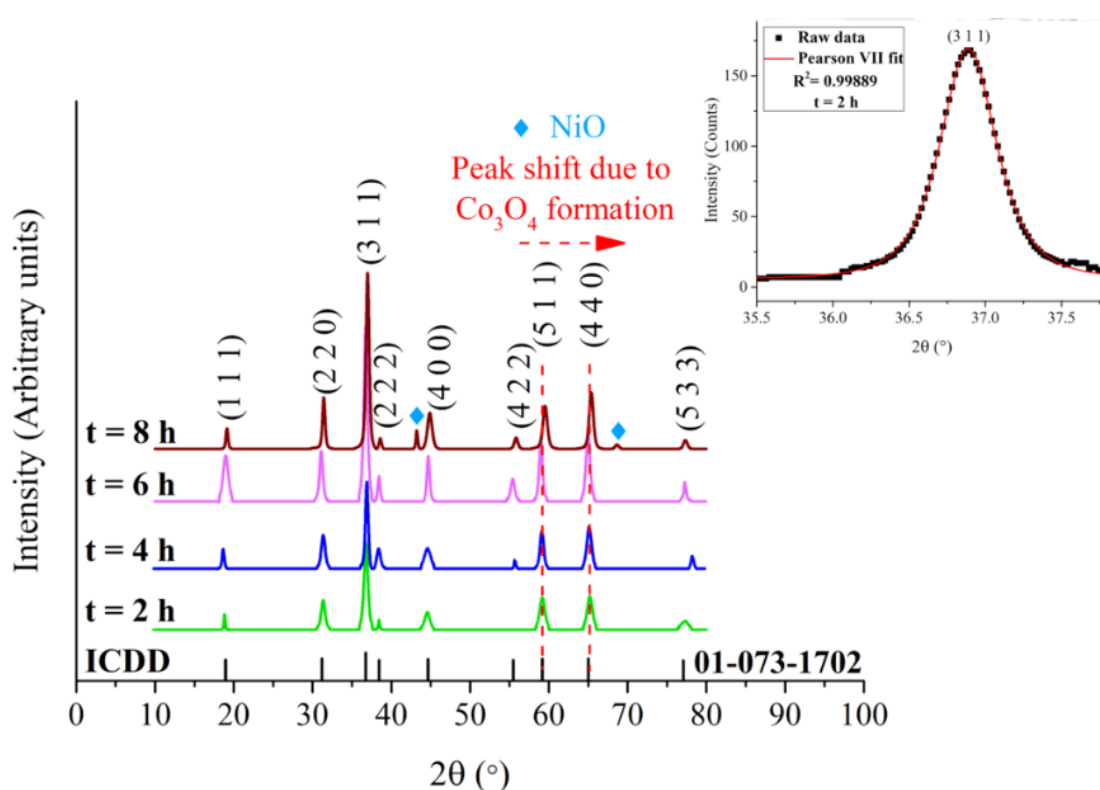
Fig. 7.5 X-ray diffractograms of NCO nanofibers obtained at t compared with ICDD file. The diffraction planes corresponding to different phase are shown in parentheses. Pearson VII function was profile fitted to the raw data (inset figure).

The slight increase in a for $t = 6$ h reflects the size reduction of NCO crystallites to nanoscale even in a highly oxygen rich environment (as per XPS, Section 7.1.2.6). The crystallite size reduction could be either to the crystal splitting or diffusion phase transformation as per crystal splitting theory (Tang and Alivisatos 2006; Umeshbabu et al. 2014; Prathap et al. 2015). It was observed in Section 7.1.2.1, that the

voids in nanoparticle aggregate morphology decrease with increase in number of particles as the NCO nanoparticles at $t = 4$ h, and later agglomerate to form rod-like structure at $t = 6$ h. Alternatively, it may be interpreted as the effect of crystal splitting of NCO, which again increases the number of particles at $t = 4$ h (Table 7.1), therefore, also resulting in decrease in crystallite size of NCO as the lattice strain tends to zero (Table 7.2 and 7.3). Increase in particle size at $t = 6$ h, relieves the lattice strain and stress in the crystal structure, by thermally induced agglomeration.

Table 7.2: Lattice and crystallite and particle parameters of NCO nanofibers synthesized at different t.

t (h)	Lattice parameter, a (Å) [Theoretical value = 8.1140]	Crystallite size, D (nm)			
		Scherrer equation	Williamson-Hall plot		Size-Strain plot
			Isotropic strain model	*Anisotropic strain model*	
2	8.0987	12.65	18.27	9.34	16.18
4	8.0944	15.95	18.52	14.25	14.40
6	8.1167	18.41	21.08	16.75	16.71

The crystallite growth of NCO was correlated to three different models, namely Scherrer equation, Williamson-Hall plot, and size-strain plot for NCO nanofibers synthesized at different t (Section II.3). The crystallite sizes calculated from these three models are listed in Table 7.2. At $t = 2$ h, the isotropic strain model of Williamson-Hall plot was in good agreement with the size-strain plot. Whereas, for $t = 4$ and 6 h, the crystallite sizes estimated from anisotropic strain model of Williamson-Hall plot were in good accordance with size-strain plots. This suggests that at $t = 2$ h, the lattice strain was uniform with large crystallite size. At $t = 4$ h, the crystallite size decreases with anisotropic strain, this may be due to the crystallite splitting in the NCO particles.

Table 7.3: Lattice strain and stress of NCO nanofibers synthesized at different t.

t (h)	Lattice strain (%)		Lattice stress (MPa)
	Williamson-Hall plot Isotropic strain model	Size-Strain plot	by Williamson-Hall plot Anisotropic strain model
2	0.22	0.102	-8480
4	0.087	-0.055	-1040
6	0.069	-0.046	-755

For t = 6 h, the anisotropic strain is retained with increased crystallite size, in spite of the thermally induced strain relief. The anisotropic strain retained for t = 6 h may be due to the particle splitting companied by thermally driven agglomeration as seen in Section 7.1.2.1. The anisotropic strain may also arise from the more number of nuclei and growth as nanocrystallite of NCO. This suggests the presence of additional nucleation sites like residual carbon compounds formed from SAN as seen in Section 7.1.1.2. A plausible mechanism is that the smaller crystallites were parented out from a larger crystallite, which has attained anisotropic strain. And thus, the crystallite splitting mechanism (Section 7.1.4.1) followed by particle splitting might explain the observations of crystallite sizes at different t (Table 7.2). NCO particles formed along the NCO nanofiber in this study are polycrystalline in nature and hence, the crystallite sizes estimated are in the limit of average particles size obtained from FESEM and HRTEM (Table 7.1 and 7.2).

7.1.2.4 HRTEM analysis
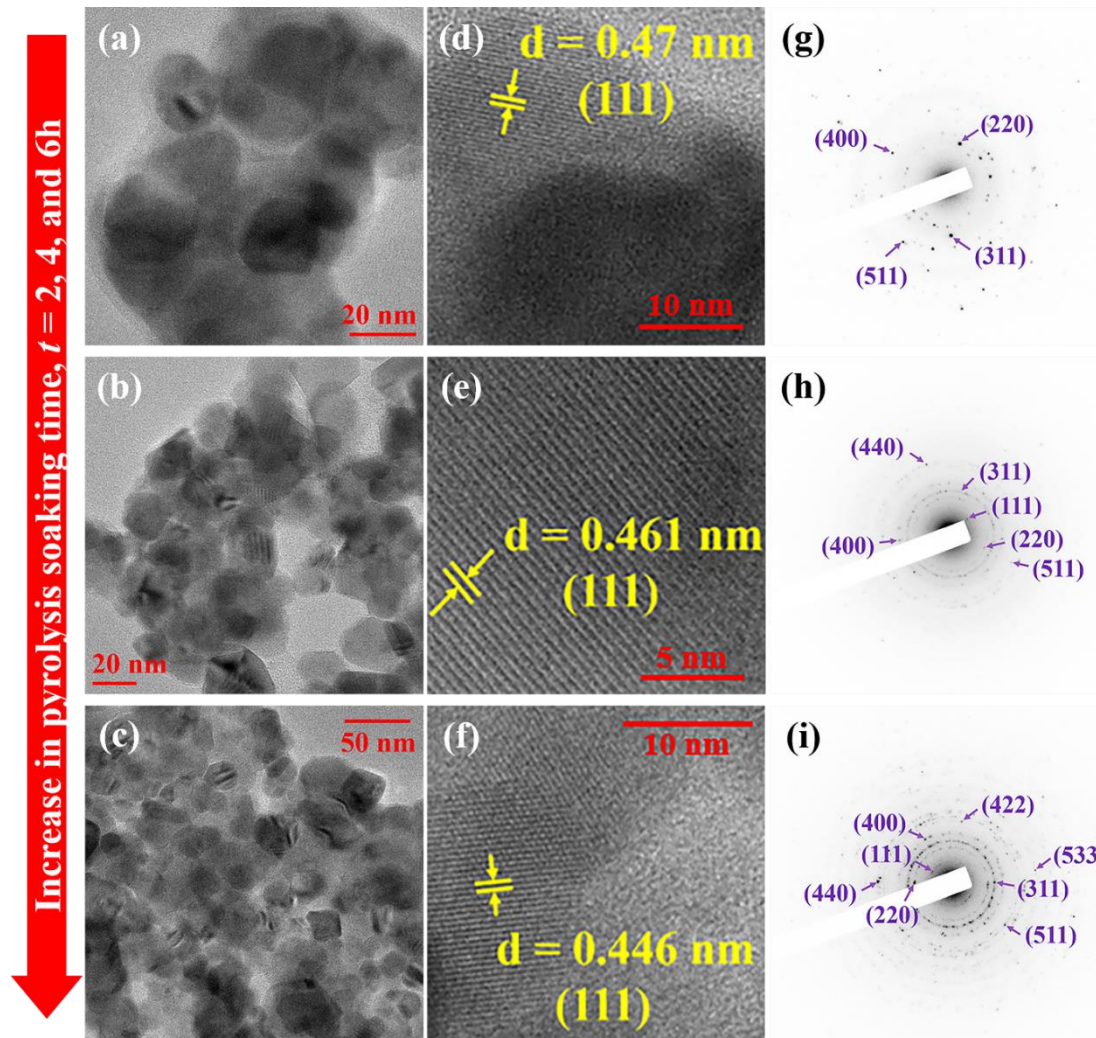
Fig. 7.6 (a-c) HRTEM micrographs, (d-f) high-resolution image showing the lattice fringes and the *d*-spacing corresponding to crystal planes of NCO, and (g-i) SAED patterns of NCO of nanofibers obtained at *t* = 2 h (a, d, and g), *t* = 4 h (b, e, and h), and *t* = 6 h (c, f, and i), respectively.

The HRTEM micrographs of NCO nanofibers obtained at *t* are shown in Figure 7.6a-c. The nanofiber reveals numerous grains that are held together with mesoporous cavities between them suggesting their high surface area (see Section 7.1.2.4). Figure 7.6d-f exhibited lattice fringes corresponding to the planes of NCO crystal are shown with yellow colored marking. The SAED patterns (Fig. 7.6g-i) of the NCO nanofibers were indexed to the planes of diffraction that correspond to NCO. It was observed from Table 7.1 that the trend in variation of crystallite sizes estimated from size-strain plot

in XRD were similar to the variation of average particle sizes of NCO measured by HRTEM, and FESEM micrographs for NCO nanofibers synthesized at different t. The average particle sizes calculated from FESEM micrographs were greater than HRTEM micrographs possibly because more number of NCO particles were measured using FESEM micrographs, giving a more accurate representation. Furthermore, a layered structure was observed bridging two particles of NCO for $t = 4$ h as shown in Figure 7.11b. This seems similar to the GL residual carbon structure, which corroborate the XPS and optical spectroscopies' results to be discussed.

7.1.2.5 *SSA and porosity analysis*

The N_2 adsorption-desorption isotherms (Fig. II.7a-c, Section II.4) suggest the mesoporous structure in the NCO nanofibers. For NCO fibers synthesized at $t = 2$ h, high pressure hysteresis was observed whereas combination of low and high-pressure hysteresis was observed for $t = 4$ and 6 h NCO nanofibers. Such abnormal hysteresis was reported in presence of porous carbon, which creates irreversible changes in the pore structure during adsorption or desorption (Bailey et al. 1971). This suggests the presence of porous carbon-based impurities, which act as an adsorption surface, might be sp^2 hybridized carbon residue. SSA was estimated by BET method using N_2 adsorption-desorption isotherms and the values are tabulated in Table 7.4. The theoretical SSA was calculated as per the procedure in appendix (Section I.6) and the NCO nanofibers have a higher BET SSA. This suggests the presence of porosity in these nanofibers. From Table 7.4, it is seen that the micropore volume decreases with increase in t, due to temperature-time driven densification and growth of crystallites, as discussed earlier. Further, the mesopore volume was calculated by BJH method and it was high for $t = 4$ h. This is because more mesopores are created after crystallite splitting, which was inferred from the XRD analysis. The macropore volume was found to have the highest value for $t = 6$ h and this is again in good accordance with the particle splitting-assisted rod-like particle formation. The decrease in the macropore volume from $t = 2$ to 4 h can be attributed to the decrease in interparticle distance within the nanofiber due to particle coalescence growth and hence the increase in nanofiber diameter. This is in conformity with FESEM, fractal dimension, and HRTEM analysis.

Table 7.4: SSA and porosity of NCO nanofibers synthesized at t = 2, 4, and 6 h.

t (h)	SSA ($m^2 \cdot g^{-1}$)		Total pore volume ($cc \cdot g^{-1}$)	Micropore volume by DFT ($cc \cdot g^{-1}$) [pore diameter less than 2 nm]	Mesopore volume by BJH method ($cc \cdot g^{-1}$) [pore diameter 20-50 nm]	Macropore volume ($cc \cdot g^{-1}$) [pore diameter greater than 50 nm]
	Theoretical	BET method				
2	5.73	24.02	0.01718	0.00754	0.00669	0.00295
4	2.49	17.2	0.01694	0.00603	0.00975	0.00116
6	2.36	18.65	0.01629	0.00429	0.00364	0.00836

7.1.2.6 XPS analysis

The XPS survey spectrum was analyzed for NCO nanofibers obtained at t. It was observed that Ni, Co, O, and C were present in these nanofibers (Fig. II.8, Section II.5). The high-resolution spectrum with deconvoluted peaks of Ni *2p*, Co *2p*, O *1s*, and C *1s* are shown in Figure 7.7 and 7.8. Here both Ni and Co exist in two different oxidation states, *i.e.*, +2 and +3 (Fig. 7.7a-f) as discussed in literature. Multiple oxidation states could be either due to (i) cationic defects formed in oxygen rich system or/and (ii) position of cations in inverse spinel system. All the peaks were akin to the reported characteristic peaks of NCO (Exarhos et al. 2007; Ding et al. 2012; Liu et al. 2013b; Babu et al. 2015; McCloy et al. 2015; Tong et al. 2016; Trivedi and Prasad 2017).

A secondary shoulder peak around 532 eV (Fig. 7.8) indicates presence of oxygen grafted to carbon. In fact, both the peaks around 531eV and 532 eV correspond to the oxygen groups of residual carbon compound like oxidized graphene, which might have come from oxidation of the GL structure (Un Lee et al. 2013) discussed in Section 7.1.1.2. Similarly, the peaks around 284 eV indicate the presence of sp^2 hybridized carbon bonding, which again may have come from reduced GL structure in NCO nanofibers as reported elsewhere (Li et al. 2014; Naveen and Selladurai 2015; Mondal et al. 2017). Further the deconvoluted peaks around 285 and 287 eV can be associated

with the functional group of oxygenated GL structure or inadvertently present atmospheric carbon (C–O–C, O–C=O, *etc.*) as per literature.
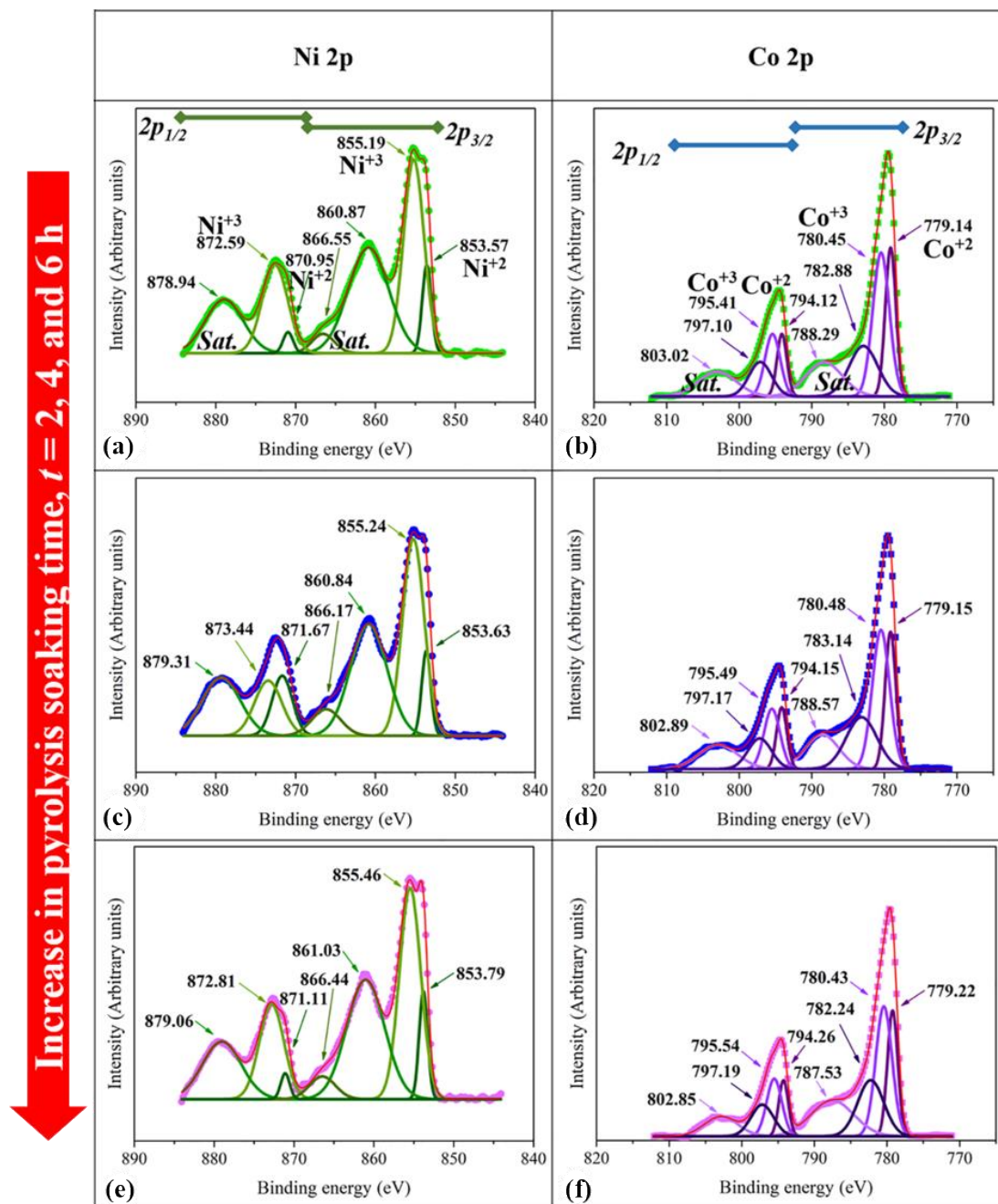
Fig. 7.7 High-resolution XPS spectra of Ni *2p* and Co *2p* for NCO nanofibers synthesized at three different *t*.
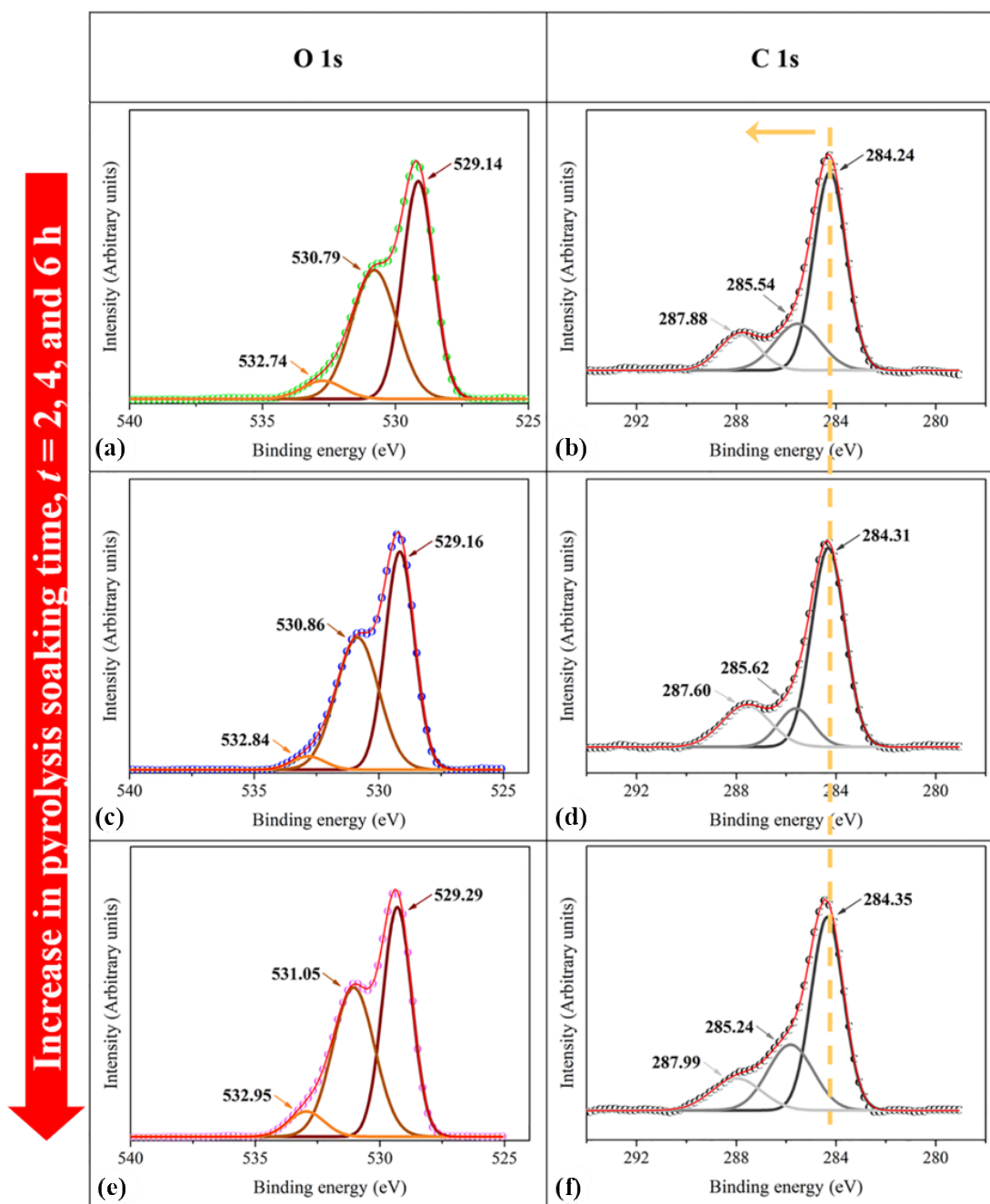
Fig. 7.8 High-resolution XPS spectra of O *1s* and C *1s* for NCO nanofibers synthesized at three different *t*.

The characteristic *2p* peaks of Ni (difference between *2p$_{1/2}$* and *2p$_{3/2}$* is between 17.3 and 18.4 eV) and Co (difference between *2p$_{1/2}$* and *2p$_{3/2}$* is between 14.7 and 15.3 eV) seen in Figure 7.7a-f as well as the lattice oxygen peaks (Fig. 7.8a, c, and e) shift to higher binding energy values, suggesting the role of oxygen enriched system in creating lattice defects with increase in *t* (Guimarães et al. 2003; Exarhos et al. 2007;

George and Anandhan 2015b). The highest peak shifts for Ni and Co were observed in case of $t = 4$ h, which decreases to lower binding energy at $t = 6$ h. This observation can be correlated with the crystallite splitting as discussed in XRD, which can occur in presence of many vacancies/defects, or vice versa. Besides, at $t = 6$ h, the particle splitting completely could lead to a decrease in cation defect concentration, which could in turn suppress the binding energy shifts. However, the prolonged oxidation would have increased the binding energies of oxygen and carbon as there are shifts observed in Figure 7.8a-f. It has to be noted that there is almost ~0.1 eV shift in the sp^2 carbon peak, which can be attributed to the increase in covalence of the (C=C) bond. In other words, the presence of amorphous carbon residues has turned to GL residual carbon at $t = 4$ h. This is in good agreement with the thermal analysis.

7.1.3   Optical spectroscopy

7.1.3.1   UV-Vis-NIR spectroscopy

As shown in Figure 7.9a, when t was increased from 2 to 6 h, the absorbance in the range of 450-800 nm, which are associated with the ligand-metal CT $O^{2-} \rightarrow Co^{3+}$ and $O^{2-} \rightarrow Ni^{3+}$, increase remarkably. This indicates that the concentration of Co^{3+} and Ni^{3+} (infer cationic defects) increase with t (Kuboon and Hu 2011). Therefore, there must be oxygen (enrichment) induced cationic defects in the system, this can be understood as the system response towards crystallite splitting, which is in accordance with XPS analysis. The peak around 310 nm and 370 nm can be attributed to n or $\pi \rightarrow \pi^*$ transition of aromatic C=O bonds (Shen et al. 2014; Srivastava et al. 2014). In the NIR region, a series of combination peaks were observed that are the characteristics of polycyclic aromatic hydrocarbons.

The major NIR absorption bands are at 1140, 1670, 2150-2180, and 2460 nm for aromatic structures. The major characteristic peak at 1670 nm (for aromatic ring) has been assigned to the first overtone of the C–H stretch. This peak shifts to lower wavelength if some electronegative polar substituents are present in aromatic compounds and vice versa. The two main peaks located around 1132 nm and 1140 nm represent second overtone of C–H and a combination band, respectively. The third and fourth overtone of aromatic C–H can be seen at 874 nm and 714 nm, correspondingly as seen from literature (Stuart 2004; Weyer and Lo 2006). The peaks observed in this

study are in the same range, but, showed shifts; this could be due to defects or polar substitutions in the polycyclic aromatic structure. Hence, it is evident from these observations that the NCO nanofibers are accompanied by the GL carbon-based structure having sp^2 hybridization (as observed in XPS) and the source to form such structures may be the residues of the SAN as seen in thermal analysis.
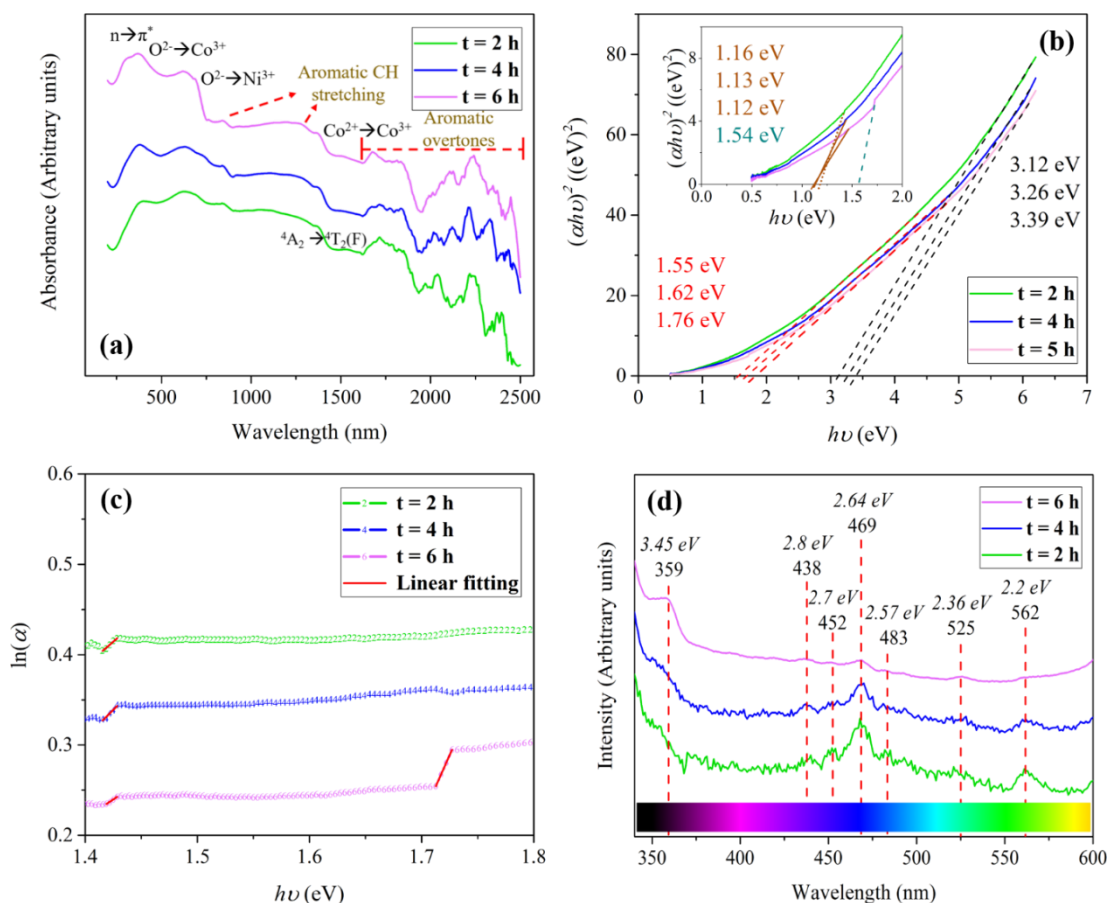
Fig. 7.9 (a) UV-Vis-NIR spectra, (b) Tauc plots (inset: enlarged lower photon energy), (c) ln(α) versus $h\upsilon$ plot to find Urbach energy, and (d) PL spectra of NCO nanofibers synthesized at three different t.

Tauc plot (Fig. 7.9b) was used to determine the band gap energy of NCO nanofibers (Section II.6.1). It was observed that each sample of NCO nanofiber obtained at different t, showed multiple band gap energies (Table 7.5). The band gap energies (E_{bg}) around 1.5-3.4 eV were found to increase with increase in t and these values were lower than the values reported in literature (Cui et al. 2009; Hu et al. 2012; Chen et al. 2013b; Prathap et al. 2015). It is well-established that the E_{bg} of a

semiconductor increases with decrease in crystallite size due to the presence of defect sites or oxygen enrichment creating cationic vacancies (George and Anandhan 2013; Prathap et al. 2015). This further corroborates the observations of reduction in crystallite size at $t = 4$ h, and the crystallite splitting phenomena as a possible mechanism.

Table 7.5: Band gap and Urbach energies of NCO nanofibers synthesized at $t = 2, 4,$ and 6 h.

t (h)	Band gap calculated using Tauc's plot, E_{bg} (eV)			Urbach energy (eV)
2	1.16	1.55	3.12	0.93
4	1.13	1.62	3.26	0.80
6	1.12 1.54	1.76	3.39	1.22 0.36

Additional E_{bg} were found around 1.1 eV for $t = 2, 4,$ and 6 h; and 1.54 eV for $t = 6$ h, respectively. In literature, three major types of photoexcitation of electrons have been proposed in NCO: (i) O *2p* → Co *3d-e$_g$* (or Ni *3d-e$_g$*), (ii) O *2p* → Co *3d-t$_{2g}$* (or Ni *3d-t$_{2g}$*), and (iii) Co *3d-t$_{2g}$* → Co *3d-e$_g$* (or Ni *3d-t$_{2g}$* to Ni *3d-e$_g$*) (Cui et al. 2009). The first two E_{bg} observed in this study between 1.55 eV and 3.4 eV can be attributed to (ii) and (i), respectively, whereas, the peak at 1.54 eV at $t = 6$ h corresponds to (iii), which has the value of 1.68 eV in literature. This peak might have arisen due to the recombination of the hole formed in Co *3d-t$_{2g}$* (or Ni *3d-t$_{2g}$*) and the electron in Co *3d-e$_g$* (or Ni *3d-e$_g$*) after particle splitting, as more defects are formed at $t = 6$ h. Furthermore, the peak around 1.1 eV indicates the NIR emission, which can be assigned to the E_{bg} of GL structure such as carbon nanotubes or reduced graphene oxide (1.1 or 1.19 eV) (Lefebvre et al. 2004; Lian et al. 2013). These band gap energies render these

materials promising candidates for photocatalytic applications and electrocatalytic cells under the irradiation of UV-Vis light.

Urbach energy was estimated for a set of lowest E_{bg} as given in Section II.6.2 and the values were tabulated E_{bg} in Table 7.5. Urbach energy increases with decrease in E_{bg}, which is consistent with the postulated mechanism of oxygen rich or defect induced reduction in the E_{bg}. The minimum Urbach energy for $E_{bg} \simeq 1.1$ eV was observed for $t = 4$ and 6 h indicating less defects in GL structure.

7.1.3.2   PL spectroscopy

To understand the nature of defects in NCO nanofibers, PL spectra of NCO nanofibers at an excitation wavelength of 325 nm was recorded. Figure 7.9d shows the PL spectra obtained from NCO nanofibers synthesized at three different t. The emission quantum yield from graphene oxides is negligible at a wavelength of ~390 nm (Eda et al. 2010).The PL emission peak around 359 eV can be ascribed to the recombination of the hole formed in O $2p$ and the electron in Co $3d$-e_g (or Ni $3d$-e_g) (Cui et al. 2009). In general, PL emission is generally divided into two regions; namely the near-band edge UV emission and deep level defect associated with the visible emission. The broad band observed at ~359 nm leads to near-band edge emission due to the direct recombination of the electrons through an exciton-exciton collision process.

The visible region emission originates due to the radiative recombination of a photo-generated hole with an electron occupying the cation and oxygen vacancies. The blue emissions from 438-483 nm could be attributed to the Co vacancies, produced due to the CT between O^{2-}, Co^{2+} and Co^{3+} as seen in Section 7.1.3.1. The green emissions around 525 nm and 562 nm are produced when O^{2-}, Ni^{2+} and Ni^{3+} transfer charge between them due to Ni vacancies (Cui et al. 2009; Qiang Chen and Wang 2010; Silambarasan et al. 2017). The E_{bg} of NCO nanofibers were estimated to be 3.45, 2.8, 2.7, 2.64, 2.57, 2.36, and 2.2 eV respectively, for the corresponding emission peaks of 359, 438, 452, 469, 483, 525, and 562 nm.

7.1.3.3   Raman spectroscopy

As shown in Figure 7.10, the peaks around 188, 489, 537, 666, and 1150 cm^{-1} correspond to the vibrational modes F_{2g}, E_g, F_{2g}, A_{1g}, and $2L_O$ of NCO, respectively, which is in good agreement with literature (Iliev et al. 2013; Liu et al. 2013c; Babu et al. 2015). A small broad shoulder peak was observed around 1358 cm^{-1} and 1385 cm^{-1} that can arise from the D-band of graphene structure. However, given that the intensity of this peak is very low, this can be better correlated to sp^2 hybridized carbon residue, though present at a very low concentration. The peak position slightly shifts with t, which can be associated with the difference in crystallite size and phonon confinement. The broad peaks observed at low t, are attributed to phonon scattering deficiency in the presence of high porosity between the grains (George et al. 2015).
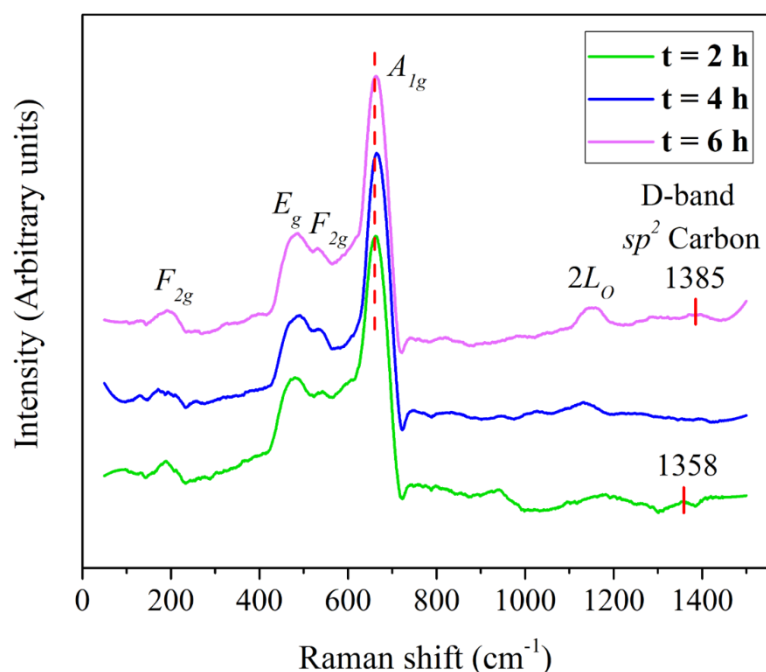
Fig. 7.10 Raman spectra of NCO nanofibers synthesized at three different t.

7.1.4   Mechanisms of fiber morphology evolution as a function of t

7.1.4.1   Mechanisms of crystallite and particle splitting

The organic sp^2 residues such as styrene and nitrile arising from the thermal degradation of SAN (Thermal analysis, Section 7.1.1.2) leads to unique structural and morphological features of NCO particles and nanofibers (George and Anandhan 2015b; George et al. 2015). The sp^2 hybridized carbon residues act as a source for formation

of GL structure in the presence of NCO as a catalyst. The XPS analysis peak shifts indicate the transformation of amorphous carbon to GL structures. The decrease in the crystallite size and lattice strain from XRD analysis suggested the crystallite splitting at $t = 4$ h. Such phenomena have already been reported for NCO materials with different morphologies (Umeshbabu et al. 2014; Prathap et al. 2015).

It has been reported that crystallite splitting phenomenon is a function of several factors. These are reaction time, temperature, critical size of the crystallite, hydrophobic attraction, *van der Waals* forces, hydrogen bonding, dipolar and electrostatic fields, intrinsic crystal contraction, crystal field attraction, and *Ostwald ripening*. However, in general, crystallite splitting mechanism is associated with fast crystal growth. Thermodynamically, the presence of GL structure enhances the nucleation and growth of NCO particles on the combined system. This is also consistent with the positive value of activation energy for crystallite growth from $t = 2$ to 4 h (Table II.2, Section II.3.4), suggesting a catalyst driven nucleation and growth.

Mechanically, the crystallites may further split due to the rupture of GL structure by oxidation as seen from XPS results as it may act as a substrate for NCO crystallite nucleation and growth. The schematic of crystallite splitting and its crystallite size reduction with decrease in interparticle distance within the nanofiber is depicted in Figure 7.11a. The increase in particle size as seen from FESEM and HRTEM is due to the thermally driven coalescence and growth by *Ostwald ripening*. The crystallites split, creating new surfaces within the particle, causing an increase in mesopore volume (Table 7.4). Further, at $t = 6$ h, the particle fractures along these new voids created by crystallite splitting and causes particle splitting as shown in Figure 7.11a. This process is analogous to fracture mechanics process, in which the energy of the newly created surface comes from elastic strain energy in the material. In the present case, the strain energy comes from the relieved lattice stress and strain in both crystallite and particle splitting mechanism (as per XRD). Simultaneously, the thermally driven crystallite growth by *Ostwald ripening* is taking place, which reduces the interparticle distance within the nanofiber (as per fractal analysis). The diffusion-limited crystallite growth along the NCO nanofibers (restricted along the individual fibers) leads to the formation of rod-like NCO particles as portrayed in Figure 7.11a. This additionally

explains the FESEM micrographs (Fig. 7.3c) and fractal dimension analysis (Table 7.1, Section 7.1.2.1). The Figure 7.11b shows the layered GL structure bridging the polycrystalline NCO particles as well as providing substrate-like support to NCO particles. Thus, the use of SAN as a polymeric binder for electrospinning precursor nanofibers is instrumental in manipulating the structure, composition, morphology, and properties of NCO nanofibers.
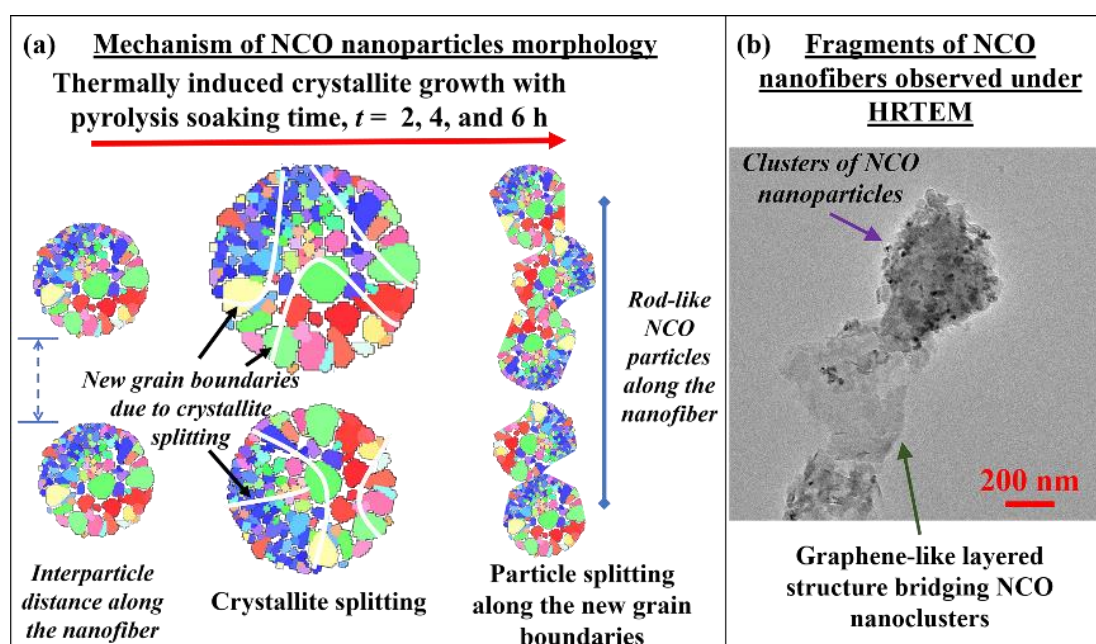
Fig. 7.11 (a) Schematic depicting the crystallite and particle splitting mechanism in NCO nanofibers with increasing *t* and (b) HRTEM micrograph showing a layered structure similar to graphene.

7.1.4.2 *Mechanisms of thermally induced fiber opening up and shrinkage*

Different mechanisms for transformation of hollow nanofibers to nanobelts/nanoribbons have been proposed earlier based on buckling effect and gas diffusion in electrospun nanofibers during pyrolysis. These mechanisms are based on the results obtained by varying the applied voltage (Li et al. 2013b) and the solution parameter (metal precursor to polymer concentration ratio) (Sakar et al. 2016). Recently, precursor nanobelts have been obtained using hybrid precursor solution of higher viscosity, which in turn produced NCO nanobelts after pyrolysis. It has been suggested that the nanobelt morphology is formed due to magnetic interactions between the Ni and Co ions (Harilal et al. 2017). The morphological changes in the present work

occur only upon pyrolysis of the precursors. Hence, the mechanism in this case is most likely to be the thermally induced fiber opening up and shrinkage from $t = 2$ h to $t = 6$ h due to coalescence of surface voids initiated at the intersections of NCO nanofibers. The formation of hollow nanofibers from $t = 0$ h to less than $t = 2$ h could be attributed to the combined phenomena of *Kirkendall* effect and *surface-diffusion* mechanism (Fan et al. 2007a). The metal precursors as well as the organic volatiles present at the core diffuse outward to the shell balancing the inward flow of voids creating hollow structure. The sacrificial polymer present in the core (slow degradation and diffusion) acts as a template for the oxidation of metal precursors at the surface. This explains the residual carbon present in the NCO nanofibers, which later transforms to GL structure above $t = 2$ h, as carbon diffuses in opposite direction to the inward flow of voids (Nam et al. 2015). This could be the reason why GL structure is seen as a template or a bridge for NCO nanoparticles in HRTEM (Fig. 7.11b). It has to be noted that the diffusivity difference in metal precursors, carbon, and voids gives rise to *Kirkendall* effect, *surface-diffusion* and sacrificial polymer template mechanism. The property of polymer to sustain residual carbon compounds at this high temperature is the most significant factor for this mechanism and this outlines the importance of SAN as a polymeric precursor in this study.

An interesting aspect of the fiber opening up was observed for NCO nanofibers, which were synthesized at $t = 2$, 4, and 6 h (Fig. 7.3). Figure 7.12 shows the schematic representing the fiber opening up mechanism of NCO nanofibers. It has been observed elsewhere that the spinel undergoes fast *surface-diffusion* creating large number of voids at the surface (Fan et al. 2007a, 2007b). When these voids meet by coalescence during particle growth by *Ostwald ripening*, the crack initiation takes place. It then propagates (interparticle distance is highest at $t = 2$ h) along the nanofiber due to thermally induced stress. The major crack propagation is seen along the longitudinal axis of the nanofiber, which has easy propagation, then the radial crack propagation. As the residual carbon compounds diffusing outward to the surface or acting as templates for particle growth and coalescence, these layered structures resist the radial crack propagation. Once sufficient voids, and free surfaces are formed, the core residuals can be easily exchanged either by dissolution or evaporation. This could be

the driving force for fiber opening up in NCO nanofibers. Furthermore, this could also be correlated to the faster thermally induced shrinkage of NCO nanofibers at $t = 4$ and 6 h producing a nanobelts/nanoribbons as seen from FESEM micrographs. In other words, this is the reason why AFD and SD of the nanofibers increased with increase in t.
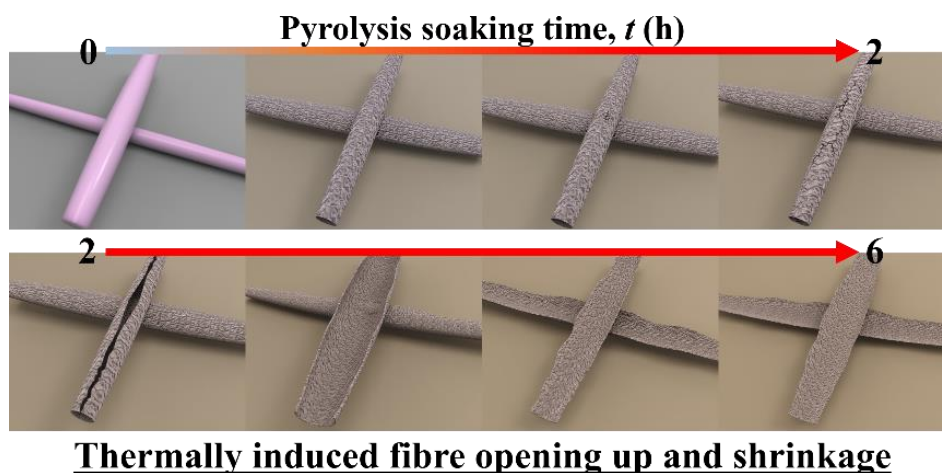
Fig. 7.12 Schematic depicting thermally induced fiber opening up and shrinkage in NCO nanofibers with increasing t.

7.2   SUMMARY AND CONCLUSIONS

The mechanisms responsible for the morphological changes in NCO nanoparticles (spherical to rod-like shape) and nanofibers (nanotube to nanobelts/nanoribbons) as a function of t were explained using various characterization techniques and fractal dimension analysis. XPS and optical spectroscopies suggest the presence of residual GL carbon-based material embedded in the NCO nanofibers. This unique phenomenon is observed only with the use of SAN as polymeric binder, as SAN has rich aromatic rings of styrene and nitrile as the functional groups.

Morphological changes reported here in NCO nanofibers profoundly affect physical and functional properties of the material. The enhanced porosity and photo-emissions due to defect-induced electron-hole recombination in visible region will facilitate the use of this material as photo-electrochemical catalyst. The multiple band gap energies from 1.1 to 3.5 eV suggest that it is a potential candidate material for solar cells and water-splitting applications.

CHAPTER 8

CHAPTER 8

GRAPHENE-LIKE STRUCTURES EMBEDDED NICKEL COBALTITE NANOFIBERS AS MULTIFUNCTIONAL ELECTROCATALYST TOWARDS BIOSENSORS AND ELECTROLYSIS
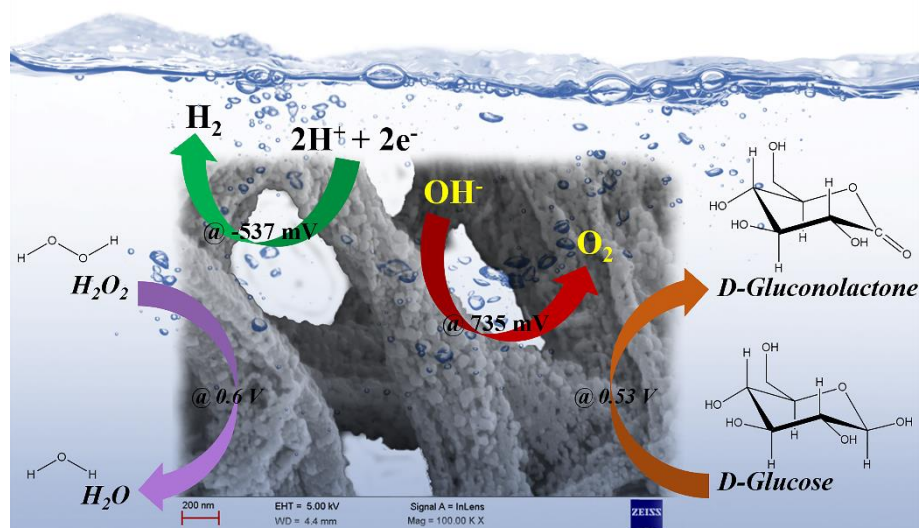
Scheme 8.1 Probable mechanism of glucose and H_2O_2 sensing, and water-splitting in presence of GL/NCO nanofibers.

The multifunctional electrocatalytic behavior of electrospun NCO nanofibers embellished with GL structure prepared in previous study (Chapter 7) was explored here. The presence of the in situ formed GL structure helped in improving the electrochemical interactions of NCO nanofibers in alkaline medium. The modified electrodes manifested a wide range of concentration for glucose detection with a lower limit of 1.2 µM and revealed a sensitivity of 1827.5 µA·mM^{-1}·mg^{-1} in 0.1 M NaOH medium. In addition, the GL/NCO detected H_2O_2 within a short amperometric response time of 1.6 s with a broad dynamic linear range. A notable detection limit of 1.7 µM, and a comparable sensitivity of 1322.5 µA·mM^{-1}·mg^{-1} were measured for the detection

of H₂O₂. GL/NCO nanofibers displayed a remarkable bifunctional electrocatalytic performance for water electrolysis in 1 M NaOH. The modified electrodes arrived at an onset potential of -0.537 V and a Tafel slope of 37.6 mV·dec⁻¹ for hydrogen evolution reactions. Besides, for oxygen evolution reaction an onset potential of 0.735 V with a Tafel slope of 67.0 mV·dec⁻¹ was observed. The excellent electrocatalytic activity of the GL/NCO nanofibers makes them a promising candidate for efficient multifunctional materials.

8.1 RESULTS AND DISCUSSION

8.1.1 Morphology and crystallinity
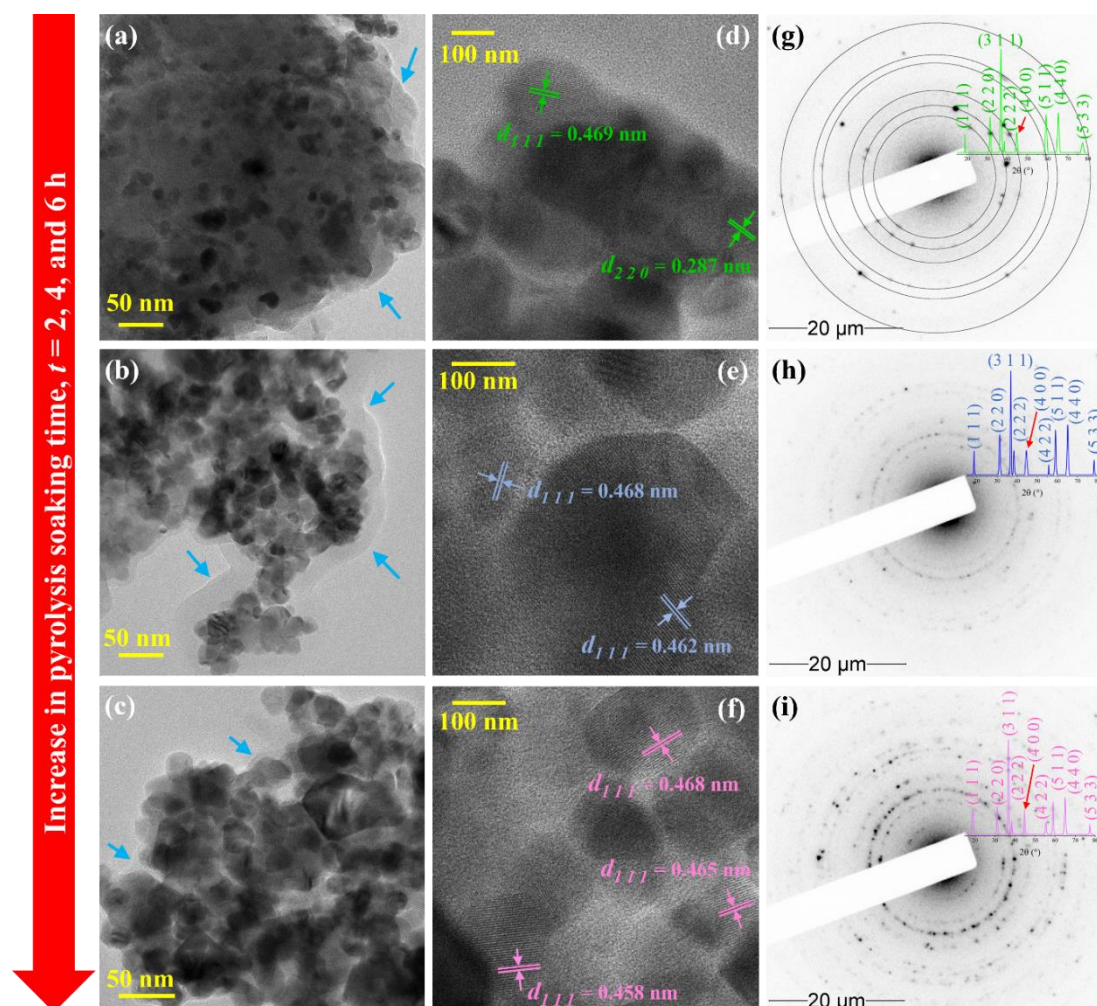
Fig. 8.1 (a-c) HRTEM micrographs, (d-f) high-resolution image showing the lattice fringes and the *d*-spacing corresponding to crystal planes, (g-h) SAED pattern, and (inset figures: g-h) XRD patterns of GL/NCO nanofibers obtained at different *t*. Blue arrows in HRTEM micrographs indicate GL layered structure.

160

Figure 8.1a-c shows the HRTEM micrographs of NCO nanoparticles deposited on GL structure obtained at different t. The evolution of NCO and GL structures during pyrolysis of precursor nanofibers is explained in detail elsewhere in a previous study (Chapter 7). The GL structure seems to decrease and diminish with increase in t due to thermal degradation. A thick layered structure was observed for NCO-2, which transforms to almost single layer for NCO-4 and slowly, diminishes for NCO-6. This suggests that the NCO-4 consists of less agglomerated and well-bridged GL structures in between the NCO nanoparticles that, in turn, improves the electrical/ionic conductivity of the NCO-4. Furthermore, the porous structure could predominantly reinforce the surface efficiency and improve the diffusion kinetics of electrolytes into the NCO samples, during electrocatalytic reactions. It can be seen from Figure 8.1a-c, that the porosity of NCO-4 is moderately higher than that of NCO-2 and NCO-6, where the particles are loosely packed with interparticle voids (Fig. 8.1a-f). This would provide a larger surface area for the catalyst to improve its catalytic performance.

A well-resolved lattice fringes of corresponding diffraction crystal planes, with respective d-spacing of NCO, for all three samples are shown in Figure 8.1d-f. The SAED patterns of the polycrystalline GL/NCO nanofibers are seen in Figure 8.1g-i, which were indexed to the XRD planes of diffraction that correspond to NCO. The inset Figure 8.1g-i, shows XRD patterns obtained for the samples at different t, and the diffraction peaks were indexed to the reflection planes of the reference spinel NCO of ICDD file no. 01-073-1702. No XRD peaks or SAED patterns were observed for GL structure and this implies that the structure is non-crystalline. The average crystallite sizes calculated for all the three GL/NCO nanofibers were in the range of 14-17 nm (Table 7.2, Section 7.1.2.3), and a lower one was for NCO-4 due to crystallite splitting phenomena. It must be noted that apart from point defects, dislocations in the crystallite act as active sites for electrochemical reactions. The D of NCO in the nanofibers as per size-strain plot of XRD analysis (Section 7.1.2.3) was considered to calculate the dislocation density (ρ_D) using Equation 4.1 of Section 4.1.1. The values of ρ_D are 3.82×10^{11}, 4.82×10^{11}, and 3.58×10^{11} cm^{-2} for NCO-2, NCO-4, and NCO-6, respectively. The ρ_D is the highest for NCO-4, which influences the electrochemical

reactions, because the CT resistance decreases with increase in ρ_D (Rafiee et al. 2013). This suggests that NCO-4 will have a better electrocatalytic activity.

8.1.2 Structural defects and non-crystallinity

CIE 1931

t	x	y
NCO-2	0.17199	0.19873
NCO-4	0.18183	0.18188
NCO-6	0.22754	0.15143
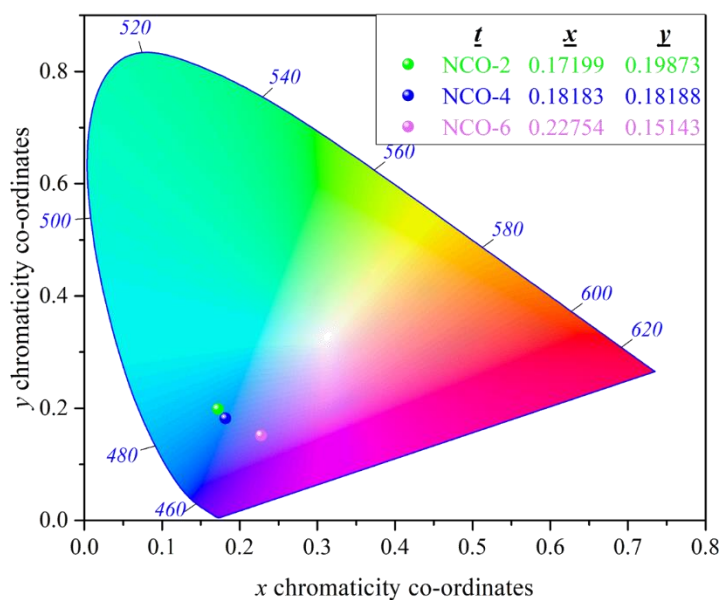
Fig. 8.2 CIE 1931 chromaticity diagram from PL spectra for GL/NCO nanofibers synthesized at different t.

Apart from structural defects observed from UV-Vis-NIR, PL, and Raman spectroscopies (Section 7.1.3, Chapter 7), PL spectroscopy (Fig. 7.9, Section 7.1.3.2) also highlights that the PL emissions (due to defects) are resultant of the synergism between NCO and GL structures (vacancies in NCO crystal; oxygenous functional groups, edges, and surfaces present in GL structure). The PL emission at ~525 nm is also attributed to the GL structure that originates from the sp^2 clusters that are isolated within the sp^3 carbon or defects in the graphene structure (Cuong et al. 2010); whereas PL emissions at ~438 nm, ~452 nm, and ~483 nm are ascribed to oxygen-free (due to intrinsic states), partially oxidized, and highly oxidized regions of GL structure, respectively (Liu et al. 2013a). Multiple band gaps (that escalate redox reactions) in the range of 1.1-3.4 eV were found to be present due to the variation in morphology, size, and defects of GL/NCO nanofibers (Section 7.1.3.1). The CIE 1931 plots are represented for the PL spectra obtained for GL/NCO nanofibers synthesized at different t in Figure 8.2. There is a significant shift in CIE plot from NCO-2, NCO-4 to NCO-6,

which indicates the incorporation of more oxygen to the system. Also, this suggests the degradation (defects arise) of GL structure and reduction of defect sites in NCO as seen from PL spectral analysis. These observations are in line with the results of HRTEM and absorption spectral analyses.
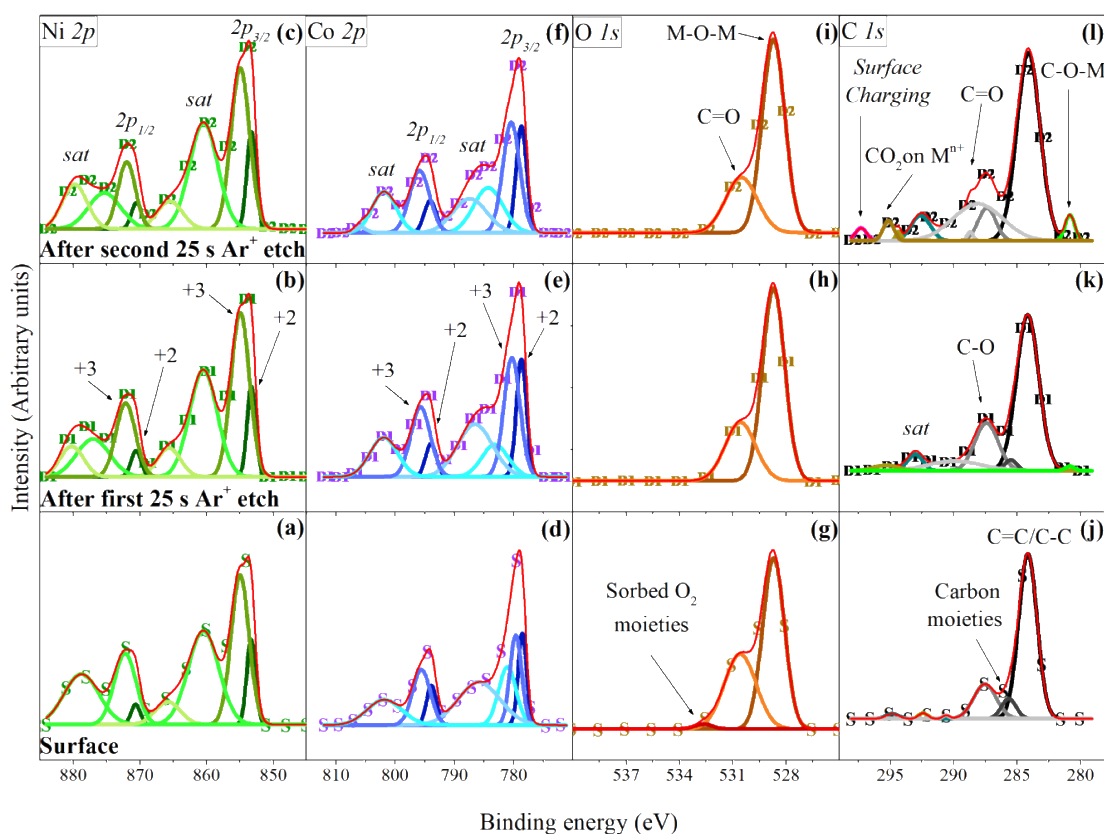
Fig. 8.3 High-resolution XPS depth profiling of NCO-4 for (a-b) Ni *2p*, (d-f) Co *2p*, (g-i) O *1s*, and (j-l) C *1s*.

Further, in this study, XPS depth profiling of NCO-4 was done to avoid the atmospheric contamination and surface defects. XPS survey spectrum of NCO-4 (Section II.8) shows the peaks corresponding to Ni, Co, O, and C; at surface and two depths. The Ni *2p* high-resolution spectrum in Figure 8.3a-c conforms to the doublet spin-orbit of *2p_{3/2}* (~853 eV) and *2p_{1/2}* (~871 eV) electronic configuration with corresponding shake-up satellite peaks denoted as *sat*. Each of the above peaks have been deconvoluted to the characteristic peaks of Ni^{2+} and Ni^{3+} (Cai et al. 2016; Huang et al. 2017a).

Similarly, Co doublet electronic configurations were conformed at binding energies of ~779 eV and 794 eV for $2p_{3/2}$ and $2p_{1/2}$, respectively. Furthermore, the deconvolution of Co $2p$ high-resolution spectrum showed the characteristic of peaks assigned to Co^{2+} and Co^{3+} along with its respective *sat* (Figure 8.3d-f) (Huang et al. 2017a; Wang et al. 2017a). These results are in line with the early literature and confirmed that both trivalent and divalent cations are well-distributed on the surface and coactive to contribute to electrocatalytic reactions. The trivalent cations are expected to aid in the electrochemical process by fast charge transportation across the electrode-electrolyte interface (Wang et al. 2017a). Also, the ample intrinsic redox couples of cations (M^{2+}/M^{3+}) well-distributed in mesoporous NCO nanoparticles could enhance the electroactive sites for catalysis reactions (Huang et al. 2017a).

Figure 8.3g-i shows the O $1s$ high-resolution spectrum at surface and two different depths of NCO-4. The deconvoluted peaks reveal the presence of inverse spinel lattice oxygen (cation replacements from parent position due oxygen vacancies) (Lee et al. 2013a) and C=O functional groups around binding energies of ~528 eV and ~530 eV, accordingly (Wang et al. 2017a). The peak at ~532 eV can be attributed to the sorbed oxygen moieties on the surface of NCO-4. Furthermore, in Figure 8.3j-l of C $1s$ high-resolution spectrum, the deconvoluted peak at ~284 eV was ascribed to C=C/C-C of graphene. The peaks between 285-290 eV belong to oxygenated carbon species such as C=O and C-O (Permatasari et al. 2016; Wang et al. 2017a).

Additional peaks arise around binding energies of 280 eV and 292 eV in Figure 8.3k and l, which correspond to C-O-M, *i.e.*, metal oxide/C interface (reason for GL structure formation in presence of cations) (Singh et al. 2012) and characteristic *sat* of graphene (Permatasari et al. 2016), respectively. Whereas, the supplementary peaks in Figure 8.3l around 295 eV and 297 eV are due to oxidation of carbon based material (CO_2 formed are adsorbed on cations) (Sajan et al. 2017) and surface charging (Schulze et al. 1999), respectively, as a result of Ar^+ ion etching during XPS analysis. The presence of GL structures boosts up the electrocatalytic activity due to the presence of large surface area, active (defective) sites (by physic or chemisorption), and enhanced electrical/ionic conductivity (Ko et al. 2017; Rao et al. 2017; Wang et al. 2017a). Hence,

the GL/NCO composite nanofibers were expected to be suitable for the electrocatalytic process with significantly improved sensitivity in detection of analytes.

8.1.3 Electrocatalytic sensing behavior of NCO nanofibers

Figure 8.4a shows typical CV curves acquired for the bare GE and NCO/GL/GE, under the applied potential from 0 to 0.7 V in 0.1 M NaOH electrolyte in presence of 1 mM glucose. For NCO-4 with 1 mM glucose, two pairs of anodic peaks at ~ 0.32 V (labelled A) and 0.48 V (labelled B), as well as cathodic peaks at ~0.20 V (labelled C) and 0.40 V (labelled D) were observed that can be ascribed to the reversible redox reactions of Ni^{2+}/Ni^{3+} and Co^{2+}/Co^{3+} (George and Anandhan 2016; Cui et al. 2017). On the contrary, no redox peaks were found for bare GE in the presence or absence of glucose (Figure 8.4) as no such redox reactions occur. The redox reactions of NCO in basic alkaline electrolyte are (Naik et al. 2015):

$$NiCo_2O_4 + OH^- + H_2O \xleftrightarrow{\text{0.1M NaOH}} NiOOH + 2CoOOH + e^- \qquad (8.1)$$

$$CoOOH + OH^- \xleftrightarrow{\text{0.1M NaOH}} CoO_2 + H_2O + e^- \qquad (8.2)$$
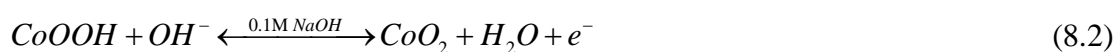
Among the three NCO/GL/GE samples, the area enclosed by the CV curves is the largest for NCO-4/GE, which suggests that NCO-4 has the highest electrocatalytic activity among all the samples. This may be explained through a combination of several factors such as the greater surface area arising from the more porous structure, enhanced active sites obtained by crystalline splitting as seen in Chapter 7 (Cui et al. 2017), multiple band gaps, and the less agglomerated GL structure (Ko et al. 2017). Besides, it has been reported in literature that the electrocatalytic activity of NCO increases in the presence of NiO. This is partly due to the increased surface cation concentration. Additionally, $Ni^{2+} \rightarrow Ni^{3+}$ oxidation occurs at more negative potential than $Co^{3+} \rightarrow Co^{4+}$ (Su et al. 2014), which is responsible for the sensing behavior. A closely related phenomenon is the transformation of inverse spinel to normal spinel with increase in t that will discussed in Chapter 9. Essentially, the Ni cations meet the electrolyte at the surface of the material as they move from T_v to O_v in the crystal structure that facilitates fast electron transfer across the interface (Naik et al. 2015; Wang et al. 2017a). However, maintaining an optimal t is also necessary as the particle shape needs to be

retained. With a similar reasoning, one may expect that NCO-4 would manifest better electrocatalytic performance.
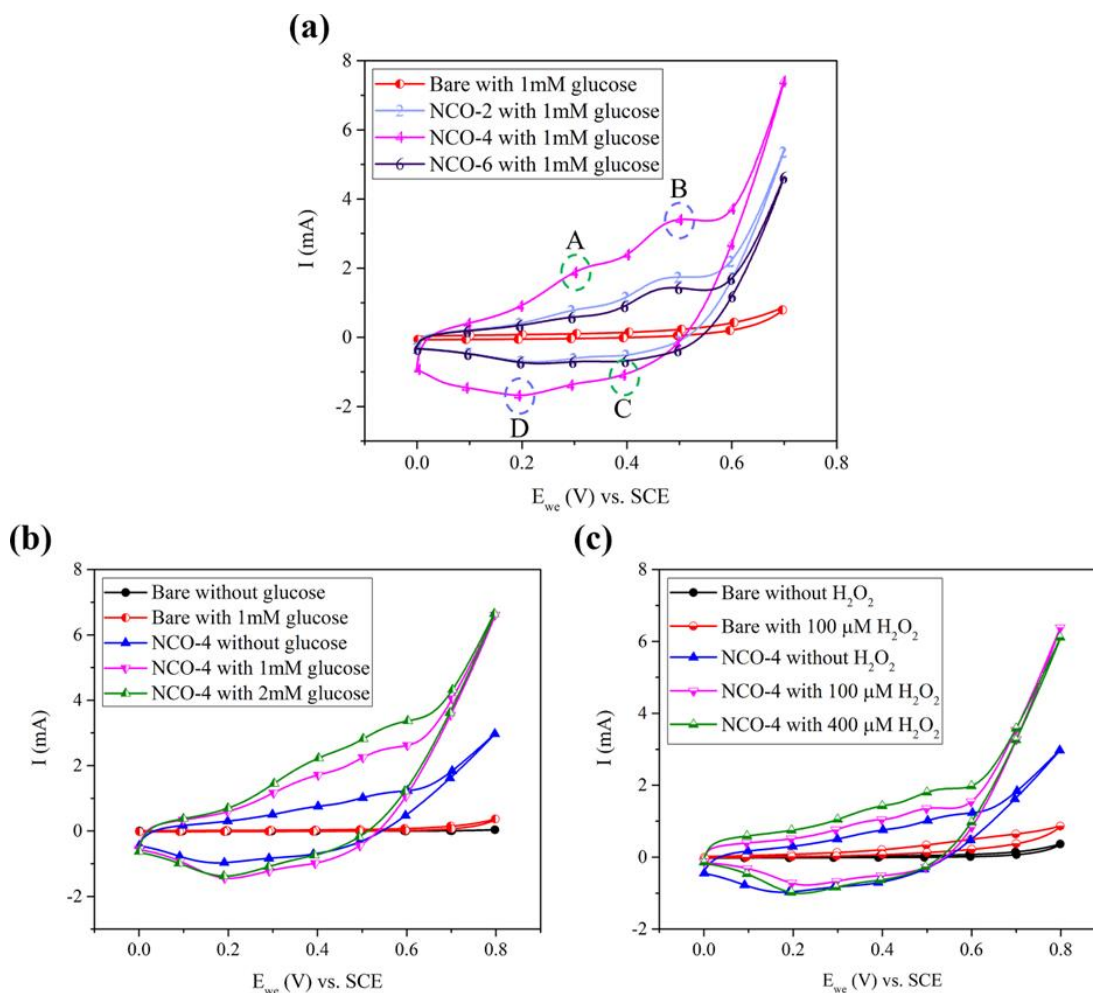
Fig. 8.4 (a) CV curves of bare GE and GE loaded with GL/NCO nanofibers synthesized at different *t* for a glucose concentration of 1mM. CV curves of bare GE and GE loaded with NCO-4 in presence of (b) 1 mM glucose and (c) 100 µM H_2O_2.

The CVs corresponding to NCO-4/GE at different concentrations of glucose are shown in Figure 8.4b in the applied potential range of 0-0.8 V. It is clear that the NCO-4/GE exhibits a significant increase in the anodic peak current after the addition of glucose, which suggests better electrocatalytic activity of NCO-4 nanofibers towards glucose oxidation. The electrocatalytic mechanism of the GL/NCO exposed to glucose in alkaline electrolyte can be described by the following equations (Cui et al. 2017; Saraf et al. 2017):

$$Ni^{2+} + Co^{2+} \xrightarrow{\quad 0.1M\ NaOH \quad} Ni^{3+} + Co^{3+} + 2e^{-} \qquad (8.3)$$

$$NiOOH + 2CoOOH + C_6H_{12}O_6 \xrightarrow{\quad 0.1M\ NaOH \quad} NiCo_2O_4 + C_6H_{10}O_6 + 2H_2O + 2e^{-} \quad (8.4)$$
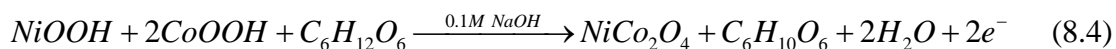
First, the Ni^{2+} and Co^{2+} cations from NCO oxidize to Ni^{3+} and Co^{3+} species due to the applied voltage by losing two electrons. This is the reason for the higher anodic peak current of NCO/GL/GE compared to bare GE. Then, upon addition of glucose to the electrolyte, glucose oxidizes to gluconolactone by transferring two electrons to the electrolyte and thus a further increase in the anodic peak current is observed. The oxidation of cations and glucose occur simultaneously at the same applied voltage, but the rate of oxidation of cations at the surface of the NCO nanofibers determines the rate of detection of glucose. Nevertheless, it can be concluded that glucose sensing is an intrinsic electrocatalytic property of NCO nanofibers and it can be tuned by controlling the morphological structure and electronic properties of the material.

The electrocatalytic sensing properties of bare GE and NCO-4/GE were evaluated at various H_2O_2 concentrations. Figure 8.4c shows the relevant CV curves. The positive anodic current for NCO-4 without H_2O_2 comes from the oxidation of cations, as described in Equation 8.3. The increase in oxidation current upon addition of H_2O_2 in NaOH can be attributed to the oxidation of H_2O_2 as:

$$H_2O_2 + 2OH^{-} \xrightarrow{\quad 0.1M\ NaOH \quad} 2H_2O + O_2 + 2e^{-} \qquad (8.5)$$
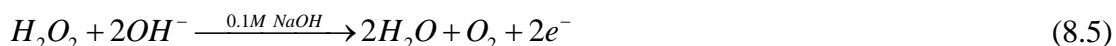
In the CV curves of NCO-4/GE with 100 µM and 400 µM H_2O_2, the anodic peaks at ~0.35 V and ~0.5 V and the cathodic peaks ~0.2 V and ~0.4 V represent the redox couples of Equations 8.1 and 8.2, respectively. The higher anodic peak current with increasing H_2O_2 concentration indicates good electrocatalytic activity of GL/NCO nanofibers for H_2O_2 oxidation. A plausible reaction mechanism for NCO with H_2O_2 in alkaline medium has been proposed in literature (Ding et al. 2013; Wang et al. 2015b):

$$2M^{2+} + H_2O_2 \xrightarrow{\quad 0.1M\ NaOH \quad} M^{2+} \overset{ads}{\leftrightarrow} OHHO \overset{ads}{\leftrightarrow} M^{2+} \qquad (8.6)$$

$$M^{2+} \overset{ads}{\leftrightarrow} OHHO \overset{ads}{\leftrightarrow} M^{2+} \xrightarrow{\quad 0.1M\ NaOH \quad} M^{3+} \rightarrow {}^{\bullet}OHHO^{\bullet} \leftarrow M^{3+} \qquad (8.7)$$

$$M^{3+} \rightarrow {}^{\bullet}OHHO^{\bullet} \leftarrow M^{3+} \xrightarrow{\quad 0.1M\ NaOH \quad} 2M^{3+} + 2OH^{-}, \qquad (8.8)$$
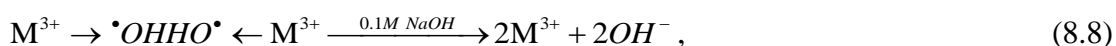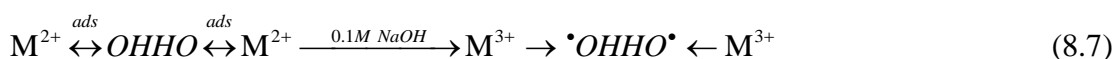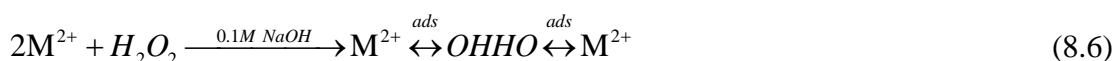
where M represents both Ni and Co cations. Essentially, the divalent cations (M^{2+}) transfer electrons from oxygen atoms of H_2O_2 to form a complex species as shown in Equation 8.6 and 8.7, which eventually results in the formation of trivalent cations (M^{3+}). Subsequently, the O-O bond elongation and electron distribution takes place, and OH$^-$ ions are released to the electrolyte along with oxidation of cations in GL/NCO nanofibers.

Figure 8.5a shows the CV curves of NCO-4/GE at various scan rates (20 to 250 mV·s^{-1}) in the presence of 1 mM glucose in NaOH electrolyte. The anodic and cathodic peak currents increase with increasing scan rate. Both the anodic and cathodic peak currents appear to satisfy a linear fit with the scan rates, as seen from Figure 8.5b. This demonstrates that electrocatalytic process for glucose detection is kinetically controlled as previously suggested (Wang et al. 2017a).
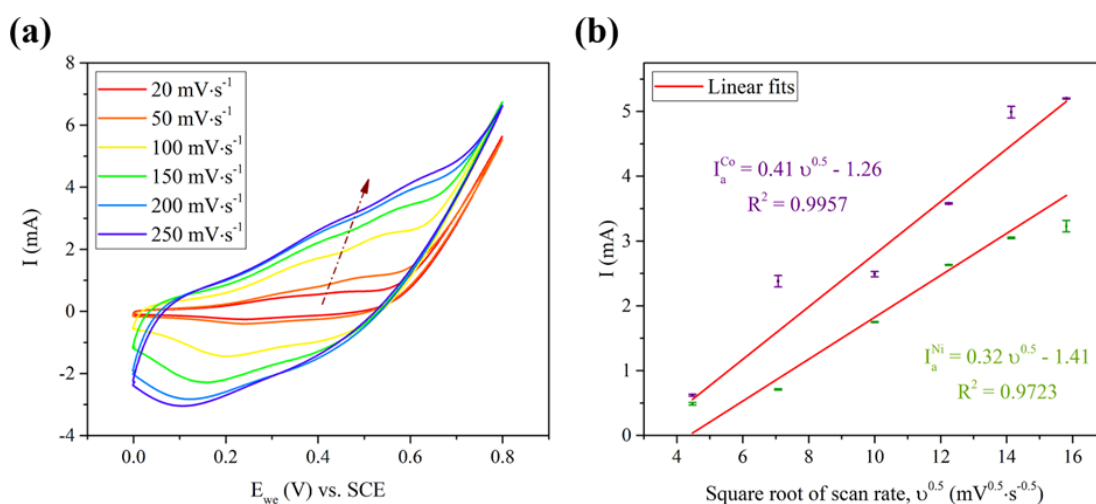
Fig. 8.5 (a) CV at various scan rates for GE loaded with NCO-4 in presence of 1mM glucose and (b) linear fits of anodic current vs. scan rates for both the cations.

8.1.4 Amperometric detection

The CA analysis was carried out to estimate the detection limit and sensitivity values of NCO-4/GE in 0.1 M NaOH electrolyte (pH = 13 and scan rate = 100 mV·s^{-1}). An optimal steady-state potential for analyte electrocatalytic performance was obtained by performing LSV at a slow scan rate (*i.e.*, 2 mV·s^{-1}). These optimal steady-state potentials vs. SCE were found to be 0.53 V and 0.6 V for glucose and H_2O_2 detection, respectively (Figure S3, ESI).

(a)

(b)

(c)
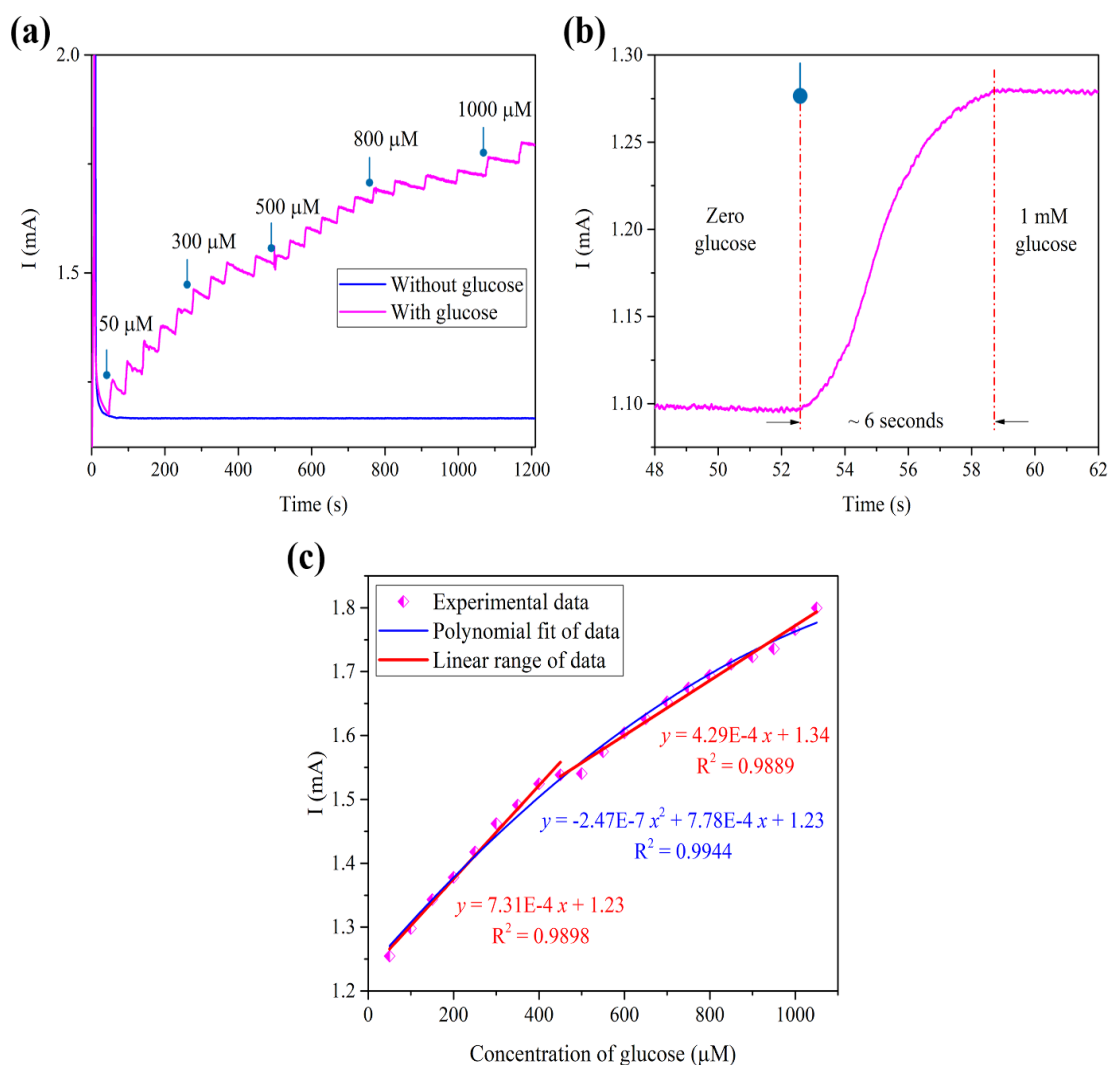
Fig. 8.6 (a) Amperometric response of NCO-4 loaded GE for successive addition of glucose to electrolyte, (b) Response time observed for single addition of glucose, and (c) calibration curve for glucose detection using NCO-4/GE.

Figure 8.6a shows a typical CA response of NCO-4/GE upon successive addition of glucose into constantly stirred electrolyte. The successive addition of glucose concentration was in the range of 50-1100 µM. The sensor responded swiftly upon addition of glucose at each step and the steady state current was reached in ~6 s (Figure 8.6c). Also, the sensor showed a step-like increase in response current with successive addition, which may be attributed to the homogenous electrocatalytic activity and enhanced conductivity obtained in NCO-4. Figure 8.6b displays the calibration curve for glucose detection, obtained by measuring the current change with

each incremental addition of glucose, and plotting the same against the specific concentration of glucose. As seen in Figure 8.6b, the response of the sensor shows a linear relationship towards glucose for the concentration of 50-400 µM and 400-1100 µM with a correlation coefficient (R^2) of ~0.989 and sensitivity values equal to 1827.5 $\mu A \cdot mM^{-1} \cdot mg^{-1}$ and 1072.5 $\mu A \cdot mM^{-1} \cdot mg^{-1}$, respectively. The *LOD* and *LOQ* of the CA glucose sensor were estimated using Equation 8.5 and 8.6 (Naik et al. 2015):

$$LOD = (3S_b)/m \tag{8.9}$$

$$LOQ = (10S_b)/m, \tag{8.10}$$

where S_b is the standard deviation of blank signal for ten measurements (0.000302 mA) and m is the slope value extracted from the calibration plot. Thus, the calculated LOD and LOQ for glucose sensor in the linear region of 50-400 µM were 1.2 µM and 4.1 µM, respectively.

The typical CA response for NCO-4/GE for an optimal applied voltage of 0.6 V, with successive addition of H_2O_2 (20-700 µM) is shown in Figure 8.7a. The sensor response towards H_2O_2 was more rapid as compared with that towards glucose, which achieved a steady-state current within ~1.6 s (Fig. 8.7b). This rapid increase in response time indicates exceptional electrocatalytic oxygen evolution reaction performance of NCO/graphene material (Umeshbabu et al. 2016). By measuring the change in current for the corresponding addition of H_2O_2, a calibration plot was designed akin to that of glucose. Here in Figure 8.7c, again two regions of linear fits were found for different range of *H_2O_2* concentration, *i.e.*, 20-200 µM for lower concentration ($R^2 = 0.959$) and 200-700 µM for higher concentration of H_2O_2 ($R^2 = 0.932$). The sensitivity of H_2O_2, for these two regions of response were 1322.5 $\mu A \cdot mM^{-1} \cdot mg^{-1}$ and 427.3 $\mu A \cdot mM^{-1} \cdot mg^{-1}$, subsequently. The *LOD* and *LOQ* for H_2O_2 sensor was estimated to be 1.7 µM and 5.7 µM, respectively, at the region of lower concentration.

The response time, *LOD*, and sensitivity for both the analytes were comparable to the earlier literature (Table 8.1). The selectivity of a sensor is a material property, and the literature suggests no significant interference of accompanying species with glucose or H_2O_2 detection when NCO and NCO/graphene derived electrodes are used.

Furthermore, it has been reported that NCO and NCO/graphene derived electrodes provide excellent selectivity towards analytes in the presence of interferents (Naik et al. 2015, 2017; Cui et al. 2017; Huang et al. 2017a, 2017b; Qin et al. 2017; Rao et al. 2017; Saraf et al. 2017; Wang et al. 2017a; Yin et al. 2017). The stable and concurrent stepwise response recorded during the successive injection of different concentrations of analytes marks the steady electrocatalytic activity. In addition, the absence of hindrance in successive stepwise response of the sensing process suggests the distinguished operational stability and repeatability of the NCO/GL/GE electrodes.
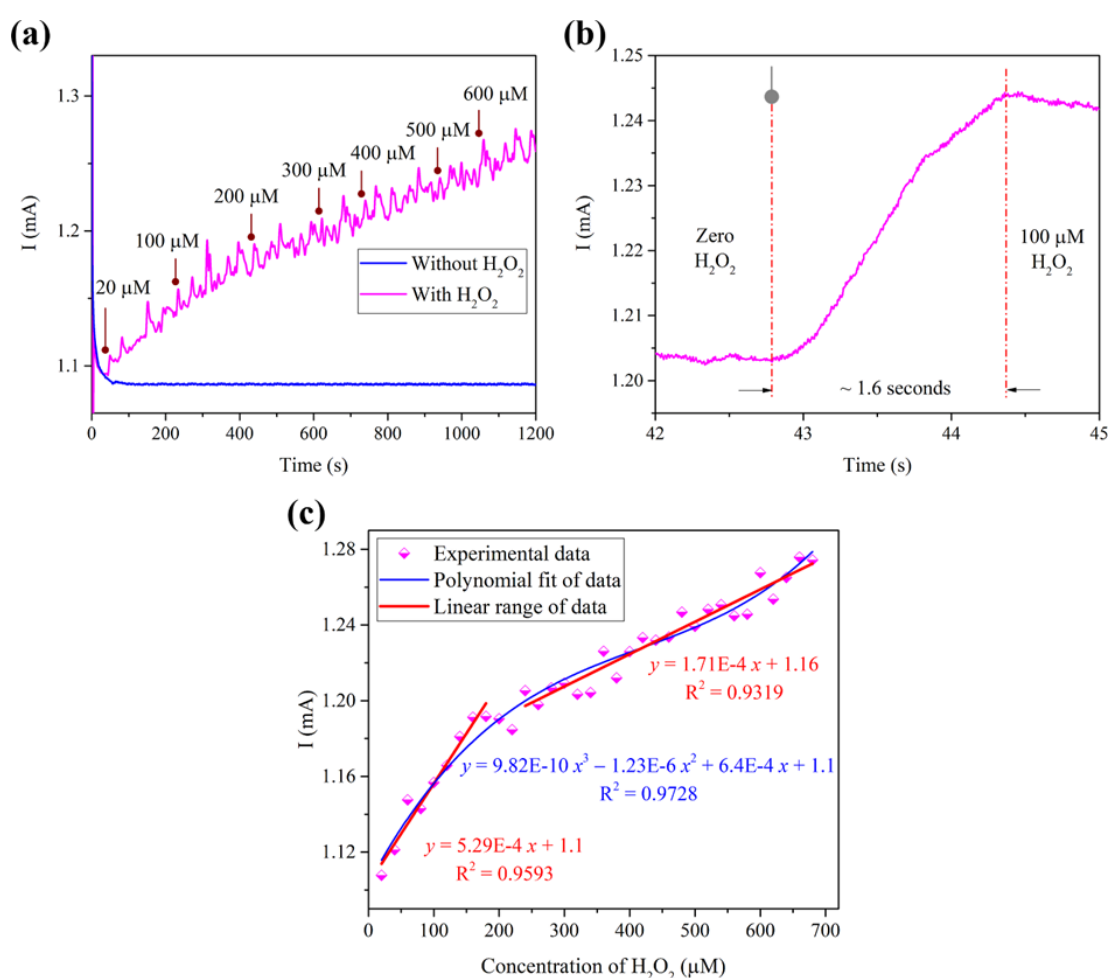
Fig. 8.7 (a) Amperometric response of NCO-4 loaded GE for successive addition of H_2O_2 to electrolyte, (b) response time observed for single addition of H_2O_2, and (c) calibration curve for H_2O_2 sensing using NCO-4/GE.

8.1.5 EIS analysis

The electrical/ionic conductivity and CT properties of NCO-4/GE electrodes are influential factors of sensor activity. EIS was conducted to evaluate the physicochemical process at the surface of the electrode. The important measurements done in this context relate to the response time variation, CT capability at high frequency and mass transfer competence at low frequency. The EIS data were analyzed using Nyquist plot, which represents the frequency response of electrode/electrolyte interface by examining the imaginary component ($-Z''$) of the impedance and the real component (Z'). The Nyquist plots of the sensors in the absence and presence of analytes are shown in Figure 8.8a and 8.8b. It was observed that the Nyquist plot in absence of analyte (Section II.10) had a less prominent semi-circular region, and a more prominent semicircle with reduced diameter in the presence of glucose. This semicircle diameter describes the CT resistance (R_{ct}) at electrode/electrolyte interface and the substantially reduced diameter therefore suggests enhanced charge conductivity at the electrode/electrolyte interface.
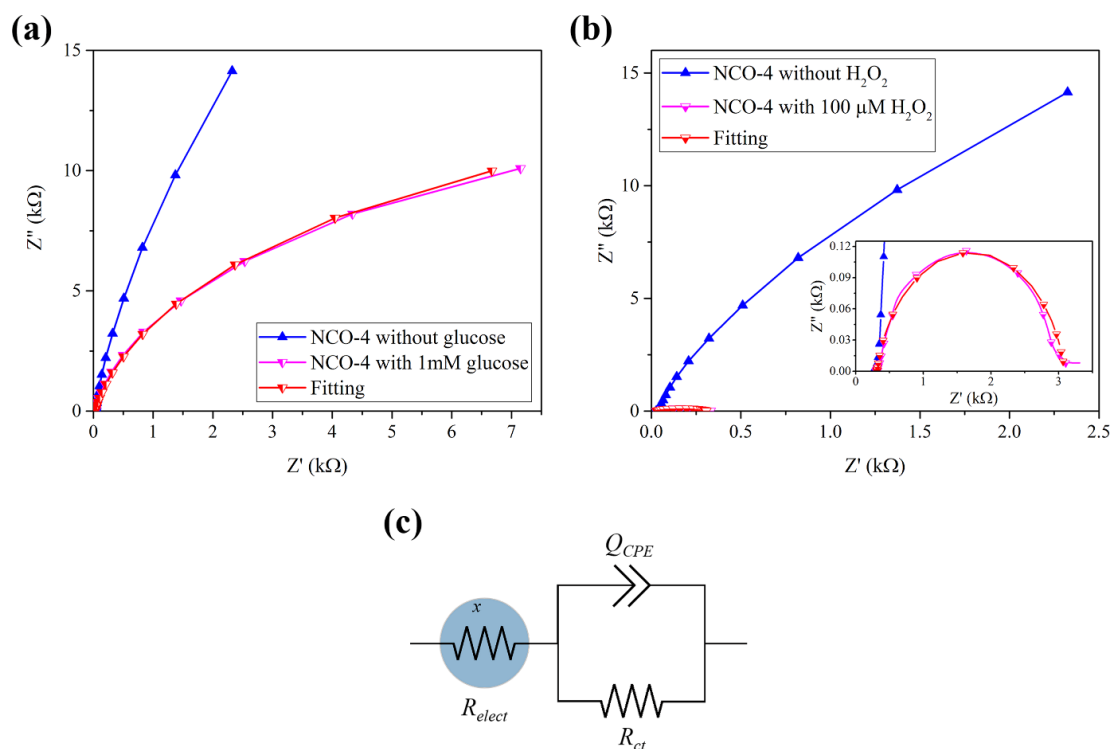
Fig. 8.8 Nyquist plots for NCO-4/GE in absence and presence of analytes: (a) 1 mM glucose and (b) 100 µM H_2O_2. (c) Randles equivalent circuit fitted for EIS spectra.

Table 8.1: Performance comparison of NCO based glucose and H_2O_2 biosensors.

Type of electrode	Analyte	Response time (s)	Linear range (μM)	Limit of detection (μM)	Sensitivity (μA·mM⁻¹·cm⁻²)	Reference
Electrospun NCO/GL nanofibers synthesized at T = 773 K and t = 4 h	Glucose	6	50-400	1.2	930.7	Present work
			400-1100	2.1	576.2	
	H_2O_2	1.6	20-200	1.7	673.5	
			200-700	5.3	216.5	
Electrospun Co_3O_4 nanofibers synthesized at T = 673 K and t = 2 h	Glucose	1.5	50-400	-	1050	(George and Anandhan 2016)
	H_2O_2	6.6	20-400	-	3250	
NCO hollow nanospheres	Glucose	10	10-300	0.6	1917	(Huang et al. 2017a)
			300-2240		703	
NCO hierarchical hollow nanorods/stainless steel	Glucose	2	0.3-1000	0.16	1685.1	(Yang et al. 2016)

NCO/three-dimensional graphene foam	Glucose	-	0.5-590	0.38	2524	(Wu et al. 2015)
NiCoO$_2$ nanoflakes/carbon nanotube	Glucose	7	10-1550	1.14	1424.41	(Tang et al. 2016)
NCO nanosheets/indium tin oxide	Glucose	26	5-65	0.38	6690	(Naik et al. 2015)
NCO/N-rGO/ionic liquid	Glucose	2	1-4555	0.18	3760	(Rao et al. 2017)
NCO nanowrinkle/rGO	Glucose	-	5-8560	2	548.9	(Ma et al. 2016)
MoS$_2$-NCO nanoplates	Glucose	5	1-1600	0.152	1748.58	(Wang et al. 2018)
NCO nanoneedles/Ni foam	Glucose	10	5-15000	1.49	91.34 mV·dec^{-1}	(Hussain et al. 2014)
NCO/rGO	Glucose	2	10-2650	3.79	1773.61	(Wang et al. 2013b)

NCO/polyaniline	Glucose	5	15-4735	0.3833	4550	(Yu et al. 2016)
Rectangular flake-like mesoporous NCO	Glucose	1	0.001-1900	0.0003	662.31	(Cui et al. 2017)
NCO hollow nanospheres/rGO	Glucose	5	40-1280	0.7	2082.57	(Wang et al. 2017a)
Urchin-like NCO	Glucose	1	0.37-2000	0.37	72.4	(Qin et al. 2017)
NCO nanosheets/Ni foam	Glucose	-	5-90	2.46	27500	(Naik et al. 2017)
NCO-Pd nanosheets/Ni foam				0.28	40030	
NCO nanorods	Glucose	3	1-880	0.063	4710	(Saraf et al. 2017)

rGO: reduced graphene oxide and N-rGO: nitrogen doped- rGO.

Along similar lines, the diameter of the semicircle was found to be smaller in presence of H_2O_2, which again suggests more intensified CT at the electrode/electrolyte interface. To have an insight into the interface dynamics, a simple Randles equivalent circuit (Figure 8.8c) was fitted to the Nyquist plots based on Bode phase plots (Section II.11) assuming defects to be present in the material. The fitted circuit is compatible with the plots, and the parameters obtained are tabulated in Table 8.2. The low frequency regions of the Nyquist plots are not linear for both the analytes. This confirms that there was no significant mass diffusion process involved at the electrode/electrolyte interface. Hence, R_{ct} (a function of the working electrode potential and the analyte concentration) alone influence the CT rate (sensing behavior) at the electrode during the oxidation of analytes without any diffusion impedance contribution (Saraf et al. 2017). The R_{elect} corresponds to the electrolyte resistance, Q_{CPE} and C_{dl} represent the constant phase element and pseudo capacitance of double-layer. In case of non-ideal capacitance, *i.e.*, material having defects, Q_{CPE} cannot be considered as capacitance and hence, C_{dl} is given by (Huang et al. 2011):

$$C_{dl} = R_{ct}^{(1-\xi)/\xi} \times Q_{CPE}^{1/\xi}, \tag{8.11}$$

where ξ is the exponential factor, which is equal to zero when Q_{CPE} represents pure resistor and unity when Q_{CPE} is pseudo capacitance.

From Table 8.2, it is observed that R_{ct} and C_{dl} decrease upon the addition of analytes to the electrolyte, which is synchronous with the increase in response current as seen from CV and CA (Saraf et al. 2017). The decrease in C_{dl} may be attributed to decrease in defects/active sites during the electrocatalytic reaction. Therefore, C_{dl} is the least for bare GE as no active sites/ionic species present in the vicinity of the electrode. This phenomenon also explains the diffusion of analytes from electrolyte to electrocatalytic active sites. Since R_{ct} is inversely proportional to CT rate at the electrode, the CV and CA analysis shows a decrease in R_{ct} with increase in the analyte concentration. This suggests that at a higher concentration of analytes, a better sensing efficiency is possible, and at a step out, it must be noted that the normal glucose level

in human blood and urine is in the range of 3.9-10 mM and 0-0.8 mM, respectively. Hence, the NCO-4/GE sensor would efficiently perform well in these regions.

Table 8.2: Circuit parameters obtained for Randles equivalent fitting.

Parameter	Bare GE	NCO-4/GE in absence of analytes	NCO-4/GE in presence of 1 mM glucose	NCO-4/GE in presence of 100 µM H_2O_2
R_{elect} (Ω)	23.17	28.24	28.77	31.52
R_{ct} (Ω)	497300	261450	26440	277.4
Q_{CPE} ($F \cdot s^{n-1}$)	0.1367×10^{-3}	1.88×10^{-3}	1.709×10^{-3}	1.904×10^{-3}
ξ	0.9	0.9425	0.9239	0.8779
C_{dl} (μF)	218.46	2743.87	2339.17	1742.25

8.1.6 Electrocatalytic water-splitting

The water-splitting properties of NCO-4 were investigated through CV and CP, and Tafel polarization studies in 1 M NaOH electrolyte medium. The steep increase in the anodic current beyond 0.6 V in Figure 8.4a, corresponds to the oxygen evolution reaction through four-electron transfer process in basic medium:

$$4OH^- \rightarrow 2H_2O + O_2 + 4e^-$$
(8.12)

CV was carried out with conventional three electrodes set-up for 50 cycles, at an optimal scanning rate of 100 mV·s^{-1}. CV were obtained in the negative potential window of 0.0 V to -1.6 V for HER and in the positive potential range of 0 V to 0.8 V. CP study was employed to study the stability of the electrocatalytic process of HER at a constant current of -300 mA and OER at a constant current of 300 mA, for a duration of 1800 s each.

8.1.6.1 HER

The CV studies of NCO-4/GE were employed for HER analysis as it describes the electrode/ion interaction at the cathode. The H$^+$ ion from electrolyte accepts electrons at cathode and becomes a nascent hydrogen atom (chemisorbed) on the electrode

surface and is later converted to H_2 gas (George et al. 2015). Also, the electrocatalytic efficiency can be explained by CV using the response current, as it is a direct indicator of the adsorbed ion concentration.
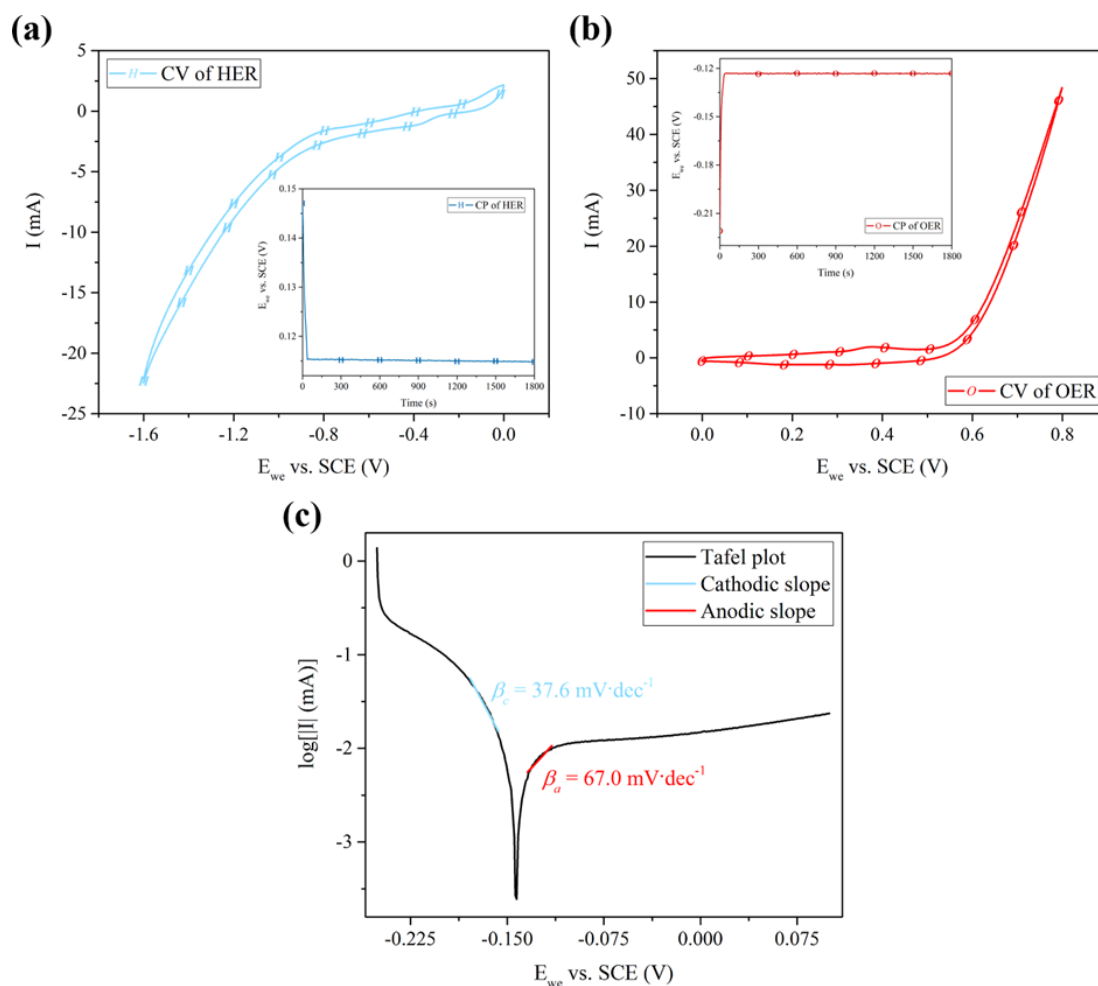
Fig. 8.9 CV curves (inset figures: CP plots) of NCO-4/GE obtained for (a) HER and (b) OER. (c) Tafel polarization plot at a slow scan rate of 5 mV·s^{-1}.

Figure 8.9a shows the HER CV curve for NCO-4/GE. The onset potential of H_2 was found to -0.781 V (-781 mV vs. SCE) or -0.914 V @ 10 mA·cm^{-2} (vs. RHE), beyond which there was a vigorous H_2 evolution and a drastic increase in the cathodic current. The present results show that the efficiency of NCO-4 as electrocatalyst is better than that of Co_3O_4 nanofibers prepared by sol-gel electrospinning in an earlier research study (George et al. 2015). The inset in Figure 8.9a is the CP curve obtained for HER, where at the constant applied current of -300 mA, a continuous reduction of the H^+ ions take place at the cathode surface and thereby resulting in continuous

evolution of H_2. The electrode potential attained during CP analysis at constant current depends on many factors such as, redox couples available in NCO-4, active sites, and H^+ concentration in electrolyte (Bhat et al. 2017). The CP result shows continuous evolution of H_2 for 1800 s with no significant change in the potential, which implies a promising long-term kinetic stability of NCO-4 for use in electrocatalytic water-splitting applications.

8.1.6.2 OER

The OER analysis was done using CV experiments of NCO-4/GE along similar lines as HER, but over a positive potential range (0-0.8 V). From the CV curve of Figure 8.9b, the onset potential of O_2 evolution was noted as 0.491 V (491 mV vs. SCE) or 0.855 V @ 10 mA·cm^{-2} (vs. RHE). The onset potential is the minimum potential at which the oxygen is formed at the electrode at given conditions. The obtained onset potential of O_2 evolution for NCO-4/GE (0.735 V vs. reference hydrogen electrode, RHE) was found to be half the value reported for NCO/reduced graphene oxide electrode (1.57 V vs. RHE) (Umeshbabu et al. 2016) and comparable to Co_3O_4 nanofibers (George et al. 2015) fabricated using similar technique. This indicates the superior electrocatalytic activity of NCO-4/GE electrodes.

The inset in Figure 8.9b shows the results of electrostatic stability studies for OER using CP at a constant applied current of +300 mA. A sharp increase in potential was observed before a stable potential range is attained where OH$^-$ is oxidized to oxygen. A stable potential is achieved, as the fresh bubbles forming at the electrode is in equilibrium with the escaping ones. The continuous evolution of oxygen gas for the entire 1800 s represents better kinetic stability of the electrocatalyst for OER. Furthermore, the onset potential (Table 8.3) conveys that the electrocatalytic performance of NCO-4 is higher towards OER compared to HER due to the affinity of active sites (cations especially in O_v) towards OH$^-$ adsorption at the surface (Un Lee et al. 2013; George et al. 2015). The Tafel polarization plot of NCO-4/GE obtained by LSV at a scan rate of 5 mV·s^{-1} is shown in Figure 8.9c. The *b* for HER and OER were measured to be 37.6 mV·dec^{-1} and 67.0 mV·dec^{-1}, respectively. The Tafel slope values are in agreement with the Volmer-Tafel mechanism for HER with the Tafel reaction being the rate-limiting step (Gao et al. 2016).

Table 8.3: Collation of electrocatalytic HER and OER characteristics for NCO based material.

Type of electrode	Onset potential of H$_2$ evolution (V vs. SCE)	Onset potential of O$_2$ evolution (V vs. SCE)	Tafel slope for HER (mV·dec^{-1})	Tafel slope for OER (mV·dec^{-1})	Electrolyte	Reference
NCO-4/GE developed at T = 773 K and t = 4 h	-0.781 or -0.537 vs. RHE or -0.914 vs. RHE @10 mA·cm^{-2}	0.491 or 0.735 vs. RHE or 0.855 vs. RHE @10 mA·cm^{-2}	37.6	67.0	1 M NaOH	Present study
Co$_3$O$_4$ nanofibers/GE developed at T = 773 K and t = 2 h	-1.26 or -1.016 vs. RHE	0.54 or 0.784 vs. RHE	-	-	1 M KOH	(George et al. 2015)
3D hierarchical porous N-doped graphene/NCO nanosheet film	-	1.54 vs. RHE	-		0.1 M KOH	(Chen and Qiao 2013)

NiCo layered double hydroxide nanoplates/ carbon paper	-	1.597 vs. RHE@10 mA·cm^{-2}	-	40	1 M KOH	(Liang et al. 2015)
NCO nanoneedles/ fluorine-doped tin oxide	-	1.553 vs. RHE@10 mA·cm^{-2}	-	312	1 M KOH	(Shi and Zhao 2014)
3D hierarchical porous Au-NCO/GL/GE	-	0.512	-	-	0.1 M KOH	(Xia et al. 2016b)
3D NCO core-shell nanowires/carbon cloth	-	1.55 vs. RHE@10 mA·cm^{-2}	-	63.1	1 M NaOH	(Chen et al. 2015)
3D hierarchical porous NiFe/NCO nanoflakes/Ni foam	Overpotential -0.105 vs. RHE@10 mA·cm^{-2}	1.47 vs. RHE	88	38.8	1 M KOH	(Xiao et al. 2016)
3D NCO/CuS nanowire/ carbon fiber paper	Overpotential -0.0723 vs. RHE@10 mA·cm^{-2}	-	41	-	0.5 M H$_2$SO$_4$	(An et al. 2015)

Material					Electrolyte	Reference
NCO/carbon black/GE	-	0.526	-	-	0.1 M KOH	(Su et al. 2014)
CFP/NCO/Co$_{0.57}$Ni$_{0.43}$ layered mixed oxide nanosheets	-	1.32 vs. RHE	-	63	0.1 M KOH	(Yin et al. 2016)
	-0.029 vs. RHE	-	34	-	0.5 M H$_2$SO$_4$	
Hierarchical NCO hollow microcuboids/Ni foam	Overpotential -0.110 vs. RHE@10 mA·cm^{-2}	1.52 vs. RHE@10 mA·cm^{-2}	49.7	53.0	1 M NaOH	(Gao et al. 2016)
NCO nanowires array/ fluorine-doped tin oxide	-	1.69 vs. RHE@10 mA·cm^{-2}	-	90	1 M KOH	(Yu et al. 2014)
Au-NCO nanorod array/Ti foil	-	1.59 vs. RHE@10 mA·cm^{-2}	-	63	1 M KOH	(Liu et al. 2014b)
1D NCO nanowire array/GE	-	0.5	-	62	1 M KOH	(Su et al. 2015)
NiTe/NiTe$_2$ nanosheets/GE	-	0.679 vs. RHE	-	115	1 M KOH	(Bhat et al. 2017)
	-0.422 vs. RHE	-	87.4	-	0.5 M H$_2$SO$_4$	

$E_{RHE} = E_{SCE} + 0.244$ V, Onset potential of OER = overpotential + 1.23 V, D: dimensional, and GE: graphite electrode.

8.2   SUMMARY AND CONCLUSIONS

The presence of GL structures deep-seated with NCO nanoparticles along the NCO nanofibers were confirmed by HRTEM, optical spectroscopies, and XPS depth profile analysis. The porosities, multiple band gap energies, NCO crystal defects, and graphene sp^2 defects favored significant improvement in the electrocatalytic activity of NCO towards sensing of glucose and water-splitting phenomena. Among the nanofibers synthesized at different t, NCO-4 showed better electrocatalytic activity because of the synergistic effects of less agglomeration in the GL structure, continuous links between NCO nanoparticles, and increase in defect concentration of NCO nanocrystallite by crystallite splitting

These features of NCO-4 resulted in better sensitivity of analytes in NCO-4/GE sensors, $i.e.$, 1827.5 $\mu A \cdot mM^{-1} \cdot mg^{-1}$ for glucose and 1322.5 $\mu A \cdot mM^{-1} \cdot mg^{-1}$ for H_2O_2, over a wide linear concentration of 50-400 μM and 20-200 μM, respectively. The response time for glucose detection was 6 s and that of H_2O_2 was 1.6 s, using NCO-4/GE sensor. The response time, LOD, and LOQ for both the analytes were comparable to the earlier literature. NCO-4/GE electrodes showed good electrocatalytic water-splitting behavior with an onset potential around -0.78 V (vs. SCE) for hydrogen evolution and ~0.49 V (vs. SCE) for oxygen evolution in alkaline medium. In summary, GL/NCO nanofibers synthesized at $t = 4$ h have a promising potential for multifunctional electrocatalytic activity such as simultaneous glucose detection and water oxidation in alkaline medium.

CHAPTER 9

CHAPTER 9

PYROLYSIS-CONTROLLED SYNTHESIS AND MAGNETIC PROPERTIES OF SOL-GEL ELECTROSPUN NICKEL COBALTITE NANOSTRUCTURES
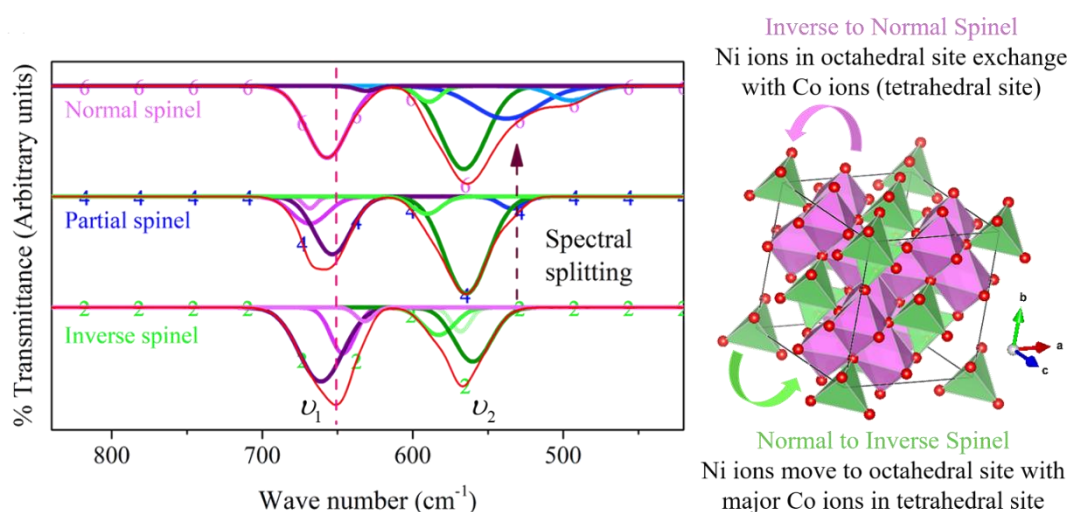
Scheme 9.1 Probable mechanism of structural change responsible for crystallite splitting and magnetic property tailoring.

NCO is a promising magnetic material due to its unique structural composition, where the cations are seated in O_v surrounded by oxygen vacancies. In this chapter, a simple and reliable method was discovered for tuning the morphological and structural changes of NCO nanoparticles, which were reshaped along the NCO nanofibers, by controlling the t. As t increases, NCO transforms from inverse spinel to normal spinel; and the morphology of NCO nanoparticles changes from spherical to rod-like. These changes were validated by the hypsochromic peak shifts in Raman, and FTIR spectroscopies. The magnetic measurements reveal changes in the shape of the hysteresis loop, which are explained on the basis of structural and morphological changes in the nanostructure. The net magnetization increases and coercivity decreases, with an increase in t. These changes in magnetic parameters are attributed to structural changes caused by the formation of oxygen vacancies, and surface effects due to switching in morphology of the NCO nanoparticle.

9.1 RESULTS AND DISCUSSION

9.1.1 Structural correlation

9.1.1.1 Raman spectroscopy
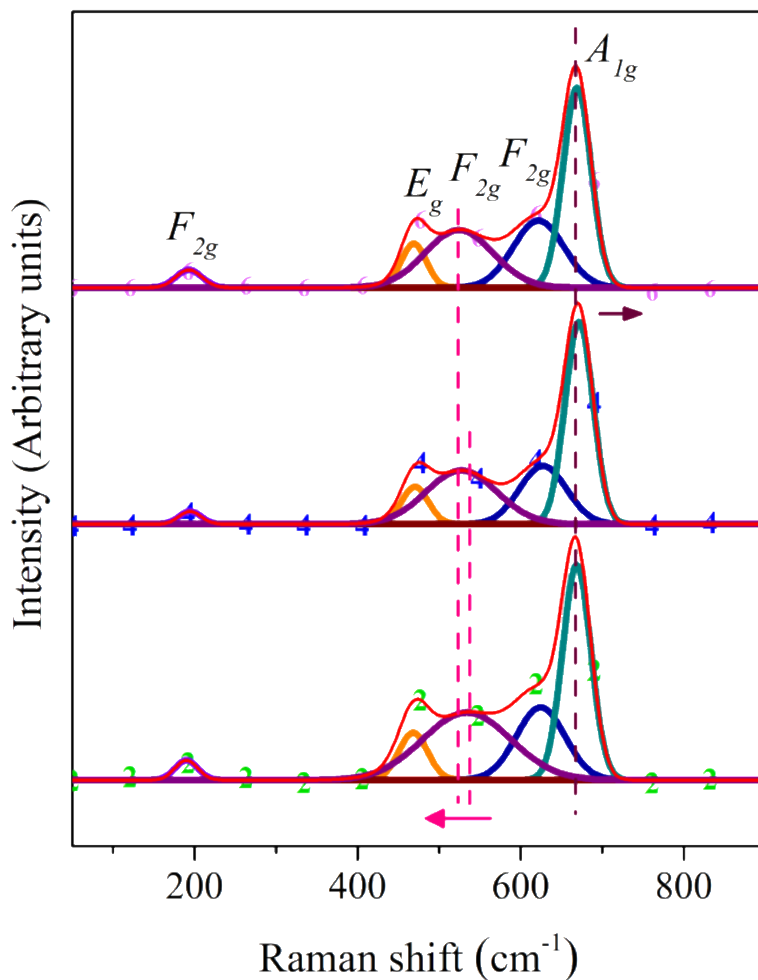
Fig. 9.1 Raman spectra of NCO nanofibers (synthesized at t = 2, 4, and 6 h) showing fingerprint Raman active modes of NCO.

Figure 9.1 shows Raman spectra of the pyrolyzed nanofibers. NCO exhibits five characteristic Raman active modes, A_{1g}, E_g, and three F_{2g}, which are indexed in the deconvoluted peaks of Figure 9.1 (Venkatachalam et al. 2017). The peak broadening indicates the disorder in NCO nanofibers, or the lack of long-range order in the quasi-crystalline form. In addition, the hypsochromic Raman shift is observed with increase in t, suggesting changes in vibrational states due to optical phonon confinement (K. Arora et al. 2007). This would in turn be reflected as changes in chemical bond lengths, causing peculiar morphological and structural changes in NCO nanofibers and

nanoparticles. The high-wave number peak, A_{1g}, has been assigned to a vibration that is largely determined by the O_v cations in normal spinel, whereas F_{2g} and E_g modes combine the vibration of both T_v and O_v of the spinel (Bahlawane et al. 2009). Hence, Raman shift of the active mode peak of NCO nanofibers could suggest changes in oxygen voids or vacancies. Even though slight Raman shifts, and peak broadening were observed, it is well-known that symmetric stretching is the only strong mode of vibration detected by Raman. Besides, nano oxides tend to have asymmetric vibrations due to oxygen vacancies. The structural properties are further analyzed using FTIR analysis, as asymmetric stretching is the prominent mode in FTIR.

9.1.1.2 FTIR spectroscopy

Figure 9.2 shows the FTIR spectra of pyrolyzed nanofibers produced at different *t*. The positional peak shifts that occur in FTIR spectra are due to relative contributions of two or more overlapped peaks (Ryu et al. 2010). The vibrational frequencies depend on factors such as cation mass, metal-oxygen bond strength, distance, and unit cell parameters (nano size/doping effect). In fact, the cobalt ions have greater tendency to occupying O_v than nickel ions do; hence, NCO shows inverse or partial inverse spinel structure. In region of υ_2 absorption, the inverse spinel shows a single absorption peak for the T_v, corresponding to the asymmetric vibration of [NiO$_4$] tetrahedron. The spectral splitting at $t = 4$ and 6 h, may be due to the presence of different cations and redistribution of the trivalent and divalent cations. Usually the lower wave number band is assigned to the [NiO$_4$] tetrahedra, and the higher wave number ones to [CoO$_6$] octahedral cluster (Allen and Paul 1995). This also signifies that there is a transformation of inverse spinel to partial and later, normal spinel with increase in the *t* (Windisch et al. 2004). It should be noted that the highest peak in each site is the consequence of highest valence cation in that oxygen void. The υ_1 absorption shows a hypsochromic shift with decrease in peak intensity as the *t* is increased. This change is due to the redistribution of the highest valence cation in an O_v, [MO$_6$] (Preudhomme and Tarte 1972; Allen and Paul 1995). This observation can be attributed also to the imbalance in oxygen ion due to oxygen vacancies, in presence of trivalent cations (K. Srivastava and Mongia 2016). This is also a characteristic of the spinel inversion taking

place in the crystal. Hence, it can be deduced that oxygen vacancies are significant in NCO nanofibers synthesized at $t = 2$ h, whereas they are the least for $t = 6$ h. These changes in trivalent and divalent ion distribution of a spinel structure plays a vital role in tailoring the electrical and magnetic properties of NCO (McCloy et al. 2015) in as-synthesized nanofibers and thus, are investigated further in VSM analysis (Section 9.1.2) and apparent resistivity (Section 9.1.3). Furthermore, the presence of in situ formed GL structures as seen from previous studies (Chapter 7 and 8) in NCO nanofibers aid the structural change, which supports the tuning of physical properties.
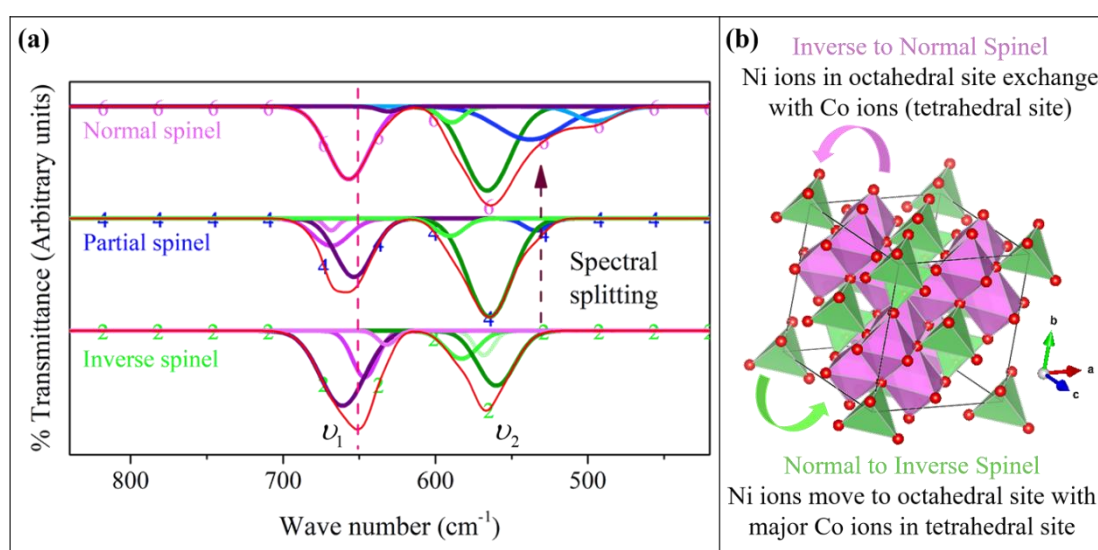
Fig. 9.2 (a) Deconvoluted FTIR spectra of NCO nanofibers (synthesized at $t = 2$, 4, and 6 h) signifying the structural changes in O_v (υ_1) and T_v (υ_2). (b) Schematic depicting the structure transformation from inverse to normal spinel.

9.1.1.3 FESEM micrographs

FESEM micrographs of NCO nanofibers are shown in Figure 9.3, in which Figure 9.3a-c are micrographs obtained at a lower magnification and Figure 9.3d-f are at higher magnification. The NCO particle size increased when t was increased from 2 to 4 h, due to thermally driven particle growth. However, there was a decrease in crystallite size in this regime as per XRD (Section 7.1.2.3), which is due to crystallite splitting in the presence of trivalent cations and in situ formed GL structure as explained in Chapter 7. The structural changes as seen from XRD (Section 7.1.2.3), Raman, and FTIR results, could lead to a change in the particle morphology (Tang and Alivisatos 2006).

Accordingly, it is observed that the changes in NCO particle morphology of nanofibers, which is spherical at $t = 2$ h and transforms to rod-like structure at $t = 6$ h (the transition can be seen from Fig. 9.3d-f). The mechanisms underlying the particle shape transformation, *viz.*, crystallite-particle splitting, and reordering are explained in Section 7.1.4. Similar trends have been reported in earlier literature, where NCO spherical particles are transformed to peanut shape and their magnetic properties are altered (Yang et al. 2017). However, those NCO particles (~500 nm) were bigger than the ones reported in this study, having average particle size of ~47-72 nm (Section 7.1.2.1).
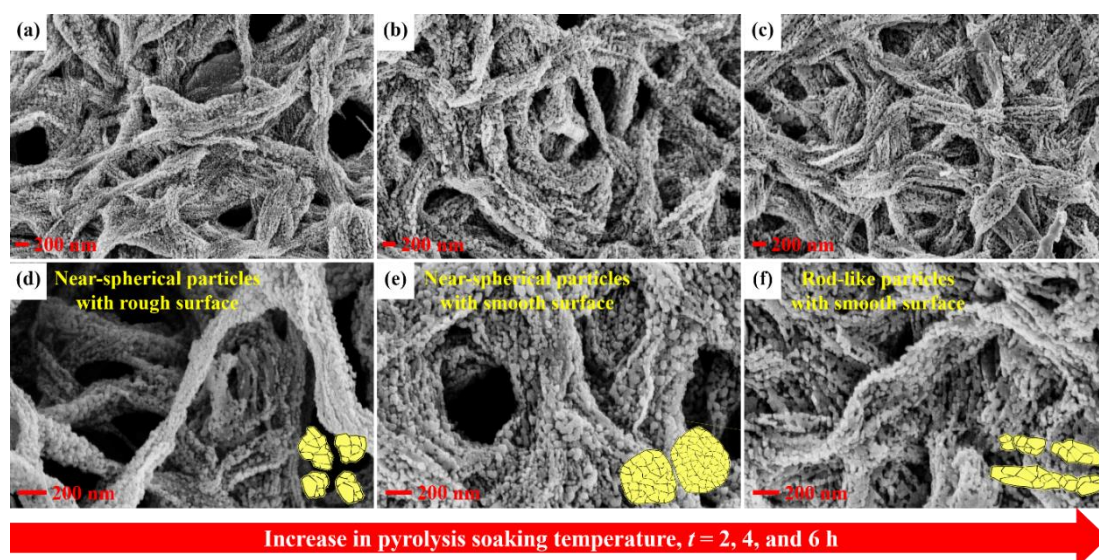
Fig. 9.3 FESEM micrographs of NCO nanofibers synthesized at different *t*: (a-c) 50,000× and (d-f) 100,000× magnification (inset figures are schematics depicting particle morphology).

9.1.2 VSM analysis

Magnetic hysteresis loops of NCO nanofibers, synthesized at different $t = 2$, 4, and 6 h, were measured (Fig. 9.4). The magnetic properties of the NCO nanofibers measured at $\theta_T = 300$ K for different *t*, had appreciable differences in H_c and M_r as shown in Table 9.1 and compared with the literature. The S, SFD, and K were calculated on similar grounds as Equations 5.1, 5.2, and 5.3 of Chapter 5. The magnetic moment of unit cell (n_B in Bohr magnetons) was estimated using the following relation (McHenry et al. 1995; Sontu et al. 2015):

$$n_B = \frac{M_{mol}M_s}{\mu_B N_A},$$ (9.1)

where M_{mol} is the molar mass of NCO, μ_B is Bohr magnetons and N_A is Avogadro number. The value of n_B was comparable with the literature (Table 9.1) and values of S, SFD, and K are tabulated in Table 9.2. The magnetic coercivity and remanence of these NCO nanofibers synthesized at different t exhibited superior values compared to the spherical and peanut shaped NCO nanostructures synthesized by hydrothermal reaction reported elsewhere in literature (Yang et al. 2017). The structure and morphology of the material are expected to influence its magnetic properties.
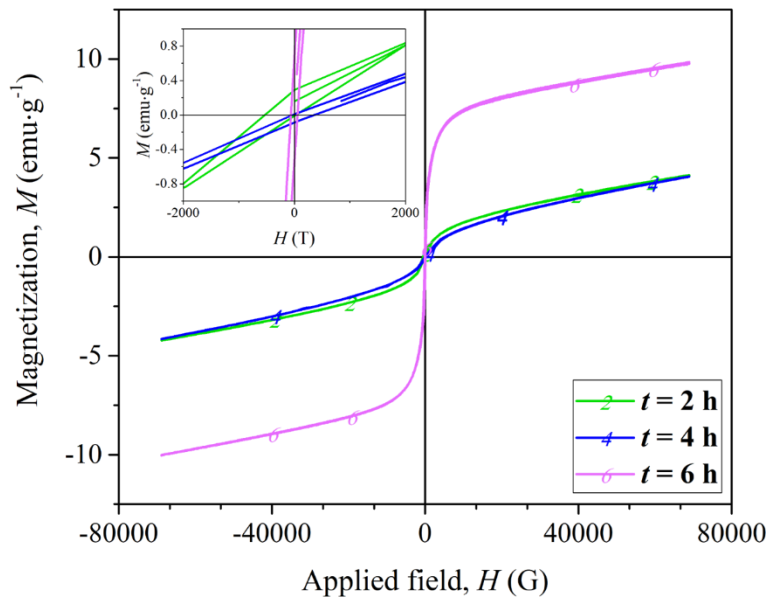
Fig. 9.4 Magnetic hysteresis loops of NCO nanofibers portraying FM to AFM ordering as a function of $t = 2$, 4, and 6 h (inset figure: Magnification of hysteresis loops).

The inset Figure 9.4 indicates FM ordering in the NCO nanofibers, through the obvious hysteresis exhibited in the M-H curves. The low M_r for $t = 2$ h and 4 h, suggests a weak FM behavior due to the existence of uncompensated spin from surface of NCO nanoparticles and spin canting effect (Silambarasan et al. 2017). The variations in M_s are attributed to surface AFM oxidation, super-exchange interactions, crystallinity, particle size, impurities, and surface spin disorder (Umeshbabu et al. 2015). In the present study, the change in M_s can be attributed to the presence of

defects, GL structure (impurity), and cationic exchange in crystal cell that imparts variation in crystallite and particle size. This in turn leads to surface spin disorder, which is a function of surface morphology. The hysteresis loops are characteristic of a soft ferro- or ferrimagnetic material, although the magnetization does not saturate even at the maximum applied field (70,000 G) as expected from magnetic surface disorder effects, often observed for nanostructures.

H_c is dependent on two other major factors apart from magneto-crystalline anisotropy: (i) K and (ii) the interface FM-AFM exchange coupling, where the defects of interfaces give rise to FM. The rod-like particles tend to have large anisotropy giving rise to the additional H_c when compared with spherical particles. In case of thin films or nanosheets, the K increases even further from that of rod-like particles and hence there is an increase in the H_c (Liu et al. 2013c). In this study, it was observed that the spherical nanoparticles tend to have flower-like/thin film structure (agglomerated interfaces with rough surfaces, Fig. 9.4d and e). This, in turn, increases the FM and AFM exchange coupling, where the FM is raised by the interface defects, which leads to increase in H_c. As per the F-center mediated BMP theory, when Ni ions in T_v replace the Co ions in O_v (inverse spinel case, Fig. 9.2b), oxygen vacancies are created in nearby Ni ions in the lattice (Marco et al. 2001; Coey et al. 2005). Subsequently, an electron entrapped in an oxygen vacancy (F-center) couples with the magnetic spins of the nearest Ni ions within the radius of the hydrogen similar orbit of the F-center and forms a BMP, which imparts FM (Su et al. 2015). Hence, an oxygen-deficient phase similar to inverse spinel formed at low temperatures can contribute to increase in H_c. It should be noted that both morphology NCO nanoparticle (K, surface irregularities, Fig. 9.3) and NCO crystal structure (oxygen deficiency or disorder phase) contributed to the variation in H_c.

Table 9.1: Comparison of magnetic parameters: H_c, M_r, M_s, and n_B (measured at $\theta_T = 300$ K) of NCO nanofibers synthesized at different t in this study and various NCO nanostructures from the literature.

Synthesis method	T (K)	t (h)	Morphology/ Stoichiometry/ Particle dimension	D (nm)	H_c (G)	M_r (emu·g⁻¹)	M_s (emu·g⁻¹)	n_B (μB)	Reference
Sol-gel assisted electrospinning followed by annealing	773	2	Spherical with rough surface ~ 56 nm	16	550.3	0.2964	4.11	0.177	Present study
		4	Spherical with smooth surface ~ 72 nm	14	393.6	0.0975	4.06	0.175	
		6	Rod-like with smooth surface ~ 47 nm	17	119.9	1.2438	9.8	0.422	
Rapid combustion followed by annealing	473	4	Near-spherical	7-12	Less than 250	-	2.24	-	(Verma et al. 2008)

eat

Method			Morphology						Reference
Hydrothermal at 453 K for 12 h and followed by annealing	673	3	Hierarchical flower-like super-structures (Nanosheets width ~ 3-4 µm)	-	258.8	0.08	-	-	(Liu et al. 2013c)
Pulsed laser deposition on single crystalline $MgAl_2O_4$ (001) substrates	773	-	Epitaxial thin films	-	494.6	-	-	0.51	(Iliev et al. 2013)
Rapid combustion followed by annealing	473	4	Near-spherical NCO	7	Less than 400	-	3.2	0.14	(Verma et al. 2014)
			Near-spherical $Ni_{0.75}Co_{2.25}O_4$	6	Less than 400	-	2.7	0.12	
Surfactant assisted hydrothermal at 393 K for 48 h and followed by annealing	623	3	Urchin-like	22.5	174	0.63	2.30	-	(Umeshbabu et al. 2015)
			Sheaf-like	25.8	73	0.07	1.90	-	

Surfactant assisted microwave irradiated followed by annealing	773	2	Flake- and hexagonal plate-like 30-50 nm	34.12	251	0.03	-	-	(Babu et al. 2015)
Microwave irradiated followed by annealing	673	2	Nanoplates 400-500 nm	14.74	1.195	0.195	1.889	-	(Nakate and Kale 2016)
Hydrothermal at 393 K and 473 K for 20 h followed by annealing	623	2	Spherical 600 nm	8	67.5	-	0.19	8.20	(Yang et al. 2017)
			Peanut-like ~ 1000 nm	14	119.7	-	1.85	79.82	

Table 9.2: Magnetic (squareness: S, switching field distribution: SFD, and anisotropy constant: K) and electrical parameters of NCO nanofibers synthesized at different t.

t (h)	S	SFD	$K \times 10^{-3}$ (erg·cm^{-3})	Sheet resistance, R_S (MΩ·cm^{-2})	Sheet thickness, ℓ (nm)	Apparent resistivity, $\rho_R = R_S \times \ell$ (Ω·cm)
2	0.072	10.93	1.42	2.9	19.55	5.67
4	0.024	23.71	1.00	2.8	20.43	5.72
6	0.127	7.77	0.74	10.2	17.73	18.08

Later, the discontinuous NCO rods with fewer interface defects (and less magneto-crystalline anisotropy) show a less H_c than the other samples. Again, this may be attributed to the decrease in oxygen deficiency (ordered structure) as the t is increased. In addition, the transformation of inverse spinel to normal spinel (Ni ions are seated in T_v allowing no oxygen vacancies, see Fig. 9.2a), drives the morphological change from spherical to rod-like structure of NCO nanoparticles (Fig. 9.3f). This in turn decreases the K of the rod-like NCO structure in comparison with spherical ones (Chen et al. 2011; Zhao et al. 2012; Liu et al. 2013c). Therefore, the value of H_c decreases with increase in t. It has been reported in earlier literature that the decrease in H_c is due to the presence of larger fraction of small crystallites (Verma et al. 2008). This is consistent with the suggested mechanism of crystallite and particle splitting, through which spherical to rod-like nanoparticles conversion takes place with increase in t as studied in earlier chapter (Chapter 7). Such cation redistribution leading to partially inverted spinel nanostructures induced by ball milling (change is particle size) having variations in magnetic properties has also been reported earlier (Jiang et al. 1999). However, the process of cation reallocation in NCO is seen to be a function of t, in the present study. Based on earlier work, it may be intuitive to expect that the complexation of cations with GL structures would give rise to variations in FM ordering in graphene/metal oxide hybrids, as a result of increased K in the system (Karim Mohammad Razaul et al. 2012). Hence, the presence of GL structures may have a minor contribution to the magnetic properties of NCO nanofibers in the present study.

The spin states of A and B sites are various in the normal and inverse spinels, and the FTIR analysis suggests inverse spinel NCO structure for the low t and normal spinel for the higher t. In the inverse spinel NCO, the cation distribution can be expressed as $(Co_x^{2+} Co_{1-x}^{3+})[Co^{3+}Co_x^{2+} Ni_x^{3+} Ni_{1-x}^{2+}]O_4^{2-}$ $\{0 < x < 1\}$, where ( ) and [ ] represents T_v (A) and O_v [B], respectively. Further, in inverse spinel NCO it is suggested that A-site can be occupied with high spin Co^{2+} ($e_g^4 t_{2g}^3$, $S_q = 3/2$), Co^{3+} ($e_g^3 t_{2g}^3$, $S_q = 2$), while B-site (O_v) is occupied with Ni^{2+} ($e_g^2 t_{2g}^6$, $S_q = 1$), low spin Ni^{3+} ($e_g^1 t_{2g}^6$, $S_q = 1/2$), and diamagnetic low spin Co^{3+} ($e_g^0 t_{2g}^6$, $S_q = 0$) (Bitla et al. 2015). The Co^{3+} ions at the O_v do not contribute to the magnetic behavior and high spin Co^{2+},

Co^{3+} in T_v contribute to the magnetic moment. An extensive literature study reveals that the ideal normal spinel state of the NCO is not yet reported. However, the mixed valence cation distribution in both T_v and O_v are reported, suggesting the presence of Ni ions in T_v, which control the order-disorder of the crystal structure, in turn affect the magnetic and electrical properties of NCO (Iliev et al. 2013; Ndione Paul F. et al. 2013). Besides, the DFT studies suggest that intermediate state can take place between the inverse and normal spinel NCO (Shi et al. 2016). In the present case with increasing the t the magnetization increases, which might be due to the oxygen vacancies as explained previously. According to the DFT analysis, oxygen vacancies can be possible at either A or B sites, which causes an extra electron in e_g state of Co ion in O_v, which causes an increase of magnetization (Shi et al. 2016). Furthermore, as per FTIR with the increase in t (spectral splitting at tetrahedral peak position), the normal spinel formation takes place gradually (Windisch et al. 2004). This suggests the redistribution of majority of the Co and Ni ions into the T_v by diffusion of Ni ions to T_v (Silwal et al. 2013) (which leads to phase separation by further increase in t), decreasing the H_c of NCO with reduced oxygen vacancies (McCloy et al. 2015).

9.1.3   Apparent resistivity

The electrical resistivity (ρ_R) values of the NCO nanofibers pyrolyzed at different t were calculated using probe station and are shown in Table 9.2. (Karim Mohammad Razaul et al. 2012) and (Tareen et al. 1984) reported that Ni^{3+} (due to oxygen deficiency in disorder structure) doping into the spinel would an yield an increase in electrical conductivity at room temperature. It was argued therein that the electronic conductivity in NCO is due to the formation of $\sigma^*(e_g)$ band *via* intervening oxygen ion through strong covalent interaction between low spin Co^{3+}-Ni^{3+} in the O_v assuming the stoichiometry $Co^{2+}[Ni^{3+}Co^{3+}]O_4$ (Appandairajan and Gopalakrishnan 1978). These Ni^{3+} ions in O_v determine the electrical behavior of NCO (Bitla et al. 2015). In addition, (Ndione Paul F. et al. 2013) observed that the electrical conductivity of NCO had increased with cationic disorder, *i.e.*, for inverse spinel structure, where Ni ions occupy the O_v. Furthermore, it has also been reported in literature that electrical conductivity of nanoparticles varies as a function of particle size (Makhlouf et al. 2013). In the present work, the ρ_R from $t = 2$ h to $t = 4$ h has no significance change. This can be

attributed to the defects concentration (or holes responsible for electrical conduction in oxides (George and Anandhan 2014b) that may remain constant before crystallite splitting (insufficient t, $t = 2$ h) and after crystallite splitting ($t = 4$ h), which has a similar trend as the M_s. On the other hand, the in situ formed GL structure/metal oxide interface present in NCO nanofibers, serves as a conductive template or bridge in the porous network of NCO nanoparticles for improving their electrical properties and CT pathways (Wu et al. 2012b). The oxidized groups of these GL structure also enhance bonding, interfacial interactions, and electrical contacts between NCO nanoparticles (Karim Mohammad Razaul et al. 2012; Wu et al. 2015). Therefore, the contribution of both crystal structure disorder as well as the GL structure could have led to the negligible change in ρ_R from $t = 2$ h to $t = 4$ h (spherical particles).

It was noted that the ρ_R has increased significantly as t is increased to 6 h. This increase is connected to the change in morphology of NCO nanoparticles to rod-like structure, though the values are only apparent ones as the nanofiber film acts as a mesh with a high degree of porosity. It can be recalled from VSM analysis (Section 9.1.2) that the rod-like structure is a result of discontinuous particles originated from particle splitting as seen from Chapter 7. Furthermore, the rise in resistivity can also be attributed to the decrease in oxygen deficiency (ordered crystal structure such as normal spinel), where the higher valence cations responsible for small polaron hopping conduction is decreased. This is in good accordance with the observation made in literature wherein the Co ions (in T_v) when replaced by Ni ions (O_v), decrease the electrical conductivity (in other words, increase ρ_R) (Windisch et al. 2001b, 2004; McCloy et al. 2015). It must be noted that the electrical resistivity of NCO nanofibers are synergetic contributions from both the NCO nanoparticles morphology (cationic redistribution) and the in situ formed GL structure (by ordered sp^2 cluster electron conductivity) in NCO nanofibers, which are also the function of defects present in both. The increase in t would degrade the GL structures or oxidize them, creating more disruptions in sp^2 ordering, which in turn reduces electrical conductivity (Mohan et al. 2015). Thus, an increase in ρ for NCO nanofibers is obtained at $t = 6$ h.

9.2 SUMMARY AND CONCLUSIONS

The as-synthesized NCO nanofibers were composed of NCO particles of different shape and size, as they reorder from spherical to rod-like structure with increase in the t. Besides, a structural mutation in T_v and O_v takes place with increase in t, which accounts for transformation of NCO crystal from inverse to partial, and then to normal spinel structure. These structural changes are due to redistribution of cations and oxygen vacancies enable NCO nanomaterials to be tailor-made with soft magnetic properties by varying the synthesis conditions. Simultaneously, the change in morphological shape (from spherical to rod-like structure) of the NCO nanoparticles contribute to the magnetic variations with an increase in t as a result of reduction in the surface defects (decrease in K). The synergism of GL and NCO nanoparticle structures enhances the electrical properties of the NCO nanofibers pyrolyzed at low t, owing to the high valence cation (formed due to oxygen deficiency) and undisrupted sp^2 rings of the GL structure. In summary, NCO nanofibers decorated with GL structure have excellent magnetic and electrical properties, which make them the material of choice for soft magnets, sensors, and electrocatalysts.

CHAPTER 10

CHAPTER 10

SUMMARY AND CONCLUSIONS
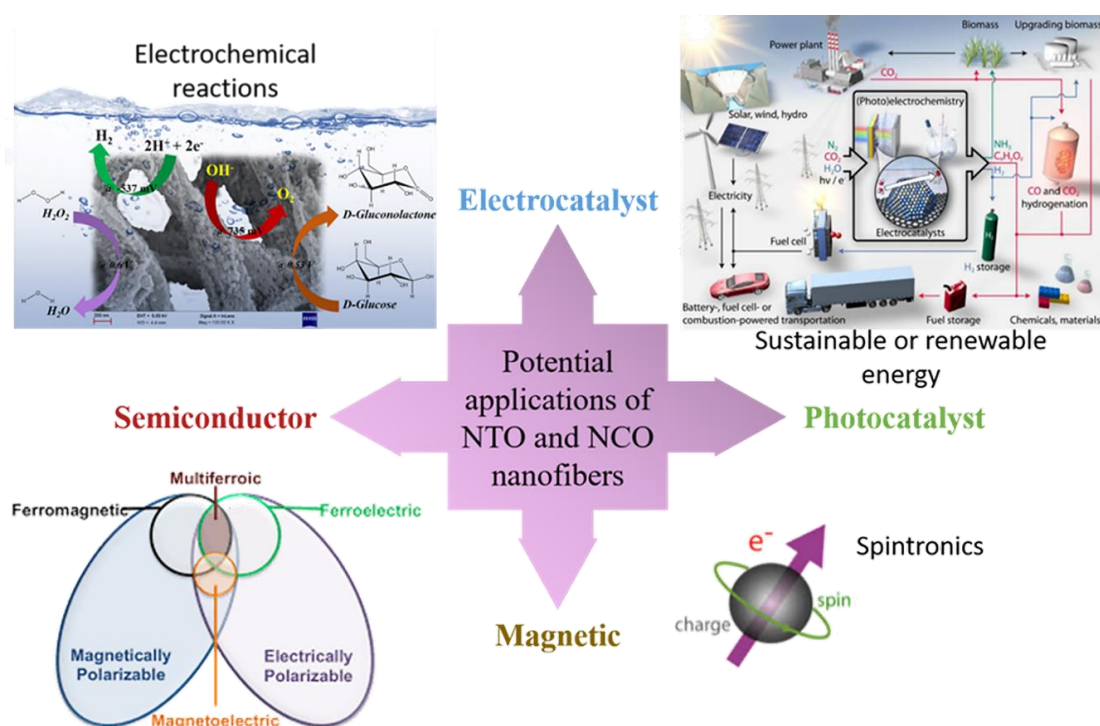
Scheme 10.1 Schematic depicting the potential applications of NTO and NCO nanofibers as sensors, energy, and environmental devices.

NTO and NCO nanofibers were successfully synthesized using sol-gel assisted electrospinning technique followed by pyrolysis. The synergistic effect of pyrolysis parameters and SAN (used as polymeric binder in electrospinning) was instrumental in manipulating the structure, morphology, composition, and physico-chemical properties of NTO and NCO nanofibers.

10.1 PART ONE

SAN was successfully used as the sacrificial polymeric binder for the synthesis of NTO nanofibers. The non-stoichiometric SNTO were imbedded in INTO nanofibers obtained due to *carbothermal reduction* occurring between Ti^{4+} complex of precursor and nitrile functional group of the SAN. The polymorphism of NTO was first observed in this study at such low temperatures of synthesis. The mosaic structured nanofibers with high

content of SNTO were obtained at 773 K and 973 K, whereas bamboo structured NTO nanofibers were obtained at 1173 K with relatively less SNTO concentration. The result suggests a new synthesis technique for obtaining non-stoichiometric materials at low temperatures such as SNTO. Furthermore, the mosaic structured NTO nanofibers, developed at T = 773 K showed superior performance as electrode for HER, while bamboo structured NTO nanofibers (T = 1173 K) were good electrode materials for OER due to the synergetic effect of SNTO content, NTO crystallite and particle size, and porosity of NTO nanofiber. In addition, DFT analysis was employed to understand the band structures and optical properties of SNTO (for the first time) and INTO as individual materials. The SNTO/INTO nanofibers unveil as potential electrocatalyst for bifunctional water-splitting and photo/electrochemical applications. In addition, the FM-AFM exchange coupling between SNTO and INTO in long-range ordering along the nanofibers, the shape anisotropy of NCO nanofibers, and the defects decide the magnetic properties of NTO nanofibers obtained at different T. SNTO/INTO are semiconducting in nature and with weak FM are found to be potential candidates for soft magnetic materials and magnetic sensors.

10.2 PART TWO

SAN was also successfully used as the sacrificial polymeric binder for the synthesis of NCO nanofibers. The additional fictitious forces acting on precursor nanofibers during electrospinning, when RDI collector was used, played a remarkable role in the formation of randomly oriented fibers. This indigenously built RDI collector was found to be optimal collector for synthesis of NCO nanofibers, which avoids agglomeration of precursor nanofibers and defects during pyrolysis. Also, theoretically proven to be an optimal collector for all inorganic nanofibers synthesized using similar techniques. The crystallite and particle splitting, and re-ordering phenomena of NCO nanoparticles transform their shape from near spherical to rod-like structure as a function of t. These morphological changes affect the physico-chemical properties of NCO nanofibers. Eventually, it was discovered that the formation and presence of GL structures, due to the unique feature of SAN (polar functional groups), are responsible for these above-mentioned phenomena. And the GL structures thus formed also affect the physico-chemical properties of NCO nanofibers.

The electrocatalytic activity of GL/NCO nanofibers obtained at different t are compared by CV analysis. The GL/NCO nanofibers obtained at $t = 4$ h had a good electrocatalytic behavior due to the synergetic effect of optimal GL structures, NCO crystallite size and particle shape, and porosity of the NCO nanofiber. These attributes of NCO nanofibers ($t = 4$ h) enhanced their sensitivity to analytes such as glucose. NCO nanofibers developed at $t = 4$ h exhibited maximum glucose sensing efficiency with bifunctional electrocatalytic property for water-splitting. Therefore, it can be used as a potential electrode material for multifunctional electrocatalyst in energy and environmental technology. Furthermore, the enhanced ionic conductivity in presence of GL structures gives rise to cationic structural mutation in T_v and O_v as a function of t, which accounts for the transformation of NCO crystal from inverse to partial and normal spinel structure. These structural changes tailor the FM-AFM exchange coupling in the NCO crystal as a function of t and with shape anisotropy (depends on morphology of NCO nanoparticle and nanofiber) and defects present decide the magnetic and electrical properties of these NCO nanofibers. The defective and undisrupted sp^2 GL structures also contribute to these properties, but, are mild and lack long-range ordering. Hence, NCO nanofibers decorated with GL structures having a tunable magnetic and electrical properties as function of t are potential candidates for soft magnets and magnetic sensors.

Overall, this study proves that SAN could be a potential polymeric binder for the synthesis of any MTMO or inorganic nanofibers through sol-gel assisted electrospinning process followed by pyrolysis; and RDI collector is an optimal collector for such combined synthesis techniques. SAN as polymeric binder in electrospinning, and pyrolysis parameters, such as T and t were contributory in tailoring the structural, morphological, compositional, and physico-chemical properties of NTO and NCO nanofibers. The NTO nanofibers are promising candidates as catalysts for bifunctional water electrolysis and other photo/electrochemical reactions. NCO nanofibers are potential material of choice for electrochemical biosensors and bifunctional water-splitting, thus can be considered as one-pot multifunctional electrocatalyst. Both NTO and NCO nanofibers could find their potential applications in the field of magnetism as soft magnets and magnetic sensors. The presence of defects and semiconducting nature

of these nanofibers make them useful in advanced devices such as multiferroics and spintronics.

SCOPE FOR FURTHER WORK

- ❖ Use of SAN as sacrificial polymeric binder for the synthesis of other MTMO nanofibers, especially more than two transition metals.
- ❖ Comparative study on the physico-chemical properties of sol-gel assisted electrospun NTO and NCO nanofibers from SAN and other different polymeric binders, at different pyrolysis conditions.
- ❖ Doping of other elements such as alkaline earth, rare earth, metalloids, nitrogen or carbon nanostructures into NTO and NCO nanofibers, which may enhance the electrocatalytic and magnetic performance.
- ❖ Applications of NTO nanofibers can be explored in:
  - o Batteries as both anode and cathode materials
  - o Fuel cells as electrodes
  - o Photocatalysis
  - o Pigments
  - o Electrochromic materials
  - o Electrical resistance sensors
  - o Multiferroics and spintronics devices.
- ❖ Applications of NCO nanofibers can be explored in:
  - o Supercapacitors and batteries (anode material)
  - o Fuel cells as electrodes
  - o Automobile catalytic convertor as catalyst
  - o Electrochromic materials
  - o Hall and electrical resistance sensors
  - o Multiferroics and spintronics devices.

APPENDIX I   PART ONE

I.1   COEFFICIENT OF FIBER UNIFORMITY

This function is a measure of size distribution, and as the size distribution is uniform, the value of C_{FU} approaches unity. The function is given by (George et al. 2015):

$$C_{FU} = \frac{A_w}{A_n},\qquad\qquad\qquad (I.1)$$

where, $A_n = \sum n_i d_i / \sum n_i$ and $A_w = \sum n_i d_i^2 / \sum n_i d_i$. The d_i is the AFD and n_i is the number of fibers with a diameter d_i.

I.2   TGA OF SAN AND PRECURSOR NANOFIBERS

The degradation of precursor nanofibers was enhanced and accelerated at a temperature less than 773 K compared to SAN nanofibers (Fig. I.1), probably due to the catalytic activity of acetic acid released from the precursor salts at an early stage (Scheirs 2000). Similar observation was found in other literature (George and Anandhan 2014b; George et al. 2015).
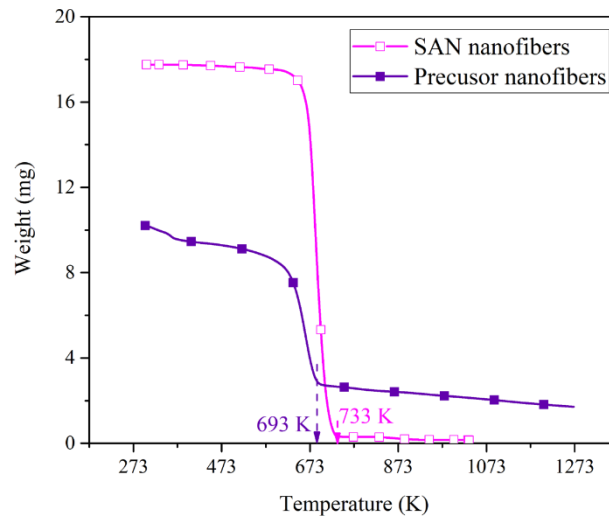
Fig. I.1 Comparison of SAN and precursor nanofibers TGA curves.

I.3   CRYSTAL PARAMETERS

The lattice parameter of spinel system was calculated assuming a cubic structure, using the formula:

$$\frac{1}{d_{hkl}^2} = \frac{(h^2 + k^2 + l^2)}{a^2} \qquad (I.2)$$

Whereas, the lattice parameter of the rhombohedral system was calculated assuming a hexagonal structure (Murugan et al. 2006; Gambhire et al. 2008; Vijayalakshmi and Rajendran 2012; Nguyen-Phan et al. 2014), using the formula:

$$\frac{1}{d_{hkl}^2} = \frac{4}{3}\left[\frac{(h^2 + k^2 + l^2)}{a^2}\right] + \left(\frac{l^2}{c^2}\right), \qquad (I.3)$$

where, d_{hkl} is d-spacing, a and c are lattice dimensions, and h, k, l are Miller indices for planes in the crystal lattice. Tables I.1, I.2, and I.3 show the crystallite parameters of SNTO/INTO nanofibers.

I.4 QUANTITATIVE ANALYSIS OF SNTO USING XRD

The weight percent of spinel NTO in ceramic nanofibers was calculated with the following equation (Kim et al. 2006a):

$$X_{SNTO} = \frac{100}{1 + \left[1.265 \times \left(\dfrac{I_{INTO}}{I_{SNTO}}\right)\right]}, \qquad (I.4)$$

where, I_{SNTO} and I_{INTO} are integrated intensities of major peaks of SNTO (4 0 0) and INTO (1 0 4) phases, respectively, obtained from XRD patterns.

I.5 WILLIAMSON-HALL METHOD

The strain induced peak broadening arising from crystal imperfections and distortion are calculated using Williamson-Hall method (George and Anandhan 2014a). The peak width at half maximum intensity is given by:

$$\beta_{hkl} = \beta_s + \beta_D \qquad (I.5)$$

$$\beta_{hkl} = \left(\frac{\kappa\lambda}{D\cos\theta}\right) + \left(4\varepsilon\tan\theta\right) \qquad (I.6)$$

Rearranging above equation,

Table I.1: Crystal parameters of SNTO/INTO nanofibers pyrolyzed at 773 K.

Crystal structure	(h k l)	Position ($2\theta°$)	d-spacing (Å)	FWHM, β_{hkl} ($2\theta°$)	Lattice parameter (Å)	
					a	c
SNTO	3 1 1	35.96423	2.49579	0.49008	Theoretical value = 8.3416 Average calculated value = 8.3158	a = c
	2 2 2	37.27572	2.41094	0.46267		
	4 0 0	43.53639	2.07765	0.50173		
	5 1 1	57.75379	1.59547	0.74665		
	4 4 0	63.03931	1.47382	0.28545		
	6 2 2	75.72008	1.25543	0.42393		
INTO	0 1 2	24.28287	3.66337	0.38857	Theoretical value = 5.0274 Average calculated value = 5.0028	Theoretical value = 13.7830 Average calculated value = 13.7539
	1 0 4	33.33643	2.68627	0.3968		
	1 1 0	35.96423	2.49579	0.49008		
	0 2 4	49.699	1.83349	0.60615		
	1 1 -6	54.27984	1.68908	0.50898		
	3 0 0	64.40157	1.4459	0.54941		

Table I.2: Crystal parameters of SNTO/INTO nanofibers pyrolyzed at 973 K.

Crystal structure	(h k l)	Position ($2\theta^\circ$)	d-spacing (Å)	FWHM, β_{hkl} ($2\theta^\circ$)	Lattice parameter (Å)	
					a	c
SNTO	3 1 1	35.82646	2.50507	0.34819	Average calculated value = 8.3282	$a = c$
	2 2 2	37.31989	2.40818	0.25737		
	4 0 0	43.37956	2.08479	0.45044		
	5 1 1	57.6028	1.59929	0.61665		
	4 4 0	63.061	1.47337	0.41449		
	6 2 2	75.64726	1.25646	0.52611		
INTO	0 1 2	24.25136	3.66806	0.29329	Average calculated value = 5.0164	Average calculated value = 13.7804
	1 0 4	33.29055	2.68987	0.34758		
	1 1 0	35.82646	2.50507	0.34819		
	0 2 4	49.54273	1.83891	0.35781		
	1 1 -6	54.0894	1.69458	0.4583		
	3 0 0	64.17448	1.45046	0.28819		

Table I.3: Crystal parameters of SNTO/INTO nanofibers pyrolyzed at 1173 K.

Crystal structure	(h k l)	Position ($2\theta^\circ$)	d-spacing (Å)	FWHM, β_{hkl} ($2\theta^\circ$)	Lattice parameter (Å)	
					a	c
SNTO	3 1 1	35.79207	2.5074	0.22928	Average calculated value = 8.3341	a = c
	2 2 2	37.34212	2.4068	0.30138		
	4 0 0	43.32969	2.08708	0.28158		
	5 1 1	57.55958	1.60039	0.23876		
	4 4 0	62.9569	1.47555	0.37477		
	6 2 2	75.58583	1.25732	0.52611		
INTO	0 1 2	24.2544	3.6676	0.24929	Average calculated value = 5.0146	Average calculated value = 13.7899
	1 0 4	33.21241	2.69602	0.18341		
	1 1 0	35.79207	2.5074	0.22928		
	0 2 4	49.55545	1.83847	0.26626		
	1 1 -6	54.07578	1.69497	0.17794		
	3 0 0	64.15709	1.45081	0.25236		

$$\beta_{hkl}\cos\theta = \left(\frac{\kappa\lambda}{D}\right) + \left(4\varepsilon\sin\theta\right) \tag{I.7}$$

The plots of $\beta_{hkl}\cos\theta$ against $4\sin\theta$ for the inorganic nanofibers are shown in Figure I.2-I.4, where T is the pyrolysis temperature. From the ordinate intercept of the linear fit, the crystallite size (D) was calculated; whereas the lattice strain was obtained from the slope of the linear fit.
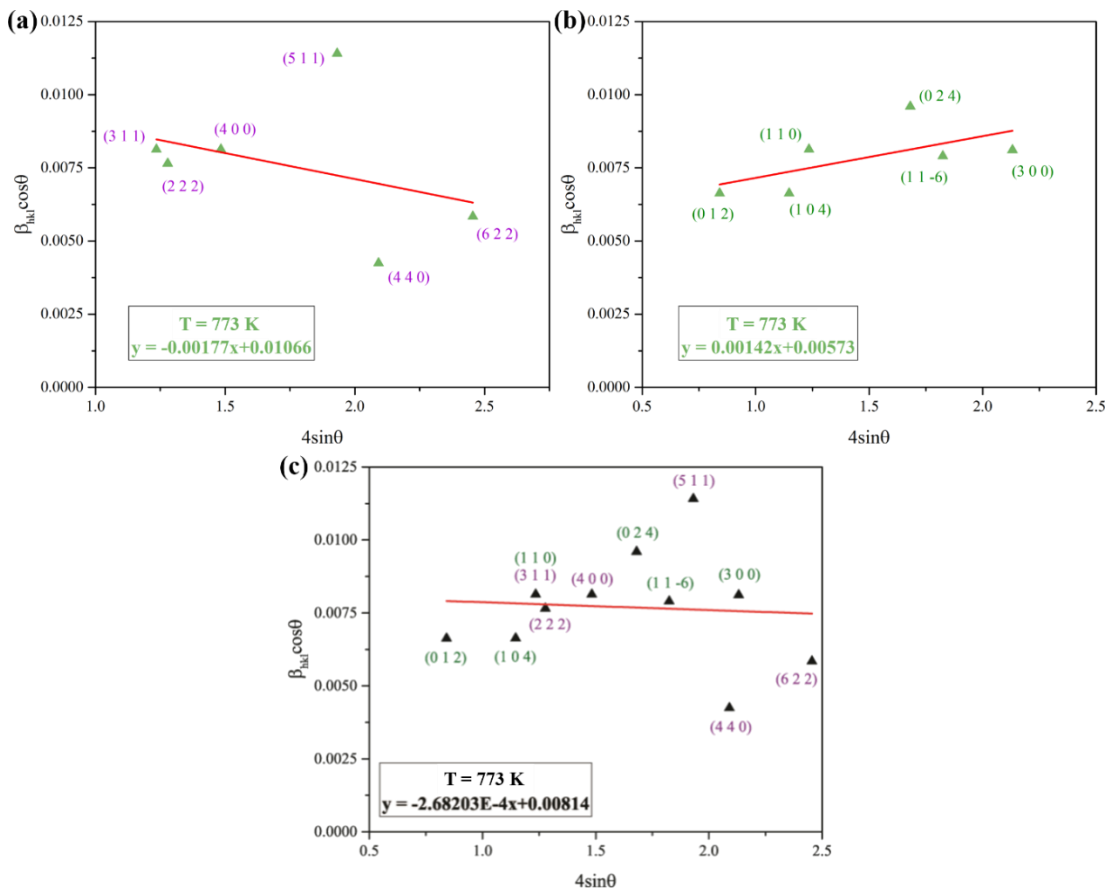
Fig. I.2 Williamson-Hall plots of NTO nanofibers developed at 773 K for (a) SNTO, (b) INTO, and (c) overall crystallites.

I.6   THEORETICAL SSA

The SSA of the nanofibers were calculated assuming that the inorganic nanofibers were smooth, and the length of each nanofiber (L) was 100 μm from FESEM (George and Anandhan 2014a). The theoretical density is given by:

$$\rho = \frac{NM}{vN_A}, \tag{I.8}$$

where, N is the number of atoms per unit cell, M denotes the molecular weight, v represents the volume of the unit cell, and N_A is the Avogadro's number. The SSA was determined considering the above theoretical density, as follows:

a. Mass of arbitrary NTO nanofiber (m) with a known AFD is given by, $m = \rho \times V$, where, V is the volume of nanofiber.

b. Cylindrical NTO nanofiber SSA is given by:

$$\mathrm{SSA} = \frac{\left[\pi(\mathrm{AFD})L\right]}{m} \tag{I.9}$$
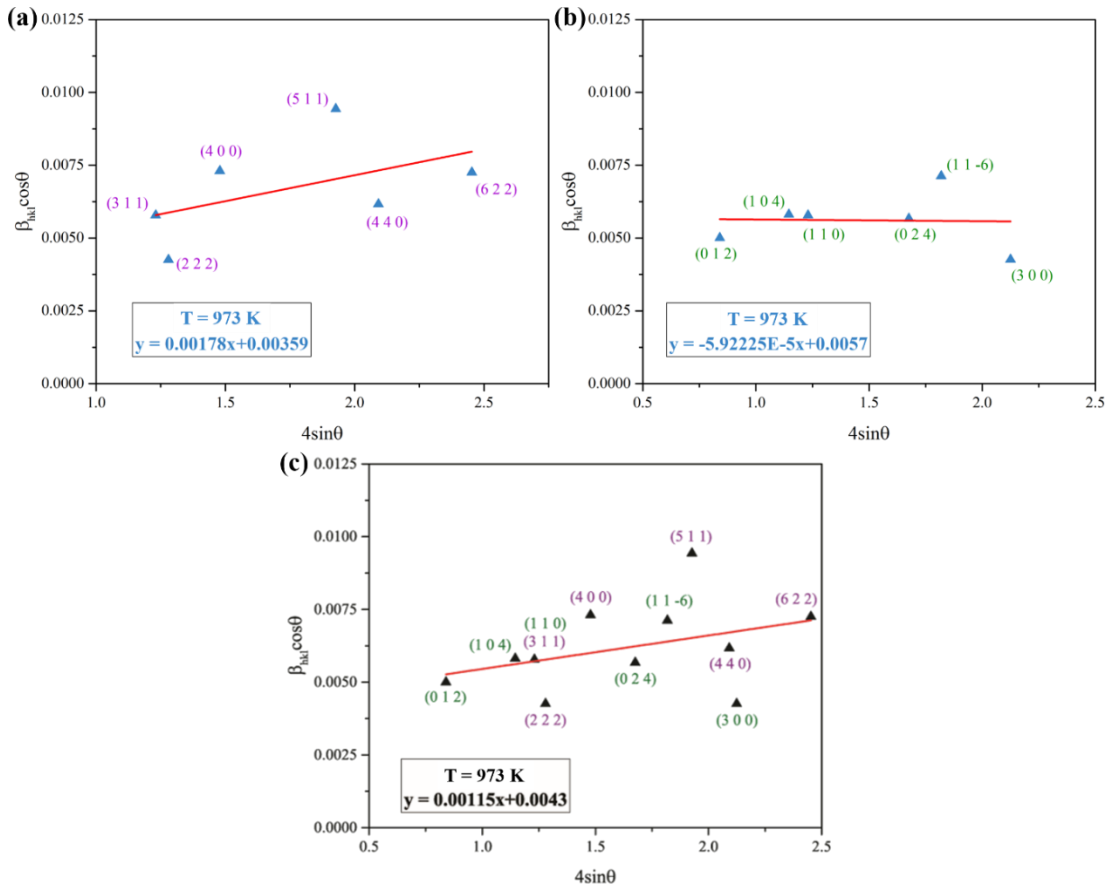
Fig. I.3 Williamson-Hall plots of NTO nanofibers developed at 973 K for (a) SNTO, (b) INTO, and (c) overall crystallites.
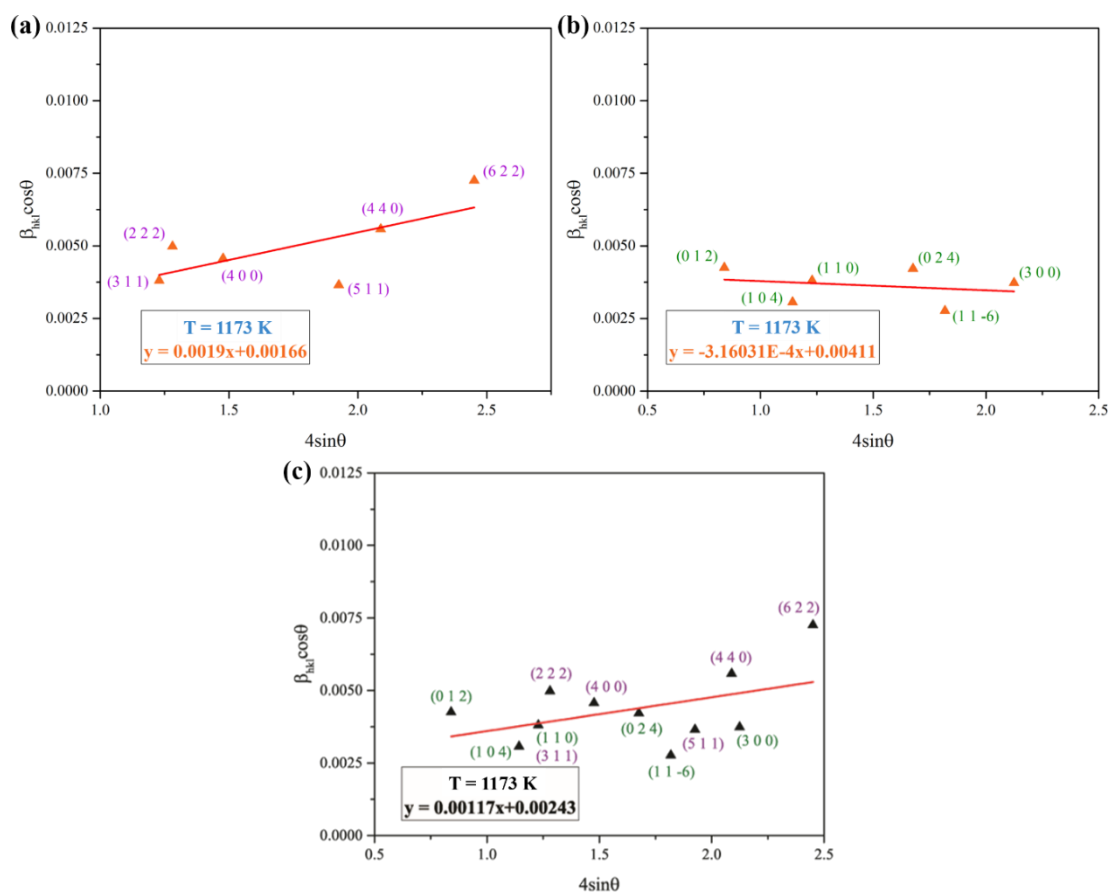
Fig. I.4 Williamson-Hall plots of NTO nanofibers developed at 1173 K for (a) SNTO, (b) INTO, and (c) overall crystallites.

I.7   FESEM-EDS ANALYSIS OF NTO NANOFIBERS ON CARBON TAPE

FESEM micrographs were used to measure the AFD and SD of NTO nanofibers using Image J software as shown in Figure I.5. The mosaic structured nanoparticles in NTO nanofibers obtained at 773 K transforms to bamboo like structure NTO nanofibers with increasing pyrolysis soaking temperature to 1173 K. EDS spectra was acquired for the selected area on the NTO nanofiber. The weight and atomic percentage of each element is shown in Figure I.5.

Pyrolysis temperature (K)	773		973		1173	
	Weight %	Atomic %	Weight %	Atomic %	Weight %	Atomic %
C K	39.57	67.51	53.14	78.62	31.24	57.08
O K	16.66	21.34	12.66	14.06	15.84	21.73
Ti K	20.64	3.08	17.49	2.26	14.21	6.61
Ni K	23.13	8.07	16.71	5.06	38.71	14.58
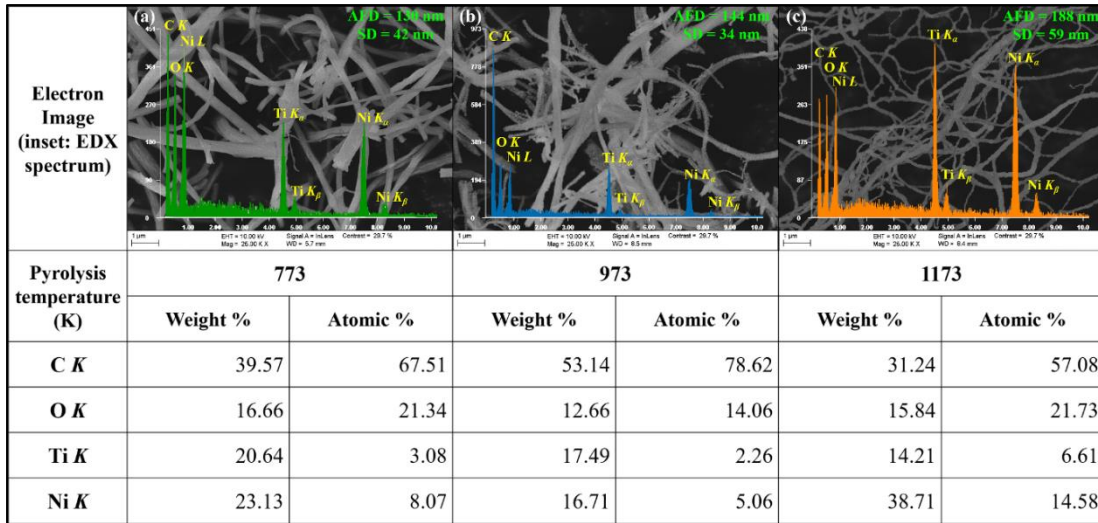
Fig. I.5 FESEM micrographs depicting AFD±SD of NTO nanofibers obtained at different T. Weight and atomic percentage of each elements present in NTO nanofibers recorded by EDS analysis.

I.8   BAND STRUTURE OF INTO AND SNTO

The band structure of INTO and SNTO estimated from first-principles DFT analysis are shown in Figure I.6.
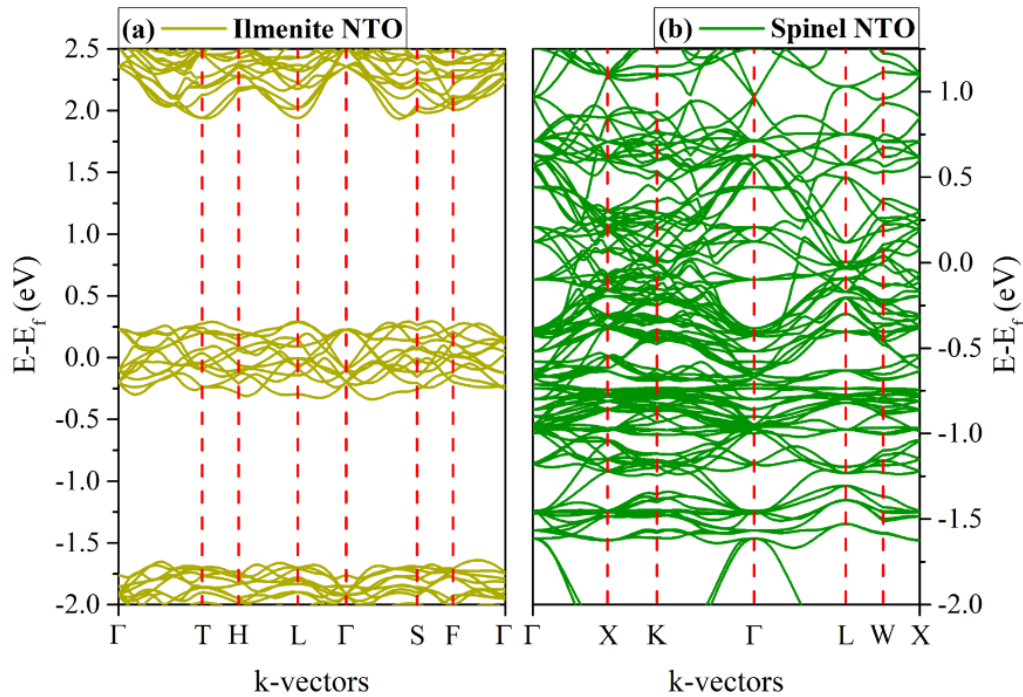
Fig. I.6 Comparison of band structure of (a) INTO and (b) SNTO acquired from DFT analysis.

I.9   XPS ANALYSIS WITH DEPTH PROFILING

Figure I.7a is the XPS survey spectra of NTO nanofibers obtained at different pyrolysis soaking temperatures. Figure I.7b-d are the high-resolution XPS spectra recorded for O, Ni, and Ti elements. The presence of both INTO and SNTO is confirmed in all samples of the NTO nanofibers.
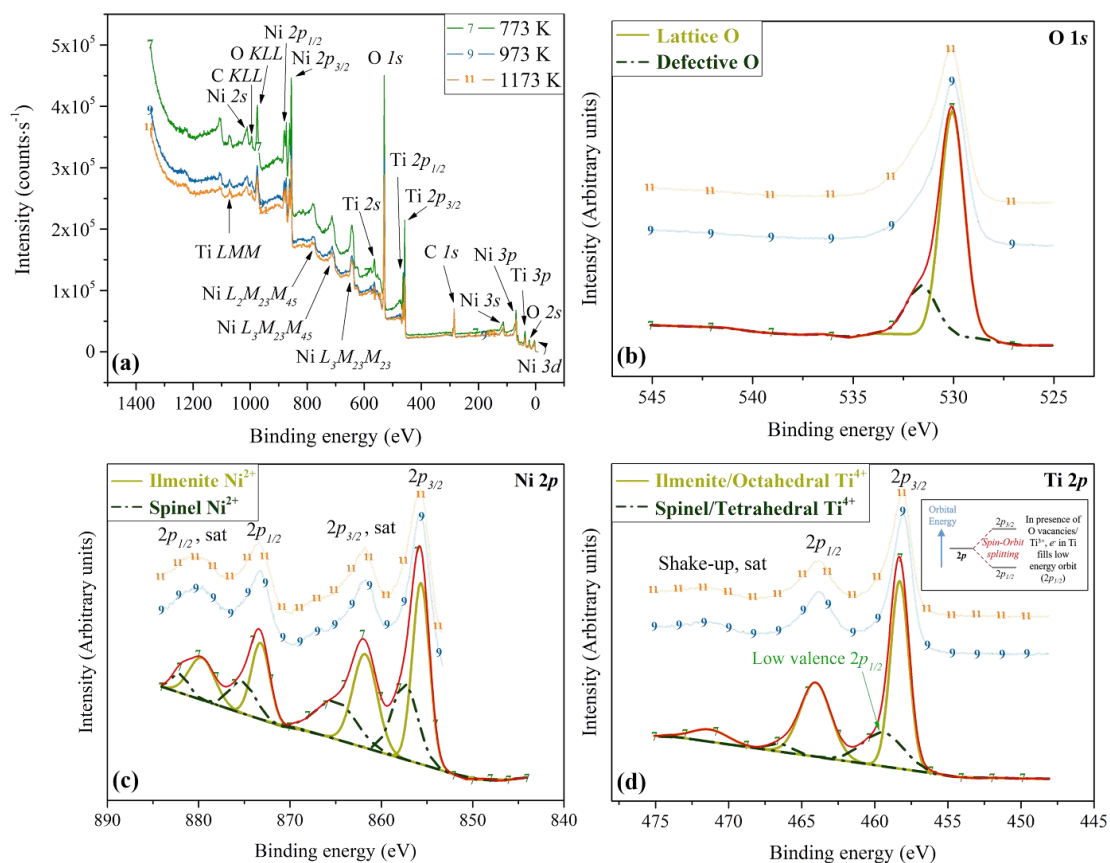
Fig. I.7 XPS of NTO nanofibers obtained at different T: (a) survey spectra, (b) high-resolution spectra for O $1s$, (c) high-resolution spectra for Ni $2p$, and (d) high-resolution spectra for Ti $2p$ (inset figure: spin-orbit splitting for Ti^{3+} ion).

I.10   HYDROGEN GAS DISCHARGE

The increase in the volume of H_2 liberated and collected with increase in negative current is shown in Figure I.8 for NTO/GE obtained from T = 773 K. The quantity of H_2 evolved increases up to -300 mA and reaches saturation. Hence, this -300 mA current can be used for rest of the electrochemical studies, as H_2 discharge is maximum here.
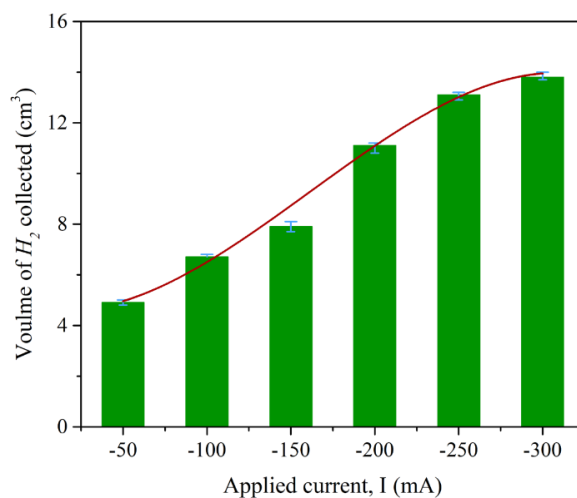
Fig. I.8 Quantity of H_2 liberated with respect to current for NTO/GE developed at T = 773 K.

I.11   OXYGEN GAS DISCHARGE

The increase in the volume of O_2 liberated and collected with increase in positive current is shown in Figure I.9 for NTO/GE obtained from T = 1173 K. The quantity of O_2 evolved increases up to +300 mA and reaches saturation. Hence, this +300 mA current can be used for rest of the electrochemical studies, as O_2 discharge is maximum here.
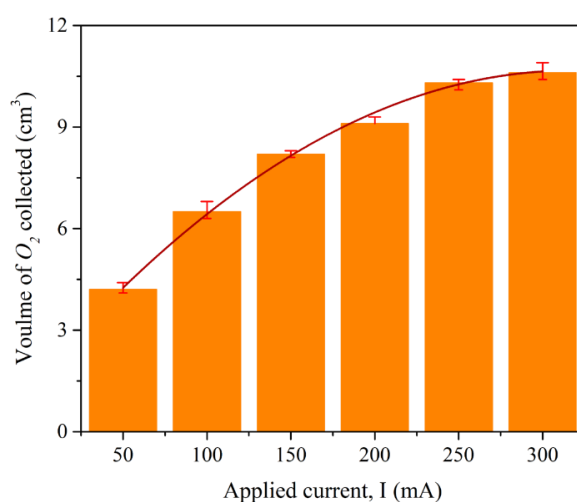
Fig. I.9 Quantity of O_2 liberated with respect to current for NTO/GE developed at T = 1173 K.

APPENDIX II   PART TWO

II.1   TGA OF SAN AND PRECURSOR NANOFIBERS

Figure II.1 shows TGA plots for SAN and precursor nanofibers. SAN undergoes single step degradation, unlike in precursor nanofibers and the complete degradation of SAN was observed at a higher temperature than that of precursor nanofibers. This is because of the acetic acid liberated by precursor salts during degradation, which accelerates the thermal degradation of the polymer chains (George and Anandhan 2015b; George et al. 2015; Kumar et al. 2017).
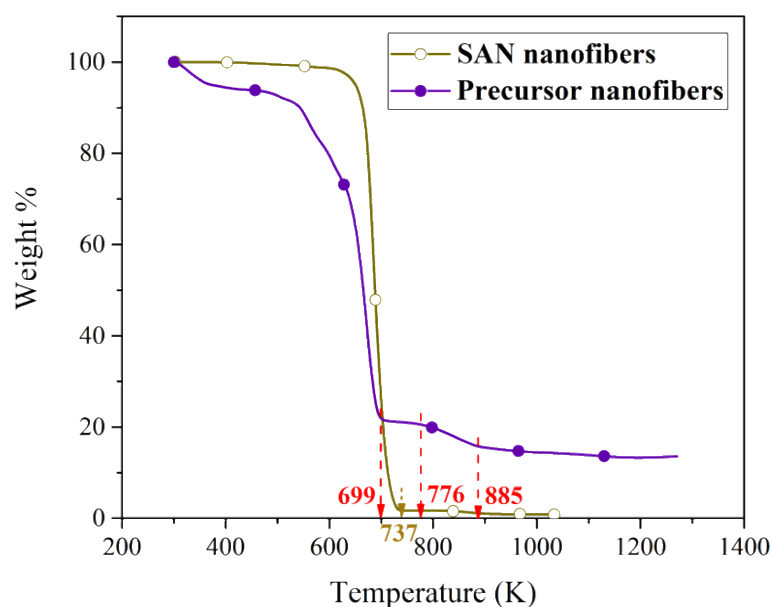
Fig. II.1 TGA plots of SAN and precursor nanofibers.

II.2   SEM-EDS

II.2.1   SEM

The SEM micrographs of NCO nanofibers produced at different t, are shown in Figure II.2a-c, and their size distributions are shown in Figure II.2d-f. The increase in AFD of nanofibers with t can be attributed to the increase in NCO particle size along the nanofibers due to thermally driven particle growth and the fiber opening up along the length of the fiber. The variation in SD suggests the non-uniformity of the fiber diameter. The significant increase in SD of fiber diameter as a function of pyrolysis soaking time can be assigned to the competition between thermally induced densification of fibers and the opening up of the fiber anisotropically along the

longitudinal direction, due to thermal stresses. This also brings about the anisotropic strain distribution in the nanofibers, which will be discussed in the context of XRD (Section 7.1.2.3).
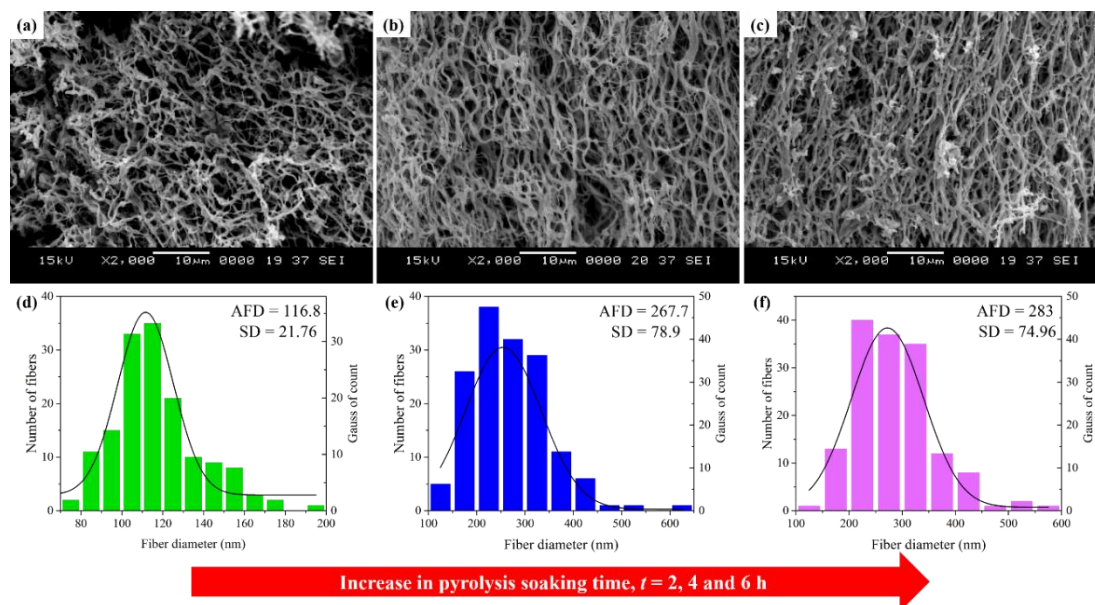
Fig. II.2 (a-c) SEM micrographs and (d-f) the corresponding histogram inferring AFD ± SD of NCO nanofibers obtained at 773 K for different t = 2, 4, and 6 h. AFD and SD are in nm.

II.2.2 EDS

FESEM-EDS enables the approximate estimation of the atomic and mass ratio of Ni, Co, and O present in the NCO nanofibers after pyrolysis. The theoretical wt% ratios of Co:Ni and O:Co are 2.00 and 0.54, respectively, for spinel NCO. The theoretical at% ratio is 2.00 for both Co:Ni and O:Co ratios in spinel NCO. Figure II.3 enlists the weight and atomic percentage of the elements corresponding to different t. It is evident from Figure II.3, that as t has increased the weight and atomic percentage ratios of Ni, Co, and O in NCO nanofibers, and were approaching the values close to that of their theoretical values (spinel structure). This suggests that the non-stoichiometry of NCO nanofibers is reduced with increasing t.

(a)

Element	Weight %	Atomic %
C K	23.12	40.72
N K	0.00	0.00
O K	32.86	43.46
Co K	30.56	10.97
Ni K	13.46	4.85
Co:Ni :: 2:1	2.27	2.26
O:Co :: 2:1	1.08	3.96

Full Scale 264 cts Cursor: 3.631 (5 cts)

$t = 2$ h

(b)

Element	Weight %	Atomic %
C K	0.00	0.00
N K	0.00	0.00
O K	29.79	60.95
Co K	46.31	25.72
Ni K	23.91	13.33
Co:Ni :: 2:1	1.94	1.93
O:Co :: 2:1	0.64	2.37

Full Scale 322 cts Cursor: 2.766 (9 cts)

$t = 4$ h

(c)

Element	Weight %	Atomic %
C K	0.00	0.00
N K	0.00	0.00
O K	29.23	60.31
Co K	46.75	26.19
Ni K	24.02	13.50
Co:Ni :: 2:1	1.95	1.94
O:Co :: 2:1	0.63	2.30

Full Scale 1457 cts Cursor: 2.353 (5 cts)

$t = 6$ h

Fig. II.3 Selected area EDS results depicting the percentage composition of Ni, Co, O, N, and C in NCO nanofibers synthesized at different t.

The presence of elemental carbon was recorded for $t = 2$ h with an wt% and at% of 23.12 and 40.72, correspondingly. This is in good accordance with the thermal and XPS analysis (Section 7.1.1.2 and 7.1.2.6) showing a carbon-based residue with NCO nanofibers. However, the elemental carbon was not detected in case of $t = 4$ and 6 h. At this point it has to be noted that the EDS was analyzed at small areas of single NCO

nanofiber and the sensitivity of EDS equipment is limited to such minute concentration of carbon-based residues.

II.3 XRD CRYSTAL AND CRYSTALLITE ANALYSIS

NCO exists in both normal and inverse spinel structure as per earlier literature (Marco et al. 2000, 2001; Iliev et al. 2013) at various conditions/temperature. Further, XRD analysis could not differentiate between these two crystal structures. Advanced neutron diffractions are used for such characterization. Besides, there are non-stoichiometric defects, and the positions of cations in inverse spinel structure is inconclusive even from advanced studies, as per literature. Hence, in a generic sense, normal spinel crystal structure is assumed while discussing XRD results, *i.e.*, normal spinel structure (AB_2O_4). The lattice parameter of NCO crystallite was estimated using the cubic crystal structure formula:

$$\frac{1}{d_{hkl}^2} = \frac{(h^2 + k^2 + l^2)}{a^2},$$ (II.1)

where, $d_{hkl} = \lambda / (2\sin\theta)$, is the *d*-spacing, θ is Bragg's angle of diffraction, $\lambda \simeq$ 0.1541 nm, is X-ray wavelength (Cu K$_\alpha$); a is cubic lattice dimension and h, k, l are Miller indices for crystal planes of the crystal lattice (Table II.1).

Crystallite sizes were estimated using three different standard models: Scherrer model, Williamson Hall model, and the size-strain model. First, the instrumental contribution to peak broadening was determined using X-ray diffraction pattern and full-width at half maxima (FWHM) of a well-annealed Silicon (Si) sample, β_i. The actual broadening (β_{hkl}) corresponding to each diffraction peak of nanocrystalline NCO was estimated using following relation:

$$\beta_{hkl} = \left[\beta_m^2 - \beta_i^2\right]^{0.5},$$ (II.2)

where β_m is the measured FWHM from fitted diffraction peaks.

II.3.1 Scherrer equation

Using Scherrer equation mentioned below, the crystallite size (D) is calculated and tabulated in Table 7.2:

$$D = \frac{\kappa\lambda}{\beta_{hkl}\cos\theta},$$ (II.3)

where $\kappa \approx 0.9$, is the dimensionless shape factor. It has to be noted that the strain induced peak broadening is neglected in Scherrer equation and this leads to decrease in crystallite size, which is an error of estimation.

II.3.2 Williamson-Hall plot

The crystal imperfections and distortion give rise to the strain induced peak broadening, which can be calculated using Williamson-Hall method.

II.3.2.1 Isotropic strain model

In this model, uniform deformation strain was assumed without considering the anisotropic nature of the crystal. That is, the microstrain (ε), in the crystal lattice was considered to be uniform in all directions of a crystal. The Williamson-Hall equation with isotropic lattice strain is given by:

$$\beta_{hkl}\cos\theta = \varepsilon(4\sin\theta) + \left(\frac{\kappa\lambda}{D}\right)$$ (II.4)

Equation II.4 is in the form of a straight line $y = mx + C$ with slope m and intercept C. Hence, we calculated the microstrain using the slope of the linear fit to the plot of $\beta_{hkl}\cos\theta$ against $4\sin\theta$ as shown in Figure II.4a-c, and the crystallite size from the *y*-axis intercept of linear fit (Table 7.2).

II.3.2.2 Anisotropic strain model

Young's modulus (E_{hkl}) of the crystal structure is anisotropic in nature and this aspect is considered in the anisotropic model. A uniform deformation stress was assumed and hence, it is a more realistic representation of the system. Williamson-Hall equation for this approach is given by:

Table II.1: Average lattice parameter of NCO nanofibers synthesized at different *t*, calculated from XRD analysis.

t (h)	Crystal planes (*h k l*)	XRD peak fit position ($2\theta°$)	*d*-spacing (Å)	FWHM, β_{hkl} ($2\theta°$)	Lattice parameter, *a* (Å) [Theoretical value = 8.1140]	
	2 2 0	31.34365	2.8524	0.57531	8.0678	
	3 1 1	36.7766	2.4425	0.58263	8.1009	
2	4 0 0	44.57589	2.0316	0.06064	8.1264	Average calculated value = 8.0987
	5 1 1	59.17453	1.5605	0.76407	8.1086	
	4 4 0	65.20073	1.4301	0.79876	8.0899	
	2 2 0	31.35722	2.8512	0.57078	8.0644	
	3 1 1	36.88354	2.4357	0.42493	8.0783	
4	2 2 2	38.40112	2.3428	0.54922	8.1157	Average calculated value = 8.0944
	5 1 1	59.11764	1.5619	0.538	8.1159	
	4 4 0	65.1266	1.4315	0.70914	8.0978	

	2 2 0	31.1022	2.874	0.46592	8.1289
	3 1 1	36.73746	2.445	0.52497	8.1092
	2 2 2	38.4346	2.3409	0.38146	8.1091	Average calculated value = 8.1167
6	4 0 0	44.69194	2.0266	0.41799	8.1064
	5 1 1	58.98703	1.565	0.49075	8.132
	4 4 0	64.97561	1.4345	0.60494	8.1148

$$\beta_{hkl} \cos\theta = \sigma\left(\frac{4\sin\theta}{E_{hkl}}\right) + \left(\frac{\kappa\lambda}{D}\right), \tag{II.5}$$

where the microstrain (ε) in Equation II.4 is replaced by $\varepsilon_{hkl} = \sigma/E_{hkl}$ and σ is the uniform deformation stress. Young's modulus, E_{hkl}, whose direction is perpendicular to the crystal planes ($h\ k\ l$) is given by:

$$E_{hkl} = s_{11} - (2s_{11} - 2s_{12} - s_{44})\left[\frac{(k^2l^2 + l^2h^2 + h^2k^2)}{(h^2 + k^2 + l^2)^2}\right], \tag{II.6}$$

where elastic compliances s_{11}, s_{12}, and s_{44} have their values for NCO crystal as 4.5662, -1.4064, and 11.9474 TPa^{-1}, respectively, by appropriate assumption as per literature (Fritsch and Ederer 2010; Zhang et al. 2015). Equation II.5 is also in the form of $y = mx + C$. Therefore, the slope of linear fit to the plot $\beta_{hkl}\cos\theta$ versus $(4\sin\theta)/E_{hkl}$, yields uniform deformation stress and the *y*-axis intercept of the linear fit measures the crystallite size (Figure II.4d-f, Table 7.2 and 7.3).

II.3.3 Size-Strain plot (SSP)

The isotropic model of Williamson-Hall plot did not provide a convincing analysis of crystallite size measurements. However, in case of isotropic strain situations, crystallite size and lattice strain could be better quantified by opting an average crystallite size-strain plot (Tagliente and Massaro 2008; Zak et al. 2011). SSP has a major significance since least weightage is considered for the diffraction data from the reflections at high Bragg's angles, which has a poor precision.

In this model, it is assumed that Lorentzian function describes the profile of crystallite size related peak broadening and Gaussian function describes the microstrain. According to this approximation, the relation follows:

$$\left(d_{hkl}\beta_{hkl}\cos\theta\right)^2 = \frac{\kappa_0}{D}\left(d_{hkl}^2\beta_{hkl}\cos\theta\right) + \left(\frac{\varepsilon}{2}\right)^2, \tag{II.7}$$

where κ_0 is a constant and for spherical crystallites it is equal to 4/3. The corresponding SSP are shown in Figure II.4g-i, and the crystallite sizes are tabulated in Table 7.2.
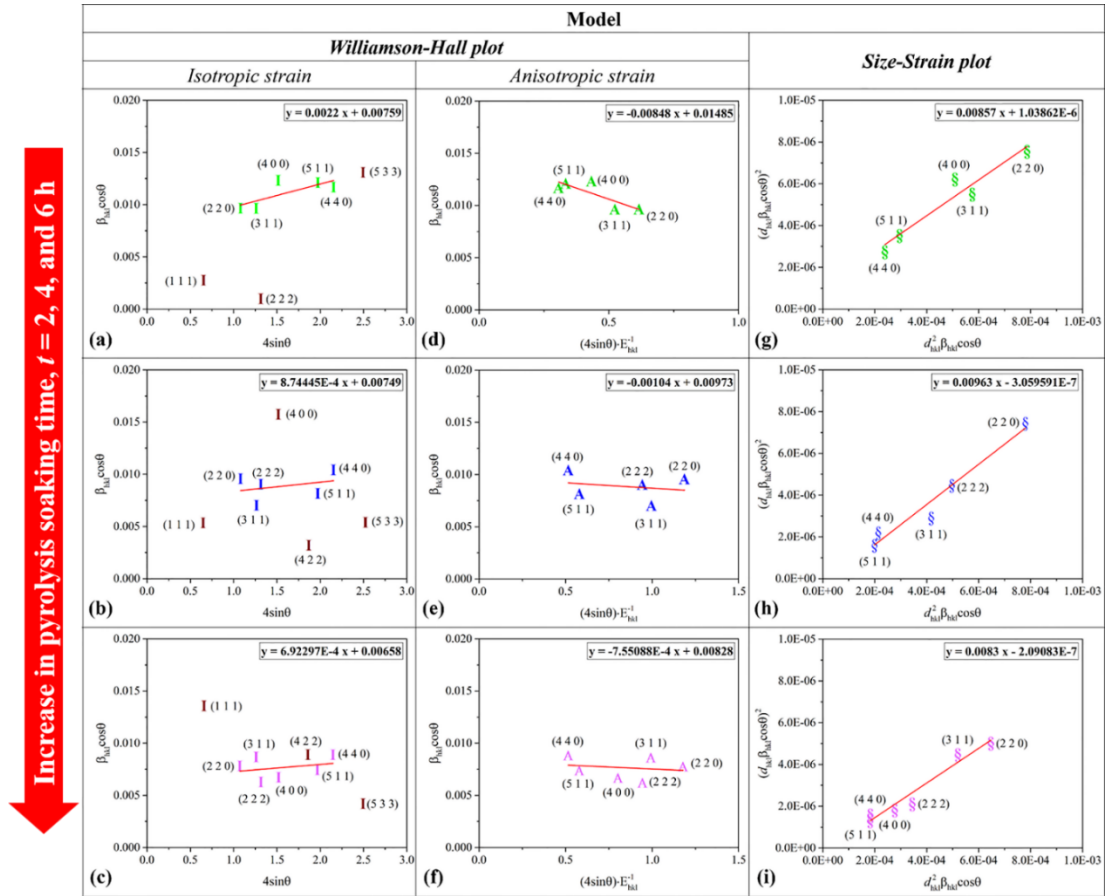
Fig. II.4 Williamson-Hall and size-strain plots of NCO nanofibers synthesized at different *t*.

II.3.4 Crystallite growth kinetics

The crystallite growth exponent (n) was estimated (Fig. II.5) by neglecting initial crystallite size (D_0) in Equation 7.1 of Section 7.1.1.2 (Table II.2), for the above-mentioned models using the formula (Park et al. 2011; Xia et al. 2012):

$$\ln(D) = \left(\frac{1}{n}\right)\ln(t) + \left(\frac{1}{n}\right)\ln(A),$$ (II.8)

where A is the temperature dependent rate constant.

From the standard model for conventional crystallite growth and crystallite boundary migration, the n value is ~2 and hence, the activation energy (E_a) for the crystallite growth and initial crystallite size (D_0) were calculated assuming $n = 2$ in Equation 7.1 as shown in Figure II.6 and tabulated in Table II.2.

Table II.2: Crystallite growth exponent (n), initial crystallite size (D_0) and activation energy for crystallite growth for different models assumed.

Model		Crystallite growth exponent, n	Initial crystallite size, D_0 (nm)	Activation energy for crystallite growth, E_a (kJ·mol⁻¹)
Scherrer equation		2.93	8.45	-28.2
Williamson-Hall plot	*Isotropic strain*	8.45	16.22	-31.3
	Anisotropic strain	1.85	1.74	-27.7
Size-Strain plot	*Pyrolysis soaking time, t = 2 to 4 h*	5.95	17.78	31.4
	Pyrolysis soaking time, t = 4 to 6 h	2.73	7.98	-29.6
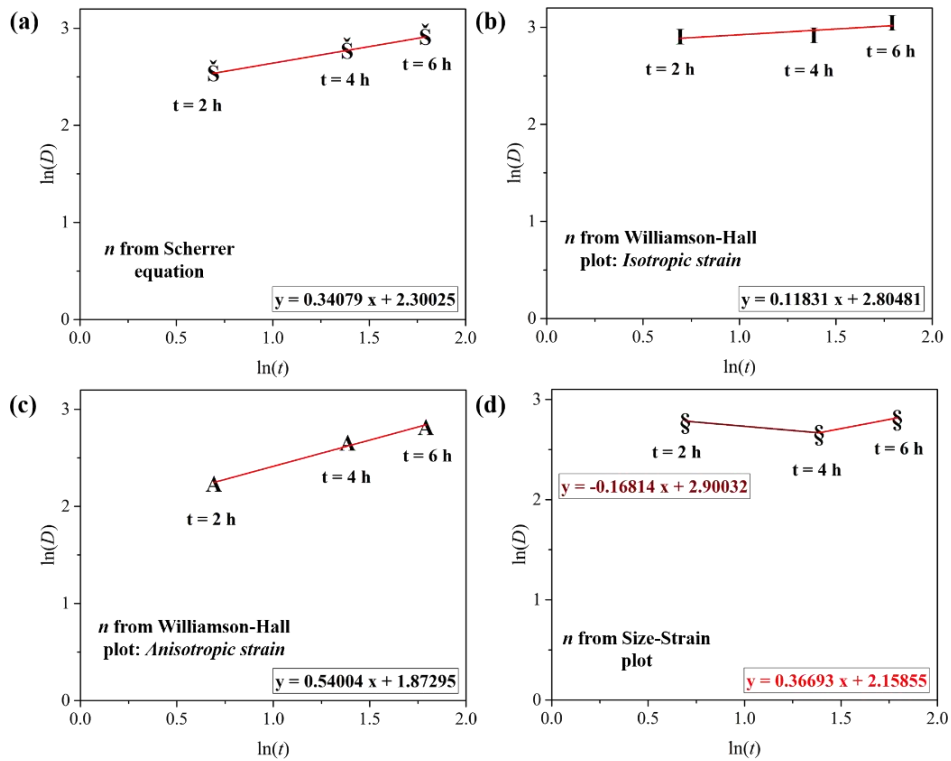
Fig. II.5 $\ln(D)$ versus $\ln(t)$ plots of NCO nanofibers for different models assumed.
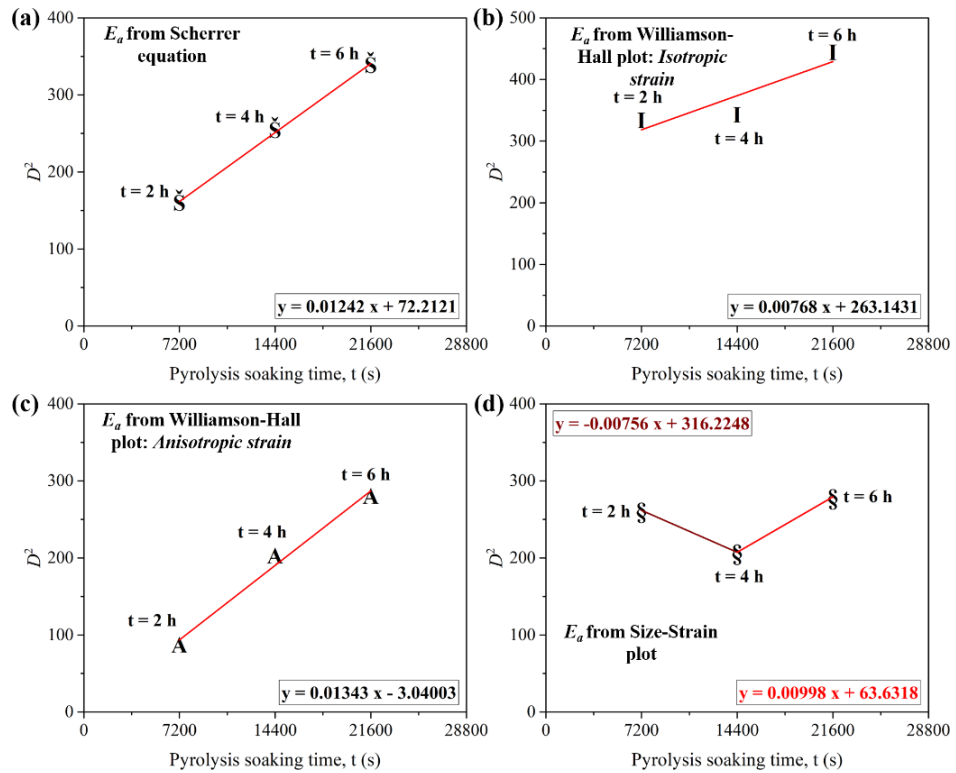
Fig. II.6 D^2 versus t plots of NCO nanofibers for different models assumed.

II.4   BET ISOTHERMS
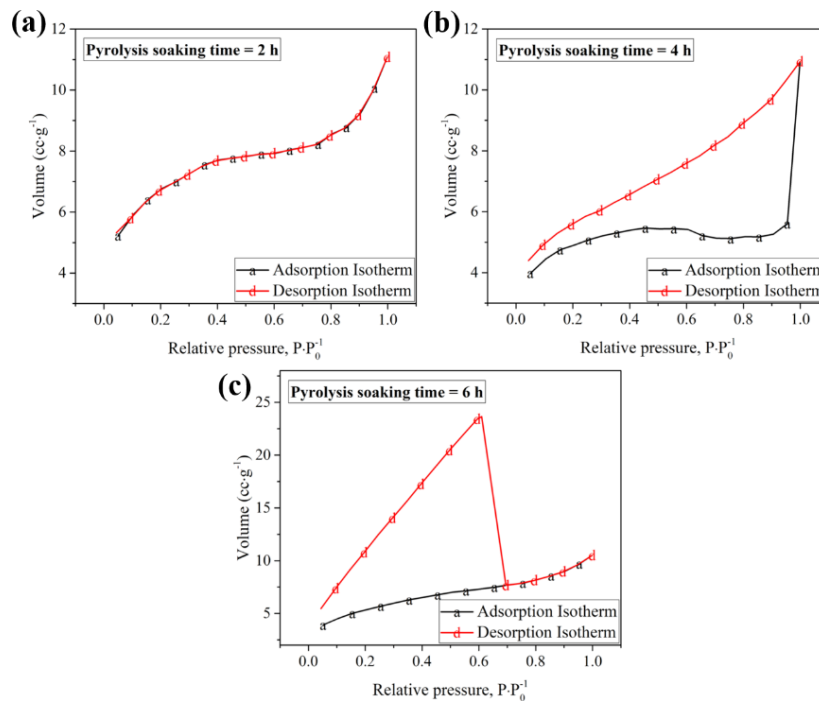
Fig. II.7 Adsorption-desorption isotherms of NCO nanofibers synthesized at different t.

Figure II.7a-c shows the nitrogen gas adsorption-desorption isotherms of NCO nanofibers with different pyrolysis soaking times, $t = 2$, 4, and 6 h; respectively.

II.5 XPS SURVEY ANALYSIS

Figure II.8 shows the survey spectrum of the prepared nanofibers at different t. NCO nanofibers is akin to that of NCO material, where the peaks corresponding to different oxidation state of Ni, Co, O, and C were observed.
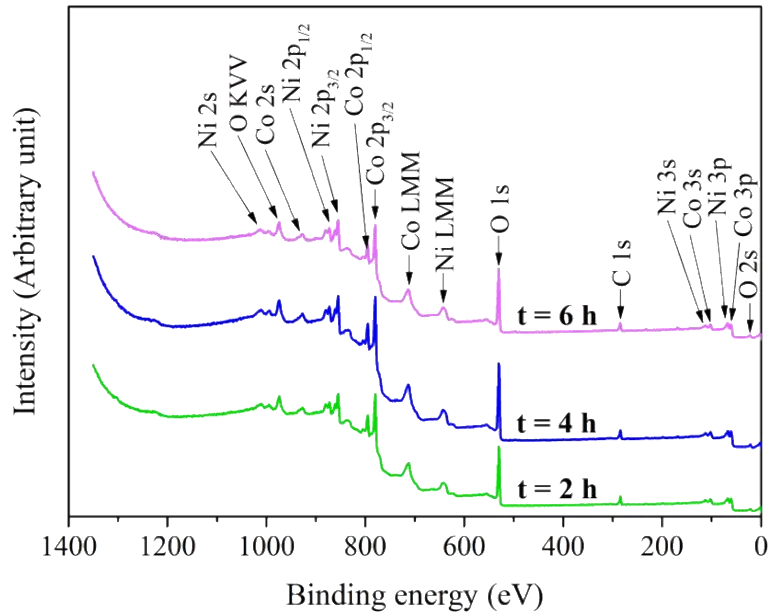
Fig. II.8 XPS survey spectra of NCO nanofibers synthesized at different t.

II.6 TAUC PLOT

II.6.1 Band gap energy

UV-vis-NIR absorption spectrum was converted to Tauc plot, as shown in the Figure 7.9b, to obtain the optical band gap energy of the material. In general, the absorption band gap energy (E_{bg}) of a semiconducting material can be determined using following equation (George and Anandhan 2015b; George et al. 2015):

$$(\alpha h\upsilon)^2 = \Psi(h\upsilon - E_g), \tag{II.9}$$

where α is the absorption coefficient, Ψ is the proportionality coefficient, and $h\upsilon$ is the photon energy.

II.6.2 Urbach energy

The non-stoichiometry of constituent compounds gives rise to differences in band gap energies in the material. Urbach energy is the modification in the band gap owing to the defects present in the material. In Figure 7.9c, the reciprocal of the slope obtained for the linear portion of the plot $\ln(\alpha)$ versus $h\nu$, quantifies Urbach energy (George et al. 2015).

II.7 ANOMALOUS HALL EFFECT

Anomalous Hall effect (AHE) is the change in sign of Hall voltage found in ferromagnetic materials as a consequence of spin orbital coupling. Hall measurements of thin film fiber mesh (porosity around 70%) were calculated and tabulated in Table II.3. AHE can occur due to the morphology, non-stoichiometry, magnetoresistance of the sample, and the impurities present in the sample such as graphene-like structure (McCloy et al. 2015). The sheet resistance (R_S) per cm^2 of the thin film mesh of the NCO nanofibers increase significantly for pyrolysis soaking time, $t = 6$ h, this could be attributed to the change in NCO particle morphology to discontinuous rod-like shape. Further, the least charge carrier density for $t = 4$ h could be due to the crystallite splitting, which increases the number of defects (holes) in the system. It has to be noted that the carrier density measured in this study is for electronic charge, e. And, this might also be reason for p-type semiconductor behavior for NCO nanofibers pyrolyzed at $t = 4$ h.

Table II.3: Hall measurements of thin film NCO nanofibers mesh synthesized at different t.

t (h)	Sheet resistance, R_S ($M\Omega \cdot cm^{-2}$)	Type of semiconductor	Sheet carrier density ($cm^{-2} \times 10^9$)	Bulk carrier density ($cm^{-3} \times 10^{14}$)	Mobility, μ_M ($cm^2 \cdot V^{-1}s^{-1}$)
2	2.85	n-type	1.15	5.79	1901.70
4	2.76	p-type	0.18	0.85	12909.36
6	10.24	n-type	0.82	4.64	743.93

The electrical conduction in NCO is usually by small polaron hopping and this might be the reason for not having a significant change in sheet resistance per cm^2 of the NCO nanofiber mesh from $t = 2$ h to 4 h, as there is no particle splitting occurring here. The samples showed both p and n-type behavior for NCO nanofibers having different pyrolysis soaking time, t. Such a behavior can also occur due to the variation in magnetism depending on the morphology of the nanoparticles, across the composition range as these oxides are highly magnetic (Windisch et al. 2001a, 2002). Some prior work reports that Ni^{3+} (the presence confirmed by XPS) doping into the spinel would also yield p-type semiconductor and increase in electrical conductivity at room temperature (Tareen et al. 1984). In this study, the presence of graphene-like structure should give rise to n-type behavior, as sp^2 configuration is rich in electrons and defective NCO nanofibers being rich in holes. Besides, the crystallite splitting proposed for $t = 4$ h could lead to the formation of large number of vacancies and holes in the NCO nanofibers, which could render them p-type behavior. The mobility (apparent) measured is the effect of the competition between the contribution of number of holes and electrons from NCO particles (polaron hopping conduction) as well as the graphene-like structure (electronic conductivity) bridging these NCO particles. However, the large apparent mobility might be due to the over-estimation of dimensions of the highly porous NCO nanofiber film. Anomalous Hall effect behavior of NCO nanofibers could be beneficial for their use as Hall sensors.

II.8   XPS DEPTH PROFILING SURVEY
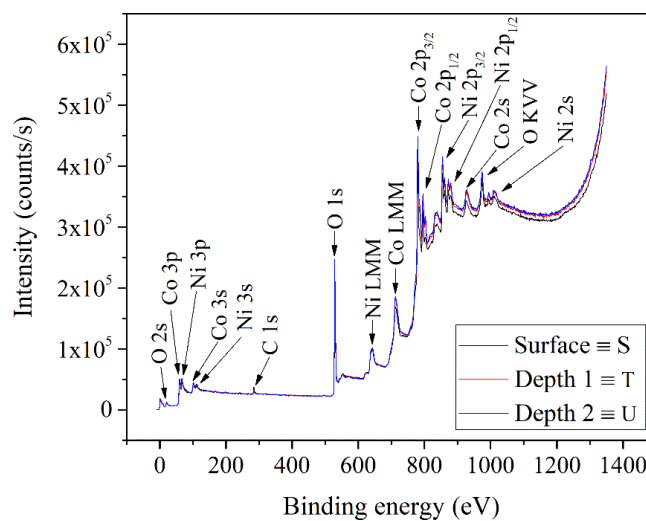
Fig. II.9 XPS depth profiling survey spectra of NCO-4.

XPS survey of depth profiling analysis of NCO-4 showed Ni, Co, O, and C elements.

II.9   LSV IN PRESENCE OF ANALYTES

LSV were recorded for NCO-4/GE in presence of 1 mM glucose and 100 µM H_2O_2.
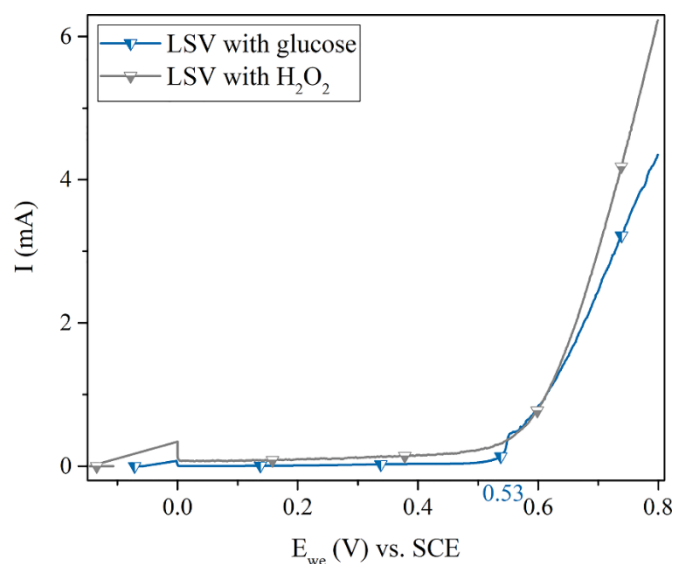
Fig. II.10 LSV of NCO-4/GE nanofibers in presence of analytes.

II.10 NYQUIST PLOTS OF BARE GE AND NCO-4/GE IN ABSENCE OF ANALYTES

EIS of bare graphite electrode and of NCO-4/GE in 0.1 M NaOH electrolyte.
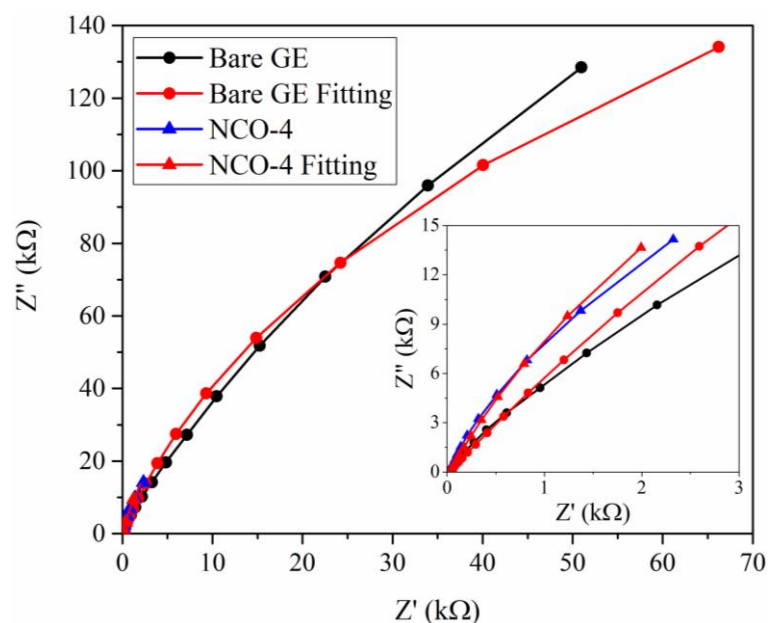
Fig. II.11 EIS spectra of bare and NCO-4 loaded GE.

II.11 BODE PHASE PLOTS OF NCO-4/GE IN PRESENCE OF ANALYTES

Bode phase plots of NCO-4/GE in presence of 1 mM glucose and 100 µM H_2O_2, obtained at a slow scanning rate of 2 mV·s^{-1}. From Figure II.12, the equivalent circuit assumed holds good fit and suggests that the conductivity of the H_2O_2 added electrolyte is more than that of the glucose.

(a)   **(b)**
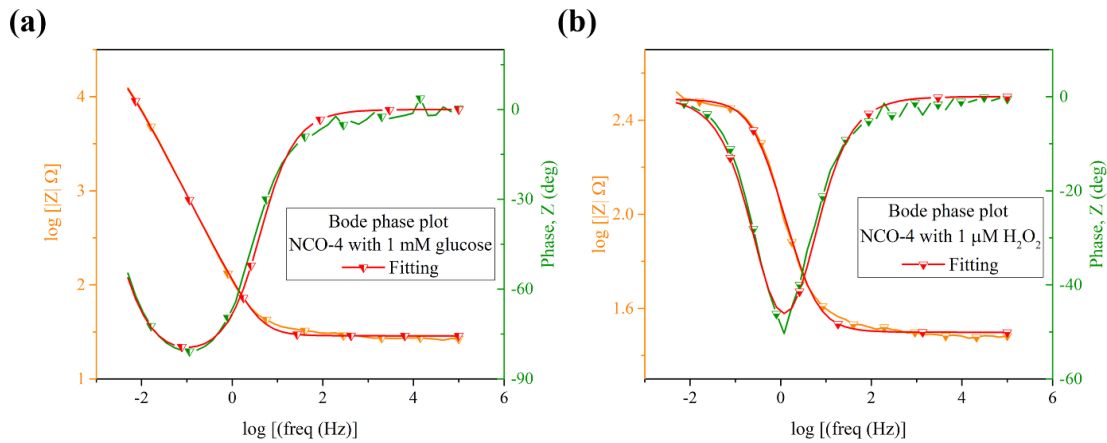
Fig. II.12 Bode phase plots of NCO-4/GE in presence of (a) 1 mM glucose and (b) 100 µM H_2O_2.

REFERENCES

Abideen, Z. U., Kim, J.-H., Lee, J.-H., Kim, J.-Y., Mirzaei, A., Kim, H. W., and Kim, S. S. (2017). "Electrospun metal oxide composite nanofibers gas sensors: A review." *Journal of the Korean Ceramic Society*, 54(5), 366–379.

Alcántara, R., Jaraba, M., Lavela, P., and Tirado, J. L. (2002). "$NiCo_2O_4$ spinel: First report on a transition metal oxide for the negative electrode of sodium-ion batteries." *Chemistry of Materials*, 14(7), 2847–2848.

Alegre, C., Busacca, C., Di Blasi, O., Antonucci, V., Aricò, A. S., Di Blasi, A., and Baglio, V. (2017). "A combination of CoO and Co nanoparticles supported on electrospun carbon nanofibers as highly stable air electrodes." *Journal of Power Sources*, 364, 101–109.

Allen, G. C., and Paul, M. (1995). "Chemical characterization of transition metal spinel-type oxides by infrared spectroscopy." *Applied Spectroscopy*, 49(4), 451–458.

Amin, B., Ahmad, I., Maqbool, M., Goumri-Said, S., and Ahmad, R. (2011). "Ab initio study of the bandgap engineering of $Al_{1-x}Ga_xN$ for optoelectronic applications." *Journal of Applied Physics*, 109(2), 023109.

Amin, B., Khenata, R., Bouhemadou, A., Ahmad, I., and Maqbool, M. (2012). "Opto-electronic response of spinels $MgAl_2O_4$ and $MgGa_2O_4$ through modified Becke-Johnson exchange potential." *Physica B: Condensed Matter*, 407(13), 2588–2592.

An, L., Huang, L., Zhou, P., Yin, J., Liu, H., and Xi, P. (2015). "A self-standing high-performance hydrogen evolution electrode with nanostructured $NiCo_2O_4$/CuS heterostructures." *Advanced Functional Materials*, 25(43), 6814–6822.

Anantharaj, S., R. Ede, S., Karthick, K., Sankar, S. S., Sangeetha, K., E. Karthik, P., and Kundu, S. (2018). "Precision and correctness in the evaluation of electrocatalytic water splitting: Revisiting activity parameters with a critical assessment." *Energy & Environmental Science*, 11(4), 744–771.

Appandairajan, N. K., and Gopalakrishnan, J. (1978). "A study of $Co_{3-x}Ni_xO_4$ ($0 \leq x \leq 1$) system." *Proceedings of the Indian Academy of Sciences - Section A, Chemical Sciences*, 87(4), 115–120.

Arillo, M. A., López, M. L., Pico, C., Veiga, M. L., Jiménez-López, A., and Rodríguez-Castellón, E. (2001). "Surface characterisation of spinels with Ti(IV) distributed in tetrahedral and octahedral sites." *Journal of Alloys and Compounds*, 317, 160–163.

Arlt, G. (1990). "The influence of microstructure on the properties of ferroelectric ceramics." *Ferroelectrics*, 104(1), 217–227.

Armbruster, T., and Lager, G. A. (1981). "Defect structure of the spinel, $Ni_{2.44}Ti_{0.77}O_4$." *Journal of Physics and Chemistry of Solids*, 42(9), 725–728.

Arumugam, G. K., Khan, S., and Heiden, P. A. (2009). "Comparison of the effects of an ionic liquid and other salts on the properties of electrospun fibers, 2-poly(vinyl alcohol)." *Macromolecular Materials and Engineering*, 294(1), 45–53.

Asahi, R., Morikawa, T., Ohwaki, T., Aoki, K., and Taga, Y. (2001). "Visible-light photocatalysis in nitrogen-doped titanium oxides." *Science*, 293(5528), 269–271.

Association, A. D. (2013). "Diagnosis and classification of diabetes mellitus." *Diabetes Care*, 36, S67–S74.

Aytimur, A., Koçyiğit, S., Uslu, İ., Durmuşoğlu, Ş., and Akdemir, A. (2013). "Fabrication and characterization of bismuth oxide-holmia nanofibers and nanoceramics." *Current Applied Physics*, 13(3), 581–586.

Azad, A.-M. (2006). "Fabrication of transparent alumina (Al_2O_3) nanofibers by electrospinning." *Materials Science and Engineering: A*, 435, 468–473.

Azad, A.-M., Matthews, T., and Swary, J. (2005). "Processing and characterization of electrospun Y_2O_3-stabilized ZrO_2 (YSZ) and Gd_2O_3-doped CeO_2 (GDC) nanofibers." *Materials Science and Engineering: B*, 123(3), 252–258.

Babu, G. A., Ravi, G., and Hayakawa, Y. (2015). "Microwave synthesis and effect of CTAB on ferromagnetic properties of NiO, Co_3O_4 and $NiCo_2O_4$ nanostructures." *Applied Physics A*, 119(1), 219–232.

Bahadur, N., Pasricha, R., Govind, Chand, S., and Kotnala, R. K. (2012). "Effect of Ni doping on the microstructure and high Curie temperature ferromagnetism in sol-gel derived titania powders." *Materials Chemistry and Physics*, 133(1), 471–479.

Bahlawane, N., Ngamou, P. H. T., Vannier, V., Kottke, T., Heberle, J., and Kohse-Höinghaus, K. (2009). "Tailoring the properties and the reactivity of the spinel cobalt oxide." *Physical Chemistry Chemical Physics*, 11(40), 9224–9232.

Bailey, A., Cadenhead, D. A., Davies, D. H., Everett, D. H., and Miles, A. J. (1971). "Low pressure hysteresis in the adsorption of organic vapours by porous carbons." *Transactions of the Faraday Society*, 67, 231–243.

Baraton, M. I., Busca, G., Prieto, M. C., Ricchiardi, G., and Escribano, V. S. (1994). "On the vibrational spectra and structure of $FeCrO_3$ and of the ilmenite-type compounds $CoTiO_3$ and $NiTiO_3$." *Journal of Solid State Chemistry*, 112(1), 9–14.

Barber, M., Connor, J. A., Guest, M. F., Hall, M. B., Hillier, I. H., and Meredith, W. N. E. (1972). "High energy photoelectron spectroscopy of transition metal complexes. Part 1.—Bonding in substituted and unsubstituted first row carbonyls." *Faraday Discussions of the Chemical Society*, 54, 219–226.

Barr, A. E. D. (1960). "2—The physics of yarn tensions and balloon shapes in spinning, winding and similar processes." *Journal of the Textile Institute Transactions*, 51(1), T17–T38.

Beattie, I. R., and Gilson, T. R. (1970). "The single-crystal Raman spectra of nearly opaque materials. iron(III) oxide and chromium(III) oxide." *Journal of the Chemical Society A: Inorganic, Physical, Theoretical*, 980–986.

Bellam, J. B., Ruiz-Preciado, M. A., Edely, M., Szade, J., Jouanneaux, A., and Kassiba, A. H. (2015). "Visible-light photocatalytic activity of nitrogen-doped $NiTiO_3$ thin films prepared by a co-sputtering process." *RSC Advances*, 5(14), 10551–10559.

Bergman, B., and Agren, J. (1986). "Immiscibility in the CoO-NiO System." *Journal of the American Ceramic Society*, 69(10), C-248–C-250.

Bharti, B., Kumar, S., Lee, H.-N., and Kumar, R. (2016). "Formation of oxygen vacancies and Ti^{3+} state in TiO_2 thin film and enhanced optical properties by air plasma treatment." *Scientific Reports*, 6, 32355.

Bhat, K. S., Barshilia, H. C., and Nagaraja, H. S. (2017). "Porous nickel telluride nanostructures as bifunctional electrocatalyst towards hydrogen and oxygen evolution reaction." *International Journal of Hydrogen Energy*, 42(39), 24645–24655.

Biswas, S. K., Dhak, D., Pathak, A., and Pramanik, P. (2008). "Chemical synthesis of environment-friendly nanosized yellow titanate pigments." *Materials Research Bulletin*, 43(3), 665–675.

Bitla, Y., Chin, Y.-Y., Lin, J.-C., Van, C. N., Liu, R., Zhu, Y., Liu, H.-J., Zhan, Q., Lin, H.-J., Chen, C.-T., Chu, Y.-H., and He, Q. (2015). "Origin of metallic behavior in $NiCo_2O_4$ ferrimagnet." *Scientific Reports*, 5(15201), 1–8.

Bläß, U. W., Barsukova, T., Schwarz, M. R., Köhler, A., Schimpf, C., Petrusha, I. A., Mühle, U., Rafaja, D., and Kroke, E. (2015). "Bulk titanium nitride ceramics – Significant enhancement of hardness by silicon nitride addition, nanostructuring and high pressure sintering." *Journal of the European Ceramic Society*, 35(10), 2733–2744.

Braski, D. N., Osborne, N. R., and Zurbuchen, J. M. (1994). "Xps Study of Ni-Fe Manganite Thermistor Material." *MRS Online Proceedings Library Archive*, 360, 139–144.

Brinker, C. J., and Scherer, G. W. (2013). *Sol-gel science: the physics and chemistry of sol-gel processing*, Academic Press, San Diego.

Cabo, M., Pellicer, E., Rossinyol, E., Castell, O., Suriñach, S., and Baró, M. D. (2009). "Mesoporous $NiCo_2O_4$ spinel: Influence of calcination temperature over phase purity and thermal stability." *Crystal Growth & Design*, 9(11), 4814–4821.

Cadafalch Gazquez, G., Smulders, V., Veldhuis, S. A., Wieringa, P., Moroni, L., Boukamp, B. A., and ten Elshof, J. E. (2017). "Influence of solution properties and process parameters on the formation and morphology of YSZ and NiO ceramic nanofibers by electrospinning." *Nanomaterials*, 7(1), 16.

Cai, B., Mao, W., Ye, Z., and Huang, J. (2016). "Facile fabrication of all-solid-state $SnO_2/NiCo_2O_4$ biosensor for self-powered glucose detection." *Applied Physics A*, 122(9), 806.

Capel-Sanchez, M. C., Campos-Martin, J. M., Fierro, J. L. G., Frutos, M. P. de, and Polo, A. P. (2000). "Effective alkene epoxidation with dilute hydrogen peroxide on amorphous silica-supported titanium catalysts." *Chemical Communications*, (10), 855–856.

Caruso, R. A., Schattka, J. H., and Greiner, A. (2001). "Titanium dioxide tubes from sol-gel coating of electrospun polymer fibers." *Advanced Materials*, 13(20), 1577–1579.

Challagulla, S., Tarafder, K., Ganesan, R., and Roy, S. (2017). "All that glitters is not gold: A probe into photocatalytic nitrate reduction mechanism over noble metal doped and undoped TiO_2." *The Journal of Physical Chemistry C*, 121(49), 27406–27416.

Chattopadhyay, S., Ayyub, P., Palkar, V. R., and Multani, M. (1995). "Size-induced diffuse phase transition in the nanocrystalline ferroelectric $PbTiO_3$." *Physical Review B*, 52(18), 13177–13183.

Chen, C., Xie, Q., Yang, D., Xiao, H., Fu, Y., Tan, Y., and Yao, S. (2013a). "Recent advances in electrochemical glucose biosensors: a review." *RSC Advances*, 3(14), 4473–4491.

Chen, H., Jiang, J., Zhang, L., Wan, H., Qi, T., and Xia, D. (2013b). "Highly conductive $NiCo_2S_4$ urchin-like nanostructures for high-rate pseudocapacitors." *Nanoscale*, 5(19), 8879–8883.

Chen, R., Wang, H.-Y., Miao, J., Yang, H., and Liu, B. (2015). "A flexible high-performance oxygen evolution electrode with three-dimensional $NiCo_2O_4$ core-shell nanowires." *Nano Energy*, 11, 333–340.

Chen, S., and Qiao, S.-Z. (2013). "Hierarchically porous nitrogen-doped graphene-$NiCo_2O_4$ hybrid paper as an advanced electrocatalytic water-splitting material." *ACS Nano*, 7(11), 10190–10196.

Chen, W., Cai, S., Ren, Q.-Q., Wen, W., and Zhao, Y.-D. (2012). "Recent advances in electrochemical sensing for hydrogen peroxide : a review." *Analyst*, 137(1), 49–58.

Chen, X., and Burda, C. (2008). "The electronic origin of the visible-light absorption properties of C-, N- and S-doped TiO_2 nanomaterials." *Journal of the American Chemical Society*, 130(15), 5018–5019.

Chen, X., Unruh, K. M., Ni, C., Ali, B., Sun, Z., Lu, Q., Deitzel, J., and Xiao, J. Q. (2011). "Fabrication, formation mechanism, and magnetic properties of metal oxide nanotubes via electrospinning and thermal treatment." *The Journal of Physical Chemistry C*, 115(2), 373–378.

Choi, S.-S., Lee, S. G., Im, S. S., Kim, S. H., and Joo, Y. L. (2003). "Silica nanofibers from electrospinning/sol-gel process." *Journal of Materials Science Letters*, 22(12), 891–893.

Choi, S.-W., Park, J. Y., and Kim, S. S. (2011). "Growth behavior and sensing properties of nanograins in CuO nanofibers." *Chemical Engineering Journal*, 172(1), 550–556.

Choquette, Y., Brossard, L., Lasia, A., and Menard, H. (1990). "Study of the kinetics of hydrogen evolution reaction on raney nickel composite-coated electrode by ac impedance technique." *Journal of The Electrochemical Society*, 137(6), 1723–1730.

Coey, J. M. D., Venkatesan, M., and Fitzgerald, C. B. (2005). "Donor impurity band exchange in dilute ferromagnetic oxides." *Nature Materials*, 4(2), 173–179.

Conway, B. E., and Tilak, B. V. (2002). "Interfacial processes involving electrocatalytic evolution and oxidation of H_2, and the role of chemisorbed H." *Electrochimica Acta*, 47(22), 3571–3594.

Cui, B., Lin, H., Li, J.-B., Li, X., Yang, J., and Tao, J. (2008). "Core-ring structured $NiCo_2O_4$ nanoplatelets: Synthesis, characterization, and electrocatalytic applications." *Advanced Functional Materials*, 18(9), 1440–1447.

Cui, B., Lin, H., Liu, Y., Li, J., Sun, P., Zhao, X., and Liu, C. (2009). "Photophysical and photocatalytic properties of core-ring structured $NiCo_2O_4$ nanoplatelets." *The Journal of Physical Chemistry C*, 113(32), 14083–14087.

Cui, S., Zhang, J., Ding, Y., Gu, S., Hu, P., and Hu, Z. (2017). "Rectangular flake-like mesoporous $NiCo_2O_4$ as enzyme mimic for glucose biosensing and biofuel cell." *Science China Materials*, 60(8), 766–776.

Cuong, T. V., Pham, V. H., Tran, Q. T., Hahn, S. H., Chung, J. S., Shin, E. W., and Kim, E. J. (2010). "Photoluminescence and Raman studies of graphene thin films prepared by reduction of graphene oxide." *Materials Letters*, 64(3), 399–401.

D'Ippolito, V., Andreozzi, G. B., Bersani, D., and Lottici, P. P. (2015). "Raman fingerprint of chromate, aluminate and ferrite spinels." *Journal of Raman Spectroscopy*, 46(12), 1255–1264.

Dai, H., Gong, J., Kim, H., and Lee, D. (2002). "A novel method for preparing ultra-fine alumina-borate oxide fibres via an electrospinning technique." *Nanotechnology*, 13(5), 674.

Dai, Y., Liu, W., Formo, E., Sun, Y., and Xia, Y. (2011). "Ceramic nanofibers fabricated by electrospinning and their applications in catalysis, environmental science, and energy technology." *Polymers for Advanced Technologies*, 22(3), 326–338.

Danilovic, N., Subbaraman, R., Strmcnik, D., Chang, K.-C., Paulikas, A. P., Stamenkovic, V. R., and Markovic, N. M. (2012). "Enhancing the alkaline hydrogen evolution reaction activity through the bifunctionality of $Ni(OH)_2$/metal catalysts." *Angewandte Chemie International Edition*, 51(50), 12495–12498.

Datsyuk, V., Kalyva, M., Papagelis, K., Parthenios, J., Tasis, D., Siokou, A., Kallitsis, I., and Galiotis, C. (2008). "Chemical oxidation of multiwalled carbon nanotubes." *Carbon*, 46(6), 833–840.

Datta, R. K., and Roy, R. (1965). "Stability of Ni_2TiO_4." *Zeitschrift für Kristallographie - Crystalline Materials*, 121(1–6), 410–417.

de Graef, M., Seinen, P. A., and Ijdo, D. J. W. (1985). "Electron microscopic study of the system NiO-TiO$_2$: I. Ni$_{2(1+x)}$Ti$_{1-x}$O$_4$ compounds." *Journal of Solid State Chemistry*, 58(3), 357–367.

De Jesus, J. C., González, I., Quevedo, A., and Puerta, T. (2005). "Thermal decomposition of nickel acetate tetrahydrate: an integrated study by TGA, QMS and XPS techniques." *Journal of Molecular Catalysis A: Chemical*, 228(1), 283–291.

de Martín, L., Fabre, A., and Ruud van Ommen, J. (2014). "The fractal scaling of fluidized nanoparticle agglomerates." *Chemical Engineering Science*, 112, 79–86.

Dharmaraj, N., Park, H. C., Kim, C. H., Viswanathamurthi, P., and Kim, H. Y. (2006). "Nanometer sized tantalum pentoxide fibers prepared by electrospinning." *Materials research bulletin*, 41(3), 612–619.

Dharmaraj, N., Park, H. C., Kim, C. K., Kim, H. Y., and Lee, D. R. (2004a). "Nickel titanate nanofibers by electrospinning." *Materials Chemistry and Physics*, 87(1), 5–9.

Dharmaraj, N., Park, H. C., Lee, B. M., Viswanathamurthi, P., Kim, H. Y., and Lee, D. R. (2004b). "Preparation and morphology of magnesium titanate nanofibres via electrospinning." *Inorganic chemistry communications*, 7(3), 431–433.

Dibenedetto, A., and Aresta, M. (2013). *Inorganic micro-and nanomaterials: synthesis and characterization*, Walter de Gruyter, Berlin.

Ding, R., Qi, L., and Wang, H. (2012). "A facile and cost-effective synthesis of mesoporous NiCo$_2$O$_4$ nanoparticles and their capacitive behavior in electrochemical capacitors." *Journal of Solid State Electrochemistry*, 16(11), 3621–3633.

Ding, R., Qi, L., Jia, M., and Wang, H. (2013). "Simple hydrothermal synthesis of mesoporous spinel NiCo$_2$O$_4$ nanoparticles and their catalytic behavior in CH$_3$OH electro-oxidation and H$_2$O$_2$ electro-reduction." *Catalysis Science & Technology*, 3(12), 3207–3215.

Diwald, O., Thompson, T. L., Zubkov, T., Walck, S. D., and Yates, J. T. (2004). "Photochemical activity of nitrogen-doped rutile TiO$_2$(1 1 0) in visible light." *The Journal of Physical Chemistry B*, 108(19), 6004–6008.

Dong, C., Liu, X., Wang, X., Yuan, X., Xu, Z., Dong, W., Sohial Riaz, M., Li, G., and Huang, F. (2017). "Hierarchical $Ni/NiTiO_3$ derived from NiTi LDHs: a bifunctional electrocatalyst for overall water splitting." *Journal of Materials Chemistry A*, 5(47), 24767–24774.

Drygaś, M., Czosnek, C., Paine, R. T., and Janik, J. F. (2006). "Two-stage aerosol synthesis of titanium nitride tin and titanium oxynitride TiO_xN_y nanopowders of spherical particle morphology." *Chemistry of Materials*, 18(13), 3122–3129.

Dubal, D. P., Gomez-Romero, P., Sankapal, B. R., and Holze, R. (2015). "Nickel cobaltite as an emerging material for supercapacitors: An overview." *Nano Energy*, 11, 377–399.

Ebrahimi, A., Pirouz, A., Abdi, Y., Azimi, S., and Mohajerzadeh, S. (2012). "Selective deposition of CuO/SnO_2 sol-gel on porous SiO_2 suitable for the fabrication of MEMS-based H_2S sensors." *Sensors and Actuators B: Chemical*, 173, 802–810.

Eda, G., Lin, Y.-Y., Mattevi, C., Yamaguchi, H., Chen, H.-A., Chen, I.-S., Chen, C.-W., and Chhowalla, M. (2010). "Blue photoluminescence from chemically derived graphene oxide." *Advanced Materials*, 22(4), 505–509.

Elias, L., Scott, K., and Hegde, A. C. (2015). "Electrolytic synthesis and characterization of electrocatalytic Ni-W alloy." *Journal of Materials Engineering and Performance*, 24(11), 4182–4191.

Esfahani, H., Jose, R., and Ramakrishna, S. (2017). "Electrospun ceramic nanofiber mats today: Synthesis, properties, and applications." *Materials*, 10(11).

Exarhos, G. J., Jr, C. F. W., Ferris, K. F., and Owings, R. R. (2007). "Cation defects and conductivity in transparent oxides." *Applied Physics A*, 89(1), 9–18.

Fan, H. J., Gösele, U., and Zacharias, M. (2007a). "Formation of nanotubes and hollow nanoparticles based on Kirkendall and diffusion processes: A review." *Small*, 3(10), 1660–1671.

Fan, H. J., Knez, M., Scholz, R., Hesse, D., Nielsch, K., Zacharias, M., and Gösele, U. (2007b). "Influence of surface diffusion on the formation of hollow nanostructures induced by the Kirkendall effect: The basic concept." *Nano Letters*, 7(4), 993–997.

Fang, Q., Cheng, H., Huang, K., Wang, J., Li, R., and Jiao, Y. (2005). "Doping effect on crystal structure and magnetic properties of chromium-substituted strontium hexaferrite nanoparticles." *Journal of Magnetism and Magnetic Materials*, 294(3), 281–286.

Fennie, C. J. (2008). "Ferroelectrically induced weak ferromagnetism by design." *Physical Review Letters*, 100(16), 167203.

Filik, J., May, P. W., Pearce, S. R. J., Wild, R. K., and Hallam, K. R. (2003). "XPS and laser Raman analysis of hydrogenated amorphous carbon films." *Diamond and Related Materials*, 12(3–7), 974–978.

Fraser, W. B., Ghosh, T. K., and Batra, S. K. (1992). "On unwinding yarn from a cylindrical package." *Proceedings of the Royal Society of London A: Mathematical, Physical and Engineering Sciences*, 436(1898), 479–498.

Frey, M. H., and Payne, D. A. (1996). "Grain-size effect on structure and phase transformations for barium titanate." *Physical Review B*, 54(5), 3158–3168.

Frites, M., Simpson, A., Gautam, R., and Khan, S.U.M. (2014). "Mixed Transition Metal Oxides for Efficient Electrochemical Splitting of Water to Hydrogen and Oxygen." *Energy and Sustainability V*, H. H. Al-Kayiem, C. A. Brebbia, and S. S. Zubir, eds., WIT Press, Southampton, 139–146.

Fritsch, D., and Ederer, C. (2010). "Epitaxial strain effects in the spinel ferrites $CoFe_2O_4$ and $NiFe_2O_4$ from first principles." *Physical Review B*, 82(10), 104117.

Fu, Z.-W., Ma, J., and Qin, Q.-Z. (2005). "Nanostructured $LiCoO_2$ and $LiMn_2O_4$ fibers fabricated by a high frequency electrospinning." *Solid State Ionics*, 176(17–18), 1635–1640.

Gabal, M. A. E.-F., Al Angari, Y. M., and Obaid, A. Y. (2013). "Structural characterization and activation energy of $NiTiO_3$ nanopowders prepared by the co-

precipitation and impregnation with calcinations." *Comptes Rendus Chimie*, 16(8), 704–711.

Gambhire, A. B., Lande, M. K., Kalokhe, S. B., Mandale, A. B., Patil, K. R., Gholap, R. S., and Arbad, B. R. (2008). "Synthesis and characterizations of $NiTiO_3$ nanoparticles prepared by the sol-gel process." *Philosophical Magazine Letters*, 88(6), 467–472.

Ganesh, I., Gupta, A. K., Kumar, P. P., Sekhar, P. S. C., Radha, K., Padmanabham, G., and Sundararajan, G. (2012). "Preparation and characterization of Ni-doped TiO_2 materials for photocurrent and photocatalytic applications." *The Scientific World Journal*, 2012, 127326.

Gao, M., Zhu, L., Li Ong, W., Wang, J., and Wei Ho, G. (2015). "Structural design of TiO_2 -based photocatalyst for H_2 production and degradation applications." *Catalysis Science & Technology*, 5(10), 4703–4726.

Gao, X., Zhang, H., Li, Q., Yu, X., Hong, Z., Zhang, X., Liang, C., and Lin, Z. (2016). "Hierarchical $NiCo_2O_4$ hollow microcuboids as bifunctional electrocatalysts for overall water-splitting." *Angewandte Chemie International Edition*, 55(21), 6290–6294.

Garg, N., Basu, M., Upadhyaya, K., M. Shivaprasad, S., and K. Ganguli, A. (2013). "Controlling the aspect ratio and electrocatalytic properties of nickel cobaltite nanorods." *RSC Advances*, 3(46), 24328–24336.

Gawande, M. B., Pandey, R. K., and V. Jayaram, R. V. (2012). "Role of mixed metal oxides in catalysis science-versatile applications in organic synthesis." *Catalysis Science & Technology*, 2(6), 1113–1125.

George, G. (2015). "Influence of polymeric binders on the physico-chemical properties of sol-gel electrospun nickel oxide and cobalt oxide nanofibers." Ph.D. thesis, National Institute of Technology Karnataka, Mangaluru, India.

George, G., and Anandhan, S. (2013b). "Structural characterization of nano-crystalline Co_3O_4 ultra-fine fibers obtained by sol-gel electrospinning." *Journal of Sol-Gel Science and Technology*, 67(2), 256–266.

George, G., and Anandhan, S. (2014a). "Glass fiber-supported NiO nanofiber webs for reduction of CO and hydrocarbon emissions from diesel engine exhaust." *Journal of Materials Research*, 29(20), 2451–2465.

George, G., and Anandhan, S. (2014b). "Synthesis and characterisation of nickel oxide nanofibre webs with alcohol sensing characteristics." *RSC Advances*, 4(107), 62009–62020.

George, G., and Anandhan, S. (2015a). "A comparative study on the physico-chemical properties of sol-gel electrospun cobalt oxide nanofibres from two different polymeric binders." *RSC Advances*, 5(99), 81429–81437.

George, G., and Anandhan, S. (2015b). "Comparison of structural, spectral and magnetic properties of NiO nanofibers obtained by sol-gel electrospinning from two different polymeric binders." *Materials Science in Semiconductor Processing*, 32, 40–48.

George, G., and Anandhan, S. (2016). "Tuning characteristics of Co_3O_4 nanofiber mats developed for electrochemical sensing of glucose and H_2O_2." *Thin Solid Films*, 610, 48–57.

George, G., Elias, L., Hegde, A. C., and Anandhan, S. (2015). "Morphological and structural characterisation of sol-gel electrospun Co_3O_4 nanofibres and their electro-catalytic behaviour." *RSC Advances*, 5(51), 40940–40949.

Gong, M., Wang, D.-Y., Chen, C.-C., Hwang, B.-J., and Dai, H. (2016). "A mini review on nickel-based electrocatalysts for alkaline hydrogen evolution reaction." *Nano Research*, 9(1), 28–46.

Gouadec, G., and Colomban, P. (2007). "Raman spectroscopy of nanomaterials: How spectra relate to disorder, particle size and mechanical properties." *Progress in Crystal Growth and Characterization of Materials*, 53(1), 1–56.

Guan, H., Shao, C., Liu, Y., Yu, N., and Yang, X. (2004). "Fabrication of $NiCo_2O_4$ nanofibers by electrospinning." *Solid State Communications*, 131(2), 107–109.

Guan, H., Shao, C., Wen, S., Chen, B., Gong, J., and Yang, X. (2003a). "Preparation and characterization of NiO nanofibres via an electrospinning technique." *Inorganic Chemistry Communications*, 6(10), 1302–1303.

Guan, H., Shao, C., Wen, S., Chen, B., Gong, J., and Yang, X. (2003b). "A novel method for preparing Co_3O_4 nanofibers by using electrospun PVA/cobalt acetate composite fibers as precursor." *Materials Chemistry and Physics*, 82(3), 1002–1006.

Guimarães, J. L., Abbate, M., Betim, S. B., and Alves, M. C. M. (2003). "Preparation and characterization of TiO_2 and V_2O_5 nanoparticles produced by ball-milling." *Journal of Alloys and Compounds*, 352(1), 16–20.

Guo, T., Yao, M.-S., Lin, Y.-H., and Nan, C.-W. (2015). "A comprehensive review on synthesis methods for transition-metal oxide nanostructures." *CrystEngComm*, 17(19), 3551–3585.

Han, L., Dong, S., and Wang, E. (2016a). "Transition-metal (Co, Ni, and Fe)-based electrocatalysts for the water oxidation reaction." *Advanced Materials*, 28(42), 9266–9291.

Han, L., Meng, Q., Wang, D., Zhu, Y., Wang, J., Du, X., Stach, E. A., and Xin, H. L. (2016b). "Interrogation of bimetallic particle oxidation in three dimensions at the nanoscale." *Nature Communications*, 7, 13335.

Hao, R., Yuan, J., and Peng, Q. (2006). "Fabrication and sensing behavior of Cr_2O_3 nanofibers via in situ gelation and electrospinning." *Chemistry letters*, 35(11), 1248–1249.

Harada, J. K., Balhorn, L., Hazi, J., Kemei, M. C., and Seshadri, R. (2016). "Magnetodielectric coupling in the ilmenites $MTiO_3$ (M = Co, Ni)." *Physical Review B*, 93(10), 104404.

Harilal, M., Krishnan, S. G., Vijayan, B. L., Venkatashamy Reddy, M., Adams, S., Barron, A. R., Yusoff, M. M., and Jose, R. (2017). "Continuous nanobelts of nickel oxide-cobalt oxide hybrid with improved capacitive charge storage properties." *Materials & Design*, 122, 376–384.

Heller, A., and Feldman, B. (2008). "Electrochemical glucose sensors and their applications in diabetes management." *Chemical Reviews*, 108(7), 2482–2505.

Heller, G. S., Stickler, J. J., Kern, S., and Wold, A. (1963). "Antiferromagnetism in $NiTiO_3$." *Journal of Applied Physics*, 34(4), 1033–1034.

Herzer, G. (1997). "Nanocrystalline soft magnetic alloys." *Handbook of Magnetic Materials*, K. H. J. Buschow, ed., Elsevier, Amsterdam, 415–462.

Hu, L., Wu, L., Liao, M., Hu, X., and Fang, X. (2012). "Electrical transport properties of large, individual $NiCo_2O_4$ nanoplates." *Advanced Functional Materials*, 22(5), 998–1004.

Hu, M. Z. (2012). *Ceramic nanomaterials and nanotechnology*, John Wiley & Sons, New York.

Huang, H., Liu, C., Ni, L., and Zhou, C. (2011). "Evaluation of microstructural evolution of thermal barrier coatings exposed to Na_2SO_4 using impedance spectroscopy." *Corrosion Science*, 53(4), 1369–1374.

Huang, L., Zhang, W., Xiang, J., and Huang, Y. (2016). "Porous $NiCo_2O_4$/C nanofibers replicated by cotton template as high-rate electrode materials for supercapacitors." *Journal of Materiomics*, 2(3), 248–255.

Huang, W., Cao, Y., Chen, Y., Peng, J., Lai, X., and Tu, J. (2017a). "Fast synthesis of porous $NiCo_2O_4$ hollow nanospheres for a high-sensitivity non-enzymatic glucose sensor." *Applied Surface Science*, 396, 804–811.

Huang, W., Lin, T., Cao, Y., Lai, X., Peng, J., and Tu, J. (2017b). "Hierarchical $NiCo_2O_4$ hollow sphere as a peroxidase mimetic for colorimetric detection of H_2O_2 and glucose." *Sensors*, 17(1), 217.

Hussain, M., Ibupoto, Z. H., Abbasi, M. A., Liu, X., Nur, O., and Willander, M. (2014). "Synthesis of three dimensional nickel cobalt oxide nanoneedles on nickel foam, their characterization and glucose sensing application." *Sensors*, 14(3), 5415–5425.

Hyun Kim, D., Sub Lee, K., Kim, Y.-S., Chung, Y.-C., and Kim, S.-J. (2006). "Photocatalytic activity of Ni 8 wt%-doped TiO_2 photocatalyst synthesized by

mechanical alloying under visible light." *Journal of the American Ceramic Society*, 89(2), 515–518.

Iliev, M. N., Silwal, P., Loukya, B., Datta, R., Kim, D. H., Todorov, N. D., Pachauri, N., and Gupta, A. (2013). "Raman studies of cation distribution and thermal stability of epitaxial spinel $NiCo_2O_4$ films." *Journal of Applied Physics*, 114(3), 033514.

International Organization for Standardization (ISO). (2015). *Technical Specification 80004-1:2015 - Nanotechnologies – Vocabulary – Part 1: Core terms*, ISO, Geneva.

Iqbal, N., Wang, X., Ahmed Babar, A., Yu, J., and Ding, B. (2016). "Highly flexible $NiCo_2O_4$/CNTs doped carbon nanofibers for CO_2 adsorption and supercapacitor electrodes." *Journal of Colloid and Interface Science*, 476, 87–93.

ISO. (2011). *Technical Specification 80004-4:2011 - Nanotechnologies – Vocabulary – Part 4: Nanostructured materials*, ISO, Geneva.

ISO. (2015). *Technical Specification 80004-2:2015 - Nanotechnologies – Vocabulary – Part 2: Nano-objects*, ISO, Geneva.

Jadhav, H. S., Kalubarme, R. S., Roh, J.-W., Jung, K.-N., Shin, K.-H., Park, C.-N., and Park, C.-J. (2014). "Facile and cost effective synthesized mesoporous spinel $NiCo_2O_4$ as catalyst for non-aqueous lithium-oxygen batteries." *Journal of The Electrochemical Society*, 161(14), A2188–A2196.

Jiang, J. Z., Goya, G. F., and Rechenberg, H. R. (1999). "Magnetic properties of nanostructured $CuFe_2O_4$." *Journal of Physics: Condensed Matter*, 11(20), 4063.

Jiao, Y., Zheng, Y., Jaroniec, M., and Qiao, S. Z. (2015). "Design of electrocatalysts for oxygen- and hydrogen-involving energy conversion reactions." *Chemical Society Reviews*, 44(8), 2060–2086.

Johnson, B., Chand, N. R. K., Sudhakar, B. K., and Rao, G. S. (2016). "Chemical durability, thermal stability and spectroscopic studies of the influence of Ni^{2+}." *Journal of Materials Science: Materials in Electronics*, 27(8), 8833–8847.

K. Arora, A., Rajalakshmi, M., Thoguluva, R., and Sivasubramanian, V. (2007). "Raman spectroscopy of optical phonon confinement in nanostructured materials." *Journal of Raman Spectroscopy*, 38, 604–617.

K. Srivastava, A., and Mongia, N. (2016). "Superparamagentic behaviour of $MgFe_2O_4$ nano-ferrite." *Science and Engineering Applications*, 1, 1–5.

K.C., R. B., Kim, C. K., Khil, M. S., Kim, H. Y., and Kim, I. S. (2008). "Synthesis of hydroxyapatite crystals using titanium oxide electrospun nanofibers." *Materials Science and Engineering: C*, 28(1), 70–74.

Kanjwal, M. A., Barakat, N. A., Sheikh, F. A., Khil, M. S., and Kim, H. Y. (2008). "Physiochemical characterizations of nanobelts consisting of three mixed oxides (Co_3O_4, CuO, and MnO_2) prepared by electrospinning technique." *Journal of materials science*, 43(16), 5489–5494.

Karim Mohammad Razaul, Shinoda Hideaki, Nakai Mina, Hatakeyama Kazuto, Kamihata Hidenobu, Matsui Takeshi, Taniguchi Takaaki, Koinuma Michio, Kuroiwa Keita, Kurmoo Mohamedally, Matsumoto Yasumichi, and Hayami Shinya. (2012). "Electrical conductivity and ferromagnetism in a reduced graphene-metal oxide hybrid." *Advanced Functional Materials*, 23(3), 323–332.

Kaskel, S., Schlichte, K., Chaplais, G., and Khanna, M. (2003). "Synthesis and characterisation of titanium nitride based nanoparticles." *Journal of Materials Chemistry*, 13(6), 1496–1499.

Katta, P., Alessandro, M., Ramsier, R. D., and Chase, G. (2004). "Continuous electro-spinning of aligned polymer nanofibers on a wire drum collector." *Nano Letters*, 4(11), 2215–2218.

Kawano, S., Takahashi, J., and Shimada, S. (2003). "Spark plasma sintering of nano-sized TiN prepared from TiO_2 by controlled hydrolysis of $TiCl_4$ and $Ti(O-i-C_3H_7)_4$ solution." *Journal of the American Ceramic Society*, 86(9), 1609–1611.

Kim, D. H., Park, H. S., Kim, S.-J., and Lee, K. S. (2006a). "Synthesis of novel TiO_2 by mechanical alloying and heat treatment-derived nanocomposite of TiO_2 and $NiTiO_3$." *Catalysis Letters*, 106(1–2), 29–33.

Kim, H.-K., Honda, W., Kim, B.-S., and Kim, I.-S. (2013). "Preparation and magnetic properties of electrospun CuO/NiO bimetallic nanofibers via sol-gel electrospinning." *Journal of Materials Science*, 48(3), 1111–1116.

Kim, H.-W., Kim, H.-E., and Knowles, J. C. (2006b). "Production and potential of bioactive glass nanofibers as a next-generation biomaterial." *Advanced Functional Materials*, 16(12), 1529–1535.

Kinoshita, M., Kingery, W. D., and Bowen, H. K. (1973). "Phase separation in NiO-CoO solid solution single crystals." *Journal of the American Ceramic Society*, 56(7), 398–399.

Ko, F. K. (2006). "Nanofiber technology." *Nanotubes and Nanofibers*, Y. Gogotsi, ed., CRC Press, Boca Raton, 233–244.

Ko, F. K., and Wan, Y. (2014). *Introduction to nanofiber materials*, Cambridge University Press, Cambridge.

Ko, T.-H., Radhakrishnan, S., Seo, M.-K., Khil, M.-S., Kim, H.-Y., and Kim, B.-S. (2017). "A green and scalable dry synthesis of $NiCo_2O_4$/graphene nanohybrids for high-performance supercapacitor and enzymeless glucose biosensor applications." *Journal of Alloys and Compounds*, 696, 193–200.

Kottegoda, I. R. M., Idris, N. H., Lu, L., Wang, J.-Z., and Liu, H.-K. (2011). "Synthesis and characterization of graphene-nickel oxide nanostructures for fast charge-discharge application." *Electrochimica Acta*, 56(16), 5815–5822.

Kuboon, S., and Hu, Y. H. (2011). "Study of NiO-CoO and Co_3O_4-Ni_3O_4 solid solutions in multiphase Ni-Co-O Systems." *Industrial & Engineering Chemistry Research*, 50(4), 2015–2020.

Kumar, B. S., Dhanasekhar, C., Venimadhav, A., Kalpathy, S. K., and Anandhan, S. (2018). "Pyrolysis-controlled synthesis, and magnetic properties of sol-gel electrospun nickel cobaltite nanostructures." *Journal of Sol-Gel Science and Technology*, 86(3), 664–674.

Kumar, B. S., Prakrthi, A. N., Senthil, T., Udaya Bhat, K., and Anandhan, S. (2016). "Organoclay enabled nanofiber formation from a polyolefin elastomer." *Advances in Polymer Technology*, 37(5), 1278-1295.

Kumar, B. S., Shanmugharaj, A. M., Kalpathy, S. K., and Anandhan, S. (2017). "Some new observations on the structural and phase evolution of nickel titanate nanofibers." *Ceramics International*, 43(9), 6845–6857.

Kuznetsov, M. V., Zhuravlev, J. F., and Gubanov, V. A. (1992). "XPS analysis of adsorption of oxygen molecules on the surface of Ti and TiN_x films in vacuum." *Journal of Electron Spectroscopy and Related Phenomena*, 58(3), 169–176.

Kwon, Y., Soon, A., Han, H., and Lee, H. (2014). "Shape effects of cuprous oxide particles on stability in water and photocatalytic water splitting." *Journal of Materials Chemistry A*, 3(1), 156–162.

Lager, G. A., Armbruster, T., Ross, F. K., Rotella, F. J., and Jorgensen, J. D. (1981). "Neutron powder diffraction study of defect spinel structures: Tetrahedrally coordinated Ti^{4+} in $Ni_{2.62}Ti_{0.69}O_4$ and $Ni_{2.42}Ti_{0.74}Si_{0.05}O_4$." *Journal of Applied Crystallography*, 14(4), 261–264.

Lapham, D. P., and Tseung, A. C. C. (2004). "The effect of firing temperature, preparation technique and composition on the electrical properties of the nickel cobalt oxide series $Ni_xCo_{1-x}O_y$." *Journal of Materials Science*, 39(1), 251–264.

Laqua, V. W., E. W., S., and B., R. (1977). "Phasenverhältnisse und reaktionen im system $NiO-TiO_2$." *Zeitschrift für anorganische und allgemeine Chemie*, 433(1), 167–180.

Larsen, G., Velarde-Ortiz, R., Minchow, K., Barrero, A., and Loscertales, I. G. (2003). "A method for making inorganic and hybrid (organic/inorganic) fibers and vesicles with diameters in the submicrometer and micrometer range via sol-gel chemistry and electrically forced liquid jets." *Journal of the American Chemical Society*, 125(5), 1154–1155.

Ledendecker, M., Krick Calderón, S., Papp, C., Steinrück, H.-P., Antonietti, M., and Shalom, M. (2015). "The synthesis of nanostructured Ni_5P_4 films and their use as a non-

noble bifunctional electrocatalyst for full water splitting." *Angewandte Chemie International Edition*, 127(42), 12538–12542.

Lee, C. W., Seo, S.-D., Kim, D. W., Park, S., Jin, K., Kim, D.-W., and Hong, K. S. (2013a). "Heteroepitaxial growth of ZnO nanosheet bands on $ZnCo_2O_4$ submicron rods toward high-performance Li ion battery electrodes." *Nano Research*, 6(5), 348–355.

Lee, M. K., Charnaya, E. V., Tien, C., Samoilovich, M. I., Chang, L. J., and Mikushev, V. M. (2013b). "Magnetic properties of some opal-based nanocomposites." *Physics of the Solid State*, 55(3), 629–633.

Lee, Y., Suntivich, J., May, K. J., Perry, E. E., and Shao-Horn, Y. (2012). "Synthesis and activities of rutile IrO_2 and RuO_2 nanoparticles for oxygen evolution in acid and alkaline solutions." *The Journal of Physical Chemistry Letters*, 3(3), 399–404.

Lefebvre, J., Fraser, J. M., Finnie, P., and Homma, Y. (2004). "Photoluminescence from an individual single-walled carbon nanotube." *Physical Review B*, 69(7), 075403.

Leinen D., Fernández A., Espinós J. P., and González-Elipe A. R. (2004). "XPS and ISS study of $NiTiO_3$ and $PbTiO_3$ subjected to low-energy ion bombardment. I. Influence of the type of ion (Ar^+ and O_2^+)." *Surface and Interface Analysis*, 20(12), 941–948.

Lemine, O. M. (2009). "Microstructural characterisation of nanoparticles using, XRD line profiles analysis, FE-SEM and FT-IR." *Superlattices and Microstructures*, 45(6), 576–582.

Leng, X., Shao, Y., Wu, L., Wei, S., Jiang, Z., Wang, G., Jiang, Q., and Lian, J. (2016). "A unique porous architecture built by ultrathin wrinkled $NiCoO_2$/rGO/$NiCoO_2$ sandwich nanosheets for pseudocapacitance and Li ion storage." *Journal of Materials Chemistry A*, 4(26), 10304–10313.

Li, C., Feng, C., Qu, F., Liu, J., Zhu, L., Lin, Y., Wang, Y., Li, F., Zhou, J., and Ruan, S. (2015). "Electrospun nanofibers of p-type NiO/n-type ZnO heterojunction with different NiO content and its influence on trimethylamine sensing properties." *Sensors and Actuators B: Chemical*, 207, 90–96.

Li, D., and Xia, Y. (2003). "Fabrication of titania nanofibers by electrospinning." *Nano Letters*, 3(4), 555–560.

Li, D., and Xia, Y. (2004). "Electrospinning of nanofibers: Reinventing the wheel?" *Advanced Materials*, 16(14), 1151–1170.

Li, D., Herricks, T., and Xia, Y. (2003). "Magnetic nanofibers of nickel ferrite prepared by electrospinning." *Applied physics letters*, 83(22), 4586–4588.

Li, D., McCann, J. T., Xia, Y., and Marquez, M. (2006a). "Electrospinning: A simple and versatile technique for producing ceramic nanofibers and nanotubes." *Journal of the American Ceramic Society*, 89(6), 1861–1869.

Li, J. Y., Dai, H., Li, Q., Zhong, X. H., Ma, X. F., Meng, J., and Cao, X. Q. (2006b). "Lanthanum zirconate nanofibers with high sintering-resistance." *Materials Science and Engineering: B*, 133(1–3), 209–212.

Li, J., Gao, L., Sun, J., Zhang, Q., Guo, J., and Yan, D. (2001). "Synthesis of nanocrystalline titanium nitride powders by direct nitridation of titanium oxide." *Journal of the American Ceramic Society*, 84(12), 3045–3047.

Li, J., Xiong, S., Liu, Y., Ju, Z., and Qian, Y. (2013a). "High electrochemical performance of monodisperse $NiCo_2O_4$ mesoporous microspheres as an anode material for Li-ion batteries." *ACS Applied Materials & Interfaces*, 5(3), 981–988.

Li, L., Peng, S., Cheah, Y., Teh, P., Wang, J., Wee, G., Ko, Y., Wong, C., and Srinivasan, M. (2013b). "Electrospun porous $NiCo_2O_4$ nanotubes as advanced electrodes for electrochemical capacitors." *Chemistry – A European Journal*, 19(19), 5892–5898.

Li, M., Liu, H., Lv, T., and Ding, M. (2018). "Synergistic effect of the valence bond environment and exposed crystal facets of the TiO_2/SnS_2 heterojunction for achieving enhanced electrocatalytic oxygen evolution." *Journal of Materials Chemistry A*, 6(8), 3488–3499.

Li, M., Tang, Z., Leng, M., and Xue, J. (2014). "Flexible solid-state supercapacitor based on graphene-based hybrid films." *Advanced Functional Materials*, 24(47), 7495–7502.

Li, M.-W., Yuan, J.-P., Gao, X.-M., Liang, E.-Q., and Wang, C.-Y. (2016a). "Structure and optical absorption properties of $NiTiO_3$ nanocrystallites." *Applied Physics A*, 122(8), 725-1–725-7.

Li, Q., Zeng, L., Wang, J., Tang, D., Liu, B., Chen, G., and Wei, M. (2011). "Magnetic mesoporous organic-inorganic $NiCo_2O_4$ hybrid nanomaterials for electrochemical immunosensors." *ACS Applied Materials & Interfaces*, 3(4), 1366–1373.

Li, X., Zhang, L., Huang, M., Wang, S., Li, X., and Zhu, H. (2016b). "Cobalt and nickel selenide nanowalls anchored on graphene as bifunctional electrocatalysts for overall water splitting." *Journal of Materials Chemistry A*, 4(38), 14789–14795.

Li, Y., Gao, X. P., Li, G. R., Pan, G. L., Yan, T. Y., and Zhu, H. Y. (2009). "titanate nanofiber reactivity: Fabrication of $MTiO_3$ (M = Ca, Sr, and Ba) perovskite oxides." *The Journal of Physical Chemistry C*, 113(11), 4386–4394.

Lian, K.-Y., Ji, Y.-F., Li, X.-F., Jin, M.-X., Ding, D.-J., and Luo, Y. (2013). "Big bandgap in highly reduced graphene oxides." *The Journal of Physical Chemistry C*, 117(12), 6049–6054.

Liang, H., Meng, F., Cabán-Acevedo, M., Li, L., Forticaux, A., Xiu, L., Wang, Z., and Jin, S. (2015). "Hydrothermal continuous flow synthesis and exfoliation of NiCo layered double hydroxide nanosheets for enhanced oxygen evolution catalysis." *Nano Letters*, 15(2), 1421–1427.

Liao, Y., Fukuda, T., and Wang, S. (2016). "Electrospun metal oxide nanofibers and their energy applications.", *Nanofiber Research-Reaching New Heights*, M. M. Rahman and A. M. Asiri, eds., InTech, London, 169–190.

Lin, Y.-J., Chang, Y.-H., Yang, W.-D., and Tsai, B.-S. (2006). "Synthesis and characterization of ilmenite $NiTiO_3$ and $CoTiO_3$ prepared by a modified Pechini method." *Journal of Non-Crystalline Solids*, 352(8), 789–794.

Liu, C., Sun, J., Shao, M., and Yang, B. (2015). "A comparison of centrifugally-spun and electrospun regenerated silk fibroin nanofiber structures and properties." *RSC Advances*, 5(119), 98553–98558.

Liu, F., Jang, M.-H., Ha, H. D., Kim, J.-H., Cho, Y.-H., and Seo, T. S. (2013a). "Facile synthetic method for pristine graphene quantum dots and graphene oxide quantum dots: Origin of blue and green luminescence." *Advanced Materials*, 25(27), 3657–3662.

Liu, S., Zhang, X., Shao, H., Xu, J., Chen, F., and Feng, Y. (2012). "Preparation of MoS_2 nanofibers by electrospinning." *Materials Letters*, 73, 223–225.

Liu, W., Lu, C., Liang, K., and Kang Tay, B. (2014a). "A three dimensional vertically aligned multiwall carbon nanotube/$NiCo_2O_4$ core/shell structure for novel high-performance supercapacitors." *Journal of Materials Chemistry A*, 2(14), 5100–5107.

Liu, X., Liu, J., Li, Y., Li, Y., and Sun, X. (2014b). "Au/$NiCo_2O_4$ arrays with high activity for water oxidation." *ChemCatChem*, 6(9), 2501–2506.

Liu, X., Shi, S., Xiong, Q., Li, L., Zhang, Y., Tang, H., Gu, C., Wang, X., and Tu, J. (2013b). "Hierarchical $NiCo_2O_4$@$NiCo_2O_4$ core/shell nanoflake arrays as high-performance supercapacitor materials." *ACS Applied Materials & Interfaces*, 5(17), 8790–8795.

Liu, Z.-Q., Xiao, K., Xu, Q.-Z., Li, N., Su, Y.-Z., Wang, H.-J., and Chen, S. (2013c). "Fabrication of hierarchical flower-like super-structures consisting of porous $NiCo_2O_4$ nanosheets and their electrochemical and magnetic properties." *RSC Advances*, 3(13), 4372–4380.

Loche, D., Marras, C., Carta, D., Casula, M. F., Mountjoy, G., and Corrias, A. (2017). "Cation distribution and vacancies in nickel cobaltite." *Physical Chemistry Chemical Physics*, 19(25), 16775–16784.

Long, X., Lin, H., Zhou, D., An, Y., and Yang, S. (2018). "Enhancing Full Water-Splitting Performance of Transition Metal Bifunctional Electrocatalysts in Alkaline Solutions by Tailoring CeO_2–Transition Metal Oxides–Ni Nanointerfaces." *ACS Energy Letters*, 3(2), 290–296.

Lopes, K. P., Cavalcante, L. S., Simões, A. Z., Varela, J. A., Longo, E., and Leite, E. R. (2009a). "NiTiO$_3$ powders obtained by polymeric precursor method: Synthesis and characterization." *Journal of Alloys and Compounds*, 468(1–2), 327–332.

Lu, Q., Hutchings, G. S., Yu, W., Zhou, Y., Forest, R. V., Tao, R., Rosen, J., Yonemoto, B. T., Cao, Z., Zheng, H., Xiao, J. Q., Jiao, F., and Chen, J. G. (2015). "Highly porous non-precious bimetallic electrocatalysts for efficient hydrogen evolution." *Nature Communications*, 6, 6567.

Lu, X., Liu, X., Zhang, W., Wang, C., and Wei, Y. (2006). "Large-scale synthesis of tungsten oxide nanofibers by electrospinning." *Journal of colloid and interface science*, 298(2), 996–999.

Lyngaas, K. (2015). "Nanotechnology in the textile and fashion business. Part two." *Sustainable Fashion Design by Buddha Jeans*, http://buddhajeans.com/2015/03/15/nanotechnology-in-the-textile-and-fashion-business-part-ii/ (Aug. 28, 2018).

M. Banerjee, A., R. Pai, M., Arya, A., and R. Bharadwaj, S. (2015). "Photocatalytic H$_2$ generation over In$_2$TiO$_5$, Ni substituted In$_2$TiO$_5$ and NiTiO$_3$ – a combined theoretical and experimental study." *RSC Advances*, 5(75), 61218–61229.

M. Barakat, N. A., Kim, B., J. Park, S., Jo, Y., Jung, M.-H., and Yong Kim, H. (2009). "Cobalt nanofibers encapsulated in a graphite shell by an electrospinning process." *Journal of Materials Chemistry*, 19(39), 7371–7378.

Ma, G., Yang, M., Li, C., Tan, H., Deng, L., Xie, S., Xu, F., Wang, L., and Song, Y. (2016). "Preparation of spinel nickel-cobalt oxide nanowrinkles/reduced graphene oxide hybrid for nonenzymatic glucose detection at physiological level." *Electrochimica Acta*, 220, 545–553.

Madhugiri, S., Sun, B., Smirniotis, P. G., Ferraris, J. P., and Balkus Jr, K. J. (2004). "Electrospun mesoporous titanium dioxide fibers." *Microporous and Mesoporous Materials*, 69(1–2), 77–83.

Maensiri, S., and Nuansing, W. (2006). "Thermoelectric oxide NaCo$_2$O$_4$ nanofibers fabricated by electrospinning." *Materials chemistry and physics*, 99(1), 104–108.

Mahmood, N., Zhang, C., and Hou, Y. (2013). "Nickel Sulfide/Nitrogen-Doped Graphene Composites: Phase-Controlled Synthesis and High Performance Anode Materials for Lithium Ion Batteries." *Small*, 9(8), 1321–1328.

Makhlouf, S. A., Bakr, Z. H., Al-Attar, H., and Moustafa, M. S. (2013). "Structural, morphological and electrical properties of Cr_2O_3 nanoparticles." *Materials Science and Engineering: B*, 178(6), 337–343.

Marco, J. F., Gancedo, J. R., Gracia, M., Gautier, J. L., Ríos, E., and Berry, F. J. (2000). "Characterization of the nickel cobaltite, $NiCo_2O_4$, prepared by several methods: An XRD, XANES, EXAFS, and XPS study." *Journal of Solid State Chemistry*, 153(1), 74–81.

Marco, J. F., Gancedo, J. R., Gracia, M., Gautier, J. L., Ríos, E. I., Palmer, H. M., Greaves, C., and Berry, F. J. (2001). "Cation distribution and magnetic structure of the ferrimagnetic spinel $NiCo_2O_4$." *Journal of Materials Chemistry*, 11(12), 3087–3093.

McCloy, J. S., Jiang, W., Bennett, W., Engelhard, M., Lindemuth, J., Parmar, N., and Exarhos, G. J. (2015). "Electrical and magnetic properties modification in heavy ion irradiated nanograin $Ni_xCo_{(3-x)}O_4$ films." *The Journal of Physical Chemistry C*, 119(39), 22465–22476.

McHenry, M. E., Majetich, S. A., and Kirkpatrick, E. M. (1995). "Synthesis, structure, properties and magnetic applications of carbon-coated nanocrystals produced by a carbon arc." *Materials Science and Engineering: A*, 204(1), 19–24.

Medford, A. J., Vojvodic, A., Hummelshøj, J. S., Voss, J., Abild-Pedersen, F., Studt, F., Bligaard, T., Nilsson, A., and Nørskov, J. K. (2015). "From the Sabatier principle to a predictive theory of transition-metal heterogeneous catalysis." *Journal of Catalysis*, 328, 36–42.

Minikayev, R., Paszkowicz, W., Piszora, P., Knapp, M., Bähtz, C., and Podsiadło, S. (2015). "Thermal expansion of polycrystalline gallium nitride: An X-ray diffraction study." *X-Ray Spectrometry*, 44(5), 382–388.

Modak, M., Pal, N., Mondal, S., Sardar, M., and Banerjee, S. (2018). "Magnetic behavior of nanostructured $NiTiO_3$ and NiO material: Anomalous increase in coercivity." *Journal of Magnetism and Magnetic Materials*, 448, 221–227.

Moghiminia, S., Farsi, H., and Raissi, H. (2014). "Comparative optical and electrochemical studies of nanostructured $NiTiO_3$ and $NiTiO_3$-TiO_2 prepared by a low temperature modified Sol-Gel route." *Electrochimica Acta*, 132, 512–523.

Mohammadi, M. R., and Fray, D. J. (2010). "Mesoporous and nanocrystalline sol-gel derived $NiTiO_3$ at the low temperature: Controlling the structure, size and surface area by Ni:Ti molar ratio." *Solid State Sciences*, 12(9), 1629–1640.

Mohan, V. B., Brown, R., Jayaraman, K., and Bhattacharyya, D. (2015). "Characterisation of reduced graphene oxide: Effects of reduction variables on electrical conductivity." *Materials Science and Engineering: B*, 193, 49–60.

Mondal, A., Maiti, S., Mahanty, S., and Baran Panda, A. (2017). "Large-scale synthesis of porous $NiCo_2O_4$ and rGO-$NiCo_2O_4$ hollow-spheres with superior electrochemical performance as faradaic electrode." *Journal of Materials Chemistry A*, 5, 16854–16864.

Mondal, K. (2017). "Recent advances in the synthesis of metal oxide nanofibers and their environmental remediation applications." *Inventions*, 2(2), 9.

Mondal, K., and Sharma, A. (2016). "Recent advances in electrospun metal-oxide nanofiber based interfaces for electrochemical biosensing." *RSC Advances*, 6(97), 94595–94616.

Morales-Guio, C. G., Stern, L.-A., and Hu, X. (2014). "Nanostructured hydrotreating catalysts for electrochemical hydrogen evolution." *Chemical Society Reviews*, 43(18), 6555–6569.

Muan, A. (1992). "Equilibrium relations in the system NiO-TiO_2 in the temperature range 1300° to 1750°C." *Journal of the American Ceramic Society*, 75(6), 1357–1360.

Mufti, N., Blake, G. R., Mostovoy, M., Riyadi, S., Nugroho, A. A., and Palstra, T. T. M. (2011). "Magnetoelectric coupling in $MnTiO_3$." *Physical Review B*, 83(10), 104416.

Murugan, A. V., Samuel, V., Navale, S. C., and Ravi, V. (2006). "Phase evolution of NiTiO$_3$ prepared by coprecipition method." *Materials Letters*, 60(15), 1791–1792.

Naik, K. K., Gangan, A., Chakraborty, B., Nayak, S. K., and Rout, C. S. (2017). "Enhanced nonenzymatic glucose-sensing properties of electrodeposited NiCo$_2$O$_4$-Pd nanosheets: Experimental and DFT investigations." *ACS Applied Materials & Interfaces*, 9(28), 23894–23903.

Naik, K. K., Kumar, S., and Rout, C. S. (2015). "Electrodeposited spinel NiCo$_2$O$_4$ nanosheet arrays for glucose sensing application." *RSC Advances*, 5(91), 74585–74591.

Nakate, U. T., and Kale, S. N. (2016). "Microwave assisted synthesis and characterizations of NiCo$_2$O$_4$ nanoplates and electrical, magnetic properties." *Materials Today: Proceedings*, 3(6), 1992–1998.

Nam, D.-H., Lee, J.-H., Kim, N.-R., Lee, Y.-Y., Yeon, H.-W., Lee, S.-Y., and Joo, Y.-C. (2015). "One-step structure modulation of electrospun metal-loaded carbon nanofibers: Redox reaction controlled calcination." *Carbon*, 82, 273–281.

Naveen, A. N., and Selladurai, S. (2015). "Novel low temperature synthesis and electrochemical characterization of mesoporous nickel cobaltite-reduced graphene oxide (RGO) composite for supercapacitor application." *Electrochimica Acta*, 173, 290–301.

Ndione Paul F., Shi Yezhou, Stevanovic Vladan, Lany Stephan, Zakutayev Andriy, Parilla Philip A., Perkins John D., Berry Joseph J., Ginley David S., and Toney Michael F. (2013). "Control of the electrical properties in spinel oxides by manipulating the cation disorder." *Advanced Functional Materials*, 24(5), 610–618.

New World Encyclopedia contributors. (2017). "Coriolis effect." *New World Encyclopedia* http://www.newworldencyclopedia.org/p/index.php?title=Coriolis_effect&oldid=100 3881 (Oct. 7, 2017).

Nguyen-Phan, T.-D., Nguyen-Huy, C., and Woo Shin, E. (2014). "Morphological evolution of hierarchical nickel titanates by elevation of the solvothermal temperature." *Materials Letters*, 131, 217–221.

Ni, Y., Wang, X., and Hong, J. (2009). "Nickel titanate microtubes constructed by nearly spherical nanoparticles: Preparation, characterization and properties." *Materials Research Bulletin*, 44(8), 1797–1801.

Niklasson, G. A., Torebring, A., Larsson, C., Granqvist, C. G., and Farestam, T. (1988). "Fractal dimension of gas-evaporated Co aggregates: Role of magnetic coupling." *Physical Review Letters*, 60(17), 1735–1738.

Nissinen, T. A., Kiros, Y., Gasik, M., and Leskelä, M. (2003). "$MnCo_2O_4$ preparation by microwave-assisted route synthesis (MARS) and the effect of carbon admixture." *Chemistry of Materials*, 15(26), 4974–4979.

Okpalugo, T. I. T., Papakonstantinou, P., Murphy, H., McLaughlin, J., and Brown, N. M. D. (2005). "High resolution XPS characterization of chemical functionalised MWCNTs and SWCNTs." *Carbon*, 43(1), 153–161.

Osgood, H., Devaguptapu, S. V., Xu, H., Cho, J., and Wu, G. (2016). "Transition metal (Fe, Co, Ni, and Mn) oxides for oxygen reduction and evolution bifunctional catalysts in alkaline media." *Nano Today*, 11(5), 601–625.

Ostermann, R., Li, D., Yin, Y., McCann, J. T., and Xia, Y. (2006). "V_2O_5 nanorods on TiO_2 nanofibers: A new class of hierarchical nanostructures enabled by electrospinning and calcination." *Nano Letters*, 6(6), 1297–1302.

Padron, S., Caruntu, D. I., and Lozano, K. (2011). "On 2D Forcespinning^{TM} Modeling." *ASME International Mechanical Engineering Congress and Exposition, Dynamic Systems and Control; Mechatronics and Intelligent Machines, Parts A and B*, American Society of Mechanical Engineers (ASME), Denver, Colorado, 7, 821–830.

Padron, S., Fuentes, A., Caruntu, D., and Lozano, K. (2013). "Experimental study of nanofiber production through forcespinning." *Journal of Applied Physics*, 113(2), 024318.

Pan, H., Yi, J. B., Shen, L., Wu, R. Q., Yang, J. H., Lin, J. Y., Feng, Y. P., Ding, J., Van, L. H., and Yin, J. H. (2007). "Room-temperature ferromagnetism in carbon-doped ZnO." *Physical Review Letters*, 99(12), 127201.

Pan, Y., Liu, Y., Zhao, J., Yang, K., Liang, J., Liu, D., Hu, W., Liu, D., Liu, Y., and Liu, C. (2015). "Monodispersed nickel phosphide nanocrystals with different phases: Synthesis, characterization and electrocatalytic properties for hydrogen evolution." *Journal of Materials Chemistry A*, 3(4), 1656–1665.

Panthi, G., Yousef, A., Barakat, N. A., Khalil, K. A., Akhter, S., Choi, Y. R., and Kim, H. Y. (2013). "Mn_2O_3/TiO_2 nanofibers with broad-spectrum antibiotics effect and photocatalytic activity for preliminary stage of water desalination." *Ceramics International*, 39(3), 2239–2246.

Park, J. Y., and Kim, S. S. (2009). "Growth of nanograins in electrospun ZnO nanofibers." *Journal of the American Ceramic Society*, 92(8), 1691–1694.

Park, J. Y., Asokan, K., Choi, S.-W., and Kim, S. S. (2011). "Growth kinetics of nanograins in SnO_2 fibers and size dependent sensing properties." *Sensors and Actuators B: Chemical*, 152(2), 254–260.

Parra, R., Góes, M. S., Castro, M. S., Longo, E., Bueno, P. R., and Varela, J. A. (2008). "Reaction pathway to the synthesis of anatase via the chemical modification of titanium isopropoxide with acetic acid." *Chemistry of Materials*, 20(1), 143–150.

Patil, A. G., Shanmugharaj, A. M., and Anandhan, S. (2015). "Interparticle interactions and lacunarity of mechano-chemically activated fly ash." *Powder Technology*, 272, 241–249.

Permatasari, F. A., Aimon, A. H., Iskandar, F., Ogi, T., and Okuyama, K. (2016). "Role of C-N configurations in the photoluminescence of graphene quantum dots synthesized by a hydrothermal route." *Scientific Reports*, 6, 21042.

Pontes Ribeiro, R. A., Lazaro, S. R. de, and Gatti, C. (2016). "The role of exchange-correlation functional on the description of multiferroic properties using density functional theory: the $ATiO_3$ (A = Mn, Fe, Ni) case study." *RSC Advances*, 6(103), 101216–101225.

Prathap, M. U. A., Wei, C., Sun, S., and Xu, Z. J. (2015). "A new insight into electrochemical detection of eugenol by hierarchical sheaf-like mesoporous $NiCo_2O_4$." *Nano Research*, 8(8), 2636–2645.

Preciado, M. A. R., Kassiba, A., Morales-Acevedo, A., and Makowska-Janusik, M. (2015). "Vibrational and electronic peculiarities of NiTiO$_3$ nanostructures inferred from first principle calculations." *RSC Advances*, 5(23), 17396–17404.

Preudhomme, J., and Tarte, P. (1972). "Infrared studies of spinels—IV: Normal spinels with a high-valency tetrahedral cation." *Spectrochimica Acta Part A: Molecular Spectroscopy*, 28(1), 69–79.

Qiang Chen, S., and Wang, Y. (2010). "Microwave-assisted synthesis of a Co$_3$O$_4$ – graphene sheet-on-sheet nanocomposite as a superior anode material for Li-ion batteries." *Journal of Materials Chemistry*, 20(43), 9735–9739.

Qin, Z., Cheng, Q., Lu, Y., and Li, J. (2017). "Facile synthesis of hierarchically mesoporous NiCo$_2$O$_4$ nanowires for sensitive nonenzymatic glucose detection." *Applied Physics A*, 123(7), 492.

Qiu, A., Liu, L., Pang, W., Lu, X., and Li, C. (2011). "Calculation of phase diagram of Ti-Ni-O system and application to deoxidation of TiNi alloy." *Transactions of Nonferrous Metals Society of China*, 21(8), 1808–1816.

Qu, Y., Zhou, W., Jiang, L., and Fu, H. (2013). "Novel heterogeneous CdS nanoparticles/NiTiO$_3$ nanorods with enhanced visible-light-driven photocatalytic activity." *RSC Advances*, 3(40), 18305–18310.

Qu, Y., Zhou, W., Ren, Z., Du, S., Meng, X., Tian, G., Pan, K., Wang, G., and Fu, H. (2012). "Facile preparation of porous NiTiO$_3$ nanorods with enhanced visible-light-driven photocatalytic performance." *Journal of Materials Chemistry*, 22(32), 16471–16476.

Rafiee, E., Farzam, M., Golozar, M. A., and Ashrafi, A. (2013). "An investigation on dislocation density in cold-rolled copper using electrochemical impedance spectroscopy." *International Scholarly Research Notices Corrosion*, 2013(921825), 6.

Ragupathi, C., Vijaya, J. J., and Kennedy, L. J. (2014). "Synthesis, characterization of nickel aluminate nanoparticles by microwave combustion method and their catalytic properties." *Materials Science and Engineering: B*, 184, 18–25.

Ramaseshan, R., Sundarrajan, S., Jose, R., and Ramakrishna, S. (2007). "Nanostructured ceramics by electrospinning." *Journal of Applied Physics*, 102(11), 111101.

Randall, C. A., Kim, N., Kucera, J.-P., Cao, W., and Shrout, T. R. (1998). "Intrinsic and extrinsic size effects in fine-grained morphotropic-phase-boundary lead zirconate titanate ceramics." *Journal of the American Ceramic Society*, 81(3), 677–688.

Rao, H., Zhang, Z., Ge, H., Liu, X., Zou, P., Wang, X., and Wang, Y. (2017). "Enhanced amperometric sensing using a $NiCo_2O_4$/nitrogen-doped reduced graphene oxide/ionic liquid ternary composite for enzyme-free detection of glucose." *New Journal of Chemistry*, 41(9), 3667–3676.

Rasiyah, P., and Tseung, A. C. C. (1983). "A mechanistic study of oxygen evolution on $NiCo_2O_4$ II . Electrochemical kinetics." *Journal of The Electrochemical Society*, 130(12), 2384–2386.

Rasiyah, P., Tseung, A. C. C., and Hibbert, D. B. (1982). "A mechanistic study of oxygen evolution on $NiCo_2O_4$ I . Formation of higher oxides." *Journal of The Electrochemical Society*, 129(8), 1724–1727.

Rawool, S. A., Pai, M. R., Banerjee, A. M., Arya, A., Ningthoujam, R. S., Tewari, R., Rao, R., Chalke, B., Ayyub, P., Tripathi, A. K., and Bharadwaj, S. R. (2018). "pn Heterojunctions in $NiO:TiO_2$ composites with type-II band alignment assisting sunlight driven photocatalytic H_2 generation." *Applied Catalysis B: Environmental*, 221, 443–458.

Reddy, M. V., Prithvi, G., Loh, K. P., and Chowdari, B. V. R. (2014). "Li storage and impedance spectroscopy studies on Co_3O_4, CoO, and CoN for Li-ion batteries." *ACS Applied Materials & Interfaces*, 6(1), 680–690.

Ruan, Y., Wang, C., and Jiang, J. (2016). "Nanostructured Ni compounds as electrode materials towards high-performance electrochemical capacitors." *Journal of Materials Chemistry A*, 4(38), 14509–14538.

Ruiz-Preciado, M. A., Kassiba, A., Gibaud, A., and Morales-Acevedo, A. (2015). "Comparison of nickel titanate ($NiTiO_3$) powders synthesized by sol-gel and solid state reaction." *Materials Science in Semiconductor Processing*, 37, 171–178.

Ryu, S. R., Noda, I., and Jung, Y. M. (2010). "What is the origin of positional fluctuation of spectral features: True frequency shift or relative intensity changes of two overlapped bands?" *Applied Spectroscopy*, 64(9), 1017–1021.

Sadjadi, M. S., Zare, K., Khanahmadzadeh, S., and Enhessari, M. (2008). "Structural characterization of $NiTiO_3$ nanopowders prepared by stearic acid gel method." *Materials Letters*, 62(21–22), 3679–3681.

Sahay, R., Suresh Kumar, P., Sridhar, R., Sundaramurthy, J., Venugopal, J., G. Mhaisalkar, S., and Ramakrishna, S. (2012). "Electrospun composite nanofibers and their multifaceted applications." *Journal of Materials Chemistry*, 22(26), 12953–12971.

Sajan, C. P., Naik, A., Girish, H. N., Ravi, H. R., and Singh, R. (2017). "Template-free processing of Ag-anchored ZnO polyscale sheets and their application in the photocatalytic degradation of organics present in pharmaceutical waste." *Water Conservation Science and Engineering*, 2(2), 31–41.

Sakar, M., Balakumar, S., Saravanan, P., and Jaisankar, S. N. (2016). "Electric field induced formation of one-dimensional bismuth ferrite ($BiFeO_3$) nanostructures in electrospinning process." *Materials & Design*, 94, 487–495.

Sangaletti, L., Mozzati, M. C., Galinetto, P., Azzoni, C. B., Speghini, A., Bettinelli, M., and Calestani, G. (2006). "Ferromagnetism on a paramagnetic host background: the case of rutile $TM:TiO_2$ single crystals (TM = Cr, Mn, Fe, Co, Ni, Cu)." *Journal of Physics: Condensed Matter*, 18(32), 7643.

Saraf, M., Natarajan, K., and M. Mobin, S. (2017). "Multifunctional porous $NiCo_2O_4$ nanorods: sensitive enzymeless glucose detection and supercapacitor properties with impedance spectroscopic investigations." *New Journal of Chemistry*, 41(17), 9299–9313.

Sawicka, K. M., and Gouma, P. (2006). "Electrospun composite nanofibers for functional applications." *Journal of Nanoparticle Research*, 8(6), 769–781.

Scheirs, J. (2000). *Compositional and Failure Analysis of Polymers: A Practical Approach*. John Wiley & Sons, Chichester.

Schulze, M., Bradke, M. v, Reissner, R., Lorenz, M., and Gülzow, E. (1999). "Characterization of polymers in PEFC-electrodes with EDX and XPS." *Fresenius' Journal of Analytical Chemistry*, 365(1–3), 123–132.

Secula, E. M. (2010). "Resistivity and Hall measurements." *National Institute of Standards and Technology*, https://www.nist.gov/pml/engineering-physics-division/resistivity-and-hall-measurements (Jul. 19, 2017).

Seh, Z. W., Kibsgaard, J., Dickens, C. F., Chorkendorff, I., Nørskov, J. K., and Jaramillo, T. F. (2017). "Combining theory and experiment in electrocatalysis: Insights into materials design." *Science*, 355(6321), eaad4998.

Senthil, T., and Anandhan, S. (2014). "Structure-property relationship of sol-gel electrospun ZnO nanofibers developed for ammonia gas sensing." *Journal of Colloid and Interface Science*, 432, 285–296.

Senthil, T., and Anandhan, S. (2015). "Fabrication of styrene-acrylonitrile random copolymer nanofiber membranes from N,N-dimethyl formamide by electrospinning." *Journal of Elastomers & Plastics*, 47(4), 327–346.

Senthil, T., George, G., and Anandhan, S. (2013). "Chemical-resistant ultrafine poly(styrene-*co*-acrylonitrile) fibers by electrospinning: Process optimization by design of experiment." *Polymer-Plastics Technology and Engineering*, 52(4), 407–421.

Senthil, T., George, G., and Srinivasan, A. (2016). "Electrospinning: From fundamentals to applications." *Advances in Polymer Materials and Technology*, A. Srinivasan and S. Bandyopadhyay, eds., CRC Press, Boca Raton, 147–218.

Shamitha, C., Senthil, T., Wu, L., Kumar, B. S., and Anandhan, S. (2017). "Sol-gel electrospun mesoporous $ZnMn_2O_4$ nanofibers with superior specific surface area." *Journal of Materials Science: Materials in Electronics*, 28(21), 15846–15860.

Shao, C., Guan, H., Liu, Y., Gong, J., Yu, N., and Yang, X. (2004a). "A novel method for making ZrO_2 nanofibres via an electrospinning technique." *Journal of Crystal Growth*, 267(1–2), 380–384.

Shao, C., Guan, H., Liu, Y., Li, X., and Yang, X. (2004b). "Preparation of Mn_2O_3 and Mn_3O_4 nanofibers via an electrospinning technique." *Journal of Solid State Chemistry*, 177(7), 2628–2631.

Shao, C., Yang, X., Guan, H., Liu, Y., and Gong, J. (2004c). "Electrospun nanofibers of NiO/ZnO composite." *Inorganic Chemistry Communications*, 7(5), 625–627.

Shao, Y., Wang, J., Wu, H., Liu, J., Aksay, I. A., and Lin, Y. (2010). "Graphene based electrochemical sensors and biosensors: A review." *Electroanalysis*, 22(10), 1027–1036.

Shen, C., Sun, Y., Wang, J., and Lu, Y. (2014). "Facile route to highly photoluminescent carbon nanodots for ion detection, pH sensors and bioimaging." *Nanoscale*, 6(15), 9139–9147.

Shi, H., and Zhao, G. (2014). "Water oxidation on spinel $NiCo_2O_4$ nanoneedles anode: Microstructures, specific surface character, and the enhanced electrocatalytic performance." *The Journal of Physical Chemistry C*, 118(45), 25939–25946.

Shi, X., Bernasek, S. L., and Selloni, A. (2016). "Formation, electronic structure, and defects of Ni substituted spinel cobalt oxide: a DFT+U study." *The Journal of Physical Chemistry C*, 120(27), 14892–14898.

Shi, X., Zhou, W., Ma, D., Ma, Q., Bridges, D., Ma, Y., and Hu, A. (2015). "Electrospinning of nanofibers and their applications for energy devices." *Journal of Nanomaterials*, 16(1), 122.

Shim, S.-H., Duffy, T. S., Jeanloz, R., Yoo, C.-S., and Iota, V. (2004). "Raman spectroscopy and X-ray diffraction of phase transitions in Cr_2O_3 to 61 GPa." *Physical Review B*, 69(14), 144107.

Shu, X., He, J., and Chen, D. (2008). "Visible-light-induced photocatalyst based on nickel titanate nanoparticles." *Industrial & Engineering Chemistry Research*, 47(14), 4750–4753.

Si, P., Huang, Y., Wang, T., and Ma, J. (2013). "Nanomaterials for electrochemical non-enzymatic glucose biosensors." *RSC Advances*, 3(11), 3487–3502.

Silambarasan, M., Ramesh, P. S., and Geetha, D. (2017). "Facile one-step synthesis, structural, optical and electrochemical properties of $NiCo_2O_4$ nanostructures." *Journal of Materials Science: Materials in Electronics*, 28(1), 323–336.

Silwal, P., La-o-vorakiat, C., Chia, E. E. M., Kim, D. H., and Talbayev, D. (2013). "Effect of growth temperature on the terahertz-frequency conductivity of the epitaxial transparent conducting spinel $NiCo_2O_4$ films." *AIP Advances*, 3(9), 092116.

Singh, G., Choudhary, A., Haranath, D., Joshi, A. G., Singh, N., Singh, S., and Pasricha, R. (2012). "ZnO decorated luminescent graphene as a potential gas sensor at room temperature." *Carbon*, 50(2), 385–394.

Sivanantham, A., Ganesan, P., and Shanmugam, S. (2016). "Hierarchical $NiCo_2S_4$ nanowire arrays supported on Ni foam: An efficient and durable bifunctional electrocatalyst for oxygen and hydrogen evolution reactions." *Advanced Functional Materials*, 26(26), 4661–4672.

Sobhani-Nasab, A., Hosseinpour-Mashkani, S. M., Salavati-Niasari, M., Taqriri, H., Bagheri, S., and Saberyan, K. (2015). "Synthesis, characterization, and photovoltaic application of $NiTiO_3$." *Journal of Materials Science: Materials in Electronics*, 26(8), 5735–5742.

Song, F., Bai, L., Moysiadou, A., Lee, S., Hu, C., Liardet, L., et al. (2018). "Transition Metal Oxides as Electrocatalysts for the Oxygen Evolution Reaction in Alkaline Solutions: An Application-Inspired Renaissance." *Journal of the American Chemical Society*, 140(25), 7748–7759.

Sontu, U. B., Yelasani, V., and Musugu, V. R. R. (2015). "Structural, electrical and magnetic characteristics of nickel substituted cobalt ferrite nano particles, synthesized

by self combustion method." *Journal of Magnetism and Magnetic Materials*, 374, 376–380.

Srivastava, M., Elias Uddin, M., Singh, J., Kim, N. H., and Lee, J. H. (2014). "Preparation and characterization of self-assembled layer by layer $NiCo_2O_4$–reduced graphene oxide nanocomposite with improved electrocatalytic properties." *Journal of Alloys and Compounds*, 590, 266–276.

Stern, L.-A., Feng, L., Song, F., and Hu, X. (2015). "Ni_2P as a Janus catalyst for water splitting: the oxygen evolution activity of Ni_2P nanoparticles." *Energy & Environmental Science*, 8(8), 2347–2351.

Stickler, J. J., Kern, S., Wold, A., and Heller, G. S. (1967). "Magnetic resonance and susceptibility of several ilmenite powders." *Physical Review*, 164(2), 765–767.

Stráská, J., Stráský, J., and Janeček, M. (2015). "Activation energy for grain growth of the isochronally annealed ultrafine grained magnesium alloy after hot extrusion and equal-channel angular pressing (EX-ECAP)." *Acta Physica Polonica, A.*, 128(4), 578–581.

Stuart, B. H. (2004). *Infrared Spectroscopy: Fundamentals and Applications*. John Wiley & Sons, Chichester.

Su, Y., Xu, Q., Zhong, Q., Shi, S., Zhang, C., and Xu, C. (2014). "$NiCo_2O_4$/C prepared by one-step intermittent microwave heating method for oxygen evolution reaction in splitter." *Journal of Alloys and Compounds*, 617, 115–119.

Su, Y.-Z., Xu, Q.-Z., Chen, G.-F., Cheng, H., Li, N., and Liu, Z.-Q. (2015). "One dimensionally spinel $NiCo_2O_4$ nanowire arrays: facile synthesis, water oxidation, and magnetic properties." *Electrochimica Acta*, 174, 1216–1224.

Subramanya, B., Ullal, Y., U. Shenoy, S., K. Bhat, D., and C. Hegde, A. (2015). "Novel Co-Ni-graphene composite electrodes for hydrogen production." *RSC Advances*, 5(59), 47398–47407.

Sun, Y., Li, J. Y., Tan, Y., and Zhang, L. (2009). "Fabrication of aluminum nitride (AlN) hollow fibers by carbothermal reduction and nitridation of electrospun precursor fibers." *Journal of Alloys and Compounds*, 471(1), 400–403.

Swaminathan, J., Subbiah, R., and Singaram, V. (2016). "Defect-rich metallic titania ($TiO_{1.23}$) – An efficient hydrogen evolution catalyst for electrochemical water splitting." *ACS Catalysis*, 6(4), 2222–2229.

Tagliente, M. A., and Massaro, M. (2008). "Strain-driven (0 0 2) preferred orientation of ZnO nanoparticles in ion-implanted silica." *Nuclear Instruments and Methods in Physics Research Section B: Beam Interactions with Materials and Atoms*, 266(7), 1055–1061.

Tahir, A. A., Mazhar, M., Hamid, M., Wijayantha, K. G. U., and Molloy, K. C. (2009). "Photooxidation of water by $NiTiO_3$ deposited from single source precursor [$Ni_2Ti_2(OEt)_2(\mu\text{-}OEt)_6(acac)_4$] by AACVD." *Dalton Transactions*, (19), 3674–3680.

Tajik, S., Dubal, D. P., Gomez-Romero, P., Yadegari, A., Rashidi, A., Nasernejad, B., Inamuddin, and Asiri, A. M. (2017). "Nanostructured mixed transition metal oxides for high performance asymmetric supercapacitors: Facile synthetic strategy." *International Journal of Hydrogen Energy*, 42(17), 12384–12395.

Tang, C.-W., Wang, C.-B., and Chien, S.-H. (2008). "Characterization of cobalt oxides studied by FT-IR, Raman, TPR and TG-MS." *Thermochimica Acta*, 473(1–2), 68–73.

Tang, J., and Alivisatos, A. P. (2006). "Crystal splitting in the growth of Bi_2S_3." *Nano Letters*, 6(12), 2701–2706.

Tang, X., Zhang, B., Xiao, C., Zhou, H., Wang, X., and He, D. (2016). "Carbon nanotube template synthesis of hierarchical $NiCoO_2$ composite for non-enzyme glucose detection." *Sensors and Actuators B: Chemical*, 222, 232–239.

Tareen, J. A. K., Małecki, A., Doumerc, J. P., Launay, J. C., Dordor, P., Pouchard, M., and Hagenmuller, P. (1984). "Growth and electrical properties of pure and Ni-doped Co_3O_4 single crystals." *Materials Research Bulletin*, 19(8), 989–997.

Teo, W. E., and Ramakrishna, S. (2006). "A review on electrospinning design and nanofibre assemblies." *Nanotechnology*, 17(14), R89.

Thakur, A., Singh, R. R., and Barman, P. B. (2013). "Structural and magnetic properties of La^{3+} substituted strontium hexaferrite nanoparticles prepared by citrate precursor method." *Journal of Magnetism and Magnetic Materials*, 326, 35–40.

Thavasi, V., Singh, G., and Ramakrishna, S. (2008). "Electrospun nanofibers in energy and environmental applications." *Energy & Environmental Science*, 1(2), 205–221.

Tian, K., Prestgard, M., and Tiwari, A. (2014). "A review of recent advances in nonenzymatic glucose sensors." *Materials Science and Engineering: C*, 41, 100–118.

Tomer, V., Teye-Mensah, R., Tokash, J. C., Stojilovic, N., Kataphinan, W., Evans, E. A., Chase, G. G., Ramsier, R. D., Smith, D. J., and Reneker, D. H. (2005). "Selective emitters for thermophotovoltaics: erbia-modified electrospun titania nanofibers." *Solar energy materials and solar cells*, 85(4), 477–488.

Tong, X., Chen, S., Guo, C., Xia, X., and Guo, X.-Y. (2016). "Mesoporous $NiCo_2O_4$ nanoplates on three-dimensional graphene foam as an efficient electrocatalyst for the oxygen reduction reaction." *ACS Applied Materials & Interfaces*, 8(42), 28274–28282.

Tripathi, A. K., Mathpal, M. C., Kumar, P., Agrahari, V., Singh, M. K., Mishra, S. K., Ahmad, M. M., and Agarwal, A. (2015). "Photoluminescence and photoconductivity of Ni doped titania nanoparticles." *Advanced Materials Letters*, 6(3), 201–208.

Trivedi, S., and Prasad, R. (2017). "Selection of cobaltite and effect of preparation method of $NiCo_2O_4$ for catalytic oxidation of CO-CH_4 mixture." *Asia-Pacific Journal of Chemical Engineering*, 12(3), 440–453.

Troyanchuk, I. O., Khomchenko, V. A., Chobot, G. M., Kurbakov, A. I., Vasil'ev, A. N., Eremenko, V. V., Sirenko, V. A., Shvedun, M. Y., Szymczak, H., and Szymczak, R. (2003). "Spin-reorientational transitions in low-doped $Nd_{1-x}Ca_xMnO_3$ manganites: The evidence of an inhomogeneous magnetic state." *Journal of Physics: Condensed Matter*, 15(50), 8865.

Typek, J., Guskos, N., Zolnierkiewicz, G., Mozia, S., and Morawski, A. (2016). "Magnetic properties of nickel doped titanium dioxide: A Case of Ni, N-TiO$_2$ nanocomposites." *Rev. Adv. Mater. Sci*, 44, 407–419.

Ullal, Y., and Hegde, A. C. (2014). "Electrodeposition and electro-catalytic study of nanocrystalline Ni-Fe alloy." *International Journal of Hydrogen Energy*, 39(20), 10485–10492.

Umeshbabu, E., Rajeshkhanna, G., and Rao, G. R. (2014). "Urchin and sheaf-like NiCo$_2$O$_4$ nanostructures: Synthesis and electrochemical energy storage application." *International Journal of Hydrogen Energy*, 39(28), 15627–15638.

Umeshbabu, E., Rajeshkhanna, G., Justin, P., and Rao, G. R. (2015). "Magnetic, optical and electrocatalytic properties of urchin and sheaf-like NiCo$_2$O$_4$ nanostructures." *Materials Chemistry and Physics*, 165, 235–244.

Umeshbabu, E., Rajeshkhanna, G., Justin, P., and Rao, G. R. (2016). "NiCo$_2$O$_4$/rGO hybrid nanostructures for efficient electrocatalytic oxygen evolution." *Journal of Solid State Electrochemistry*, 20(10), 2725–2736.

Un Lee, D., Jung Kim, B., and Chen, Z. (2013). "One-pot synthesis of a mesoporous NiCo$_2$O$_4$ nanoplatelet and graphene hybrid and its oxygen reduction and evolution activities as an efficient bi-functional electrocatalyst." *Journal of Materials Chemistry A*, 1(15), 4754–4762.

Uslu, İ., and Tunç, T. (2012). "The synthesis of boron carbide ceramic via electrospinning technique." *Journal of Inorganic and Organometallic Polymers and Materials*, 22(1), 183–189.

Valipouri, A., Ravandi, S. A. H., Pishevar, A., and Părău, E. I. (2015). "Experimental and numerical study on isolated and non-isolated jet behavior through centrifuge spinning system." *International Journal of Multiphase Flow*, 69, 93–101.

Van Uitert, L. G., Sherwood, R. C., Williams, H. J., Rubin, J. J., and Bonner, W. A. (1964). "Magnetic properties of a number of divalent transition metal tungstates, molybdates and titanates." *Journal of Physics and Chemistry of Solids*, 25(12), 1447–1451.

Varga, T., Droubay, T. C., Bowden, M. E., Colby, R. J., Manandhar, S., Shutthanandan, V., Hu, D., Kabius, B. C., Apra, E., Shelton, W. A., and Chambers, S. A. (2013). "Coexistence of weak ferromagnetism and polar lattice distortion in epitaxial NiTiO$_3$ thin films of the LiNbO$_3$-type structure." *Journal of Vacuum Science & Technology B*, 31(3), 030603.

Varga, T., Droubay, T. C., Bowden, M. E., Kovarik, L., Hu, D., and Chambers, S. A. (2015a). "Strain-dependence of the structure and ferroic properties of epitaxial NiTiO$_3$ thin films grown on different substrates." *Advances in Condensed Matter Physics*, 2015, 1–9.

Varga, T., Droubay, T. C., Bowden, M. E., Nachimuthu, P., Shutthanandan, V., Bolin, T. B., Shelton, W. A., and Chambers, S. A. (2012). "Epitaxial growth of NiTiO$_3$ with a distorted ilmenite structure." *Thin Solid Films*, 520(17), 5534–5541.

Varga, T., Droubay, T. C., Bowden, M. E., Stephens, S. A., Manandhar, S., Shutthanandan, V., Colby, R. J., Hu, D., Shelton, W. A., and Chambers, S. A. (2015b). "Strain-dependence of the structure and ferroic properties of epitaxial Ni$_{1-x}$Ti$_{1-y}$O$_3$ thin films grown on sapphire substrates." *Thin Solid Films*, 578, 113–123.

Venkatachalam, V., Alsalme, A., Alghamdi, A., and Jayavel, R. (2017). "Hexagonal-like NiCo$_2$O$_4$ nanostructure based high-performance supercapacitor electrodes." *Ionics*, 23(4), 977–984.

Verma, S., Joshi, H. M., Jagadale, T., Chawla, A., Chandra, R., and Ogale, S. (2008). "Nearly monodispersed multifunctional NiCo$_2$O$_4$ spinel nanoparticles: Magnetism, infrared transparency, and radiofrequency absorption." *The Journal of Physical Chemistry C*, 112(39), 15106–15112.

Verma, S., Kumar, A., Pravarthana, D., Deshpande, A., Ogale, S. B., and Yusuf, S. M. (2014). "Off-stoichiometric nickel cobaltite nanoparticles: Thermal stability, magnetization, and neutron diffraction studies." *The Journal of Physical Chemistry C*, 118(29), 16246–16254.

Vesel, A., Mozetic, M., Kovac, J., and Zalar, A. (2006). "XPS study of the deposited Ti layer in a magnetron-type sputter ion pump." *Applied Surface Science*, 253(5), 2941–2946.

Vijayalakshmi, R., and Rajendran, V. (2012). "Effect of reaction temperature on size and optical properties of $NiTiO_3$ nanoparticles." *Journal of Chemistry*, 9(1), 282–288.

Vijayalakshmi, R., and Rajendran, V. (2013). "Synthesis, structural characterisation and optical properties of nanoparticles of $MTiO_3$ (M = Ni and Co) obtained by the chemical method." *International Journal of Nanoparticles*, 6(1), 28.

Viswanathamurthi, P., Bhattarai, N., Kim, H. Y., Khil, M. S., Lee, D. R., and Suh, E.-K. (2004). "GeO_2 fibers: Preparation, morphology and photoluminescence property." *The Journal of chemical physics*, 121(1), 441–445.

Volkov, S. V., Ogenko, V. M., Dubrovina, L. V., Holdun, O. V., Senkevich, A. I., and Danylenko, N. I. (2007). "Solutions of polystyrene as a carbonization precursor for the matryx synthesis of carbon nanostructures." *Hydrogen Materials Science and Chemistry of Carbon Nanomaterials*, T. N. Veziroglu, S. Y. Zaginaichenko, D. V. Schur, B. Baranowski, A. P. Shpak, V. V. Skorokhod, and A. Kale, eds., Springer, Dordrecht, 521–528.

Vranješ, M., Konstantinović, Z., Pomar, A., Kuljanin Jakovljević, J., Stoiljković, M., Nedeljković, J. M., and Šaponjić, Z. (2014). "Room-temperature ferromagnetism in Ni^{2+} doped TiO_2 nanocrystals synthesized from nanotubular precursors." *Journal of Alloys and Compounds*, 589, 42–47.

Wan, Y.-Q., Guo, Q., and Pan, N. (2011). "Thermo-electro-hydrodynamic model for electrospinning process." *International Journal of Nonlinear Sciences and Numerical Simulation*, 5(1), 5–8.

Wang, B., Cao, Y., Chen, Y., Lai, X., Peng, J., Tu, J., and Li, X. (2017a). "Rapid synthesis of rGO conjugated hierarchical $NiCo_2O_4$ hollow mesoporous nanospheres with enhanced glucose sensitivity." *Nanotechnology*, 28(2), 025501.

Wang, C., Li, X., Cai, Z., Huang, J., Fan, X., Liu, H., Xu, W., and Fang, D. (2017b). "A review on the electrospun oxide nanofibers for anode electrodes in lithium-ion batteries." *Current Nanoscience*, 13(4), 394–409.

Wang, G., Ji, Y., Huang, X., Yang, X., Gouma, P.-I., and Dudley, M. (2006a). "Fabrication and characterization of polycrystalline WO_3 nanofibers and their application for ammonia sensing." *The Journal of Physical Chemistry B*, 110(47), 23777–23782.

Wang, H., Shao, H., and Hu, X. (2006b). "Structure of silk fibroin fibers made by an electrospinning process from a silk fibroin aqueous solution." *Journal of Applied Polymer Science*, 101(2), 961–968.

Wang, J.-L., Li, Y.-Q., Byon, Y.-J., Mei, S.-G., and Zhang, G.-L. (2013a). "Synthesis and characterization of $NiTiO_3$ yellow nano pigment with high solar radiation reflection efficiency." *Powder Technology*, 235, 303–306.

Wang, L., Lu, X., Ye, Y., Sun, L., and Song, Y. (2013b). "Nickel-cobalt nanostructures coated reduced graphene oxide nanocomposite electrode for nonenzymatic glucose biosensing." *Electrochimica Acta*, 114, 484–493.

Wang, M., Singh, H., Hatton, T. A., and Rutledge, G. C. (2004). "Field-responsive superparamagnetic composite nanofibers by electrospinning." *Polymer*, 45(16), 5505–5514.

Wang, S. F., Gu, F., Lü, M. K., Song, C. F., Xu, D., Yuan, D. R., and Liu, S. W. (2003). "Photoluminescence of sol-gel derived $ZnTiO_3:Ni^{2+}$ nanocrystals." *Chemical Physics Letters*, 373(1–2), 223–227.

Wang, S., Zhang, S., Liu, M., Song, H., Gao, J., and Qian, Y. (2018). "MoS_2 as connector inspired high electrocatalytic performance of $NiCo_2O_4$ nanoplates towards glucose." *Sensors and Actuators B: Chemical*, 254, 1101–1109.

Wang, X., Wen, W., Mi, J., Li, X., and Wang, R. (2015a). "The ordered mesoporous transition metal oxides for selective catalytic reduction of NO_x at low temperature." *Applied Catalysis B: Environmental*, 176, 454–463.

Wang, Y., and Santiago-Avilés, J. J. (2003). "Synthesis of lead zirconate titanate nanofibres and the Fourier-transform infrared characterization of their metallo-organic decomposition process." *Nanotechnology*, 15(1), 32.

Wang, Y., Cheng, K., Cao, D., Yang, F., Yan, P., Zhang, W., and Wang, G. (2015b). "Preparation of NiCo$_2$O$_4$ nanosheet arrays and its high catalytic performance for H$_2$O$_2$ electroreduction." *Fuel Cells*, 15(2), 298–305.

Wang, Z., Cai, W., Hong, X., Zhao, X., Xu, F., and Cai, C. (2005). "Photocatalytic degradation of phenol in aqueous nitrogen-doped TiO$_2$ suspensions with various light sources." *Applied Catalysis B: Environmental*, 57(3), 223–231.

Watanabe, H., Yamauchi, H., and Takei, H. (1980). "Magnetic anisotropies in MTiO$_3$ (M = Co, Ni)." *Journal of Magnetism and Magnetic Materials*, 15, 549–550.

Wen, Y., Liu, J., Song, J., Gong, J., Chen, H., and Tang, T. (2015). "Conversion of polystyrene into porous carbon sheets and hollow carbon shells over different magnesium oxide templates for efficient removal of methylene blue." *RSC Advances*, 5(127), 105047–105056.

Weyer, L. g., and Lo, S.-C. (2006). "Spectra-structure correlations in the near-infrared." *Handbook of Vibrational Spectroscopy*, J. M. Chalmers and P. Griffiths, eds., John Wiley & Sons, Chichester, 1, 1-21.

Windisch, C. F., Exarhos, G. J., and Owings, R. R. (2004). "Vibrational spectroscopic study of the site occupancy distribution of cations in nickel cobalt oxides." *Journal of Applied Physics*, 95(10), 5435–5442.

Windisch, C. F., Exarhos, G. J., Ferris, K. F., Engelhard, M. H., and Stewart, D. C. (2001a). "Infrared transparent spinel films with p-type conductivity." *Thin Solid Films*, 398, 45–52.

Windisch, C. F., Ferris, K. F., and Exarhos, G. J. (2001b). "Synthesis and characterization of transparent conducting oxide cobalt-nickel spinel films." *Journal of Vacuum Science & Technology A: Vacuum, Surfaces, and Films*, 19(4), 1647–1651.

Windisch, C. F., Ferris, K. F., Exarhos, G. J., and Sharma, S. K. (2002). "Conducting spinel oxide films with infrared transparency." *Thin Solid Films*, 420, 89–99.

Wolf, D. A., and Schwarz, R. P. (1991). *Technical paper 3143 - Analysis of gravity-induced particle motion and fluid perfusion flow in the NASA-designed rotating zero-head-space tissue culture vessel*. National Aeronautics and Space Administration (NASA) Technical Reports Server, Washington, D. C., 19920004122.

Wu, C., Li, J., Zhang, D., Yang, B., Li, L., Zhou, T., Zhang, C., Yang, G., and Shan, Y. (2016). "Electrospun transition/alkaline earth metal oxide composite nanofibers under mild condition for hydrogen evolution reaction." *International Journal of Hydrogen Energy*, 41(32), 13915–13922.

Wu, H., and Pan, W. (2006). "Preparation of zinc oxide nanofibers by electrospinning." *Journal of the American Ceramic Society*, 89(2), 699–701.

Wu, H., Lin, D., and Pan, W. (2006). "Fabrication, assembly, and electrical characterization of CuO nanofibers." *Applied physics letters*, 89(13), 133125.

Wu, H., Pan, W., Lin, D., and Li, H. (2012a). "Electrospinning of ceramic nanofibers: Fabrication, assembly and applications." *Journal of Advanced Ceramics*, 1(1), 2–23.

Wu, M., Meng, S., Wang, Q., Si, W., Huang, W., and Dong, X. (2015). "Nickel-cobalt oxide decorated three-dimensional graphene as an enzyme mimic for glucose and calcium detection." *ACS Applied Materials & Interfaces*, 7(38), 21089–21094.

Wu, Z.-S., Zhou, G., Yin, L.-C., Ren, W., Li, F., and Cheng, H.-M. (2012b). "Graphene/metal oxide composite electrode materials for energy storage." *Nano Energy*, 1(1), 107–131.

Xia, G., Zhang, L., Fang, F., Sun, D., Guo, Z., Liu, H., and Yu, X. (2016a). "General synthesis of transition metal oxide ultrafine nanoparticles embedded in hierarchically porous carbon nanofibers as advanced electrodes for lithium storage." *Advanced Functional Materials*, 26(34), 6188–6196.

Xia, W.-Y., Li, N., Li, Q.-Y., Ye, K.-H., and Xu, C.-W. (2016b). "Au-NiCo$_2$O$_4$ supported on three-dimensional hierarchical porous graphene-like material for highly effective oxygen evolution reaction." *Scientific Reports*, 6, 23398.

Xia, X., Dong, X., Wei, Q., Cai, Y., and Lu, K. (2012). "Formation mechanism of porous hollow SnO$_2$ nanofibers prepared by one-step electrospinning." *Express Polymer Letters*, 6(2).

Xia, Y., Yang, P., Sun, Y., Wu, Y., Mayers, B., Gates, B., Yin, Y., Kim, F., and Yan, H. (2003). "One-dimensional nanostructures: Synthesis, characterization, and applications." *Advanced Materials*, 15(5), 353–389.

Xiang Ming Kong, Rahn, C. D., and Goswami, B. C. (1999). "Steady-state unwinding of yarn from cylindrical packages." *Textile Research Journal*, 69(4), 292–306.

Xiao, C., Li, Y., Lu, X., and Zhao, C. (2016). "Bifunctional porous NiFe/NiCo$_2$O$_4$/Ni foam electrodes with triple hierarchy and double synergies for efficient whole cell water splitting." *Advanced Functional Materials*, 26(20), 3515–3523.

Xin, C., Wang, Y., Sui, Y., Wang, Y., Wang, X., Zhao, K., Liu, Z., Li, B., and Liu, X. (2014). "Electronic, magnetic and multiferroic properties of magnetoelectric NiTiO$_3$." *Journal of Alloys and Compounds*, 613, 401–406.

Xu, C., Wang, X., Zhu, J., Yang, X., and Lu, L. (2008). "Deposition of Co$_3$O$_4$ nanoparticles onto exfoliated graphite oxide sheets." *Journal of Materials Chemistry*, 18(46), 5625–5629.

Xu, H., Chen, H., Li, X., Liu, C., and Yang, B. (2014). "A comparative study of jet formation in nozzle- and nozzle-less centrifugal spinning systems." *Journal of Polymer Science Part B: Polymer Physics*, 52(23), 1547–1559.

Xu, X., Gao, J., and Hong, W. (2016). "Ni-based chromite spinel for high-performance supercapacitors." *RSC Advances*, 6(35), 29646–29653.

Xu, Y., and Xu, R. (2015). "Nickel-based cocatalysts for photocatalytic hydrogen production." *Applied Surface Science*, 351, 779–793.

Xue, J., Xie, J., Liu, W., and Xia, Y. (2017). "Electrospun nanofibers: New concepts, materials, and applications." *Accounts of Chemical Research*, 50(8), 1976–1987.

Xue, T. J., and Wilkie, C. A. (1997). "Thermal degradation of poly(styrene-*g*-acrylonitrile)." *Polymer Degradation and Stability*, 56(1), 109–113.

Yan, K., Kong, L.-B., Dai, Y.-H., Shi, M., Shen, K.-W., Hu, B., Luo, Y.-C., and Kang, L. (2015a). "Design and preparation of highly structure-controllable mesoporous carbons at the molecular level and their application as electrode materials for supercapacitors." *Journal of Materials Chemistry A*, 3(45), 22781–22793.

Yan, X., Tian, L., and Chen, X. (2015b). "Crystalline/amorphous Ni/NiO core/shell nanosheets as highly active electrocatalysts for hydrogen evolution reaction." *Journal of Power Sources*, 300, 336–343.

Yang, D., Lu, B., Zhao, Y., and Jiang, X. (2007). "Fabrication of aligned fibrous arrays by magnetic electrospinning." *Advanced Materials*, 19(21), 3702–3706.

Yang, G., Chang, W., and Yan, W. (2014a). "Fabrication and characterization of $NiTiO_3$ nanofibers by sol-gel assisted electrospinning." *Journal of Sol-Gel Science and Technology*, 69(3), 473–479.

Yang, J., Cho, M., and Lee, Y. (2016). "Synthesis of hierarchical $NiCo_2O_4$ hollow nanorods via sacrificial-template accelerate hydrolysis for electrochemical glucose oxidation." *Biosensors and Bioelectronics*, 75, 15–22.

Yang, X., Shao, C., Liu, Y., Mu, R., and Guan, H. (2005). "Nanofibers of CeO_2 via an electrospinning technique." *Thin Solid Films*, 478(1–2), 228–231.

Yang, X., Yu, X., Yang, Q., Zhao, D., Zhang, K., Yao, J., Li, G., Zhou, H., and Zuo, X. (2017). "Controllable synthesis and magnetic properties of hydrothermally synthesized $NiCo_2O_4$ nano-spheres." *Ceramics International*, 43(12), 8585–8589.

Yang, Y. C., Liu, Y., Wei, J. H., Pan, C. X., Xiong, R., and Shi, J. (2014b). "Electrospun nanofibers of p-type $BiFeO_3$/n-type TiO_2 hetero-junctions with enhanced visible-light photocatalytic activity." *RSC Advances*, 4(60), 31941–31947.

Yao, Y., Yang, Z., Sun, H., and Wang, S. (2012). "Hydrothermal synthesis of Co_3O_4–graphene for heterogeneous activation of peroxymonosulfate for decomposition of phenol." *Industrial & Engineering Chemistry Research*, 51(46), 14958–14965.

Yin, H., Zhan, T., Qin, D., He, X., Nie, Q., and Gong, J. (2017). "Self-assembly of dandelion-like $NiCo_2O_4$ hierarchical microspheres for non-enzymatic glucose sensor." *Inorganic and Nano-Metal Chemistry*, 47(11), 1–8.

Yin, J., Zhou, P., An, L., Huang, L., Shao, C., Wang, J., Liu, H., and Xi, P. (2016). "Self-supported nanoporous $NiCo_2O_4$ nanowires with cobalt-nickel layered oxide nanosheets for overall water splitting." *Nanoscale*, 8(3), 1390–1400.

Yoshimatsu, K., Mashiko, H., Umezawa, N., Horiba, K., Kumigashira, H., and Ohtomo, A. (2017). "Electronic structures and photoanodic properties of ilmenite-type $MTiO_3$ epitaxial films (M = Mn, Fe, Co, Ni)." *The Journal of Physical Chemistry C*, 121(34), 18717–18724.

Yousef, A., Barakat, N. A. M., Amna, T., Al-Deyab, S. S., Hassan, M. S., Abdel-hay, A., and Kim, H. Y. (2012). "Inactivation of pathogenic Klebsiella pneumoniae by CuO/TiO_2 nanofibers: A multifunctional nanomaterial via one-step electrospinning." *Ceramics International*, 38(6), 4525–4532.

Yu, N., Shao, C., Liu, Y., Guan, H., and Yang, X. (2005). "Nanofibers of $LiMn_2O_4$ by electrospinning." *Journal of colloid and interface science*, 285(1), 163–166.

Yu, X., Sun, Z., Yan, Z., Xiang, B., Liu, X., and Du, P. (2014). "Direct growth of porous crystalline $NiCo_2O_4$ nanowire arrays on a conductive electrode for high-performance electrocatalytic water oxidation." *Journal of Materials Chemistry A*, 2(48), 20823–20831.

Yu, Z., Li, H., Zhang, X., Liu, N., Tan, W., Zhang, X., and Zhang, L. (2016). "Facile synthesis of $NiCo_2O_4$@polyaniline core-shell nanocomposite for sensitive determination of glucose." *Biosensors and Bioelectronics*, 75, 161–165.

Yuan, C., Wu, H. B., Xie, Y., and Lou, X. W. (David). (2014). "Mixed transition-metal oxides: Design, synthesis, and energy-related applications." *Angewandte Chemie International Edition*, 53(6), 1488–1504.

Yuan, P., Fan, C., Ding, G., Wang, Y., and Zhang, X. (2012). "Preparation and photocatalytic properties of ilmenite $NiTiO_3$ powders for degradation of humic acid in water." *International Journal of Minerals, Metallurgy, and Materials*, 19(4), 372–376.

Yuh, J., Nino, J. C., and Sigmund, W. M. (2005). "Synthesis of barium titanate ($BaTiO_3$) nanofibers via electrospinning." *Materials Letters*, 59(28), 3645–3647.

Yuvaraj, S., Nithya, V. D., Fathima, K. S., Sanjeeviraja, C., Selvan, G. K., Arumugam, S., and Selvan, R. K. (2013). "Investigations on the temperature dependent electrical and magnetic properties of $NiTiO_3$ by molten salt synthesis." *Materials Research Bulletin*, 48(3), 1110–1116.

Zak, A. K., Majid, W. H. A., Abrishami, M. E., and Yousefi, R. (2011). "X-ray analysis of ZnO nanoparticles by Williamson-Hall and size-strain plot methods." *Solid State Sciences*, 13(1), 251–256.

Zeng, K., and Zhang, D. (2010). "Recent progress in alkaline water electrolysis for hydrogen production and applications." *Progress in Energy and Combustion Science*, 36(3), 307–326.

Zeng, Y., Wang, Y., Chen, J., Jiang, Y., Kiani, M., Li, B., and Wang, R. (2016). "Fabrication of high-activity hybrid $NiTiO_3/g-C_3N_4$ heterostructured photocatalysts for water splitting to enhanced hydrogen production." *Ceramics International*, 42(10), 12297–12305.

Zhang, C., Deng, L., Zhang, P., Ren, X., Li, Y., and He, T. (2017a). "Mesoporous $NiCo_2O_4$ networks with enhanced performance as counter electrodes for dye-sensitized solar cells." *Dalton Transactions*, 46(13), 4403–4411.

Zhang, G., Kataphinan, W., Teye-Mensah, R., Katta, P., Khatri, L., Evans, E. A., Chase, G. G., Ramsier, R. D., and Reneker, D. H. (2005). "Electrospun nanofibers for potential space-based applications." *Materials Science and Engineering: B*, 116(3), 353–358.

Zhang, G., Xia, B. Y., Wang, X., and (David) Lou, X. W. (2014). "Strongly coupled $NiCo_2O_4$-rGO hybrid nanosheets as a methanol-tolerant electrocatalyst for the oxygen reduction reaction." *Advanced Materials*, 26(15), 2408–2412.

Zhang, Q., Wang, L., Wei, Z., Wang, X., Long, S., and Yang, J. (2012a). "Large-scale aligned fiber mats prepared by salt-induced pulse electrospinning." *Journal of Polymer Science Part B: Polymer Physics*, 50(14), 1004–1012.

Zhang, Q., Wang, Y., Wang, Y., M. Al-Enizi, A., A. Elzatahry, A., and Zheng, G. (2016). "Myriophyllum -like hierarchical TiN@Ni$_3$N nanowire arrays for bifunctional water splitting catalysts." *Journal of Materials Chemistry A*, 4(15), 5713–5718.

Zhang, S., Zhu, X., Zheng, C., Hu, D., Zhang, J., and Gao, X. (2017b). "Study on catalytic soot oxidation over spinel type ACo_2O_4 (A = Co, Ni, Cu, Zn) catalysts." *Aerosol and Air Quality Research*, 17(9), 2317–2327.

Zhang, W., Li, H.-P., and Pan, W. (2012b). "Ferromagnetism in electrospun Co-doped SrTiO$_3$ nanofibers." *Journal of Materials Science*, 47(23), 8216–8222.

Zhang, X., and Lu, Y. (2014). "Centrifugal spinning: An alternative approach to fabricate nanofibers at high speed and low cost." *Polymer Reviews*, 54(4), 677–701.

Zhang, Y., Li, J., Li, Q., Zhu, L., Liu, X., Zhong, X., Meng, J., and Cao, X. (2007). "Preparation of In$_2$O$_3$ ceramic nanofibers by electrospinning and their optical properties." *Scripta materialia*, 56(5), 409–412.

Zhang, Y., Wang, Y., Jia, J., and Wang, J. (2012c). "Nonenzymatic glucose sensor based on graphene oxide and electrospun NiO nanofibers." *Sensors and Actuators B: Chemical*, 171–172, 580–587.

Zhang, Z., Koppensteiner, J., Schranz, W., and Carpenter, M. A. (2015). "Variations in elastic and anelastic properties of Co$_3$O$_4$ due to magnetic and spin-state transitions." *American Mineralogist*, 97(2–3), 399–406.

Zhao, J., Cheng, Y., Yan, X., Sun, D., Zhu, F., and Xue, Q. (2012). "Magnetic and electrochemical properties of CuFe$_2$O$_4$ hollow fibers fabricated by simple electrospinning and direct annealing." *CrystEngComm*, 14(18), 5879–5885.

Zhao, Y., Jia, X., Chen, G., Shang, L., Waterhouse, G. I. N., Wu, L.-Z., Tung, C.-H., O'Hare, D., and Zhang, T. (2016). "Ultrafine NiO nanosheets stabilized by TiO$_2$ from

monolayer NiTi-LDH precursors: An active water oxidation electrocatalyst." *Journal of the American Chemical Society*, 138(20), 6517–6524.

Zhou, G.-W., and Kang, Y. S. (2006). "Synthesis and characterization of the nickel titanate $NiTiO_3$ nanoparticles in CTAB micelle." *Journal of Dispersion Science and Technology*, 27(5), 727–730.

Zhou, L., Zhang, S., Cheng, J., Zhang, L., and Zeng, Z. (1997). "Optical absorptions of nanoscaled $CoTiO_3$ and $NiTiO_3$." *Materials Science and Engineering: B*, 49(2), 117–122.

Zhou, M., Lu, F., Lv, T., Yang, X., Xia, W., Shen, X., He, H., and Zeng, X. (2015). "Loss mechanism and microwave absorption properties of hierarchical $NiCo_2O_4$ nanomaterial." *Journal of Physics D: Applied Physics*, 48(21), 215305.

Zuo, F., Wang, L., Wu, T., Zhang, Z., Borchardt, D., and Feng, P. (2010). "Self-doped Ti^{3+} enhanced photocatalyst for hydrogen production under visible light." *Journal of the American Chemical Society*, 132(34), 11856–11857.

BIO-DATA

Sachin Kumar B.

Permanent address:

#507, First Floor,
SHESHAKRISHNA,
80 Feet Road, Maruthi Layout,
Vasanthapura, BENGALURU,
Karnataka, INDIA.
Pin Code - 560061

Contact Details:

Email ✉: u.sachy@gmail.com
Phone 📱 : +91-9964499597

Academic Qualifications:

Bachelor of Engineering in Mechanical Engineering (2011), from Department of Mechanical Engineering, The National Institute of Engineering (Autonomous College under Visvesvaraya Technological University, Belgaum), Mysuru, Karnataka, India.

Master of Technology in Materials Engineering (2013), from Department of Metallurgical and Materials Engineering, National Institute of Technology Karnataka, Mangaluru, Karnataka, India.

Research publications:

Articles in International Journals: 06
Articles in Conference Proceedings: 06
Chapters in Book: 01

List of Publications Based on Phd Research Work

In peer-reviewed journals:

Sachin Kumar, B., Shanmugharaj, A. M., Kalpathy, S. K., and Anandhan, S. (2017). "Some new observations on the structural and phase evolution of nickel titanate nanofibers." *Ceramics International*, 43(9), 6845-6857.

Sachin Kumar, B., Kalpathy, S. K., and Anandhan, S. (2018). "Synergism of fictitious forces on nickel cobaltite nanofibers: electrospinning forces revisited." *Physical Chemistry Chemical Physics*, 20(7), 5295–5304.

Sachin Kumar, B., Dhanasekhar, C., Venimadhav, A., Kalpathy, S. K., and Anandhan, S. (2018). "Pyrolysis-controlled synthesis and magnetic properties of sol-gel electrospun nickel cobaltite nanostructures." *Journal of Sol-Gel Science and Technology*, 86(3), 664-674.

Sachin Kumar, B., Gudla, V. C., Ambat, R., Kalpathy, S. K., and Anandhan, S. (2018). "A Mechanistic Study on the Structure Formation of $NiCo_2O_4$ Nanofibers Decorated with In Situ Formed Graphene-Like Structure." *Journal of Inorganic and Organometallic Polymers and Materials*, 28(5), 1885-1900.

Sachin Kumar, B., Gudla, V. C., Ambat, R., Kalpathy, S. K., and Anandhan, S. "Graphene Nanoclusters Embedded Nickel Cobaltite Nanofibers as Multifunctional Electrocatalyst for Glucose Sensing and Water-splitting Applications." *Under Review in Ceramics International*.

Sachin Kumar, B., Anandhan, S., and Kalpathy, S. K. "Magnetic properties of Electrospun Ilmenite/Spinel Nickel Titanate Nanofibers." *In the pipeline*.

Sachin Kumar, B., Tarafder, K., Shetty, A., Hegde, A. C., Gudla, V. C., Ambat, R., Kalpathy, S. K. and Anandhan, S. "Polymorph Nickel Titanate Nanofibers as Bifunctional Electrocatalyst towards Hydrogen and Oxygen Evolution Reactions." *In the pipeline*.

In conference proceedings:

Sachin Kumar, B., Kalpathy, S. K., and Anandhan, S. (2016). "Electrospun nanofibers of Spinel/ilmenite Nickel Titanate." *Second International Conference*

on Materials Science and Technology, ICMST-2016, St. Thomas College Palai, Kottayam, Kerala, India.

Sachin Kumar, B., Shanmugharaj, A. M., Kalpathy, S. K., and Anandhan S. (2016). "Some New Observations on the Structural and Phase Evolution of Nickel Titanate Nanofibers." *International Conference on Advanced Materials, SCICON-2016,* Amrita University, Coimbatore, Tamil Nadu, India (Invited paper).

Sachin Kumar, B., Kalpathy, S. K., and Anandhan, S. (2017). "Structural and Magnetic Properties of Polymorphic Nickel Titanate Nanofibers." *The 12th International Pacific Rim Conference on Ceramic and Glass Technology, PACRIM-12,* The American Ceramic Society, Waikoloa, Hawaii, USA (Received International Travel Scheme grants from Science and Engineering Research Board, Department of Science and Technology; and Alumni association, National Institute of Technology Karnataka).

Sachin Kumar, B., Gudla, V. C., Ambat, R., Kalpathy, S. K., and Anandhan, S. (2018). "Graphene Nanoclusters Embedded Nickel Cobaltite Nanofibers as Multifunctional Electrocatalyst for Glucose Sensing and Water-splitting Applications." *International Conference on Advanced Ceramics and Nanomaterials for Sustainable Development, ACeND-2018,* Indian Ceramic Society Karnataka Chapter and Christ (Deemed to be University), Bengaluru, Karnataka, India.